



UNIwersytet  
IM. ADAMA MICKIEWICZA  
W POZNANIU

Doctoral thesis

**Photoelectrochemical processes on nanosilicon –  
based nanocomposites produced by ALD**

**Procesy fotoelektrochemiczne w  
nanokompozytach na bazie nanokrzemu  
wytwarzanych metodą ALD**

by

Mykola Pavlenko

Doctoral dissertation conducted at the NanoBioMedical Centre under the  
supervision of **Prof. UAM dr hab. Igor Iatsunskyi**

Assistant supervisor: Dr. Mikhael Bechelany

The dissertation is submitted for the degree of  
*Doctor of Philosophy in Physics*

Faculty of Physics  
Adam Mickiewicz University, Poznań  
Poznań 2023

## Acknowledgments

This work was conducted under co-financial support by the project „Środowiskowe interdyscyplinarne studia doktoranckie w zakresie nanotechnologii” No. POWR.03.02.00-00-I032/16 under the European Social Fund - Operational Programme Knowledge Education Development, Axis III Higher Education for Economy and Development, Action 3.2 PhD Programme.

Significant financial support was also provided by PRELUDIUM 12 project (2016/23/N/ST3/01356) “Novel nanocomposites based on nanosilicon/metal oxide (TiO<sub>2</sub>, ZnO) for efficient hydrogen production by photoelectrochemical water splitting” and Visegrad Fund in the context of the project “Novel heterostructures based on metal oxide and graphene materials for efficient water-splitting and hydrogen production” (scholarship individual number 51810284)

\*\*\*

*I would like to express my deep gratitude to my supervisor for the motivation and support that he provided to me during my research work. I also want to thank all co-authors for their productive collaboration and contribution to the realization of my research.*

\*\*\*

*I'm grateful to the collective of the NanoBioMedical Centre for the pleasant atmosphere. I appreciate the incentive efforts and energy invested by Prof. Stefan Jurga into the development and evolution of the CNBM research facility.*

\*\*\*

*I would like to thank Dr. Lidia Szutkowska for her organizational work and efforts in the management of the POWR project.*

\*\*\*

*I'm deeply grateful to my mother Natalia for her kindness, endorsement and confidence in me.*

## Contents

Acknowledgments.....	I
Abstract .....	IV
Streszczenie .....	VI
Author publication included into thesis .....	IX
List of abbreviations.....	X
Declaration .....	XI
Introduction and motivation .....	12
Chapter 1 Photoelectrochemical water-splitting process .....	15
1.1. Approach to the hydrogen economy development .....	15
1.2. Water-splitting reaction .....	16
1.3. Physicochemical mechanisms of OER and HER .....	17
1.4. Requirements for the development of an efficient photoanode.....	22
1.5. Concepts of water-splitting cells.....	26
1.6. Materials for photocatalytic water-splitting .....	31
1.6.1. Metal oxides .....	34
1.6.2. Complex oxide compounds .....	36
1.6.3. Chalcogenides .....	39
1.6.4. Nitrides and oxynitrides.....	40
1.6.5. Plasmonic materials .....	41
Chapter 2 Silicon material in photocatalytic applications .....	47
2.1. Photoelectrochemical properties of silicon.....	47
2.1.1. Surface textures .....	48
2.1.2. Protective layer implementation .....	48
2.1.3. Catalysts application .....	49
2.1.4. Silicon photoelectrode designing.....	50
2.2. Fabrication of 1D silicon nanostructures .....	52
2.2.1. Metal-assisted chemical etching of silicon.....	54
2.2.2. Nanosphere lithography .....	57
2.3. Production of silicon-metal oxide nanocomposites by ALD .....	58
Chapter 3 Main research topics .....	63

<b>3.1. Co-authorship statements .....</b>	<b>63</b>
<b>3.2. Tailoring the structure, optical and photoluminescence properties of porous silicon/TiO<sub>2</sub> nanostructures .....</b>	<b>80</b>
<b>3.3. Enhancement of optical and mechanical properties of Si nanopillars by ALD TiO<sub>2</sub> coating.....</b>	<b>89</b>
<b>3.4. Silicon/TiO<sub>2</sub> core-shell nanopillar photoanodes for enhanced photoelectrochemical water oxidation .....</b>	<b>97</b>
<b>3.5. Enhancing photocatalytic performance and solar absorption by Schottky nanodiodes heterojunctions in mechanically resilient palladium coated TiO<sub>2</sub>/Si nanopillars by atomic layer deposition .....</b>	<b>108</b>
<b>3.6. Enhanced solar-driven water splitting of 1D core-shell Si/TiO<sub>2</sub>/ZnO nanopillars .....</b>	<b>116</b>
<b>Chapter 4 Papers, not included in the main research.....</b>	<b>125</b>
<b>4.1. Porous silicon-zinc oxide nanocomposites prepared by atomic layer deposition for biophotonic applications .....</b>	<b>125</b>
<b>4.2. Effect of porous silicon substrate on structural, mechanical and optical properties of MOCVD and ALD ruthenium oxide nanolayers .....</b>	<b>127</b>
<b>4.3. One and two-phonon Raman scattering from nanostructured silicon .....</b>	<b>129</b>
<b>4.4. Structural and XPS studies of PSi/TiO<sub>2</sub> nanocomposites prepared by ALD and Ag-assisted chemical etching .....</b>	<b>131</b>
<b>Chapter 5 Summary.....</b>	<b>133</b>
<b>5.1. Outline of research presented in this thesis.....</b>	<b>133</b>
<b>5.2. Future prospects .....</b>	<b>137</b>
<b>Grants and scholarships .....</b>	<b>139</b>
<b>Author publication list .....</b>	<b>140</b>
<b>Conference presentations and proceedings.....</b>	<b>142</b>
<b>References .....</b>	<b>145</b>
<b>Copyrights and permissions .....</b>	<b>163</b>
<b>List of figures .....</b>	<b>164</b>
<b>List of tables.....</b>	<b>165</b>

## Abstract

Photocatalytic hydrogen production from water with solar light at a commercial scale is an attractive approach for developing the so-called hydrogen economy and solving the problem of the increasing demand for renewable energy sources. Implementing an effective and low-cost photocatalytic nanomaterial could diminish the reliance on fossil fuels and decrease carbon pollution in the atmosphere. Such a nanomaterial is needed to match a number of requirements to sustain the uphill thermodynamic reactions effectively in the water-splitting process. This simple thermodynamic process requires the energy of 1.23 eV to conduct two half-reactions: HER, which implies a reduction of hydrogen ions to H<sub>2</sub> gas, and OER, which implies an oxidation of water to O<sub>2</sub> gas. These chemical reactions depend on the effective transport of protons and electrons. They require a suitable catalyst that effectively transforms the incident photons into the energy for the charge transfer. Various materials have been investigated for use in photocatalytic water-splitting applications over recent years. Most of them show the maximal absorbance and charge carriers separation efficiency in the solar spectrum's UV range. The IR and VIS ranges of the spectrum represent the major amount of incident solar energy. Therefore, it is a serious challenge for contemporary photovoltaics to develop nanomaterials that effectively separate and transfer the charge carriers in those ranges of the incident light spectrum. Achieving this goal is possible through engineering a nanocomposite material that combines the effectiveness of single materials in different solar spectrum ranges.

Transition metal oxides have received growing attention in photocatalytic studies due to their high abundance, low cost, facile synthesis and nontoxicity, and unique electronic properties. Among other metal oxides, owing to the high mobility of charge carriers and robust stability in electrolyte solutions, TiO<sub>2</sub> and ZnO gained much interest in engineering photoelectrode nanomaterials. Unfortunately, because of band gaps higher than 3.0 eV, the absorbance of these materials is only effective in the UV range. However, combining TiO<sub>2</sub> and ZnO with another material could efficiently use its properties and overcome the problem of low PEC efficiency in the whole solar spectrum. Silicon is a good choice because it is a well-studied, highly abundant and easily tuneable semiconductive material. Changing the doping concentration and type can readily tailor its electronic properties. At the same time, silicon's morphology and optical properties can be tuned by nanostructuralization via etching by various techniques. Besides, it can absorb light in the VIS range, as the band gap value is about 1.1 eV, which could be effective for photocatalytic applications. On the other hand, silicon's chemical stability is the main drawback of photocatalytic purpose usage. This problem could be solved

by applying a protective layer to the silicon surface. Such a layer must be chemically stable in harsh electrolytic solutions under different pH values and efficiently absorb the incident light.

In this thesis, consistent research was addressed to investigate the structural, optical and PEC properties of PSi material with a protective photocatalytic layer of transition metal oxide. Thin conformal layers of  $\text{TiO}_2$  and  $\text{ZnO}$  were deposited by the ALD technique on the PSi substrate, which was previously fabricated by MACE. Due to facile control of a surface-to-volume ratio during the MACE fabrication process, PSi represents a highly capable platform for nanocomposite engineering. A further increase in the specific area was realized through one-dimensional structurization by NSL. Owing to the high penetration ability of the deposited layer into the porous nanostructure, which is a noticeable feature of the ALD process, either  $\text{TiO}_2$  and/or  $\text{ZnO}$  form nanocrystallites inclusions inward of the PSi. These nanocrystallites inside the mesoporous silicon entail the quantum confinement effect, which is detected through changes in the optical properties of the nanocomposite. It results in enhanced separation, decreased recombination and facile transfer of photoinduced electron-hole pairs in the nanocomposite.

Studies represented in this thesis are focused on PSi/ $\text{TiO}_2$ , PSi/ $\text{ZnO}$  and PSi/ $\text{TiO}_2$ / $\text{ZnO}$  nanocomposites that exhibit efficient light harvesting, advanced mechanical and chemical stability, as well as the noticeable positive effect of quantum confinement on photocurrent yield. It demonstrated a comprehensive investigation of the influence of structure and morphology on the optical properties of fabricated nanocomposites. They were tested under solar-simulated light to prove photocurrent yield depending on pH and morphological features. The application of plasmonic nanoparticles and its impact on photocurrent yield is demonstrated as well.

The work presented in this thesis provides valuable information for applying silicon and transition metal oxides in the water-splitting process and achieving an increased PEC performance using these widely used semiconductors. The presented results could be useful in designing and engineering the photoanodes in PEC cells to realize an effective photocatalytic water-splitting.

## Streszczenie

Fotokatalityczna produkcja wodoru z wody na skalę komercyjną, przy wykorzystaniu światła słonecznego, jest atrakcyjnym podejściem do rozwoju tzw. gospodarki wodorowej i rozwiązania problemu rosnącego zapotrzebowania na odnawialne źródła energii. Wdrożenie skutecznego i taniego nanomateriału fotokatalitycznego może pomóc zmniejszyć zależność od paliw kopalnych oraz wpłynąć na zmniejszenie zanieczyszczenia atmosfery dwutlenkiem węgla. Taki nanomateriał powinien spełnić szereg wymagań, aby skutecznie podtrzymać reakcję termodynamiczną rozszczepiania wody. Ten proces termodynamiczny wymaga energii 1,23 eV niezbędnej do przeprowadzenia dwóch reakcji połówkowych: wydzielania wodoru, co oznacza redukcję jonów wodoru do gazowego  $H_2$ , oraz wydzielania tlenu, co oznacza utlenianie wody do gazowego  $O_2$ . Reakcje te wymagają również odpowiedniego katalizatora, który skutecznie przekształca padające fotony w energię niezbędną do przenoszenia ładunku. Ponadto efektywność rozszczepienia wody zależy również od efektywnego transportu protonów i elektronów. W ostatnich latach zbadano różne materiały fotokatalityczne stosowane do rozszczepienia wody. Większość z nich wykazuje maksymalną skuteczność absorpcji światła i separacji nośników ładunku w zakresie promieniowania ultrafioletowego (UV) widma słonecznego. Natomiast znaczna ilość padającej energii słonecznej jest reprezentowana przez promieniowanie podczerwone (IR) i światło widzialne (VIS). Dlatego też poważnym wyzwaniem dla współczesnej fotowoltaiki jest rozwój nanomateriałów, które skutecznie separują i przenoszą nośniki ładunku w tych zakresach widma. Osiągnięcie tego celu jest możliwe poprzez rozwój materiału nanokompozytowego, który łączy w sobie efektywność jednolitych materiałów w różnych zakresach widma słonecznego.

Tlenki metali przejściowych cieszą się coraz większym zainteresowaniem w badaniach fotokatalitycznych nie tylko ze względu na dużą liczebność, niski koszt, łatwą syntezę i nietoksyczność, ale także ze względu na unikalne właściwości elektroniczne. Wśród innych tlenków metali,  $TiO_2$  i  $ZnO$  zyskały duże zainteresowanie w inżynierii nanomateriałów fotoelektrod, ze względu na wysoką mobilność nośników ładunku i dobrą stabilność w roztworach elektrolitów. Niestety, ze względu na pasmo wzbronione większe od 3,0 eV, absorpcja światła w tych materiałach jest efektywna tylko w zakresie promieniowania UV. Jednakże połączenie  $TiO_2$  i  $ZnO$  z innym materiałem mogłoby skutecznie połączyć właściwości obu tych materiałów i przewyciężyć problem niskiej wydajności fotoelektrochemicznej w całym widmie światła słonecznego. Krzem jest pod tym względem dobrym wyborem, ponieważ jest dobrze przebadanym, występującym w dużej ilości i łatwo modyfikowalnym materiałem

półprzewodnikowym. Jego właściwości elektroniczne można łatwo zmodyfikować, zmieniając stężenie i rodzaj domieszki. Jednocześnie morfologię i właściwości optyczne krzemu można dostosować za pomocą nanostrukturyzacji poprzez wytrawianie różnymi metodami. Poza tym krzem może absorbować światło w zakresie widzialnym VIS, ponieważ wartość pasma wzbronionego wynosi około 1,1 eV, co jest skuteczne w zastosowaniach fotokatalitycznych. Z drugiej strony stabilność chemiczna krzemu jest jego główną wadą w zastosowaniach fotokatalitycznych. Problem ten można rozwiązać, nakładając na powierzchnię krzemu warstwę ochronną. Taka warstwa musi być chemicznie stabilna w mocno reaktywnych roztworach elektrolitycznych przy różnych wartościach pH i skutecznie absorbować padające światło.

Niniejsza praca składa się z zestawu spójnych tematycznie badań mających na celu badania właściwości strukturalnych, optycznych i fotoelektrochemicznych porowatego materiału krzemowego (PSi) z ochronną warstwą fotokatalityczną wykonaną z tlenków metali przejściowych. Cienkie warstwy  $\text{TiO}_2$  i  $\text{ZnO}$  zostały osadzone za pomocą techniki osadzania warstw atomowych (ALD) na podłożu PSi, które zostało wcześniej wytworzone metodą trawienia chemicznego ze wspomaganie katalizatora metalicznego (MACE). Dzięki łatwej kontroli stosunku powierzchni do objętości podczas procesu trawienia chemicznego MACE, PSi stanowi wysoce wydajną platformę do inżynierii nanokompozytów. Dalszy wzrost powierzchni właściwej uzyskano dzięki jednowymiarowej strukturyzacji za pomocą litografii nanocząstek polistyrenowych (NSL). Ze względu na dużą zdolność penetracji osadzonej warstwy w porowatą nanostrukturę, co jest zauważalną cechą procesu ALD,  $\text{TiO}_2$  i/lub  $\text{ZnO}$  tworzą charakterystyczne wtrącenia nanokrystalitów w porach PSi. Te nanokrystaliny wewnątrz PSi są źródłem efektu uwięzienia kwantowego (ang. quantum confinement), który jest wykrywany poprzez zmiany właściwości optycznych nanokompozytu. Wynikiem tego efektu jest dłuższy czas życia par elektron-dziura, zmniejszona rekombinacja ładunków oraz większa efektywność przenoszenia fotoindukowanych par elektron-dziura w nanokompozycie.

Badania przedstawione w tej pracy skupiają się na nanokompozytach PSi/ $\text{TiO}_2$ , PSi/ $\text{ZnO}$  i PSi/ $\text{TiO}_2$ / $\text{ZnO}$ , które wykazują wydajną absorpcję światła w całym zakresie długości fal. Ponadto wykazują się dobrą stabilnością mechaniczną i chemiczną, a ich główną zaletą jest zauważalny wpływ efektu uwięzienia kwantowego na zwiększoną wydajność fotoprądu. W pracy przedstawiono kompleksowe badanie wpływu struktury i morfologii nanokompozytów na ich właściwości optyczne pod kątem zastosowań fotokatalitycznych. Nanokompozyty przetestowano w warunkach symulowanego światła słonecznego, aby wykazać wydajność fotoprądu w zależności od pH i cech morfologicznych. Zademonstrowano również



zastosowanie nanocząstek plazmonicznych i ich wpływ na wydajność fotoprądu. Przedstawione wyniki badań mogą być przydatne w projektowaniu i inżynierii nowoczesnych fotoanod w ogniwach fotoelektrochemicznych co zapewni efektywniejsze w stosunku do elektrolizy, rozszczepienia wody.

## Author publication included into thesis

1. *Tailoring the Structural, Optical, and Photoluminescence Properties of Porous Silicon/TiO<sub>2</sub> Nanostructures*  
Igor Iatsunskyi, **Mykola Pavlenko**, Roman Viter, Mariusz Jancelewicz, Grzegorz Nowaczyk, Ieva Baleviciute, Karol Załęski, Stefan Jurga, Arunas Ramanavicius and Valentyn Smyntyna  
The Journal of Physical Chemistry C: 119, 13, 7164-7171, 2015  
[doi.org/10.1021/acs.jpcc.5b01670](https://doi.org/10.1021/acs.jpcc.5b01670)
2. *Enhancement of optical and mechanical properties of Si nanopillars by ALD TiO<sub>2</sub> coating*  
**M. Pavlenko**, E. L. Coy, M. Jancelewicz, K. Załęski, V. Smyntyna, S. Jurga and I. Iatsunskyi  
The Royal Society of Chemistry (RSC Advances): 6, 99, 97070-97076, 2016  
[doi.org/10.1039/c6ra21742g](https://doi.org/10.1039/c6ra21742g)
3. *Silicon/TiO<sub>2</sub> core-shell nanopillar photoanodes for enhanced photoelectrochemical water oxidation*  
**Mykola Pavlenko**, Katarzyna Siuzdak, Emerson Coy, Mariusz Jancelewicz, Stefan Jurga, Igor Iatsunskyi  
International Journal of Hydrogen Energy: 42, 51, 30076-30085, 2017  
[doi.org/10.1016/j.ijhydene.2017.10.033](https://doi.org/10.1016/j.ijhydene.2017.10.033)
4. *Enhancing Photocatalytic Performance and Solar Absorption by Schottky Nanodiodes Heterojunctions in Mechanically Resilient Palladium Coated TiO<sub>2</sub>/Si Nanopillars by Atomic Layer Deposition*  
Emerson Coy, Katarzyna Siuzdak, **Mykola Pavlenko**, Karol Załęski, Octavio Graniel, Marcin Ziółek, Sebastien Balme, Philippe Miele, Matthieu Weber, Mikhael Bechelany, Igor Iatsunskyi  
Chemical Engineering Journal: 392, 123702, 2020  
[doi.org/10.1016/j.cej.2019.123702](https://doi.org/10.1016/j.cej.2019.123702)
5. *Enhanced solar-driven water splitting of 1D core-shell Si/TiO<sub>2</sub>/ZnO nanopillars*  
**Mykola Pavlenko**, Katarzyna Siuzdak, Emerson Coy, Karol Załęski, Mariusz Jancelewicz, Igor Iatsunskyi  
International Journal of Hydrogen Energy: 45, 50, 26426-26433, 2020  
[doi.org/10.1016/j.ijhydene.2019.11.231](https://doi.org/10.1016/j.ijhydene.2019.11.231)

## List of abbreviations

<b>ABPE</b> – applied bias photon-to-current efficiency	<b>PL</b> - photoluminescence
<b>AFM</b> – atomic force microscopy	<b>PS I</b> – photosystem I
<b>ALD</b> – atomic layer deposition	<b>PS II</b> – photosystem II
<b>AM 1.5G</b> – 1.5 atmosphere thickness (global)	<b>PSi</b> – porous silicon
<b>CB</b> – conduction band	<b>PSi/MO<sub>x</sub></b> – porous silicon – metal oxide
<b>CVD</b> – chemical vapor deposition	<b>PVD</b> – physical vapour deposition
<b>DFT</b> – density functional theory	<b>PV-EL</b> – photovoltaic - electrolysis
<b>EDX</b> – energy-dispersive X-ray spectroscopy	<b>PV-PEC</b> – photovoltaic - PEC
<b>EIS</b> – electrochemical impedance spectroscopy	<b>QD</b> – quantum dot
<b>FIB</b> – focused ion beam	<b>RGO</b> – reduced graphene oxide
<b>GIXRD</b> – grazing incidence X-ray diffraction	<b>RHE</b> – reversible hydrogen electrode
<b>GPC</b> – growth per cycle	<b>RIE</b> – reactive ion etching
<b>hcp</b> – hexagonal close-packed	<b>SEM</b> – scanning electron microscopy
<b>HER</b> – hydrogen evolution reaction	<b>SPP</b> – surface plasmon polariton
<b>HOMO</b> – highest occupied molecular orbital	<b>SPR</b> – surface plasmon resonance
<b>HRTEM</b> – high resolution TEM	<b>STH</b> – solar-to-hydrogen
<b>IPCE</b> – incident photon-to-current efficiency	<b>TEM</b> – transmission electron microscopy
<b>IR</b> – infrared light	<b>TMC</b> – transition metal chalcogenides
<b>JDOS</b> – joint density of states	<b>TMD</b> – transition metal dichalcogenides
<b>LUMO</b> – lowest unoccupied molecular orbital	<b>UV</b> – ultraviolet light
<b>LSPR</b> – localized surface plasmon resonance	<b>VB</b> – valence band
<b>MACE</b> – metal-assisted chemical etching	<b>VIS</b> – visible light
<b>MBE</b> – molecular beam epitaxy	<b>VLS</b> – vapor-liquid-solid
<b>MOCVD</b> – metal-organic CVD	<b>XPS</b> – X-ray photoelectron spectroscopy
<b>NHE</b> – normal hydrogen electrode	
<b>NSL</b> – nanosphere lithography	
<b>OER</b> – oxygen evolution reaction	
<b>PC</b> – photocatalysts system	
<b>PEC</b> – photoelectrochemical	

## Declaration

### Declaration of the Author of this dissertation:

I hereby declare that this dissertation entitled “**Photoelectrochemical processes on nanosilicon-based nanocomposites produced by ALD**” submitted to the Faculty of Physics at the Adam Mickiewicz University for obtaining the degree of Doctor of Philosophy in Physics is original work except where specific reference is made to the work of other authors. The contents of this dissertation are original and have not been submitted in whole or in part for consideration for any other degree, award, or qualification to other universities. This dissertation is an authentic work of the Author and all the contents of the dissertation have been obtained by legal means.

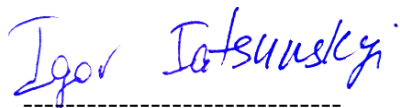


MSc Mykola Pavlenko

### Declaration of the thesis Supervisor:

I hereby certify that the above statement is true to the best of my knowledge and this dissertation is ready to be reviewed.

#### Supervisor



Prof. dr hab. Igor Iatsunskyi  
NanoBioMedical Centre  
Adam Mickiewicz University  
Poznan, Poland

#### Assistant supervisor



Dr. Mikhael Bechelany  
Institut Européen des Membranes  
(IEM)  
Université de Montpellier  
Montpellier, France

## Introduction and motivation

As a primary material of contemporary technologies, silicon has been one of the most investigated semiconductors since the mid-20<sup>th</sup> century. However, a discovery of intensive tunable luminescence in the visible spectrum on mesoporous silicon samples, caused by the quantum confinement effect in the nanocrystallites, was conducted only in the early 90<sup>th</sup>. Since then, PSi has been widely investigated and applied to various fields of applied science, such as optical emitters, biosensors, drug delivery components, batteries and fuel cell design, etc. Owing to its physicochemical properties, high surface-to-volume ratio, and facile fabrication, PSi is a prominent material for photocatalytic applications, except for its fast degradation in electrolytic media. Nevertheless, it is an appealing idea to use the narrow band gap of this semiconductor to utilize the visible part of the solar spectrum, which consists of the major part of incident solar energy. One of the extensively used photocatalytic material, TiO<sub>2</sub> possess an outstanding PEC performance in the UV range and good chemical stability. A thin layer of TiO<sub>2</sub> could be a robust protection of PSi photoelectrode and be transparent for IR and VIS light, which would directly be absorbed by silicon and induce excitation of electron-hole pairs. The quantum confinement effect, which is a distinctive feature of nanosilicon material, should provide additional enhancement to charge separation and hinder recombination. Proper technology and fabrication processes must be used to realize this idea. First, the morphology, pore proliferation and size of PSi must be precisely controlled. A typical MACE method is an excellent solution to this problem, considering the capability of implementing various lithographic methods. Second, the TiO<sub>2</sub> or another transition metal oxide layer must be deposited evenly with low thickness-derivation along the nanosilicon surface and effectively proliferate into the pores. The ALD technique is an obvious choice to solve this problem. Thus, the fabrication of PSi/TiO<sub>2</sub> nanocomposite with the aforementioned methods as well as its characterization and investigation of the PEC properties, represents the *main goal of this thesis*.

In order to reach this goal, it is necessary to answer the following questions:

1. How do morphological and structural properties affect the optical properties of PSi/TiO<sub>2</sub> nanocomposite fabricated by MACE and ALD?
2. How does PSi/TiO<sub>2</sub> nanocomposite act as a photoanode? What parameters are crucial for its operation?
3. How can the photocatalytic properties of the PSi/TiO<sub>2</sub> nanocomposite be enhanced?
4. How does engineering a core-shell nanocomposite based on PSi/TiO<sub>2</sub> affect the PEC properties?

Thus, this thesis presents research on structural, optical and PEC properties of P*Si*/TiO<sub>2</sub> that has been conducted by the Author mostly at the NanoBioMedical Centre at Adam Mickiewicz University in Poznan, under the supervision of Dr. Igor Iatsunskyi and co-supervision of Dr. Mikhael Bechelany. The thesis is divided into five main chapters. The first two chapters describe criteria, approaches and materials for photocatalytic water-splitting as well as a review of literature sources on this topic. In Chapter 1 discusses the main practices and approaches in photocatalytic water-splitting as well as single and multi-component materials used in this field. Chapter 2 is devoted to the technological processing of nanosilicon, its application in water-splitting, and the use of various transition metal oxides and approaches to make it an effective photocatalytic material. The main part of the thesis is Chapter 3, which is divided into six sections. The authorship and co-authorship statements are combined in the first section. Each following section consists of a peer-reviewed research article and answers to the questions prompted in this thesis.

The first article (section 3.2) shows the fabrication and characterization of P*Si* and P*Si*/TiO<sub>2</sub> nanocomposite. In this research, the morphological and structural properties were investigated and discussed. The correlation of structural features with optical characteristics of P*Si*/TiO<sub>2</sub> was demonstrated and explained. The impact of quantum confinement was demonstrated and examined by analyzing PL spectra under room temperature, and a model of PL excitation was proposed. The second article (section 3.3) is devoted to the 1D patterning of P*Si*/TiO<sub>2</sub> nanocomposite and the characterization of its structural and optical properties. The mechanical properties were also examined by nanoindentation testing since it is important for the mechanical stability of 1D P*Si*/TiO<sub>2</sub> photoanode under hydrodynamic impact in an aqueous electrolyte solution. In the third article (section 3.4), the 1D P*Si*/TiO<sub>2</sub> nanocomposite is investigated as a photoanode for water photooxidation. Here the correlation of PEC properties with morphological and structural features, like the length of the nanopillars, dependence on the thickness of the ALD-grown TiO<sub>2</sub> layer and pH value in the electrolyte were studied. The influence of the conductivity type of Si and TiO<sub>2</sub> on the PEC performance of the 1D core-shell P*Si*/TiO<sub>2</sub> nanocomposite was discussed as well. The fourth article (section 3.5) elucidates the impact of Pd nanoparticles on the mechanical, structural, optical and PEC properties of the 1D core-shell P*Si*/TiO<sub>2</sub> nanocomposite. Here the positive effect of SPR at Pd nanoparticles on the absorbance and PEC performance was demonstrated. It also proposed and discussed the principal model of charge carriers transfer inward the 1D core-shell P*Si*/TiO<sub>2</sub>/Pd nanocomposite structure. And the last article (section 3.6) shows a study on 1D core-shell P*Si*/TiO<sub>2</sub>/ZnO nanocomposite. Examining the structural, optical and PEC properties showed a

positive effect on charge separation and overall efficiency of  $\text{TiO}_2/\text{ZnO}$  compared to the  $\text{TiO}_2$  shell. The model and explanation of such results are also provided.

Chapter 4 contains research papers with the Author's contribution related to engineering and study on PSi and PSi/ $\text{MO}_x$  materials. The conclusions, main results and prospects of the research in this thesis are discussed in Chapter 5. The obtained results are important for further implementing nanosilicon and transition metal oxides into developing photocatalytic nanomaterials.



MSc Mykola Pavlenko

## Chapter 1 Photoelectrochemical water-splitting process

### 1.1. Approach to the hydrogen economy development

Throughout the whole history of humanity, humans have used the energy of chemical bonds stored in various fossil fuels, like wood, coal, oil and natural gases. Through centuries till the present day, overall energy consumption has only increased. Sustainable and renewable fuel is key to the development of the future of our civilization for the next generations. Excluding nuclear energy, the Sun is the most powerful available energy source [1]; it irradiates hundreds of watts per square meter diurnally [2]. Contemporary semiconductor technologies have enabled a relatively efficient harness of solar light since the discovery of the photovoltaic effect [3]. From simple silicon solar cells to today's complex nanomaterials, like perovskites [4], [5] and organic material [6], [7], the employment of quantum effects and complex nanoengineering approaches made solar panels relatively efficient but not cost-effective. Although solar cell technology is very promising and important, the world economy requires a more cheap and more useful energy source. Since our planet possesses plenty of water sources, the hydrogen extraction with solar energy is an obvious solution to this problem [8].

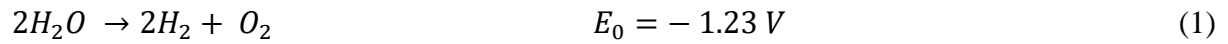
Hydrogen is an effective and renewable fuel, though its storage is not trivial [9]. Currently, hydrogen is mainly produced (around millions of tons per annum) from methane using substantial external energy, which depends on fossil fuels. Therefore, a realization of an appealing idea of hydrogen extraction with solar energy could significantly bolster the world's economic development and decrease carbon emissions into the atmosphere. A transition to hydrogen as the primary fuel is called hydrogen economy and is considered the most effective solution to the current energy and ecology crisis [10]–[12]. According to uphill chemical redox reactions, an extraction of H<sub>2</sub> from water with solar energy is possible through water dissociation. This process is called water-splitting and has already been accomplished by nature in natural photosynthesis [13], [14]. Thus, the most effective artificial water-splitting strategy is mimicking the photosynthesis process. It is realized in so-called artificial leaves, made from semiconductor materials like silicon [15]. However, stability and efficiency are still to be improved. Incident light excites electron-hole pairs separated in semiconductors, transferring to the active sites and taking part in chemical processes. Due to recombination on defect sites and low mobility of charge carriers, the efficiency of this process is relatively low. Therefore, the external bias of sufficient potential and catalysts are needed to make this process efficient.



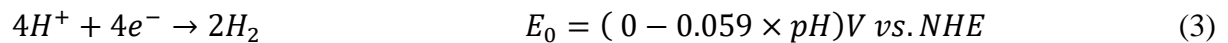
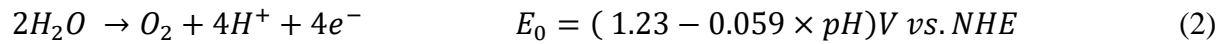
Thus, realizing-effective photocatalytic water-splitting relies mainly on the development of effective, robust and cheap materials.

## 1.2. Water-splitting reaction

The photocatalytic water-splitting process is an endogenic uphill chemical reaction with free Gibbs energy of  $\Delta G = 237 \text{ kJ/mol}$  (at 25 °C), induced by light on liquid water and results in the production of two gases, hydrogen and oxygen, as:



The thermodynamic potential of the reaction, noted here as  $E_0$ , is the most essential requirement for occurring of water-splitting. It defines the value of a band gap of more than 1.23 eV for semiconductors suitable for overall water-splitting. The effective separation, extraction and low recombination of photoexcited charge carriers, electrons and holes is also an important issue in driving HER and OER, respectively. These reactions are represented by two half-reactions, which could be realized on two different materials separately. The chemical equations are following:



The thermodynamic potentials of the reactions depend on the pH of the aqueous electrolyte solution in which the semiconductor is immersed. Its values can be calculated through the Nernst equation compared to NHE as shown in (2) and (3). External energy input is required since the reaction does not occur spontaneously and is thermodynamically unfavorable at ambient conditions (standard pressure and temperature). Considering a “classical” method of water-splitting via electrolysis, where the HER and OER occur at the electrode and anode separately, the external input should be more than 1.23 V (because of different losses), to sustain the reactions. This external input is called an overpotential [16]. An external voltage bias shifts the electrode potential from the equilibrium with the electrolyte solution and alters the potential difference along the electrical double layer at the electrode’s surface. Activation energies of every electrochemical step during the redox reactions are

functions of applied potential. The well-known Butler-Volmer equation [17] describes the dependence of activation energies at the electrode under applied potential in terms of overpotential. Under experimental conditions, the overpotential is simply defined as the additional applied potential to drive a given current density to achieve the OER with different catalysts. From the theoretical point of view, overpotential describes the additional voltage over 1.23 V vs. RHE that is needed to lower the highest free Gibbs energy for the electrochemical reaction's step.

### 1.3. Physicochemical mechanisms of OER and HER

The corresponding reactions of electrocatalytic water-splitting are:



The overall reaction considering (4) and (5) is:



Comparing the HER and OER reactions, the last one requires more energy to proceed. This reaction's occurrence significantly depends on pH and overcoming the activation energies during oxygen bond formation. These energy barriers can be decreased by using catalytic materials in acidic or basic electrolytes and tuning the concentration of active sites on the surface. The OER is a complex multi-step reaction [18]–[20], investigation requiring thorough theoretical, computational and experimental studies. A theoretical representation of OER occurrence steps at a metal electrode surface is shown as Scheme 1 in Table 1. In the case of metal, a high concentration of electron acceptors is located near the Fermi level. Generally, charge accumulation at either catalysts or co-catalyst materials has a crucial impact on the reaction rate. Some recent research [21] has shown that the activation energy decreases linearly with the amount of accumulated charge. Some other research [22]–[24] has elucidated the occurrence mechanisms of OER on oxide-hydroxide composites with the employment of extensively used co-catalysts based on Co, Fe and Ni.

## Chapter 1 Photoelectrochemical water-splitting process

In contrast to the metal material, the occurrence of OER on a semiconductor depends on holes concentration and transport at the surface. In this case, the main steps are shown as Scheme 2 in Table 1. An elucidation of charge carrier's behaviour under water-splitting conditions requires investigations on drift and diffusion mechanisms, rate constants of electrons and holes transport, and definition of boundary conditions [25]. Generally, the OER on the semiconductor surface can be described by a set of oxidation reactions involving holes, and reduction reactions involving electrons, of the intermediate species. The loss entailed by recombination processes could be described by reactions marked as (\*) in Scheme 2, neglecting the reduction of unbound molecular oxygen. More precise identification and investigation of chemical reactions with surface-bound species requires a thorough computational via DFT and spectroscopic analysis [26]–[28].

**Table 1. Schematic representation of OER occurrence involving active surface sites (M - notation of active surface site)**

Scheme 1: OER on the metal surface	Scheme 2: OER on the semiconductor surface (the collected concentration of holes $h^+$ at the surface is involved)
$M + H_2O \rightarrow M - H_2O$ $M - H_2O \rightarrow M - OH + H^+ + e^-$ $M - OH \rightarrow M - O + H^+ + e^-$ $M - O + H_2O \rightarrow M - OOH + H^+ + e^-$ $M - OOH \rightarrow M - O_2 + H^+ + e^-$ $M - O_2 \rightarrow M + O_2$	$M + H_2O \rightarrow M - H_2O$ $M - H_2O + h^+ \rightarrow M - OH + H^+$ $M - OH + H^+ + e^- \rightarrow M - H_2O (*)$ $M - OH + h^+ \rightarrow M - O + H^+$ $M - O + H^+ + e^- \rightarrow M - OH (*)$ $M - O + H_2O + h^+ \rightarrow M - OOH + H^+$ $M - OOH + H^+ + e^- \rightarrow M - O + H_2O (*)$ $M - OOH + h^+ \rightarrow M - O_2 + H^+$ $M - O_2 + H^+ + e^- \rightarrow M - OOH (*)$ $M - O_2 \rightarrow M + O_2$

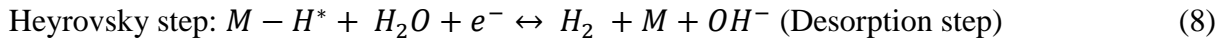
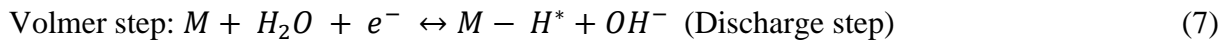
The light-driven OER on the semiconductor surface is a minority carrier reaction, which means that the surface concentration of reacting holes is determined by their generation rate as well as accumulation and recombination mechanisms. An applied potential changes the width of the space charge region and, as a result, influences the accumulation of photoinduced holes at the surface. At the same time, the external potential controls the rate of reduction reactions

## Chapter 1 Photoelectrochemical water-splitting process

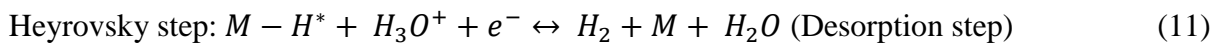
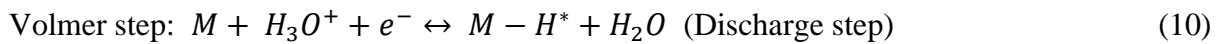
(shown in Scheme 2 in Table 1) by altering the electron concentration. Consequently, the holes are able to accept electrons of intermediate species from the oxidation reactions.

Compared to OER, the HER reaction is more effective due to its occurrence through multi-electron pathways than the single-electron pathway as the OER [29]–[31]. It demands lower overpotential compared to OER, but the presence of a catalyst is also required. The Platinum metal group is the most widely used catalytic material for HER. Generally, adding sacrificial agents, electron donors, and acceptors increases the water-splitting process's outcome.

The hydrogen production rate depends on surface reactions, including adsorption, desorption, discharge, and recombination processes. These processes are substantially dependent on surface features, like passivation. In an alkaline solution, the HER originally takes place with adsorption and dissociation processes, which break the H-O-H bonds and release H\* captured on the catalyst surface (M). The electron's kinetics follows Volmer-Heyrovsky or Volmer-Tafel processes. The following reactions could describe each step of which occurring:



The Volmer step in alkaline media is quite intricate compared to acidic HER; it involves adsorption and dissociation of water molecules at the catalyst's surface. The occurrence of these steps in acidic media includes a primary discharge step and following desorption or recombination (still the same as in alkaline media) steps are described as:



Wide band gap semiconductors, like transition metal oxides such as TiO<sub>2</sub>, usually have a band gap value of more than 3.0 eV and absorb light in the UV part of the solar spectrum. The resulting efficiency of overall water-splitting on single materials is low and requires additional catalyst and co-catalyst materials. The band gap could be narrowed through

## Chapter 1 Photoelectrochemical water-splitting process

additional levels induced by doping or structural changes, and the light absorbance would increase. Polymorphs of  $\text{TiO}_2$ , anatase and rutile, show different activity toward water-splitting reactions, for example. Defect states, such as interstitial Ti ions or oxygen vacancies, also substantially affect light absorbance and conductivity. For instance, in  $\text{ZnO}$ , another widely used in photocatalytic applications transition metal oxide, oxygen vacancies substantially changes the optical properties.

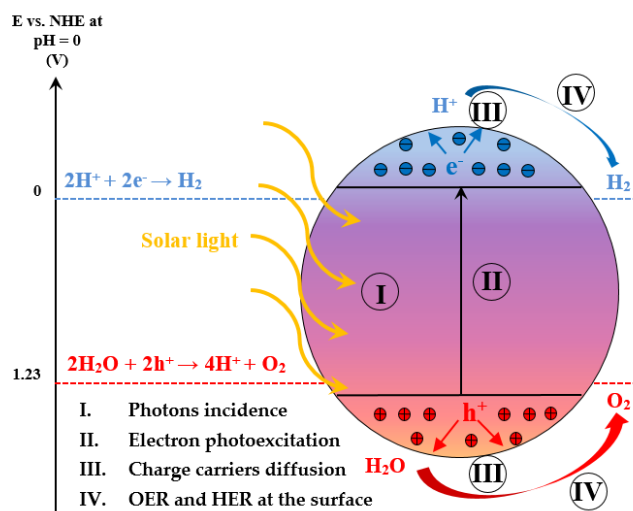


**Figure 1.** Graphic representation of photo-driven water-splitting process occurring on  $\text{TiO}_2$  nanoparticle as an example of main stages of water-splitting process occurring.

The main stages of the overall photocatalytic water-splitting process are shown in Fig. 1. First is the light incidence; at this step, the photon energy higher than the band gap value is absorbed by the semiconductor and induces free charge carriers. It should be noted that excessive thermal energy under intensive solar light or artificial AM 1.5 G illumination during the experiment could result in severe thermal degradation of semiconductor material and significantly decrease photoexcitation and charge carriers diffusion processes, stages 2 and 3, respectively. The low recombination and sufficient mobility of charge carriers in the semiconductor are crucial factors for efficient photocurrent response. At stage 4, the HER and OER proceed at the surface of the semiconductor material. The rate of these chemical reactions significantly depends on the presence and quality of catalysts and co-catalysts. The diverse photocatalysts are usually used to enhance light absorption, charge separation and transfer, and reduce the activation energy of gas evolution. Generally, these photocatalysts contain transition metal cations of  $d^0$  electronic configuration, like  $\text{Ti}^{4+}$ ,  $\text{V}^{5+}$ ,  $\text{Mo}^{2+}$ , etc., or cations of  $d^{10}$  electronic

## Chapter 1 Photoelectrochemical water-splitting process

configuration, like  $\text{Ag}^+$ ,  $\text{Zn}^{2+}$ ,  $\text{Ge}^{4+}$ , etc. The co-catalyst materials are usually represented by noble metals (e.g. Pt, Ag, Au) or transition metal oxides separately (e.g.  $\text{RuO}_2$ ,  $\text{IrO}_2$ ), or combined into complex multicomponent nanocomposites (e.g.  $\text{SrTiO}_3$ ,  $\text{RhCr}_2\text{O}_3$ ). Doped by Cr and Fe, the  $\text{TiO}_2$  material has demonstrated a stable and relatively efficient production of  $\text{H}_2$ .

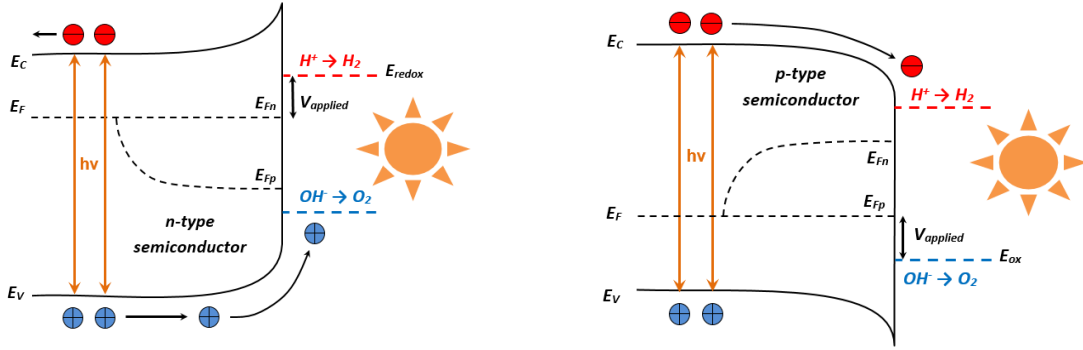


**Figure 2.** Schematic illustration of charge carriers photoexcitation on n-type and p-type semiconductors, and transfer to OER and HER sites, respectively.

The effectiveness of charge separation and excitation can be tuned through changes in the doping type or concentration. In Fig. 2 are demonstrated mechanisms of charge excitation and transfer to active sites for n-type and p-type semiconductors as occurrences of OER and HER, respectively. Positions of the Fermi quasi levels ( $E_{F_n}$  and  $E_{F_p}$ ) define the charge carriers kinetics under the light irradiation and rate of the water oxidation or reduction. At the same time, positions in the band gap and concentration of defect sites define the bulk and surface recombination processes. This problem is usually solved by engineering the nanocomposite's energy band structure. The built-in electric field induced by the deposited catalytic layer (e.g.  $\text{MoS}_2$ ,  $\text{MoSe}_2$ ,  $\text{CdS}$ ) facilitates the diminishing of the bulk recombination and the surface passivation layer hinders the surface recombination.

The concentrations of charge carriers under light irradiation are defined as:

$$n = N_C \left( \frac{1}{1 + \exp\left(\frac{E_C - nE_f}{k_b T}\right)} \right) \quad (12)$$

$$p = N_V \left( \frac{1}{1 + \exp\left(\frac{pE_f - E_V}{k_b T}\right)} \right) \quad (13)$$

## Chapter 1 Photoelectrochemical water-splitting process

where  $n$  and  $p$  are concentrations of electrons and holes,  $N_C$  and  $N_V$  are densities of states in CB and VB, respectively. Considering the n-type semiconductor under dark conditions, the equilibrium concentration of holes is too low as minority carriers. After irradiation of light with photons energy higher than the energy band gap of the semiconductor, the photoexcitation and separation of electrons and holes proceed. As a result, concentrations of excessive electrons in CB and holes in VB are accumulating. This excessive concentration of electrons can be neglected and the position of  $E_{F_n}$  almost coincides with the Fermi level  $E_F$  under dark. Conversely, the holes excessive concentration induces a shifting of  $E_{F_p}$  towards VB, resulting in a driving force for OER occurring. The difference between  $E_{F_p}$  at the surface and the equilibrium redox Fermi level of water oxidation (depicted as  $\text{OH}^- \rightarrow \text{O}_2$  in Fig. 2) determines the occurrence of OER on the active site and defines the overpotential for minority charge carriers.

Considering the reaction (4) in terms of the concentration of reactive species at the surface, the overall rate can be determined as:

$$\frac{d(\text{O}_2)}{dt} = k[\text{OH}^-]^\alpha p^\beta \quad (14)$$

where  $\alpha$  and  $\beta$  are the reaction orders,  $k$  is the rate constant and  $p$  is the holes concentration at the interface between the semiconductor and electrolyte, determined by Fermi quasi level. The chemical reaction orders can be theoretically estimated considering the kinetic mechanisms of the OER on a specific semiconductor. At the same time, the experimental estimation is quite complicated and requires complex investigations, for example in [32]–[35].

### 1.4. Requirements for the development of an efficient photoanode

The OER proceeds on the photoanode material, which is an n-type semiconductor with a band gap suitable for efficient light absorption in the broad spectrum range. It must possess sufficient mobility of charge carriers and stability under PEC operational conditions in the aqueous electrolyte solution. The non-toxicity and low-cost requirements are also reasonable for usability in real-life PEC systems. Increasing the photoanode material's specific area allows photocurrent and gas evolution scalability. Therefore, the nanostructured, nanoparticle and porous materials attract much interest in engineering PEC cells. For instance, various metal oxide materials (e.g.  $\text{TiO}_2$ ,  $\text{ZnO}$ ,  $\text{Fe}_2\text{O}_3$ ,  $\text{WO}_3$ ) have already demonstrated an enhanced

## Chapter 1 Photoelectrochemical water-splitting process

efficiency as mesoporous, nanowires, hierarchical and nanoparticles systems. But the PEC behavior of nanostructured porous materials is significantly affected by bulk and surface states introducing a non-ideality in a semiconductor material. Thus, the influence of morphological and structural features such as boundary grains, structural defects, pore size and nanocrystallite size must be considered when investigating photoanode properties.

First of all, the estimation of the semiconductor-electrolyte junction behavior of the photoanode material is important for the necessary calculations and models development. A convenient approach in this regard is the flat band potential  $U_{fb}$ , which describes the potential and charge carriers distribution at the semiconductor-electrolyte interface. Its value represents the photoelectrode potential at which CB and VB energies are constant, and there is no electrical field in the semiconductor site at the semiconductor-electrolyte junction. Under applied potential, the depletion or space-charged region is formed. This disturbance enables the withdrawal of the majority of charge carriers out of the junction. If the semiconductor possesses an n-type of conductivity, the positive space charge region is formed when the applied potential is more positive than  $U_{fb}$ . In the case of p-type (for HER) the converse statement is true. The doping type is represented by immobile ionized donors (n-type) or acceptors (p-type) inward the crystalline structure of the semiconductor. The width of the space-charged region  $W_{sc}$  depends on the doping density  $N$  and potential drop  $\Delta\varphi_{sc}$  across the space-charged region. This potential drop is corresponding to band bending  $q\Delta\varphi_{sc}$  at the semiconductor-electrolyte interface and allows estimation of energy barriers for charge carriers transport. The whole equation is:

$$W_{sc} = \left( \frac{2\Delta\varphi_{sc}\varepsilon\varepsilon_0}{qN} \right)^{\frac{1}{2}} \quad (15)$$

where  $\varepsilon$  is the relative permittivity of the semiconductor material.

The charge in the space charge region is balanced by an opposite charge at the electrolyte site induced by ions. The electrical double layer at the interface of the semiconductor-electrolyte allocates this charge along the outer Helmholtz plane. This distribution of charge is more effective for concentrated electrolytes. In terms of capacitance, the n-type semiconductor-electrolyte junction can be described by the following Mott-Schottky equation:

$$\frac{1}{C_{sc}^2} = \frac{2}{\varepsilon\varepsilon_0 N_d} \left( \Delta\varphi_{sc} - \frac{k_b T}{q} \right) \quad (16)$$



## Chapter 1 Photoelectrochemical water-splitting process

where  $C_{sc}$  is the capacitance of the space charge region in series with Helmholtz capacitance  $C_H$ . If the doping concentration is low or moderate, it is considered that  $C_H \gg C_{sc}$  and changes in the electrolyte potential occur mainly in the space charge region. For this condition, under applied potential  $U$ , the  $\Delta\varphi_{sc}$  can be replaced by  $U - U_{fb}$ . But, in the water-splitting process, it is possible that  $C_H \sim C_{sc}$  (e.g. for the non-stoichiometric oxides) and some additional charge could be accumulated at the surface of the semiconductor due to surface defect states. In such a situation, an effect of so-called Fermi level pinning takes place and the semiconductor could behave almost like a metal. Even in the case of passivated surfaces, like N-terminated TiO<sub>2</sub> or H-terminated Si, for instance, changes in potential drop appear along the Helmholtz layer and the potential is varied.

Holes are minority charge carriers in the n-type semiconductor. Characteristic lengths for their movement are represented by the width of the space charge region, the incident light penetration depth and diffusion length  $L_p$ . The last one is determined by the following equation:

$$L_p = \sqrt{\frac{k_b T}{q} \mu_p \tau_p} \quad (17)$$

where  $\mu_p$  is the holes mobility and  $\tau_p$  is the bulk lifetime of holes, which substantially depends on electron-hole recombination processes. The concept of diffusion length does not consider the surface and space charge region recombination processes. In the case of mesoporous semiconductor photoanode, the majority charge carriers density depends on the external bias voltage. Therefore the recombination rate is changing and the diffusion length is hard to determine. Also, the characteristic length scale could be much smaller than the Debye length  $L_D$ :

$$L_D = \left( \frac{\varepsilon \varepsilon_0 k_b T}{2q^2 N} \right)^{\frac{1}{2}} \quad (18)$$

This fact implies that the size of the nanostructure constituents (nanoparticles or nanocrystallites) is too small for a substantial band bending. Considering a spherical nanoparticle, the solution of the Maxwell-Boltzmann equation allows estimation of the maximal potential drop  $\Delta\varphi_{max}$  between the center of the nanoparticle and its surface, as:

$$\Delta\varphi_{max} = \frac{k_b T}{6q} \left( \frac{r_0}{L_D} \right)^2 = \frac{1}{3} \frac{r_0^2 q N}{\varepsilon \varepsilon_0} \quad (19)$$

Estimating small-size nanoparticles about a few tens of nanometers gives bend bending value in the order of meV. It is smaller than the thermal energy of  $k_b T$  order. Therefore, the bend-

## Chapter 1 Photoelectrochemical water-splitting process

bending effect can be neglected for minor constituents of nanocomposite materials. It can be considered that photoexcited charge carriers reach the surface by a diffusion process.

Under a light-driven OER, transferring minority charge carriers through the interface is quite a slow process. During the transfer, the minority charge carriers could be reflected back from the interface or recombined on the defect sites. In general, the recombination processes in the nanostructured oxide electrodes are still a wide topic for research.

To summarize, in the case of complex nanostructured photoelectrodes the small constituents can be almost field-free and significant electrical fields are only presented in the space charge regions at the larger constituents of the nanocomposite. For example, in the highly doped nanorods, the electron-hole separation processes are assisted mainly by the electric field perpendicular to the long axis, if the radius of the nanorod is larger than  $W_{sc}$ . In other words, the large parts of the nanocomposite structure accumulate the electrical field in the space charge region and this field assists the charge separation processes. At the same time, smaller nanostructures are mostly field-free, and only diffusion mechanisms occur. Therefore, in the hierarchical complex nanocomposites with different length scales, the space charge regions are confined at the larger morphological features and the collection of charge carriers proceeds at the small features via the diffusion mechanisms. Thus, the overall charge transfer is quite complicated and for fundamental investigations, it is better first to estimate the flat material surface.

The efficiency of nanocomposite photoanode in the photo-driven water-splitting process can be estimated through Gartner equation by the IPCE parameter:

$$IPCE = \frac{j_{photo}}{qI_0} = \frac{g}{I_0} = 1 - \exp\left(-\frac{\alpha W_{sc}}{1+L_p}\right) \quad (20)$$

where  $I_0$  is the intensity of incident light,  $g$  is the minority charge flux (holes for the photoanode),  $\alpha$  is the light absorption coefficient.

Considering the recombination processes in the semiconductor, the IPCE equation could be rewritten as:

$$IPCE = \frac{j_{photo}}{qI_0} = \frac{qg - j_{recomb}}{qI_0} = \frac{g}{I_0} \left( \frac{k_{tr}}{k_{tr} + k_{recomb}} \right) \quad (21)$$

where  $j_{recomb}$  is the recombination current,  $k_{tr}$  and  $k_{recomb}$  are the constants of holes transfer and electron-hole recombination.

## Chapter 1 Photoelectrochemical water-splitting process

For practical use, during the collection of the experimental data, the IPCE is usually estimated as:

$$IPCE(\lambda) = \frac{j_{photo}(mA \cdot cm^{-2}) \times 1239,8(V \cdot nm)}{P_{mono}(mW \cdot cm^{-2}) \times \lambda(nm)} \times 100\% \quad (22)$$

where  $j_{photo}$  is the measured photocurrent,  $1239,8 (V \cdot nm)$  is  $hc$  value (multiplication of the Plank constant to the speed of light in vacuum),  $P_{mono}$  is the intensity of incident monochromatic light. Since the IPCE value gives the photoanode's performance under specific light wavelength value, engineering complex multi-layer materials, where each layer is effective at a specific wavelength, would significantly increase the integral IPCE yield of such a nanocomposite. Additionally, the band gaps engineering would also impact the total performance.

### 1.5. Concepts of water-splitting cells

Generally, engineering systems have three primary strategies for water-splitting to produce hydrogen. There are photocatalysts (PC), photoelectrochemical systems (PEC) and photovoltaic-photoelectrochemical systems (PV-PEC) [36]–[38]. Basic concepts of the implementation of these systems are represented in Fig. 3.

The first strategy is considered the cheapest, potentially scalable and simple compared to PEC and PV-PEC. Usually, photocatalysts are used as powders, dispersed in water or deposited on a substrate to form a layered film, like photocatalysts sheet [39]. Employing powder photocatalysts does not require additional electrodes, electrical circuits and directional light focusing. On the other hand, this type of water-splitting system possesses some significant disadvantages that limit its applications. The PC systems efficiency is quite low, because the collection of produced gases from HER and OER is complicated and requires additional engineering approaches that consume energy. Additionally, backward reactions reduce the overall efficiency and lead to a photostationary state, where rates of forward and backward reactions are the same and overall water splitting significantly impedes.

## Chapter 1 Photoelectrochemical water-splitting process

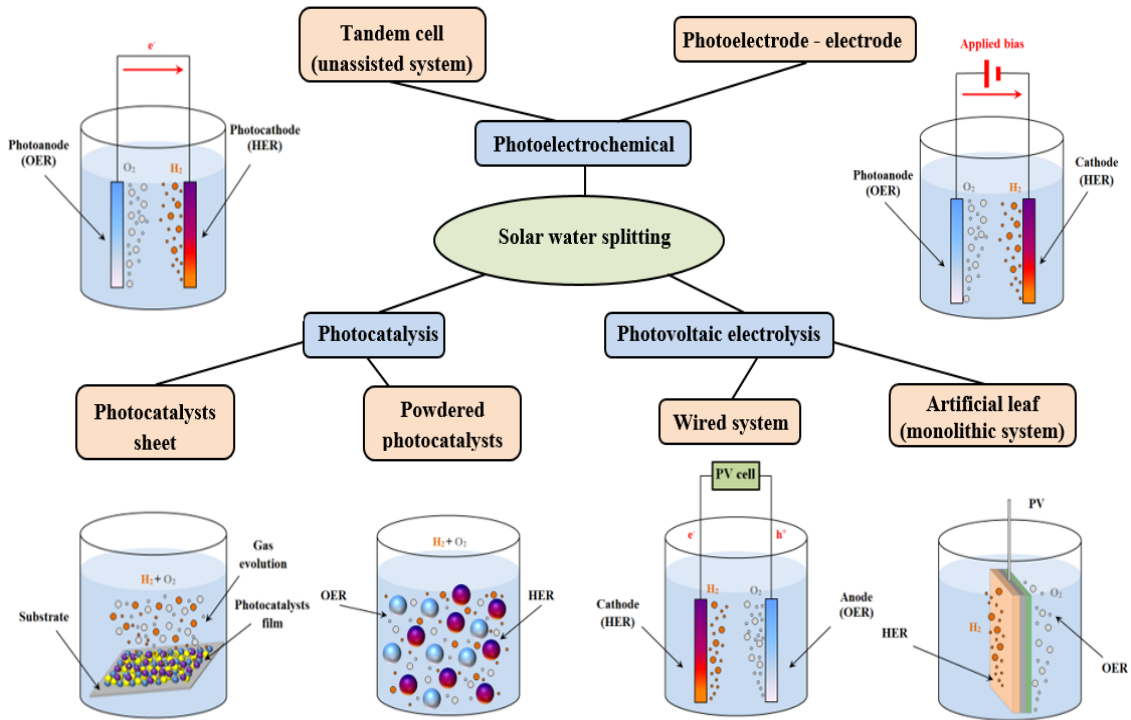


**Figure 3.** Various approaches in designing cell configurations for solar water splitting.

The second strategy is derived from the photoelectrochemical properties of metal oxides, like  $\text{TiO}_2$ , which was first reported as a photoelectrode [40]. PEC cell consists of two photoelectrodes, one or both made from semiconductor material, or one counter electrode could be metal, like Pt for  $\text{TiO}_2$  photoanode. In such a system, the photocatalytic material is deposited on a conductive substrate and it acts as a photoanode or photocathode in the PEC cell, where external bias is applied to sustain the water splitting. An excitation of photocurrent occurs on the photoactive electrode due to the separation and transfer of photoexcited electrons and holes in the semiconductor material. Depending on the conduction type of semiconductor, the minor and major charge carriers travel to active sites and sustain the occurrence of HER or OER. Combining the photoanode and photoelectrode in one PEC cell enables a realization of overall water splitting with two half-reactions.

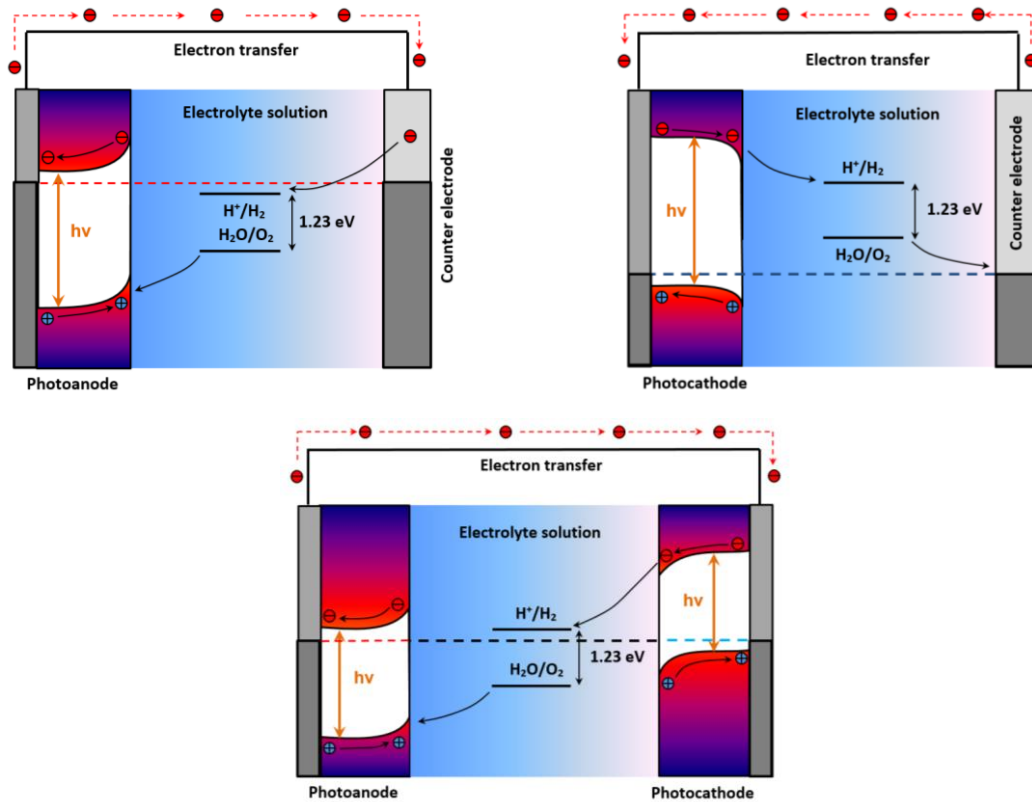


**Figure 4.** Configurations of photoanode, photocathode and combined PEC cells considering the energy diagrams of the employed semiconductor material.

In Fig. 4 are shown three configurations of PEC cells where OER and HER proceed separately on photocathode and photoanode sites. The electric circuit is completed through a platinum wire connected to the counter electrode. In the n-type semiconductor, the CB and VB bands are bent up and facilitate the OER (Fig. 4a) through holes transfer to the semiconductor-electrolyte interface. In the case of the HER, energy bands are bent down in the p-type semiconductor and facilitate the transfer of electrons (Fig. 4b). A combination of n-type and p-type semiconductors in one PEC cell enables the simultaneous occurrence of HER and OER (Fig. 4c). In this configuration, semiconductors with smaller band gap values could be used against larger band gaps in configurations for separate HER and OER. Therefore, the high photovoltage requirement is divided for two semiconductors with narrower band gaps. As a result, a higher photocurrent value can be achieved at two combined photoelectrodes configurations because of a more effective light absorbance by narrower band gaps semiconductors. Thus, this configuration has a significant advantage over the two previous ones, resulting in a higher STH production level. Since the HER and OER sites are spatially separated, the produced gas collection is much simpler than the PC system.

## Chapter 1 Photoelectrochemical water-splitting process

In order to avoid using external bias, a concept of unassisted water-splitting was developed to be realized in a so-called tandem scheme. This concept implies the employment of double light absorbers [41] in photoanode-photocathode configuration (PEC-PEC) or coupling with a photovoltaic device (PEC-PV) [42], [43]. A resulting tandem cell could generate a sufficient driving force to sustain a self-driven solar water-splitting. In the PEC-PEC cell, semiconductor photoelectrodes are connected in series, like top-on-bottom, where the top photoanode absorbs shorter wavelengths and the remaining longer wavelengths are absorbed by the photocathode. The PEC-PV tandem cell [44] consists external PV energy source and the PEC part comprises a photoelectrode and metal counter electrode.

Another variation of self-driven water-splitting could be considered a photovoltaic-electrolysis system (PV-EL), where OER and HER on the metal electrodes are sustained by external bias induced by the solar cell [45]. Such a system consists only the p-n junctions of the solar cell instead of the semiconductor-electrolyte junctions.

The overall water splitting could be achieved through a one-component photocatalyst by one-step photoexcitation or heterojunction-type photocatalysts comprised of II-type heterojunction. However, a single photocatalyst requires a sufficiently narrow band gap to utilize the significant part of incident light and favourable positions of CB and VB edges regarding water redox potentials. These two requirements are mutually exclusive. It is not feasible for a single-component material to satisfy the simultaneous requirement of a narrow band gap and sufficiently strong redox potential. Additionally, the density of charge carriers is restricted by surface and bulk recombinations [46]. Thus, employing of II-type heterojunction enables the induction of photoexcited electrons and holes at two different semiconductors. It noticeably increases the lifetime of photoinduced charge carriers. Schematic illustrations of one-component and II-type heterojunction photocatalysts are represented in Fig. 5a and Fig. 5b. To enhance the charge transfer and efficiency of water-splitting, a concept of the so-called Z-scheme system was proposed.

The concept of Z-scheme for overall photo-driven water-splitting is a combined system in which two-photon excitation processes proceed (Fig. 5c). This system was first proposed by Bard et al. in 1979 [47] to implement the idea of mimicking the natural photosynthesis process.

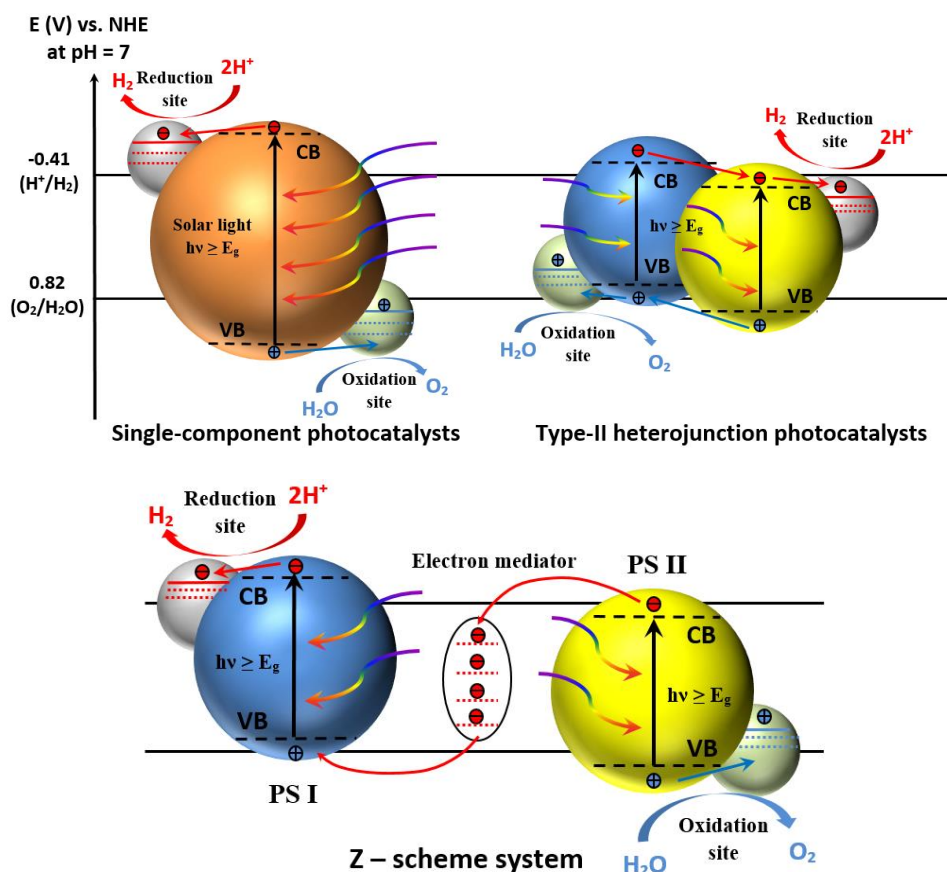


**Figure 5.** Graphical representation of the photoinduced water-splitting on (a) single-component photocatalysts, (b) type-II heterojunction photocatalysts and (c) Z-scheme with electron mediator involved.

Generally, the Z-scheme system consists of two photocatalysts for the implementation of HER and OER separately on different sites, and an electron mediator [48], [49]. These photocatalysts are referred to as photosystem I (PS I) and photosystem II (PS II) in Fig 5c. An electron mediator sustains the electron transport between these two photosystems. The presence of the electron mediator enables a formation of an electron-relaying channel through which the charge carriers could be accommodated at two different photocatalysts. Thus, PS II becomes a hole-rich site and sustains the OER, whereas PS I promotes the HER with accumulated electrons [50], [51]. Compared to single-component and type II heterojunctions, Z-scheme requires a lower change in the Gibbs energy to sustain overall water-splitting [52]. The concentration of electron mediator, pH value and type of co-catalyst have the most significant impact on the operation of Z-scheme systems.

In the first generation of PEC systems built with the Z-scheme, was used liquid electron mediator, like  $IO_3^-/I^-$  [53], as a source of donor-acceptor pairs. In such systems, the efficiency is affected by the possibility of backward charge carriers transfer and light absorption by the

mediator. As the next step, the second generation of the all-solid Z-scheme was proposed. In such a system, the ionic liquid mediator is substituted by the metal conductor, such as Au [54]. This change overcomes the backward reactions occurrence and decreases the path of electron flow [55]. A significant shortcoming of the second-generation Z-scheme is the employment of high-cost noble metals like Au and Pt. However, the substitution of the metal conductor as a mediator by carbon nanostructures, like carbon nanotubes [56], [57] or carbon quantum dots [58], could potentially solve this issue. A mediator-free approach represents the third generation of Z-scheme systems. In such a system, the solid-solid contact interface between two photosystems induces the internal electric field that controls the flow of electrons. Parameters of this field are strongly dependent on the properties of semiconductors. Such a type of Z-scheme was found in coupling ZnO with CdS [59] by chemical formation method [60]. And later, the solid-solid interface was investigated in physically formed SrTiO<sub>3</sub>:Rh – BiVO<sub>4</sub> Z-scheme under pH variation [61]. The Z-scheme solid-solid system is different from the type II heterojunction since the contact between two semiconductors is formed by the physical method [55] and represents the Ohmic contact properties. Such a system can be further implemented by employing synergistic effects in ternary compounds [62].

### 1.6. Materials for photocatalytic water-splitting

Materials for water-splitting use are chosen according to requirements such as the properties of constituent atoms, the crystalline structure, electronic properties, light absorption and interface/boundary properties. The most important requirement is stability under PEC operation conditions. This term usually implies stability against phase changing, segregation into constituents and dissolution in aqueous electrolyte. The electronic properties imply band gap value and its structure (direct or indirect), mobility of charge carriers (estimated by effective masses), separation and a lifetime of charge carriers and defects. The band bending at the interface with the electrolyte solution results from charge accumulation at the surface of the photoelectrode and an opposite charge at the electrolyte side of the interface. The interface properties depend on the electrolyte's pH and applied potential, and substantially affecting the extraction of charge carriers through the interface.



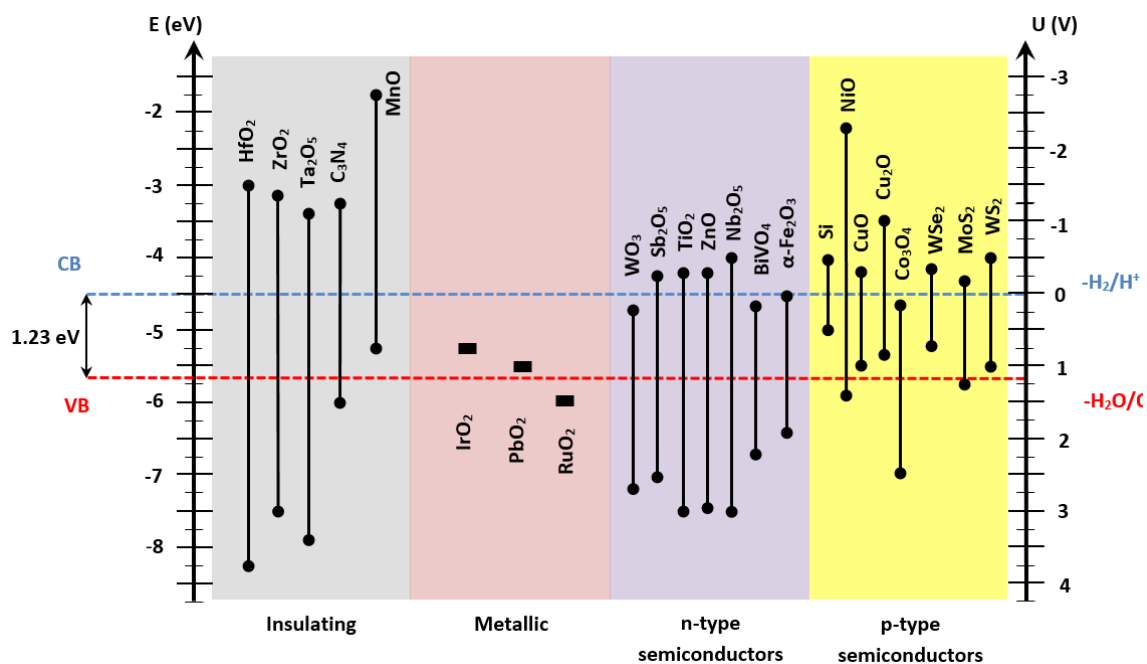


**Figure 6.** Band gap values comparison of some materials widely used for photocatalytic water-splitting applications.

Fig. 6. shows some examples of widely used photocatalysts regarding their band gap values (left axis) and redox potential values (right axis). Generally, the photocatalytic materials could be assigned to four groups: insulating (with wide energy band gap), metallic (with narrow band gap), n-type and p-type semiconductors. Thermodynamics places a stringent restriction on the occurrence of chemical reactions on the surface of photocatalysts. In order to proceed, the reduction reaction must correspond to a requirement that the potential level of CB is higher (more negative) than the redox potential of the LUMO of the acceptor molecules. On the contrary, for the oxidation reaction, the VB level must be lower (more positive) than the donor molecules' redox potential of the HOMO. Taking into account the positions of water oxidation and hydrogen reduction levels, it means that the CB level of the photocatalyst must be more negative than the H<sub>2</sub> reduction level, depicted as  $-H_2/H^+$  in Fig. 6. And the VB level must be more positive than the water oxidation level, depicted as  $-H_2O/O_2$ .

The reasonable requirements for an ideal photocatalytic material for overall photo-driven water-splitting are following:

1. Under light exposure, it must generate photovoltage of more than 1.23 V.
2. The band gap must be small enough to absorb as much light as possible.
3. The energy levels of the band gap must straddle the redox potentials of HER (0 eV) and OER (1.23 eV). Taking into account the overpotential value to compensate the

## Chapter 1 Photoelectrochemical water-splitting process

thermodynamic loss, the optimal band gap should be less than 2.2.eV. Still, the most suitable semiconductors in this range are exposed to degradation in electrolytic media.

4. It must be robust in aqueous electrolyte media. The metal oxides meet this requirement, but are ineffective due to a wide band gap.
5. Minimal energy loss in charge carriers transfer due to the kinetic overpotential.
6. It should be cost-effective.
7. It should gain at least 80% quantum yield to be commercially viable.

Unfortunately, till the current moment, there is no material that meets all these requirements simultaneously [63]. But, through the engineering of intrinsic properties of semiconductors, it is possible to hinder such detrimental effects as incomplete light trapping, nonradiative recombination, nonideal energy bands alignment, etc. Additionally, the employment of sensitizers, like QD [64]–[66], for instance, has already shown a positive effect on enhancing the properties of photocatalytic materials. The sensitizers are easily tunable in size and shape, enable the employment of quantum confinement effect, robust against photodegradation effects, possess a broad range of light absorption, etc.

The majority of binary compounds express photocatalytic activity after nanostructuring or doping. The VB location, in most cases, is located deeper than the water redox level. The oxygen substituting with nonmetal elements, like sulfur or phosphorous, shifts the VB and CB upward. Thus, approaches to independent band edge engineering in binary compounds are restricted and applying more complex materials is preferable for photocatalytic use. However, the application of catalysts could significantly improve the PEC activity. For example, GaP is an indirect semiconductor with a band gap of 2.3 eV that can sustain water-splitting due to band edges above hydrogen's reduction potential. However, its n-type is unstable in water in contrast to the p-type, which demonstrates longer stability under cathodic conditions [67], [68]. Due to interface properties, GaP does not yield the expected photocurrent, but adding Pt nanoparticles changes the interface properties and increases the photocurrent yield [69]. Another well-known semiconductive material, like GaP from the III-V semiconductors group, is InP. It has a direct band gap of 1.35 eV and CB located slightly above the water reduction potential [70], [71]. It could be used as a photocathode, but p-type InP is not stable in acidic electrolytes due to photocorrosion. This issue could be solved by the deposition of a TiO<sub>2</sub> protective layer [72].

Therefore, in order to create an efficient material, a set of criteria should be considered:

1. To overcome limitations of poor stability, wide band gap and poor transport of charge carriers.

2. To predict optoelectronic properties of the material considering the crystal structure and defect states.
3. To achieve long-term stability of the material in contact with an electrolyte solution.
4. To estimate carrier diffusion length and its increasing through lowering the recombination influence.
5. To optimize band gap positions compared to redox potentials of the water, through doping or structural changes.

### 1.6.1. Metal oxides

Generally, metal oxides are well known due to their stability in electrolytic media, especially as photoanode materials, due to a relatively high electronegativity of oxygen, which could form stable compounds based on  $O^{2-}$ . These materials possess wide range of band gaps, good electrical conductivity, favorable electronic transitions, relatively high absorption and dielectric constant. Transition metal oxides comprise ions with  $d^0$ , like  $Ti^{4+}$ ,  $Zr^{4+}$ ,  $Ta^{5+}$ , etc., and  $d^{10}$ , like  $Ga^{3+}$ ,  $Ge^{4+}$ ,  $Sb^{5+}$ , etc., electron configuration.

The simple binary metal oxides were discovered as the first stable and relatively efficient photocatalysts. In 1972 Fujishima and Honda [40] first achieved UV-light-assisted electrochemical water splitting using a  $TiO_2$  photoanode in a PEC cell. The main drawback of transition metal oxides, like  $TiO_2$  or  $WO_3$ , is the high energy band gap value. An incorporation of  $d^0$  cations in the crystalline structure of metal oxides leads to empty d-bands and the electronic structure consists of  $O\ 2p \rightarrow Ti\ 3d$  (or  $O\ 2p \rightarrow W\ 5d$  for  $WO_3$ , for example) transitions. The wide energy band gap results in poor light harvesting, since only a small part of solar energy lies in the UV range. Therefore,  $TiO_2$  and  $WO_3$  are not much efficient photocatalysts by themselves.

On the other hand,  $TiO_2$  has been widely implemented as a protective layer for various photoelectrodes that are not stable in water, like Si, InP or  $CuO_2$ , for example [72]–[74]. Significant efforts were addressed to engineering its band gap to enhance light absorption [75]–[78]. The nitridation of hydrothermally derived  $TiO_2$  in the  $NH_3$  atmosphere resulted in the narrowed band gap of up to 2.4 eV [79]. Adding co-catalysts, like Co or Ag, also demonstrated promising results. The further improvement of photocatalytic properties can be achieved through nanostructures, like nanotubes, that are widely used in PEC applications and photoelectrodes design [80].

## Chapter 1 Photoelectrochemical water-splitting process

$\text{WO}_3$  is an n-type semiconductor with an indirect band gap of 2.5-2.8 eV and is used as an inexpensive and nontoxic material for photoanode. It is stable in acidic media [81] and demonstrates an enhanced photocurrent yield after hydrothermal treatment and morphology adjustment [82], [83].

$\text{ZnO}$  is an environmentally friendly and inexpensive n-type semiconductor with a band gap of 3.2 eV. It is similar to  $\text{TiO}_2$  but possesses higher mobility of charge carriers. Thus, overcoming its limitations allows for the enhancement of photocatalytic properties [84]–[86]. For example, engineering p-n junctions of  $\text{TiO}_2/\text{ZnO}$  results in effective charge separation and chemical stability in OER [87]. Another effective p-n junction could be formed with  $\text{NiO}$  [88]. This semi-transparent and wide band gap (about 4.0 eV) p-type semiconductor possesses such features as high hole mobility, low resistance and low lattice mismatch with  $\text{ZnO}$ . The last one is a key feature for designing an efficient p-n junction [89], [90]. Despite a low photocurrent,  $\text{NiO}$  has demonstrated sufficient enhancement with  $\text{CdSe}$  sensitizers [91].

Another n-type semiconductive metal oxide, the hematite ( $\text{Fe}_2\text{O}_3$ ) has a band gap value of about 2.0-2.2 eV and a position of the VB suitable for OER [92]. This feature of hematite is ascribed to cations with partially filled d orbitals and allowing d-to-d transitions. The  $\alpha\text{-Fe}_2\text{O}_3$  possesses high stability to photocorrosion in harsh electrolytic media [93]–[95] and demonstrates a noticeable anisotropic behavior. For example, the transfer of electrons and holes is more accessible along the (001) crystal plane than in other directions. Hematite drawbacks are related to low absorption, low conductivity and short diffusion length (2 to 4 nm). The main shortcoming of the  $\alpha\text{-Fe}_2\text{O}_3$  usage as a single photocatalyst is a high surface recombination rate. These factors could be overcome through various synthesis methods that yield low defects concentration and achieve higher charge carriers mobility. Additionally, applying cobalt-phosphate and  $\text{IrO}_2$  co-catalysts has shown promising results in photocurrent stability and overpotential reduction [96].

$\text{Cu}_2\text{O}$  is one of the most investigated semiconductors and demonstrated a reasonable rate of charge transport and separation as a photocatalytic material. It has been widely used as a p-type photocathode material due to the direct band gap with a value of 1.9-2.2 eV and conduction band position enabling the HER. A noticeable drawback of  $\text{Cu}_2\text{O}$  is poor chemical stability, since the electrochemical potential for reduction to  $\text{Cu}^0$  is positive than the water reduction potential. Therefore, protective layers are needed to sustain its PEC operation usability. In combination with a  $\text{TiO}_2$  protective layer,  $\text{Cu}_2\text{O}$  demonstrated a good cathodic reduction of  $\text{Cu}^{2+}$  ions in pH 12 aqueous solution with photocurrent  $-7.6 \text{ mA/cm}^2$  at 0V vs. RHE [97]. Another variant of Cu-based oxide is  $\text{CuO}$ . It is a p-type semiconductor with an indirect

band gap of 1.2-1.8 eV. Therefore it can achieve a higher photocurrent than  $\text{Cu}_2\text{O}$  and demonstrate a noticeable hydrogen reduction [98]. The drawback of  $\text{CuO}$  is photocorrosion, which could be overcome by employing a protective layer [99], [100].

In summary, the shortcomings of employing metal oxides for either reduction or oxidation photo-driven reactions can be overcome through engineering multilayer and composite photoelectrodes. Thus, these materials are still promising for the designing of PEC cells as well as the development of more complex materials.

### 1.6.2. Complex oxide compounds

Binary metal oxides have been investigated as photocatalytic materials over decades. However, without complex nanoengineering approaches and modification of intrinsic properties, these photocatalysts represent a poor choice for developing cost-effective photoelectrodes. A prominent strategy to accumulate already available knowledge on binary metal oxide photocatalysts and overcome their drawbacks is synthesizing ternary or even more complex oxide material. There is a tenth of thousands of possible compositions of such materials, some of which could be effective in photocatalytic water-splitting. Band gap energy and positions of CB and VB depend on stoichiometry in such multi-component materials. One of the extensively investigated ternary metal oxides is bismuth vanadate ( $\text{BiVO}_4$ ), with a band gap energy of 2.4 eV, which has demonstrated noticeable performance in PEC reactions under VIS incident light [101]. Its CB position is located near the HER potential and the VB position requires a low onset potential for OER. The  $\text{BiVO}_4$  and its monoclinic polymorph, clinobisvanite, have an intricate band gap structure. For example, in the electron structure of  $\text{BiVO}_4$ , the  $s^2$  cation of  $\text{Bi}^{3+}$  is mixed with the  $d^0$  cation of  $\text{V}^{5+}$  and the electronic structure can exhibit a coupling between the s and the O 2p states forces an upward dispersion of the VB while the coupling between the d bands from the  $d^0$  cation and the p band from the  $s^2$  cation keeps the CB minimum low [102]. In the clinobisvanite variation of  $\text{BiVO}_4$ , the band gap is formed of a mixture of unhybridized O 2p states pushed up by Bi 6s states and form the VB edge, whereas V 3d states form the CB edge [103], [104]. The fabrication of  $\text{BiVO}_4$  material is relatively easy and implies extensively used and well-developed methods, like sol-gel coating, electrodeposition, spray deposition, etc. Usually, the fabrication process is implemented on conductive glass with subsequent annealing at  $500^\circ\text{C}$  to obtain a photoactive crystalline material. Although  $\text{BiVO}_4$  shows low photocurrent efficiency, fast recombination, slow water oxidation kinetics and charge transfer, it significantly enhanced nanostructured heterojunction

## Chapter 1 Photoelectrochemical water-splitting process

structures, like  $\text{BiVO}_4/\text{WO}_3/\text{SnO}_2$ . Incorporating  $\text{BiVO}_4$  into multi-component or multi-layered composite structures also protects it in strong basic and acidic electrolytes, where the PEC cells operate with the best results. Despite the oxide nature, the best chemical stability of pure  $\text{BiVO}_4$  is achieved at  $\text{pH}=7$ . The capability of water oxidation could be increased by the addition of the group VI metals, like Mo and W. Thus, further experiments with morphology control, doping concentration and co-catalysts could be promising.

Another promising class of complex oxides is ternary ferrites [105]. The ferrite formula is  $\text{AFe}_2\text{O}_4$  (where A is a metal cation in 2+ state, like Ba, Ca, Cu, Co, Mg, Mn, Ni and Zn) and the structure is based on  $\text{Fe}^{3+}$  cation, where the partially filled d-orbital states result in a higher lying of the VB edge comparing to the O 2p states and the hybridization of A cation with the CB results in tuning the band gap energy to avoid the localized Fe 3d-3d transitions. Ferrite materials can be used for photoanodes (e.g.  $\text{ZnFe}_2\text{O}_4$ ) and photocathodes (e.g.  $\text{CaFe}_2\text{O}_4$ ). The fabrication process includes preparing an amorphous thin film from various precursors by solution-based method and subsequent annealing to obtain a crystalline material in a spinel structure. As a light absorber by itself, ferrite displays low performance compared to  $\text{Fe}_2\text{O}_3$ , like  $\text{CuFe}_2\text{O}_4$  [106], for example. A thin ferrite layer is mainly used to enhance the light absorption properties of binary oxide, like the  $\text{ZnFe}_2\text{O}_4$  [107] light absorber layer on  $\text{Fe}_2\text{O}_3$ , for instance. However, the kinetic limitations for charge extraction in this structure result in restricted quantum efficiency.

Generally, Cu-based complex oxides are materials with noticeable features for PEC applications [108]–[111]. The instability of the previously mentioned  $\text{CuO}$  and  $\text{CuO}_2$  can be bypassed by introducing additional cations into their structure, which allows employing the copper 3d energy states for engineering the electronic properties. A strategy for developing Cu-based complex oxides, like niobates, tantalates, vanadates, etc., implies controlling the oxidative states of copper ( $\text{Cu}^+$ ,  $\text{Cu}^{2+}$ ) and the introduced cation. A good example of such material is  $\text{CuWO}_4$ , which contains  $\text{Cu}^{2+}$  and  $\text{W}^{6+}$  cations in a triclinic crystal structure [112]. Its indirect band energy (2.1 eV) semiconductor was successively applied as a photoanode and displayed good compatibility with commonly used photocatalysts [113], [114]. However, the charge transport properties in thin films are not sufficient enough. The main drawback of  $\text{CuWO}_4$  and materials of the same composition, like  $\text{CuTiO}_3$ , is a complex fabrication technology. Though the theoretical properties of such material could be promising, real-life synthesis and properties of as-prepared material are still significant issues. On the other hand, the potential of efficient band gap engineering is quite promising, since p-type  $\text{CuBi}_2\text{O}_4$  has demonstrated a band gap of 1.7 eV, determined by a complex structure, including O 2p and Cu

## Chapter 1 Photoelectrochemical water-splitting process

3d orbitals [115], [116]. The insufficient charge transport and stability issues have been demonstrated to be solved by optimized Ag doping. Additionally, developing electrodeposition [117] and hydrothermal [118] techniques for  $\text{CuBi}_2\text{O}_4$  synthesis could sufficiently improve the PEC characteristics along with tuning the structural properties.

An enhancement of PEC properties could also be achieved by engineering the crystallite structure in a sub-class of complex nanocomposites called delafossites. A general formula of this material is  $\text{ABO}_2$ , where A is a cation in a +1 oxidation state, like Ag, Pt, Pd or Cu, and B is a cation in a 3+ oxidation state, like transition metal, p-block elements or rare-earth metal. These materials with A cations as  $\text{Ag}^+$  and  $\text{Cu}^+$  as well as B cations as  $\text{Al}^{3+}$ ,  $\text{Cr}^{3+}$  and  $\text{Ga}^{3+}$ , demonstrated a noticeable oxidation activity as photoanodes for PEC applications [119]. Despite complex multi-step fabrication processes [120], delafossites are promising candidates for developing photocathode material for effective PEC cells, owing to narrow band gaps, high chemical stability in electrolytes and large absorption coefficient [121]. Application of electron-extracting overlayer of  $\text{TiO}_2$ , for example, or engineering a heterostructure on a delafossite base could improve the IPCE yield significantly [122].

A good example of delafossite material is  $\text{CuFeO}_2$ , with a band gap of 1.5 -1.6 eV, allowing absorption of VIS light [123]. It is stable in an electrolyte solution, but expresses low charge transport capability [124]. However, enhancing the crystalline quality through multi-step annealing and adding electrocatalysts, like NiFe or RGO, enhances the photocatalytic activity of  $\text{CuFeO}_2$  [125].

The noticeable structure of complex metal oxide compounds is also represented by perovskite material with the  $\text{ABO}_3$  formula. In general, these materials have demonstrated high chemical stability and promising optoelectronic properties, like small band gap energy [117], [126], [127]. As an example of such material,  $\text{LaFeO}_3$ , which demonstrated enhanced overall PEC response after additional doping with metals in 2+ oxidation state, like  $\text{Mg}^{2+}$  or  $\text{Zn}^{2+}$  [128]. Some perovskites, like hybrid lead halide [129], consist of lead and are considered not ecologically friendly materials, but express high charge carriers mobility and performance in photovoltaic devices. For instance, the high light absorption coefficient of lead halide perovskites, like  $\text{CN}_3\text{NH}_3\text{PbI}_3$ , is a result of direct transition at the band gap, which involves Pb s and p states. The efficiency of these materials has been demonstrated as 21% in photovoltaic devices and solar-to-hydrogen conversion about 12% in the presence of earth-abundant catalysts [130], [131].

### 1.6.3. Chalcogenides

TMC attracted much attention due to the facile tuning of the morphology and electronic properties [132]. These materials are often used as electrocatalysts for HER and OER. The main approaches to improving the TMC properties are building hierarchical assemblies, element doping, crystal phase manipulation and energy band engineering.

Reducing the dimension of material into 2D or 1D results in additional features not specific to a single material [133], [134]. Tuning the thickness in 2D material affects the electronic and structural properties, and enhances stability in the electrolytic solution. As an example, MoS<sub>2</sub> is an indirect band gap (1.23 eV) semiconductor, but its modification into a monolayer structure results in a direct energy band gap (1.8 eV) transformation [135]. As a result, optical properties are significantly changed, and the capability of light harvesting is changed as well. Additional improvements of such effects could be realized through heterojunction and defect engineering as well as alloy fabrication [136], [137].

Changing the structure of mono or dichalcogenides, like MoS<sub>2</sub>, WSe<sub>2</sub> or SnS, into 2D material substantially increases its PEC capabilities [138]–[140]. Since light absorption is one of the crucial factors for efficiency in the PEC process, the high JDOS near the VB and CB is highly preferential, because the total light absorption can be assumed to be proportional to JDOS. A high JDOS value results from various flat band locations, like d-bands, for example, near the VB and CB edges. Such an effect happened in FeS<sub>2</sub> [141] and MoS<sub>2</sub> [142] and entails a high light absorption in these materials. However, photoinduced charge carriers can form excitons, the bound electron-hole pairs. The excitons have large effective masses and screened Coulomb interaction. The structuralization of material into 3D, 2D or 1D noticeably affects the influence of excitons on charge transfer. In 3D inorganic semiconductors, the exciton energy is small, about 0.01 eV [143]. However, the screening is reduced in 2D and 1D materials, and the dielectric constant is increased. As a result, the exciton energy values are higher. In a monolayer of MoS<sub>2</sub>, for instance, the excitons binding energy is about 0.6 eV compared to bulk MoS<sub>2</sub> material with 0.1 eV [144].

One of the most studied materials for photocatalytic water-splitting is CdS due to a direct band gap of 2.4 eV. The location of the CB and VB edges of CdS is suitable to sustain both OER and HER [145]–[148]. However, the low separation, insufficient transport of charge carriers and photocorrosion make CdS a poor choice for effective photoelectrode material. Thus, improving the efficiency is possible through the fabrication of 2D nanostructures, which



## Chapter 1 Photoelectrochemical water-splitting process

increases the specific area and accumulation of charge carriers. Additionally, the stability of CdS could be improved in combination with another material [149], [150].

The next extensively used chalcogenide is ZnS, with the capability to sustain HER due to fast electron transport, high CB potential and the presence of active sites toward HER at the surface. The last feature suggests that expensive co-catalysts for HER, like RuO<sub>2</sub> or Pt, are redundant for ZnS [151], [152]. The wide band gap of 3.6 eV enables its employment only for the UV range. However, doping with transition metals, like Cu or Ni, improves hydrogen production under VIS light [153], [154]. Additionally, PEC properties could be enhanced through defect engineering in thin film layers [155].

Noticeable photoelectronic properties are also displayed by chalcopyrite materials, such as CuInS<sub>2</sub> or CuGaS<sub>2</sub>, for photocathode applications. CuInS<sub>2</sub> has a direct band gap of 1.5 eV and effective absorption of VIS light with a coefficient of about 10<sup>5</sup> cm<sup>-1</sup>. Though its fabrication is complex and expensive, developing such a method as spray pyrolysis could make the fabrication of CuInS<sub>2</sub> more effective [156]–[158]. CuGaS<sub>2</sub> has a wider band gap of 2.4 eV and requires more cathodic potential, but its localization of CB is more favorable for HER than in CuInS<sub>2</sub> [159]. Also, using co-catalysts such as Zn and Ti improved PEC efficiency [160].

### 1.6.4. Nitrides and oxynitrides

The CB edge in metal oxides is formed of empty d orbital (for transition metal) or s, p orbitals (for typical metal) that are located above the HER potential, whereas the VB edge includes O 2p orbitals that are located more positively than the OER potential. Considering the N 2p orbital, which is located higher than the O 2p orbital, it is promising to use nitride or oxynitride in PEC applications. Some oxynitride materials can be fabricated by facile methods from oxide powders [161]. Oxynitrides possess a narrower band gap compared to metal oxides. It is a result of the less negative position of the N 2p orbital related to oxygen orbitals.

Oxynitrides with d<sup>0</sup> electronic configuration based on ions Ta<sup>5+</sup>, Nb<sup>5+</sup>, Ti<sup>4+</sup> possess band gaps of 1,7–2,5 eV and positions of band edges suitable for overall water-splitting under visible light. However, some oxynitrides, like CaTaO<sub>2</sub>N, SrTaO<sub>2</sub>N and BaTaO<sub>2</sub>N [162], demonstrated low photocatalytic activity toward OER in the presence of sacrificial agents, like methanol and silver nitride. Considering the electronic structure, the d<sup>10</sup> configuration is more favorable to d<sup>0</sup> since the hybridized s,p orbitals possess large dispersion, which increases the mobility of photoexcited electrons in the CB. Solid solutions of (Ga<sub>1-x</sub>Zn<sub>x</sub>)(N<sub>1-x</sub>O<sub>x</sub>) and (Zn<sub>1-x</sub>Ge)(N<sub>2</sub>O<sub>x</sub>) [163] with d<sup>10</sup> electronic configuration are stable and photoactive materials for overall water-

splitting realization. However, its optical properties depend on stoichiometry, and a thorough analysis of the band gap structure is required for PEC applications [164]. As an example of oxynitride photocatalysts, TaON is an n-type semiconductor with a band gap of 2.5 eV, which can sustain an overall water-splitting reaction [165]. It is noticeable due to the relatively high achieved maximum quantum efficiency of 34% [166]. Though its band edges alignment allows sustaining OER and HER simultaneously, the H<sub>2</sub> production is low compared to O<sub>2</sub> [167]. The presence of N 2p orbitals in the VB results in low stability; therefore, additional catalysts, like Ru nanoparticles, or surface treatment are required [168], [169].

The structure of metal nitrides consists of the parent metal and nitrogen atoms allocated at the interstitial sites [170]. The introduction of interstitial nitrogen results in the increase of lattice distances, which changes the electron structure similarly to noble metals. Thus, metal nitrides demonstrate high catalytic activity toward HER. Therefore, metal nitrides, like W<sub>x</sub>N, Mo<sub>x</sub>N, TiN, Ni<sub>x</sub>N, Fe<sub>x</sub>N, Co<sub>x</sub>N are considered as a viable option for replacement the noble metals for photocatalytic applications. As an example, Ta<sub>3</sub>N<sub>5</sub> has a narrow band gap of 2.1 eV, which band edges positions could possibly sustain an unassisted water-splitting process and demonstrate good chemical stability [171]–[173]. Shortcomings of this material are low charge carriers transport, light absorption and photocurrent [174]–[176]. As with a variety of other materials, nanostructuring into 1D material and engineering of surface morphology result in improved PEC efficiency [177].

### 1.6.5. Plasmonic materials

During the interaction of the resonant electric field of the incident light with the metal surface, the resonant collective oscillations of conduction electrons, so-called plasmons, are excited. Plasmons are considered as quasi-particles. The term “resonant” is referred to matching the incident light frequency to the oscillation frequency of conduction electrons in the metal with negative real and positive imaginary dielectric constants.

The influence of plasmons on the optical properties can be controlled by the morphology of nanostructures through varying shapes, sizes, and periodicity of constituent parts. In noble metal nanoparticles, plasmons are localized at the surface, and this effect is called SPR. The plasmonic properties are easily tunable and open up a lot of opportunities for control of light interaction with the surface of nanoscale noble metal structures, such as nanoparticles, metallic arrays or thin films. This approach is widely used to enhance the properties of photoelectrode materials in photovoltaic or photoelectrocatalytic devices, for instance [178].

## Chapter 1 Photoelectrochemical water-splitting process

The SPR effect has two basic models: LSPR and SPP. The first one, LSPR, describes the stationary collective oscillations of valence electrons in the metal nanostructures. The second one, describes surface plasmon polaritons, represented by traveling waves of charge oscillations along the metal-dielectric interface, that could be observed during light interaction with ordered nanoholes, for example.

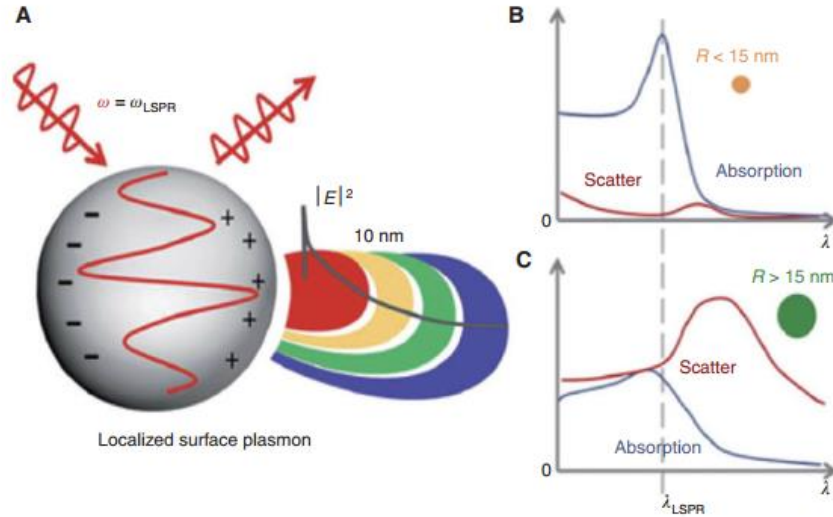


**Figure 7.** Graphical representation of LSPR influence on the optical properties of the material [179]. (a) Plasmon oscillations in phase with the incident light induce field perturbation resulting in absorption and scattering changes. Effect for nanoparticles: (b) smaller than 15 nm and (c) larger than 15 nm.

The electric field near the localized plasmons is increased by several times and decays exponentially with the distance. This perturbation of electromagnetic field along the surface induces a sharp optical absorption or scattering. The graphical representation of this effect is shown in Fig. 7.

Considering the Mie solution and Maxwell's equations [179], for light scattering and absorption on spherical nanoparticles with size less than incident light wavelength, the scattering cross-section  $\sigma_{exp}$  depends on:

$$\sigma_{exp} = 9 \frac{\omega}{c} \varepsilon_m^3 V_0 \frac{\varepsilon_2(\omega)}{(\varepsilon_1(\omega) + 2\varepsilon_m)^2 + \varepsilon_2(\omega)^2} \quad (23)$$

where  $V_0$  is the particle's volume,  $\omega$  is the angular frequency of the incident light,  $\varepsilon_m$  is the dielectric function of the medium in which the particle is located,  $\varepsilon_1(\omega)$  and  $\varepsilon_2(\omega)$  are the real and imaginary parts of the dielectric function of the nanoparticle material. Therefore, the crucial

## Chapter 1 Photoelectrochemical water-splitting process

impact on light scattering is provided by the dielectric properties of nanoparticles material and size as well as the dielectric properties of media. The changes in the dielectric function result in a change in the related LSPR peak in the absorption spectrum, where the real part affects the position of the peak, while the imaginary part affects the broadening. The resonant enhancement of the field in the vicinity of the particle is defined by condition  $\varepsilon_1(\omega) = -2\varepsilon_m$ . This condition is satisfied in VIS and IR ranges for Au and Ag nanoparticles.

Therefore, employing LSPR nanoparticles in engineering the photoelectrode material leads to stimulation of light absorption. In a situation when the minority charge carriers with relatively short lifetimes are not involved in water-splitting reactions, the inclusion of LSPR nanoparticles at the interface leads to minority carriers generation and transfer closer to the active sites of whether OER or HER. For effective application of LSPR nanoparticles their stability, Fermi level and band bending should be considered under PEC conditions. An example of a successful implementation of plasmon-enhanced PEC reactions can be considered for Ag nanoparticles [180]. The presence of Ag plasmonic nanoparticles at the surface of N-TiO<sub>2</sub> induce an increased electric field and facilitates the increase in the rate of electron-hole pairs formation in the vicinity of Ag nanoparticles. As a result, the photocurrent noticeably increases. Engineering of a more complex structure with Au nanoparticles, like flower-like core-shell Au/Ag/TiO<sub>2</sub> nanocomposite [181], significantly enhances the photocatalytic activity in the VIS range for commercially available P25-TiO<sub>2</sub>. The enhancement mechanism implies the employment of hot electrons from photoexcited Ag/Au core for injection into CB of TiO<sub>2</sub>. An effective charge separation prevents the recombination of electron-hole pairs and increases the photocatalytic activity 4.7 times compared to pure P25-TiO<sub>2</sub>. Implementing plasmonic nanoparticles on 1D nanostructures of metal oxides resulted in the realization of complex charge transfer and separation mechanisms for enhancing the PEC activity. As an example, in [182] demonstrated increased photocurrent density and photoconversion efficiency on the heterostructure of ZnO sensitized by Au plasmonic nanoparticles. The proposed mechanism is presented in Fig. 8. Under illumination, ZnO absorbs UV light and photoexcited electrons and holes accumulate at the CB and VB edges. At the same time, the Au nanoparticles introduced on the surface of 1D ZnO ordered nanostructure absorb VIS light and produce photoelectrons due to LSPR. As sensitizers, Au nanoparticles generate hot electrons and inject them into the CB of ZnO through the Schottky barrier. These electrons, driven through the electric circuit to the Pt electrode, induce additional electron flow for sustaining HER. At the same time, photoexcited holes in the VB transfer to the surface and proceed the OER. The efficiency of charge separation and transfer depends on ZnO's crystalline quality and the ZnO-Au interface's

properties. Therefore, properly engineering such nanostructures is highly required to avoid recombination on defect states. Such a relatively simple PEC system clearly demonstrates the effect of plasmonic nanoparticles on the enhancement of photocurrent density and water-splitting efficiency.

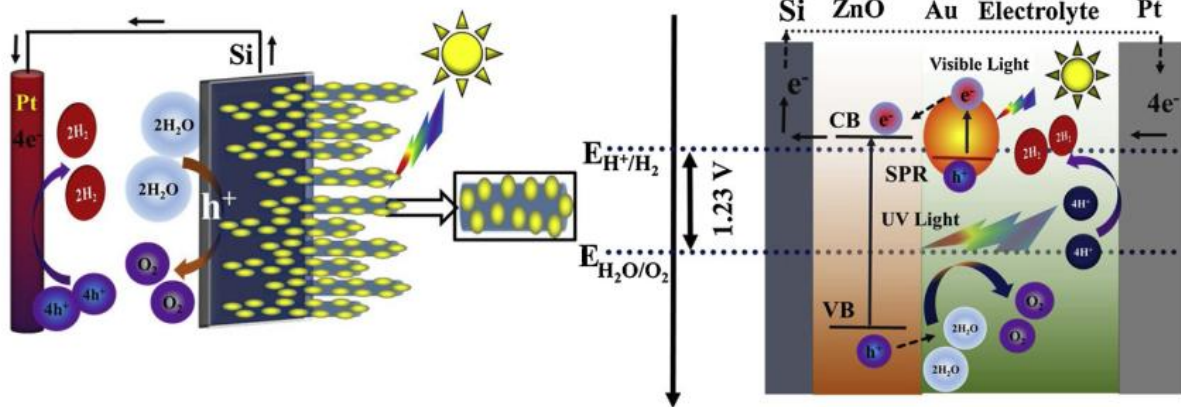


**Figure 8.** Schematic representation of PEC operation of 1D ZnO heterostructures enhanced by Au plasmonic nanoparticles [182].

Enhancement of PEC efficiency can be demonstrated for other metal oxide materials. A noticeable improvement in Faraday efficiency was detected for  $\text{WO}_3/\text{Au}$  [183] composite photoanode, from 74% for  $\text{WO}_3$  up to 94% with the presence of plasmonic Au. With proper engineering of heterojunctions for efficient separation and transfer of charge carriers, the employment of LSPR significantly improves the performance of composite materials, like  $\text{TiO}_2/\text{Fe}_2\text{O}_3/\text{Ag}$  [184],  $\text{WO}_3/\text{Cu}/\text{Bi}_2\text{S}_3$  [185],  $\text{Au}/\text{BiVO}_4/\text{ZnO}$  [186], etc. Generally, the LSPR efficiency depends on the rational design and nanoarchitecture of the nanostructures where the plasmon effects are mentioned to use. An example of such an approach can be considered for 3D hollow nanospheres, like  $\text{Au}/\text{SrTiO}_3/\text{TiO}_2$  [187].

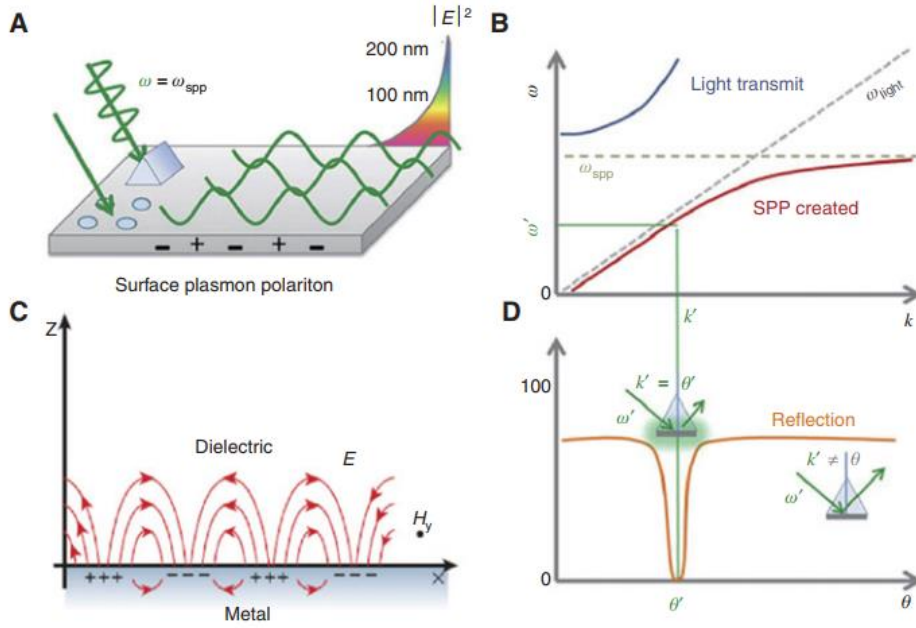


**Figure 9.** Graphical representation of SPP [179]: (a) propagation of SPP along the metal-dielectric interface boundary and decaying of its amplitude out of the interface, (b) representation of SPP existence and extreme values in  $\omega(k)$  space, (c) an illustration of SPP wave at the interface metal-dielectric, (d) representation of SPP existence under certain incident angles.

In contrast to LSPR, SPP is not able to be excited by VIS light. A basic representation of SPP theory is described in [188] and [189]. The SPP exists at the boundary of two dielectric media (Fig. 9a) and decays with distance (Fig. 9b). The dispersion relation could be described as:

$$K_{spp} = k \sqrt{\frac{\epsilon_d \epsilon_m}{\epsilon_d + \epsilon_m}} \quad (24)$$

where  $\epsilon_d$  and  $\epsilon_m$  are dielectric functions of the metal and dielectric media,  $K_{spp}$  and  $k$  are wave vectors for SPP and free-space, respectively. More detailed theory and experimental approach can be found in [190] and [191]. The coupling condition between light and SPP is  $\epsilon_d + \epsilon_m = 0$ . This condition overcome the mismatch in SPP and incident light momentum, and result to a resonance condition with the resonance frequency  $\frac{\omega_p}{\sqrt{1+\epsilon_d}}$ .

As seen from a graphical representation of the SPP wave in Fig. 9c, the penetration depth into the dielectric is longer than in the metal.

As an example of SPP employed in PEC applications, it could be used to control the behavior of hot electrons in photoelectrodes [192] with structure engineering that includes nanohole arrays in Au thin film [193].

## **Chapter 1 Photoelectrochemical water-splitting process**

To summarise, the main advantages of plasmonic materials are tunable resonating wavelength, enhanced light absorption, reduced diffusion length, enhanced local electric field, and capability of Schottky junction employment.

# Chapter 2 Silicon material in photocatalytic applications

### 2.1. Photoelectrochemical properties of silicon

Owing to a band gap of about 1.12 eV the Si material is beneficial to absorb light in the major part of the solar spectrum. The theoretical maximum photocurrent of the Si photoelectrode can reach a value up to 44 mA/cm<sup>2</sup> under a simulated one Sun AM 1.5 G incident light, making Si a promising material for PEC applications [194], [195]. However, there are some limitations to employing a pure Si material for photoelectrode designing. In contact with aqueous electrolytes, the Si surface suffers from photoanodic corrosion and the growing layer of oxidized Si results in drastic degradation of PEC performance. Thus, an operational Si photoelectrode design requires using protective layers against a harsh electrolytic environment. Besides, the sluggish kinetics of water-splitting reactions substantially limit the efficiency of the Si photoelectrode [196], [197].

One of the most important requirements for the photoelectrode material is long-term stability in the aqueous media. The thermodynamic stability of the semiconductive material under the PEC conditions is defined by the alignments of the reduction and oxidation potentials relative to respective potentials for HER (H<sup>+</sup>/H<sub>2</sub> potential) and OER (O<sub>2</sub>/H<sub>2</sub>O potential), for the photocathode and photoanode respectively [198]. Thus, considering the respective potentials for Si, corrosion takes place under anodic conditions. Additionally, the influence of electron-hole pairs photoexcitation, surface electronic properties, electrolyte properties and biasing conditions should also be considered in the elucidation of the corrosion mechanism [199]. Though Si is theoretically stable under cathodic conditions, the practical applications revealed the formation of a SiO<sub>2</sub> layer due to the presence of oxygen species in the electrolyte solution. This layer insulates the surface and impedes PEC performance [200]. For example, such a layer can form a 3.1 eV barrier at the surface of the n<sup>+</sup>p-Si photocathode in the acidic electrolyte [201].

The oxidation of the Si surface under light irradiation could be reduced by improving the charge transfer at the silicon-electrolyte interface by catalyst application. However, under dark conditions, a chemically stable layer must protect the Si surface to avoid oxidation. This layer should possess sufficient conductivity and transparency to sustain effective light harvesting [202], [203]. Commonly used earth-abundant photocatalysts could be used with silicon material [204]. Such layers, like ALD-derived Al<sub>2</sub>O<sub>3</sub> or TiO<sub>2</sub> [73], [205], can also



enhance its PEC properties. This enhancement can be quite noticeable, for example, the SrTiO<sub>3</sub> protective layer displayed a current density of 35 mA/cm<sup>2</sup> and long-term stability under photocathode operation conditions [206].

Thus, the Si photoelectrode requires additional processing to sustain its PEC properties in an electrolytic environment.

### 2.1.1. Surface textures

The crystalline Si material possesses poor optical properties compared to the direct band gap materials and at least a 50 μm-thick layer is required to achieve proper optical absorption [207]. Additionally, about 25% of the incident light is reflected at the planar Si surface [208]. This drawback of Si surface can be solved by the introduction of surface texture as arrays of nanowires [209], [210] or microwires [211], nanopores [208] or macropores [212], nanopyramids [213] or micropyramids [214], nanoholes [215], etc. Such an approach results in substantial enhancement of the light absorption and broadening of the absorption wavelength range as well as allows to minimize sensitivity to the incident light angle and polarization [197], [216]. Besides, the texturing of the Si surface results in enlarged junction areas and substantially enhances the collection of the photogenerated minority charge carriers [217]. Since the photogenerated charge carriers are distributed over a high surface area of the textured Si [218], the overpotential is reduced due to decreasing local current density over the textured surface-electrolyte interface [208].

On the other hand, the surface texture induces some problems. First of all, the texturing produces a lot of defects and impurities which can generate surface states acting as traps for charge carriers. As a result, the measured PEC efficiency could be lower compared to the theoretically predicted value [219]. The second problem lies in the deposition of a thin and conformal protective layer on the textured surface with high roughness [213]. Therefore, surface texturing is required to achieve low recombination and superior light absorption.

### 2.1.2. Protective layer implementation

The surface of either silicon photoanode or photocathode can be stabilized in the electrolyte by the deposition of a protective layer, which prevents the corrosion processes [220], [221]. Such a layer is required to possess sufficient conductivity, optical transparency and effectively prevent direct contact of the photoelectrode's surface with the electrolyte as well as

## Chapter 2 Silicon material in photocatalytic applications

suppress the recombination processes through surface states [199], [222]. Therefore, the selection of an appropriate material is not a trivial task.

Depending on its intrinsic properties metals could be applied as a protective layer. For example, Ni film has been demonstrated as a protective layer for photocathodes and photoanodes in alkaline electrolyte solutions. Whereas, Ti film was effectively applied for photocathodes in acidic electrolytes [201]. Nevertheless, the application of metal films is not favorable for effective light absorption.

On the other hand, transparent semiconductive metal oxides like  $\text{Al}_2\text{O}_3$  [223] or  $\text{TiO}_2$  [224] have demonstrated effectiveness as passivation layers for Si solar cells and proved promising for PEC applications. The application of  $\text{TiO}_2$  as a protective layer in photoelectrode design is dictated by its chemical stability in electrolyte solutions with various pH values under conditions of both HER and OER. Additionally, the large band gap of bulk  $\text{TiO}_2$  (about 3 eV) results in excellent optical transmittance of the  $\text{TiO}_2$  protective layer, since only a small fraction of solar light is absorbed in the UV range. However, the conductivity of the thin  $\text{TiO}_2$  film significantly depends on the deposition method and conditions, which makes it difficult to control. The thickness and conformity of the polycrystalline thin film are required to be sufficient to avoid the permeability of the electrolyte solution and not inhibit the charge transfer at the same time [220], [225]. Thus, an implementation of a protective layer requires a thoroughly performed design to achieve an optimal PEC performance.

### 2.1.3. Catalysts application

The charge-transfer kinetics of the semiconductor-electrolyte interface is described by a conventional statistical model proposed by Gerischer [226] and later confirmed by experimental results provided by Shreve and Levis [227]. According to this theory, in the absence of loaded catalysts the charge transfer kinetic of the bare Si surface is defined by the change in the surface charge density. Since the Si material is characterized by low exchange current density, the reaction kinetics of multielectron processes of HER (two-electron) and OER (four-electron) are quite sluggish at the silicon-electrolyte interface [228]. As a result, useful current values that are achievable for pure Si photoelectrode are characterized by high overpotential. Therefore, an application of catalysts on the Si surface is required to reduce the overpotential and to improve the interfacial charge transfer kinetics [22].

Owing to its high catalytic activity as well as its stability under acidic and alkaline conditions rare-earth metals like Pt, Ru or Ir are widely used for PEC applications [229]. For

## Chapter 2 Silicon material in photocatalytic applications

instance, the Pt catalyst is useful for HER, whereas Ru and Ir as well as its oxides substantially bolster the OER [14], [230]. However, the research activity in the field of practical PEC applications has shifted to more abundant and low-cost materials for catalytic applications.

Various catalysts like Co-, Ni- and Fe-based oxides and oxy-hydroxides demonstrate a noticeable efficiency in the realization of OER. These materials have demonstrated comparable activity with  $\text{IrO}_x$  or  $\text{RuO}_x$  in neutral and alkaline media, though the exchange current densities for such catalysts are still lower compared to noble metals [231], [232]. Notably, metal-based alloys are widely investigated regarding HER catalytic activity, however, their stability in strong acidic electrolytes is insufficient. Nevertheless, their stability and catalytic activity in alkaline-based electrolytes are prominent [233].

TMD has demonstrated the effective realization of HER like  $\text{MoS}_2$  and  $\text{WS}_2$ , for instance, that showed efficiency in acidic media [234], [235]. Such materials represent a most promising alternative for Pt-based catalysts for HER. The catalytic activity of bulk TMD depends on the number of basal plane edges exposed to the electrolyte which act as active sites for HER occurrence, while basal planes are inert by themselves. Therefore, increasing the catalytic activity for HER could be achieved through nanostructure engineering in order to increase the number of catalytically active edge sites [236] or additional doping by non-metal and metal ions [237]. Other transition metal compounds, like phosphides, selenides and carbides have also demonstrated prominent results as HER catalysts in both basic and acidic media [22].

Generally, earth-abundant catalysts should be applied with higher loading compared to noble metal catalysts for lower overpotential. In the case of Si-based photoelectrode, a higher quantity of earth-abundant catalysts results in increased parasitic optical absorption losses. Thus, additional approaches like back-illumination of Si substrate or spatially and functionally decoupled optical and catalytic activity, should be applied to avoid optical losses and find an optimal balance between the optical transparency of the photoelectrode and its catalytic performance [238], [239].

### 2.1.4. Silicon photoelectrode designing

A typical Si-based photoelectrode is comprised of a modified Si substrate which acts as a light absorber, protective layer and catalyst material. Several factors should be considered in a proper design approach, like effective absorption of incident light and charge carriers generation, efficient charge carriers separation and transport to the photoelectrode's surface,

## Chapter 2 Silicon material in photocatalytic applications

and the performance of catalytically driven chemical reactions. The properties of the silicon-catalyst interface and surface features of the catalyst material impose crucial effects on the overall performance and stability of the photoelectrode. The interface between silicon material and catalyst material is essential for the effective transport of the photo-induced charge carriers to the silicon-electrolyte interface. At the same time, the surface properties of the incorporated catalyst define the number of active sites for HER and/or OER occurrence.

Generally, the texturing and nanoengineering of the Si substrate result in enhanced light absorption, but the inducing of surface defect states that act as recombination centers take place as well. In this regard, a proper protective layer is supposed not only to protect the Si material from corrosion but also to reduce the recombination loss by passivating the surface states. Concurrently, the conductivity and thickness of the protective layer are required to be optimal for efficient charge transfer to the electrolyte solution.

Usually, the catalyst material is incorporated at the top of the protective layer since in such a scenario the PEC processes are activated more effectively. Albeit, in some cases, the catalysts overlayer could act as a protective layer against the corrosion effects and increase the overall durability of the photoelectrode as well [240]. Still, it should be noted, the Si material is not chemically compatible with some catalysts, the incorporation of which results in the formation of defect states at the Si-catalyst interface [241]. Additionally, control of the structural properties of the catalytic layer is also challenging.

The efficiency of water-splitting reactions on the Si-based photoelectrode depends on the charge carriers separation that is substantially influenced by band-bending at the Si-electrolyte junction. The presence of a metal catalyst overlayer at the Si photoelectrode's surface results in the formation of a Schottky barrier that depends on the difference between the Fermi level of the silicon and the work function of the incorporated metal. Thus, the effectiveness of the Si photoelectrode – electrolyte junction is influenced by the work function of the employed metal catalysts. On the other hand, the presence of Schottky contact results in the formation of a density of states in the Si band gap. This effect involves a Fermi level pinning, subsequently decreasing the energy bands bending at the Si-electrolyte interface [242]. This effect can be overcome by applying the catalyst in the form of nanoparticles with a size comparable to the thickness of the space charge region.

## 2.2. Fabrication of 1D silicon nanostructures

One-dimensional nanostructures have been receiving increased attention in different fields of nanotechnology. Such nanostructures as nanowires, nanorods, nanowhiskers, nanobelts, etc., have already demonstrated noticeable features of light-trapping ability, tunability of band gap, thermal conductivity, adjustable surface-to-volume ratio as well as efficient charge carriers collection, mobility and separation. These properties of 1D nanostructures are widely employed for enhancing the performance of optoelectronic devices based on semiconductive materials, like  $\text{TiO}_2$ ,  $\text{ZnO}$ ,  $\text{SnO}_2$ ,  $\text{Ga}_2\text{O}_3$ , etc. Owing to its photoelectronic properties and wide application in contemporary electronics, Si material represents an important topic for the investigation of 1D nano- and microstructures on its base, and solar light harvesting is one of the promising ones. Examples of various applications of the 1D Si arrays are represented in Fig. 10.

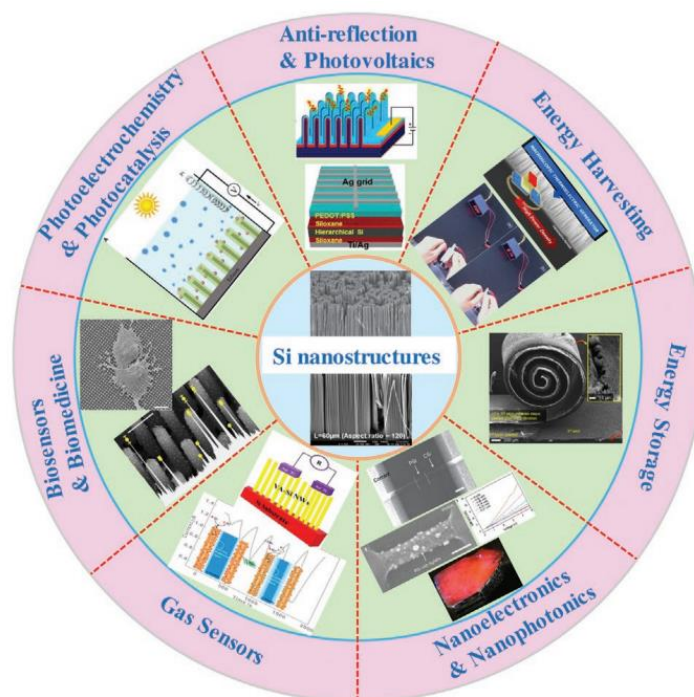


*Figure 10 . Some examples of 1D Si nanostructures applications [243].*

Various top-down and bottom-up synthesis strategies have been developed for 1D Si nanostructures, including wet chemical etching, gas-phase (VLS) growth and dry etching approaches.

Dry etching allows the fabrication of 1D nanostructures with a high degree of homogeneity and controllability. In this approach, the geometrical pattern of 1D arrays is

## Chapter 2 Silicon material in photocatalytic applications

controlled through a patterned etch-mask transferred onto the silicon substrate. As an example of dry etching could be considered the deep reactive ion etching [244] or ion-beam lithography [245] methods. The etching process is controlled by adjusting the applied radio frequency power and gas flow rate in the chamber, where the etching plasma consists of accelerated ions and electrons. During the etching process, the physicochemical reactions of the silicon surface with reactive gases (e.g.  $C_4F_8$ ,  $SF_6$ ,  $O_2$ ) and momentum transfer of accelerated ions lead to the removal of silicon atoms along the previously deposited mask. The yield of this process is 1D Si nanostructure with controlled geometrical parameters, like specific diameter, length, aspect ratio, etc [246].

In opposite to dry etching, wet etching is realized in a liquid solution under atmospheric conditions. This approach enables the fabrication of large-scale 1D Si arrays cost-effectively. In the wet chemical etching process the silicon wafer with the previously deposited mask is immersed in a solution of alkaline or acidic etchants [247]. Usually, the HF,  $HNO_3$  and  $NH_4F$  combinations are used for dissolving Si and  $SiO_2$ . The wet chemical etching is a highly selective and isotropic process that yields well-ordered Si arrays with facile control of geometrical parameters through adjustment of etching time, etchant concentration and temperature of the etching solution. However, the quality of the resulting Si arrays is significantly affected by the crystalline orientation of the Si substrate. For example, the etching rate along the  $\langle 111 \rangle$  is lower than along the  $\langle 100 \rangle$  [248], [249]. Applying an anodic bias to the silicon substrate can enhance the wet etching method. This variation of chemical etching is called electrochemical etching. The induced electrical field creates a charged double layer at the silicon substrate, which assists the etching process [250]. This approach allows the fabrication of complex silicon nanostructures through additional control of the electrical field and light irradiation [251], [252].

Gas-phase growing of the 1D Si nanostructures or VLS growth is the most commonly used method of the bottom-up approach. In this method, gold nanoparticles (as a metal catalyst) on the substrate are used as sites for growing the silicon nanopillars from the vapor phase [253]. The gold nanoparticles are heated up to  $950\text{ }^{\circ}C$  and form a gold-silicon alloy. A mixture of hydrogen and silicon tetrachloride represents the gas phase. The liquid Au-Si alloy acts as an attraction site for Si atoms, and saturation of this site with Si leads to the formation of a Si pillar below the liquid particle. Usually, CVD is used for this method, but electron beam evaporation, laser ablation or physical transport are also suitable for the synthesis of 1D Si nanostructures from the gas phase [254]. The controllability of the growing nanopillars morphology also can be adjusted by electron beam lithography [255]. Additionally, the shape, length and sidewall

morphology of the Si nanopillars are determined by the surface migration of the gold nanoparticles [256]. To obtain large arrays of Si nanopillars, the diffusion of gold on the Si substrate is controlled by templates [257]. Also, the agglomeration of the gold nanoparticles could be avoided by the introduction of an oxide barrier between the nanoparticles [258], [259].

### 2.2.1. Metal-assisted chemical etching of silicon

Among methods of silicon nanostructuralization into porous or arrayed nanostructures, the wet chemical etching approach allows facile processing, high-throughput and large-scale production. The MACE, as a variation of the wet chemical etching method, allows a precise and scalable formation of silicon nanostructures [260], [261]. In this method, the noble metal nanoparticles or thin film are used as a catalyst for increasing the etching rate of the silicon substrate in an  $\text{H}_2\text{O}_2/\text{HF}$  solution. Also, another oxidant can be used instead of  $\text{H}_2\text{O}_2$ , like  $\text{HNO}_3$ ,  $\text{KMnO}_4$ ,  $\text{V}_2\text{O}_5$ ,  $\text{FeNO}_3$  or various metal salts like  $\text{M}(\text{NO}_3)_2$ , where M denotes Ni, Mn, Cu, etc. The main requirement for the employed oxidizer for MACE is a sufficiently high electrochemical potential to inject holes into the VB of Si in the presence of metal catalysts and effectively facilitate the charge transfer between the Si substrate and the oxidant. The schematic representation of a typical MACE process is shown in Fig. 11a. Main stages of the catalytic etching process include the reduction of oxidant by noble metal catalysts (Stage 1), injection of the generated by the reduction reaction holes through the metal into the silicon substrate (Stage 2), diffusion of holes to the sidewalls of the pores and to the surface (Stage 3), dissolution of oxidized silicon by HF at the metal-silicon interface (Stage 4), transport of the byproducts out of the silicon surface to the bulk solution (Stage 5). The choice of noble metal catalysts depends on the redox potential value in relation to the redox potential of the oxidant and positions of CB and VB levels of Si. As shown in Fig. 11b, the optimal catalysts in this regard are Au, Pt and Ag. These metals can effectively extract electrons from the VB of Si, which leads to effective Si oxidation and dissolution of  $\text{SiO}_x$ .

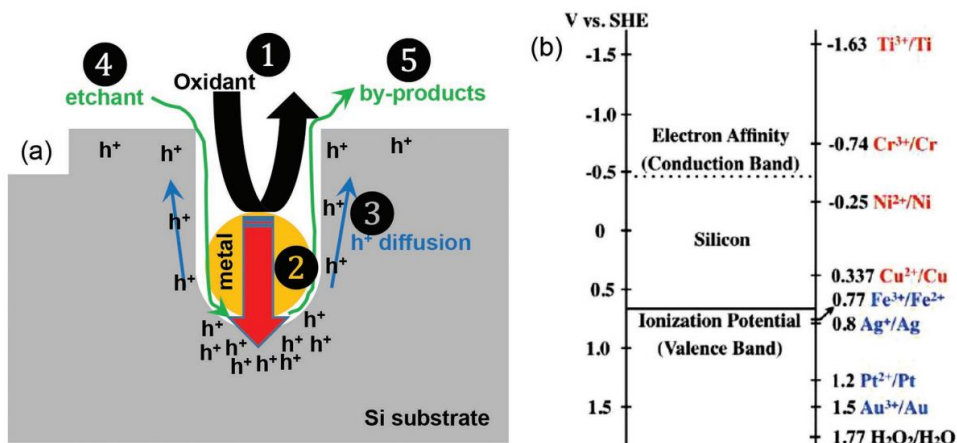


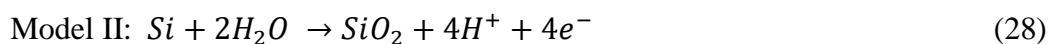
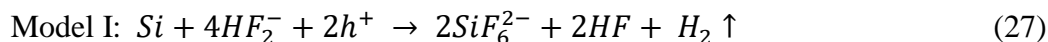
**Figure 11 .** (a) Graphical representation of main stages in a typical MACE process. (b) A representation of redox levels of commonly used metal catalysts in MACE along with the H<sub>2</sub>O<sub>2</sub> oxidant in relation to Si energy levels [243].

Dissolution of Si can occur in either divalent or tetravalent states, therefore the detailed mechanisms of the MACE process are still under discussion [262]–[265]. However, two widely accepted models can describe an overall etching process. In general, during the occurrence of MACE reactions, the noble metal particles or film act as a cathode, and the silicon substrate acts as an anode. The etching process occurs according to the chemical equations as:

Cathode (noble metal film or particle):



Anode (Si substrate):



At the cathode side, the oxidant agent H<sub>2</sub>O<sub>2</sub> is reduced near the noble metal catalyst and produces holes involved in the chemical reaction at the anode side. These holes are diffusing to the Si-Au interface and oxidize Si according to models represented by the reactions (27) and (28). Then, after the oxidation of Si to SiO<sub>2</sub> and its dissolution by HF, the catalytic metal



## Chapter 2 Silicon material in photocatalytic applications

particles attract to the newly exposed Si surface by Van der Waals interaction, and the etching cycle repeats.

The chemical equation of Model I describes a direct dissolution of Si in the tetravalent state in the presence of diffused holes. At the same time, Model II describes two competing mechanisms of Si dissolution and SiO<sub>2</sub> formation. The overall etching rate during the occurrence of the MACE process depends on the relative oxidant concentration [H<sub>2</sub>O<sub>2</sub>/HF] ratio. If this value is sufficiently high, then the dissolution rate by HF can be slower than the Si oxidation rate. In this case, the hole concentration is not fully consumed at the Au-Si interface and some holes are diffused to the adjacent Si, inducing a mesoporous structure formation. Thus, the resulting etched substrate possesses a porous Si/SiO<sub>x</sub> layer that is composed of a mixture of Si nanocrystallites (usually less than 10 nm) introduced in a highly defective SiO<sub>x</sub> layer (up to 100 nm thick). This feature of as-prepared MACE-derived Si nanostructures could be undesirable for further nanocomposites fabrication due to a number of defect sites. Therefore, additional treatment in HF solution is required to remove the residual SiO<sub>x</sub> layer. However, the increased specific area and prominent photoluminescence properties of the Si/SiO<sub>x</sub> layer could be favorable for sensors and optical applications [266]–[269]. The estimation of relative concentrations for H<sub>2</sub>O<sub>2</sub> and HF in the solution is usually performed by a parameter  $\rho = \frac{[HF]}{[HF]+[H_2O_2]}$ . Since the increase in [H<sub>2</sub>O<sub>2</sub>] concentration results in the increased rate of holes injection, the etching rate can be controlled through  $\rho$  value: Si substrate's structure changes from non-porous solid, mesoporous and polished as the  $\rho$  decreases [270].

Along with the  $\rho$  parameter, the resulting morphology of the MACE-derived nanostructure is affected by the crystallographic orientation of the initial Si substrate, doping type and level, and temperature of the etchant solution. The last one affects the etch rate which depends on the consumption of injected holes at the metal-Si interface [271], [272]. At higher temperatures, the holes consumption at the metal site is quite fast and their diffusion off the metal area is low. Thus, the etching process occurs faster with a vertical etching rate. On the opposite, with the temperature decreasing the lateral etching occurs more efficiently due to holes diffusion off the metal area.

A back-bond breaking theory can explain the directional dependence of the etching rate in MACE since the number of back-bonds determines the strength of the back-bonds. There are only two back-bonds along with the <100> direction, whereas along the <111> direction there are four back-bonds. Thus, the dissolving of Si along the <100> direction is faster than along the <111>. This feature of MACE can be used for the fabrication of so-called zig-zag Si

nanostructures by controlling temperature and oxidant concentration during the etching process [273], [274].

In general, p-type Si demonstrates a lower etching rate compared to n-type. This feature is related to band bending at the metal-Si interface, where the injected holes are confined at the n-type Si, whereas at the p-type Si, holes are driven away from the surface. Therefore, the etching rate is faster for the n-type substrate than for the p-type. However, the majority of holes in p-type Si lead to higher porosity compared to n-type at similar conditions. Generally, the porosity increases with the doping concentration [275]–[277].

### 2.2.2. Nanosphere lithography

The NSL is based on the self-assembly of nanospheres or nanoparticles into a hcp lattice during a monolayer formation on the substrate [278]. This monolayer is usually self-assembled [279] from nanospheres of size order from tens of nanometers to hundreds of micrometers and used as a lithographic mask for physical deposition methods, like ALD [280], thermal evaporation, sputtering, etc. As a material for colloidal nanospheres could be used silica or polystyrene. Due to the low cost, simple synthesis and processing, the last one is the more commonly used option. Polystyrene nanospheres solution is a commercially available material. It is synthesized in variable size scales with different methods, like the emulsifier-free emulsion, dispersion, suspension and seed polymerization. The NSL technique is usually employed to fabricate various periodic disconnected nanostructures, like nanostructured arrays, nanoholes, nanomesh, nanoparticles, nanotriangles, etc [281]–[284]. The main advantage of NSL is the capability to engineer uniform nanoarrays with a relatively high resolution without involving lasers, photoresists, UV exposure tools, etc. It makes NSL a simpler and more effective method than other commonly used techniques for nanopatterning, like photolithography, electron beam lithography, focused ion beam lithography, etc.

The NSL technique offers a flexible and inexpensive fabrication technology and can be considered a hybrid of top-down and bottom-up approaches. It enables large-scale fabrication of nanostructured materials, but with limited features since only an hcp monolayer is used. As a result, the shape and size of angstrom scale nanostructure fabrication are challenging. In general, there are three main steps of realization of the NSL technique: mask preparation, material deposition and mask removal. The mask formation is a result of the self-assembling of nanospheres into a monolayer on the required rigid or flexible surface. A transfer of the monolayer could be assisted with well-known methods like dip coating [285], spin coating

[286] and Langmuir-Blodgett [287]. Then, through plasma etching processing, like RIE, the size of nanospheres is reduced to the required value [288]. At this step is controlled the characteristic size of the fabricated periodic nanostructure. The next step, material deposition, could be realized by diverse methods, like e-beam evaporation, magnetron sputtering, ALD or solution-based methods. During the deposition process, the required material penetrates the interstitial spaces of the hcp-packed nanospheres and forms a periodic-patterned array. The final step of NSL, mask removal, could also be realized in various simple ways, like ultrasonic cleaning, water flashing [289], solvent application (toluene, tetrahydrofuran, etc.) or mechanical removal by sticky type. The processing steps could be variable depending on the required results. Generally, NSL could be combined with another technology to increase the fabrication scalability of nanostructures.

### 2.3. Production of silicon-metal oxide nanocomposites by ALD

ALD is a technical process derived from vapor-to-solid deposition techniques and used to grow conformal pinhole-free thin films on various substrates [290]. It is commonly used for the fabrication of oxides [291], [292], sulfides [293] or nitrides [294] layers for engineering photoelectrodes for water-splitting research. The main advantage of ALD is the capability of thin film deposition under lower pressure and temperature compared to CVD, MBE or PVD, for example. Generally, a typical ALD is a continuous cyclic deposition process, where each cycle contains two half-cycles. The required substrate is exposed to a precursor in a gaseous phase at each half-cycle. A differentiation of precursors' interaction with the substrate's surface allows for avoiding their interaction in the gas phase, and only the interaction directly at the substrate is promoted. The half-cycle of precursor deposition consists of two parts. The first part is exposing the surface to precursor, and the second is purging the ALD chamber with inert gas. All by-products and redundant precursors are removed from the chamber during the gas purging.

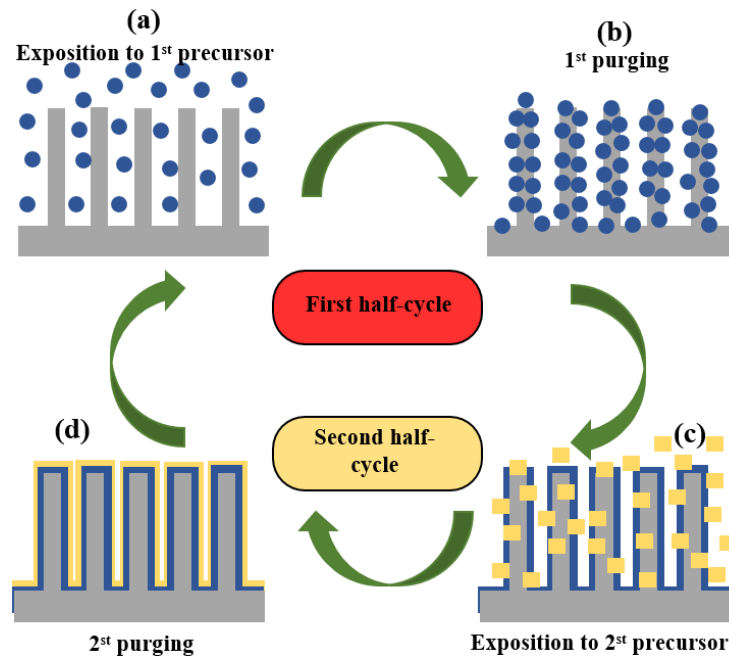


**Figure 12.** Schematic representation of main steps of a typical ALD process: (a) the introduction and chemisorption of the first precursor; (b) the first purging of the operational chamber with chemically inert gas, like argon or nitrogen; (c) the introduction of the second precursor to react with the first one chemisorbed on the substrate; (d) the second purging the inert gas to remove the byproducts.

The schematic representation of the ALD process at the 1D arrayed substrate is represented in Fig. 12. It could be considered the four-step procedure for two-precursor deposition, commonly used for depositing binary oxides [295]. At the first step, as shown in Fig. 12a, the precursor in the gas phase is introduced inside the ALD operational chamber. The chemical species of the precursor are chemisorbed at the substrate's surface and start self-terminated chemical reactions. It means that the introduced precursor is nucleated on the substrate's surface without alteration, and the layer formation is limited only by surface sites. Thus, only a monolayer of the precursor is absorbed by the surface during this process. The feature of self-limiting deposition is a major distinguishing characteristic of the ALD process [296].

The inert gas purges away the excessive amount of the precursor at step 2 (Fig. 12b). Then, the second precursor is introduced in the ALD chamber and reacts with the already absorbed first precursor (Fig. 12c). As a result of this reaction, a thin atomic layer of the required material forms on the substrate. After the second purging with the inert gas (Fig. 12d), the process sequentially proceeds from the first step to reach the required thickness of the deposited

## Chapter 2 Silicon material in photocatalytic applications

layer. These four steps delineate an ALD cycle. The separated deposition steps are the distinguishing feature of the ALD process that enables the resulting thin film atomic scale uniformity.

The growing process starts with the first iteration of the ALD cycle, and the growth rate can be estimated by GPC value. The substrate's temperature is the most crucial parameter for ALD film growth. An ALD window is a temperature range in which the ALD process occurs. Its graphical representation is shown in Fig. 13. In the region before the ALD window, precursors do not possess sufficient energy to sustain chemical reactions at the substrate's surface or condense on the ALD chamber's walls. These processes are marked as "limited condensation" and "limited activation" in the scheme. At the high-temperature region beyond the ALD window, precursors are decomposed or desorbed from the substrate. These processes are marked as "limited decomposition" and "limited desorption". Considering the ALD window related to GPC value, it is stable under ALD conditions, whereas in "limited condensation" and "limited decomposition", the GPC is increased as well as decreased in "limited activation" and "limited desorption" regions.

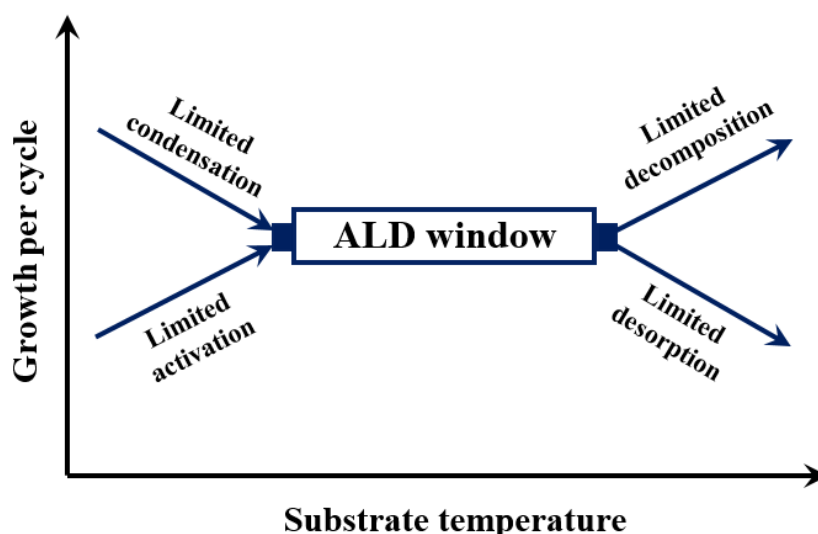


*Figure 13.* A representation of the ALD window related to the substrate temperature and the growth per cycle value.

An occurrence of ALD requires that chemical reactions should be self-saturating and complementary. The first requirement means that the deposition process stops when all sites at the surface are saturated and the chemisorbed layer evenly covers the entire surface. The

## Chapter 2 Silicon material in photocatalytic applications

second one means that after the chemisorption, each chemical reactant should render the surface to the subsequent layer to complete the reaction of an ALD cycle.

Depending on the ALD film's required features and the substrate's parameters, the ALD method can be considered in two categories: substrate-based and parameters-based. Substrate-based methods include thin film ALD and powder ALD techniques, used for stationary and non-stationary substrates, respectively. The flat or porous surface can be considered stationary, and the ALD film is growing in contact with precursor exposure. In contrast, particles or rods are considered powder substrates and the total ALD coverage is achieved due to their movement.

ALD on a stationary substrate implies a layer-by-layer conformal deposition of a thin film of the required material. Considering the high aspect ratio substrates, like porous substrates, the exposure time should be adjusted appropriately according to the kinetic of the precursor inlet to achieve a uniform deposition [297], [298]. This adjustment could be realized by increasing the partial pressure of the precursor in the chamber. In this case, the exposure time is decreased. On the other hand, the exposure time must be increased for precursors with a high molecular mass, which leads to better nucleation and growth rate. It could be achieved by adding a stop-flow step after introducing the precursor [299]. Additionally, the precursor flow must be stabilized to avoid desorption or control the nucleation density on the surface [300], [301]. However, the unstable flow of the precursor could result in thickness variation caused by defects and edge sites at the substrate. During the synthesis of 2D nanomaterials by ALD, it could induce out-of-plane growth [302], developing nanoflakes on the surface, which is beneficial as active sites for OER or HER.

The powder ALD implies a conformal deposition on substrates with particle morphology [303]. It is widely used for metals [304] and metal oxides [305], [306] to fabricate core-shell nanoparticles. The principles of the powder ALD are similar to a typical ALD process. Still, special rotary [307] or fluidized bed reactors [308] are required to achieve full and conformal coverage of particle substrate. Additionally, appropriate parameters of the ALD process must be selected to avoid the agglomeration of nanoparticles during the deposition steps [309].

The parameter-based methods include thermal, plasma-enhanced, hotwire-assisted and photo-assisted ALD. In the thermal ALD, a relatively higher temperature compared to the typical ALD is used to sustain the occurrence of self-limiting reactions and deposition of material with higher crystallinity. However, this method imposes a requirement of sufficient thermostability of the substrate and precursors. In the plasma-enhanced ALD, highly reactive

## Chapter 2 Silicon material in photocatalytic applications

species in plasma conditions are used to decrease the temperature required for the deposition. This method allows an ALD deposition of various materials with a wider range of suitable precursors. In the hotwire-assisted ALD, a heated filament is used as an energy source to sustain the deposition process. Owing to the operating temperature up to 2000 °C this method allows effective application of the precursors avoiding unwanted side reactions [310]. This method is effective for metals [311] and nitrides deposition [310]. In photo-assisted ALD, UV light sustains and accelerates surface reactions. The employment of light energy allows for the reduction of the deposition temperature. This method is widely used for depositing metal oxides, boron nitride, and metals [312].

## Chapter 3 Main research topics

### 3.1. Co-authorship statements

In this chapter, the Author presents statements on the co-authorship of his research papers attached to the thesis. The Author's contributions and concise description of every piece of research are summarised in the introduction to each article separately. The provided co-authorship statements justify each author's contribution to the final version of the published papers presented in this thesis.

It should be noted that all the studies were realized in close collaboration with research groups where the author's contribution was not directly included or was partly included in work with highly specialized or hazardous equipment and techniques. Thus, the Author has not been personally involved in direct operations with FIB, TEM, XPS, GIXRD and nanoindentation equipment during the data acquisition for the presented pieces of research. Therefore, he only processed, structured and interpreted the acquired data, and developed models as well as made necessary calculations.

At the same time, the preparation process of PSi by MACE and implementation of the ALD technique for the nanocomposites fabrication as well as data acquisition using (diffuse) reflectance, absorbance, transmittance, Raman, and photoluminescence spectroscopies were performed personally by Author under assistance of the supervisor (dr hab. Igor Iatsunskyi).

Measurements and data interpretation of linear/cyclic voltammetry, chronoamperometry and electrochemical impedance spectroscopy were performed in close collaboration with dr hab. Katarzyna Siuzdak.

Nanoindentation data were acquired and processed by dr hab. Emerson Coy. As well as the raw data on GIXRD and HRTEM imaging were collected in close collaboration with him.

Some ALD procedures related to Pd deposition on the investigated samples were realized in close collaboration with Dr. Mikhael Bechelany.

Contributions of co-authors are declared in the co-authorship statements attached below.



MSc. Mykola Pavlenko  
NanoBioMedical Centre  
Adam Mickiewicz University  
3 Wszechnicy Piastowskiej Str.  
61614, Poznan, Poland  
E-mail: mykpav@amu.edu.pl  
Tel.: +48 73 777 2499

### A declaration

Hereby I declare my contribution to the following papers:

1. *Tailoring the Structural, Optical, and Photoluminescence Properties of Porous Silicon/TiO<sub>2</sub> Nanostructures*

Igor Iatsunskyi, **Mykola Pavlenko**, Roman Viter, Mariusz Jancelewicz, Grzegorz Nowaczyk, Ieva Baleviciute, Karol Załęski, Stefan Jurga, Arunas Ramanavicius and Valentyn Smyntyna

The Journal of Physical Chemistry C: 119, 13, 7164-7171, 2015

doi.org/10.1021/acs.jpcc.5b01670

In this publication, I have contributed to the fabrication of porous silicon samples by MACE. Also, I have made the acquisition and processing of all photoluminescence data and contributed to the development of the model of photoluminescence excitation mechanisms.

2. *Enhancement of optical and mechanical properties of Si nanopillars by ALD TiO<sub>2</sub> coating*

**M. Pavlenko**, E. L. Coy, M. Jancelewicz, K. Załęski, V. Smyntyna, S. Jurga and I. Iatsunskyi

The Royal Society of Chemistry (RSC Advances): 97070-97076, 6, 2016

doi.org/10.1039/C6RA21742G

In this publication, I have contributed to the fabrication of Si/TiO<sub>2</sub> nanopillars by all required methods and techniques (NSL, RIE, MACE, ALD). I have processed the SEM/TEM and GIXRD data. I have prepared Figures 1 and 3 as well as made calculations of nanocrystallite sizes and strain values from GIXRD. Also, I assisted in the acquisition and processing of data obtained by photoluminescence, reflectance and Raman spectroscopies. I contributed to the manuscript writing in the introduction part, experimental part and description of structural properties in the "Results and discussion".

3. *Silicon/TiO<sub>2</sub> core-shell nanopillar photoanodes for enhanced photoelectrochemical water oxidation*

**Mykola Pavlenko**, Katarzyna Siuzdak, Emerson Coy, Mariusz Jancelewicz, Stefan Jurga, Igor Iatsunskyi

International Journal of Hydrogen Energy: 42, 51, 30076-30085, 2017  
doi.org/10.1016/j.ijhydene.2017.10.033

In this publication, I have contributed to the fabrication of ordered silicon nanopillar arrays with TiO<sub>2</sub> layer by all required methods and techniques (NSL, RIE, MACE, ALD). I have contributed to SEM, Raman and reflectance data acquisition as well as performed its processing along with visualization in Figures 1 and 2. Also, I drew Figure 3 and significantly contributed to the writing of all parts of the article except the discussion of linear voltammetry results.

4. *Enhancing Photocatalytic Performance and Solar Absorption by Schottky Nanodiodes Heterojunctions in Mechanically Resilient Palladium Coated TiO<sub>2</sub>/Si Nanopillars by Atomic Layer Deposition*

Emerson Coy, Katarzyna Siuzdak, **Mykola Pavlenko**, Karol Załęski, Octavio Graniel, Marcin Ziólek, Sebastien Balme, Philippe Miele, Matthieu Weber, Mikhael Bechelany, Igor Iatsunskyi

Chemical Engineering Journal: 392, 123702, 2020  
doi.org/10.1016/j.cej.2019.123702

In this publication, I have contributed to the synthesis of silicon nanopillar arrays with relative procedures such as MACE, NSL and RIE as well as the ALD for the fabrication of Si/TiO<sub>2</sub> nanocomposite. I have assisted in the acquisition and processing of the optical spectroscopy data from Si/TiO<sub>2</sub> and Pd/TiO<sub>2</sub>/Si samples. Also, I have contributed to the discussion of the obtained results, draft reviewing and development of the charge transfer model in the Pd/TiO<sub>2</sub>/Si.


5. *Enhanced solar-driven water splitting of 1D core-shell Si/TiO<sub>2</sub>/ZnO nanopillars*

**Mykola Pavlenko**, Katarzyna Siuzdak, Emerson Coy, Karol Zaleski, Mariusz Jancelewicz, Igor Iatsunskyi

International Journal of Hydrogen Energy: 45, 50, 26426-26433, 2020  
doi.org/10.1016/j.ijhydene.2019.11.231

In this publication, I have contributed to the fabrication of silicon nanopillar arrays and assisted in the ALD of TiO<sub>2</sub>/ZnO layers. I have contributed to the acquisition and processing of data from SEM/TEM, GIXRD and optical spectroscopies as well as made calculations of nanocrystallite sizes, band gap values and photoconversion efficiency characteristics. I have prepared all figures and significantly contributed to the writing of all parts of the paper. Also, I have contributed to the development of the model of charge carriers transport in 1D core-shell Si/TiO<sub>2</sub>/ZnO nanocomposites and performed simulations of EIS spectra to prove the proposed model.

Date      Signature

16.11.2022 

Dr. Igor Iatsunskyi  
NanoBioMedical Centre  
Adam Mickiewicz University  
3 Wszechnicy Piastowskiej Str.  
61614, Poznan, Poland  
E-mail: igoyat@amu.edu.pl  
Tel.: +48 61 829 6711

A declaration

Hereby I declare my contribution to the following papers:

1. *Tailoring the Structural, Optical, and Photoluminescence Properties of Porous Silicon/TiO<sub>2</sub> Nanostructures*

**Igor Iatsunskyi**, Mykola Pavlenko, Roman Viter, Mariusz Jancelewicz, Grzegorz Nowaczyk, Ieva Baleviciute, Karol Załęski, Stefan Jurga, Arunas Ramanavicius and Valentyn Smyntyna

The Journal of Physical Chemistry C: 119, 13, 7164-7171, 2015  
doi.org/10.1021/acs.jpcc.5b01670

In this publication, I have contributed to problem definition, planning of the experiments, discussions concerning obtained results and evaluation of the manuscript.

2. *Enhancement of optical and mechanical properties of Si nanopillars by ALD TiO<sub>2</sub> coating*  
M. Pavlenko, E. L. Coy, M. Jancelewicz, K. Załęski, V. Smyntyna, S. Jurga and **I. Iatsunskyi**

The Royal Society of Chemistry (RSC Advances): 97070-97076, 6, 2016  
doi.org/10.1039/C6RA21742G

In this publication, I have contributed to problem definition, planning of the experiments, discussions concerning obtained results and evaluation of the manuscript.

3. *Silicon/TiO<sub>2</sub> core-shell nanopillar photoanodes for enhanced photoelectrochemical water oxidation*

Mykola Pavlenko, Katarzyna Siuzdak, Emerson Coy, Mariusz Jancelewicz, Stefan Jurga, **Igor Iatsunskyi**

International Journal of Hydrogen Energy: 42, 51, 30076-30085, 2017  
doi.org/10.1016/j.ijhydene.2017.10.033

In this publication, I have contributed to problem definition, planning of the experiments, discussions concerning obtained results and evaluation of the manuscript.

4. *Enhanced solar-driven water splitting of 1D core-shell Si/TiO<sub>2</sub>/ZnO nanopillars*  
Mykola Pavlenko, Katarzyna Siuzdak, Emerson Coy, Karol Załęski, Mariusz Jancelewicz,  
**Igor Iatsunskyi**

International Journal of Hydrogen Energy: 45, 50, 26426-26433, 2020  
doi.org/10.1016/j.ijhydene.2019.11.231

In this publication, I have contributed to problem definition, planning of the experiments, discussions concerning obtained results and evaluation of the manuscript.

5. *Enhancing Photocatalytic Performance and Solar Absorption by Schottky Nanodiodes Heterojunctions in Mechanically Resilient Palladium Coated TiO<sub>2</sub>/Si Nanopillars by Atomic Layer Deposition*  
Emerson Coy, Katarzyna Siuzdak, Mykola Pavlenko, Karol Załęski, Octavio Graniel, Marcin Ziółek, Sebastien Balme, Philippe Miele, Matthieu Weber, Mikhael Bechelany,  
**Igor Iatsunskyi**

Chemical Engineering Journal: 392, 123702, 2020  
doi.org/10.1016/j.cej.2019.123702

In this publication, I have contributed to problem definition, planning of the experiments, discussions concerning obtained results and evaluation of the manuscript.

15.11.2022  
Date  Signature

Dr. Emerson Coy  
NanoBioMedical Centre  
Adam Mickiewicz University  
3 Wszechnicy Piastowskiej Str.  
61614, Poznan, Poland  
E-mail: coyeme@amu.edu.pl  
Tel.: +48 61 829 6709

### A declaration

Hereby I declare my contribution to the following papers:

1. *Enhancement of optical and mechanical properties of Si nanopillars by ALD TiO<sub>2</sub> coating*  
M. Pavlenko, **E. L. Coy**, M. Jancelewicz, K. Załeski, V. Smyntyna, S. Jurga and I. Iatsunskyi

The Royal Society of Chemistry (RSC Advances): 97070-97076, 6, 2016  
[doi.org/10.1039/C6RA21742G](https://doi.org/10.1039/C6RA21742G)

In this publication, I have contributed to XRD measurements and investigation of nanomechanical properties by nanoindentation technique. I was involved in the discussion of obtained results, and have contributed to manuscript writing (discussion of mechanical properties) and evaluation.

2. *Silicon/TiO<sub>2</sub> core-shell nanopillar photoanodes for enhanced photoelectrochemical water oxidation*

Mykola Pavlenko, Katarzyna Siuzdak, **Emerson Coy**, Mariusz Jancelewicz, Stefan Jurga, Igor Iatsunskyi

International Journal of Hydrogen Energy: 42, 51, 30076-30085, 2017  
[doi.org/10.1016/j.ijhydene.2017.10.033](https://doi.org/10.1016/j.ijhydene.2017.10.033)

In this publication, I have contributed to data acquisition by (high resolution) transmission electron microscopy (HRTEM) and electron diffraction as well as discussion of obtained results and manuscript evaluation.

3. *Enhancing Photocatalytic Performance and Solar Absorption by Schottky Nanodiodes Heterojunctions in Mechanically Resilient Palladium Coated TiO<sub>2</sub>/Si Nanopillars by Atomic Layer Deposition*

**Emerson Coy**, Katarzyna Siuzdak, Mykola Pavlenko, Karol Załeski, Octavio Graniel, Marcin Ziółek, Sebastien Balme, Philippe Miele, Matthieu Weber, Mikhael Bechelany, Igor Iatsunskyi

Chemical Engineering Journal: 392, 123702, 2020  
[doi.org/10.1016/j.cej.2019.123702](https://doi.org/10.1016/j.cej.2019.123702)

In this publication, I have contributed as a first author to the problem definition and conceptualization of experimental and theoretical approaches to research realization. I have obtained results of SEM, TEM, HRTEM, GIXRD, nanoindentation measurement and made all the necessary calculations. I have written the major part of the manuscript and contributed to the discussion of obtained results.

4. *Enhanced solar-driven water splitting of 1D core-shell Si/TiO<sub>2</sub>/ZnO nanopillars*  
Mykola Pavlenko, Katarzyna Siuzdak, **Emerson Coy**, Karol Zaleski, Mariusz Jancelewicz, Igor Iatsunskyi

International Journal of Hydrogen Energy: 45, 50, 26426-26433, 2020  
doi.org/10.1016/j.ijhydene.2019.11.231

In this publication, I have contributed to data acquisition by HRTEM, GIXRD and EDX as well as to the discussion of obtained results and the manuscript evaluation.

Date 16.11.2022  
Signature   
Emerson Coy

Dr. Mariusz Jancelewicz  
NanoBioMedical Centre  
Adam Mickiewicz University  
3 Wszechnicy Piastowskiej Str.  
61614, Poznan, Poland  
E-mail: marjan7@amu.edu.pl  
Tel.: +48 61 829 6711

A declaration

Hereby I declare my contribution to the following papers:

1. *Tailoring the Structural, Optical, and Photoluminescence Properties of Porous Silicon/TiO<sub>2</sub> Nanostructures*

Igor Iatsunskyi, Mykola Pavlenko, Roman Viter, **Mariusz Jancelewicz**, Grzegorz Nowaczyk, Ieva Baleviciute, Karol Załęski, Stefan Jurga, Arunas Ramanavicius and Valentyn Smyntyna

The Journal of Physical Chemistry C: 119, 13, 7164-7171, 2015  
doi.org/10.1021/acs.jpcc.5b01670

In this publication, I have contributed to the application of the atomic layer deposition technique (ALD), deposition of TiO<sub>2</sub> ultrathin film, discussion of the obtained results and manuscript evaluation.

2. *Enhancement of optical and mechanical properties of Si nanopillars by ALD TiO<sub>2</sub> coating*  
M. Pavlenko, E. L. Coy, **M. Jancelewicz**, K. Zaleski, V. Smyntyna, S. Jurga and I. Iatsunskyi

The Royal Society of Chemistry (RSC Advances): 97070-97076, 6, 2016  
doi.org/10.1039/C6RA21742G

In this publication, I have contributed to the TiO<sub>2</sub> ultrathin film deposition by ALD technique, discussion of the obtained results and manuscript evaluation.

3. *Silicon/TiO<sub>2</sub> core-shell nanopillar photoanodes for enhanced photoelectrochemical water oxidation*

Mykola Pavlenko, Katarzyna Siuzdak, Emerson Coy, **Mariusz Jancelewicz**, Stefan Jurga, Igor Iatsunskyi

International Journal of Hydrogen Energy: 42, 51, 30076-30085, 2017  
doi.org/10.1016/j.ijhydene.2017.10.033

In this publication, I have contributed to the TiO<sub>2</sub> layer deposition by ALD technique, discussion of the obtained results and manuscript evaluation.

4. *Enhanced solar-driven water splitting of 1D core-shell Si/TiO<sub>2</sub>/ZnO nanopillars*  
Mykola Pavlenko, Katarzyna Siuzdak, Emerson Coy, Karol Zaleski, **Mariusz Jancelewicz**, Igor Iatsunskyi

International Journal of Hydrogen Energy: 45, 50, 26426-26433, 2020  
doi.org/10.1016/j.ijhydene.2019.11.231

In this publication, I have contributed to the deposition of TiO<sub>2</sub> and ZnO thin layers by ALD technique, discussion of the obtained results and manuscript evaluation.

Date      Signature

16/11/2022

Mariusz  
Jancelewicz



Dr. Karol Załęski  
NanoBioMedical Centre  
Adam Mickiewicz University  
3 Wszechnicy Piastowskiej Str.  
61614, Poznan, Poland  
E-mail: zaleski@amu.edu.pl  
Tel.: +48 61 829 6713

### A declaration

Hereby I declare my contribution to the following papers:

1. *Tailoring the Structural, Optical, and Photoluminescence Properties of Porous Silicon/TiO<sub>2</sub> Nanostructures*

Igor Iatsunskyi, Mykola Pavlenko, Roman Viter, Mariusz Jancelewicz, Grzegorz Nowaczyk, Ieva Baleviciute, **Karol Załęski**, Stefan Jurga, Arunas Ramanavicius and Valentyn Smyntyna

The Journal of Physical Chemistry C: 119, 13, 7164-7171, 2015  
doi.org/10.1021/acs.jpcc.5b01670

In this publication, I have contributed to the lamella preparation by focused ion beam technique (FIB) for further HRTEM investigation as well as to the evaluation of the manuscript.

2. *Enhancement of optical and mechanical properties of Si nanopillars by ALD TiO<sub>2</sub> coating*  
M. Pavlenko, E. L. Coy, M. Jancelewicz, **K. Załęski**, V. Smyntyna, S. Jurga and I. Iatsunskyi

The Royal Society of Chemistry (RSC Advances): 97070-97076, 6, 2016  
doi.org/10.1039/C6RA21742G

In this publication, I have contributed to FIB for HRTEM realization and to the discussion of the obtained results as well as the evaluation of the manuscript.

3. *Enhancing Photocatalytic Performance and Solar Absorption by Schottky Nanodiodes Heterojunctions in Mechanically Resilient Palladium Coated TiO<sub>2</sub>/Si Nanopillars by Atomic Layer Deposition*

Emerson Coy, Katarzyna Siuzdak, Mykola Pavlenko, **Karol Załęski**, Octavio Graniel, Marcin Ziólek, Sebastien Balme, Philippe Miele, Matthieu Weber, Mikhael Bechelany, Igor Iatsunskyi

Chemical Engineering Journal: 392, 123702, 2020  
doi.org/10.1016/j.cej.2019.123702

### Chapter 3 Main research topics

In this publication, I have contributed to FIB for HRTEM realization and to the discussion of the obtained results as well as the evaluation of the manuscript.

4. *Enhanced solar-driven water splitting of 1D core-shell Si/TiO<sub>2</sub>/ZnO nanopillars*

Mykola Pavlenko, Katarzyna Siuzdak, Emerson Coy, **Karol Zaleski**, Mariusz Jancelewicz, Igor Iatsunskyi

International Journal of Hydrogen Energy: 45, 50, 26426-26433, 2020

[doi.org/10.1016/j.ijhydene.2019.11.231](https://doi.org/10.1016/j.ijhydene.2019.11.231)

In this publication, I have contributed to FIB for HRTEM realization and to the discussion of the obtained results as well as the evaluation of the manuscript.

16.11.22  
Date

  
Signature

dr hab inż. Katarzyna Siuzdak, prof. IMP PAN  
Centre of Laser and Plasma Engineering  
Institute of Fluid-Flow Machinery  
Polish Academy of Sciences  
Fiszera 14 Str., 80-231 Gdansk, Poland  
e-mail: ksiuzdak@imp.gda.pl  
Tel.: +48 58 5225 120

Gdańsk, 10.03.2023

A declaration

Hereby I declare my contribution to the following papers:

1. *Silicon/TiO<sub>2</sub> core-shell nanopillar photoanodes for enhanced photoelectrochemical water oxidation*  
Mykola Pavlenko, **Katarzyna Siuzdak**, Emerson Coy, Mariusz Jancelewicz, Stefan Jurga, Igor Iatsunskyi  
International Journal of Hydrogen Energy: 42, 51, 30076-30085, 2017  
doi.org/10.1016/j.ijhydene.2017.10.033

In this publication, I have contributed to measurements and experiments related to linear voltammetry, chronoamperometry and discussions concerning obtained results.

2. *Enhancing Photocatalytic Performance and Solar Absorption by Schottky Nanodiodes Heterojunctions in Mechanically Resilient Palladium Coated TiO<sub>2</sub>/Si Nanopillars by Atomic Layer Deposition,*  
Emerson Coy, **Katarzyna Siuzdak**, Mykola Pavlenko, Karol Załęski, Octavio Graniel, Marcin Ziółek, Sebastien Balme, Philippe Miele, Matthieu Weber, Mikhael Bechelany, Igor Iatsunskyi  
Chemical Engineering Journal: 392, 123702, 2020 (doi.org/10.1016/j.cej.2019.123702)

In this publication, I have contributed to measurements and experiments related to chronoamperometry, linear and cyclic voltammetry as well as the conceptualization and realization of electrochemical impedance spectroscopy and results discussion.

3. *Enhanced solar-driven water splitting of 1D core-shell Si/TiO<sub>2</sub>/ZnO nanopillars*  
Mykola Pavlenko, **Katarzyna Siuzdak**, Emerson Coy, Karol Załęski, Mariusz Jancelewicz, Igor Iatsunskyi  
International Journal of Hydrogen Energy: 45, 50, 26426-26433, 2020  
doi.org/10.1016/j.ijhydene.2019.11.231

In this publication, I have contributed to measurements and experiments related to chronoamperometry, linear and cyclic voltammetry as well as the electrochemical impedance spectroscopy, results discussion and evaluation of the manuscript.



### Chapter 3 Main research topics

Dr. Roman Viter  
Institute of Atomic Physics and Spectroscopy  
University of Latvia  
Jelgavas 3, LV-1004 Riga, Latvia  
E-mail: roman.viter@lu.lv

#### A declaration

Hereby I declare my contribution to the following paper:

*Tailoring the Structural, Optical, and Photoluminescence Properties of Porous Silicon/TiO<sub>2</sub> Nanostructures*

Igor Iatsunskyi, Mykola Pavlenko, **Roman Viter**, Mariusz Jancelewicz, Grzegorz Nowaczyk, Ieva Baleviciute, Karol Załęski, Stefan Jurga, Arunas Ramanavicius and Valentyn Smyntyna

The Journal of Physical Chemistry C: 119, 13, 7164-7171, 2015  
[doi.org/10.1021/acs.jpcc.5b01670](https://doi.org/10.1021/acs.jpcc.5b01670)

In this publication, I have contributed to problem definition, the photoluminescence model development, discussions concerning obtained results and evaluation of the manuscript.

Date                      Signature



Dr. Mikhael Bechelany  
Institut Européen des Membranes (IEM)  
Université de Montpellier  
2 Place Eugène Bataillon  
34095, Montpellier CEDEX 5, France  
E-mail: mikhael.bechelany@umontpellier.fr  
Tel.: +33 4 67 14 91 67

A declaration

Hereby I declare my contribution to the following paper:


*Enhancing Photocatalytic Performance and Solar Absorption by Schottky Nanodiodes Heterojunctions in Mechanically Resilient Palladium Coated TiO<sub>2</sub>/Si Nanopillars by Atomic Layer Deposition*

Emerson Coy, Katarzyna Siuzdak, Mykola Pavlenko, Karol Załęski, Octavio Graniel, Marcin Ziólek, Sebastien Balme, Philippe Miele, Matthieu Weber, **Mikhael Bechelany**, Igor Iatsunskyi

Chemical Engineering Journal: 392, 123702, 2020  
[doi.org/10.1016/j.cej.2019.123702](https://doi.org/10.1016/j.cej.2019.123702)

In this publication, I have contributed to the problem definition, ALD application to Pd nanoparticles deposition and a discussion of the obtained results.

Date      Signature

04/07/2022 

Prof. habil. dr. Arunas Ramanavičius  
Department of Physical Chemistry  
Faculty of Chemistry and Geoscience Vilnius University  
Naugarduko Str.24, 03225, Vilnius, Lithuania  
E-mail: arunas.ramanavicius@chf.vu.lt  
Tel.: +37 060 032 332

#### A declaration

Hereby I declare my contribution to the following paper:

*Tailoring the Structural, Optical, and Photoluminescence Properties of Porous Silicon/TiO<sub>2</sub> Nanostructures*

Igor Iatsunskiy, Mykola Pavlenko, Roman Viter, Mariusz Jancelewicz, Grzegorz Nowaczyk, Ieva Baleviciute, Karol Załęski, Stefan Jurga, **Arunas Ramanavicius** and Valentyn Smyntyna

The Journal of Physical Chemistry C: 119, 13, 7164-7171, 2015  
[doi.org/10.1021/acs.jpcc.5b01670](https://doi.org/10.1021/acs.jpcc.5b01670)

In this publication, I have contributed to problem definition and discussions concerning obtained results.

Date



Signature

### Chapter 3 Main research topics

Prof. Marcin Ziólek  
Faculty of Physics  
Adam Mickiewicz University  
2 Uniwersytetu Poznańskiego Str.  
61-614 Poznań, Poland  
E-mail: marziol@amu.edu.pl  
Tel.: +48 61 829 5011

#### A declaration

Hereby I declare my contribution to the following paper:

*Enhancing Photocatalytic Performance and Solar Absorption by Schottky Nanodiodes Heterojunctions in Mechanically Resilient Palladium Coated TiO<sub>2</sub>/Si Nanopillars by Atomic Layer Deposition*

Emerson Coy, Katarzyna Siuzdak, Mykola Pavlenko, Karol Załęski, Octavio Graniel, **Marcin Ziólek**, Sebastien Balme, Philippe Miele, Matthieu Weber, Mikhael Bechelany, Igor Iatsunskyi

Chemical Engineering Journal: 392, 123702, 2020  
[doi.org/10.1016/j.cej.2019.123702](https://doi.org/10.1016/j.cej.2019.123702)

In this publication, I have contributed to the planning and carrying out the experiments related to dyes photodegradation, discussions concerning obtained results and evaluation of the manuscript.

4.6.11.2022      M Ziólek  
Date                      Signature

Dr. Grzegorz Nowaczyk  
NanoBioMedical Centre  
Adam Mickiewicz University  
3 Wszechnicy Piastowskiej Str.  
61614, Poznan, Poland  
E-mail: nowag@amu.edu.pl  
Tel.: +48 61 829 6708

A declaration

Hereby I declare my contribution to the following paper:

*Tailoring the Structural, Optical, and Photoluminescence Properties of Porous Silicon/TiO<sub>2</sub> Nanostructures*

Igor Iatsunskyi, Mykola Pavlenko, Roman Viter, Mariusz Jancelewicz, **Grzegorz Nowaczyk**, Ieva Baleviciute, Karol Załęski, Stefan Jurga, Arunas Ramanavicius and Valentyn Smyntyna

The Journal of Physical Chemistry C: 119, 13, 7164-7171, 2015  
[doi.org/10.1021/acs.jpcc.5b01670](https://doi.org/10.1021/acs.jpcc.5b01670)

In this publication, I have contributed to data acquisition by transmission electron microscopy (TEM) and energy-dispersive x-ray spectroscopy (EDX) as well as to the discussions concerning obtained results and evaluation of the manuscript.

Date	Signature
16.11.22	



### 3.2. Tailoring the structure, optical and photoluminescence properties of porous silicon/TiO<sub>2</sub> nanostructures

Silicon-transition metal oxide nanostructures demonstrate enhanced charge carriers separation, resulting in improved photocatalytic activity and promising applications for photovoltaics, biosensors, and photo-induced water splitting in particular. In this paper, the efforts were addressed to investigate heterojunction formation between Si and TiO<sub>2</sub>, and its optical features. In this regard, a thorough investigation of intrinsic properties and PL spectra would shed light on the conductivity mechanism and defect sites formation in Si/TiO<sub>2</sub> heterojunction.

In this study, a combination of advanced MACE and ALD methods was used to fabricate Si/TiO<sub>2</sub> nanocomposite. A typical MACE method was applied to synthesize macro- and mesoporous p-type silicon with defined structural characteristics. Then, a further ALD process was performed to introduce TiO<sub>2</sub> into a silicon matrix and to produce Si/TiO<sub>2</sub> nanocomposite. Diverse methods, such as SEM, TEM, GIXRD, EDX, Raman spectroscopy, ellipsometry, and PL spectroscopy performed investigations of as-prepared and annealed Si/TiO<sub>2</sub> samples. The influence of annealing on the structural and optical properties of Si/TiO<sub>2</sub> nanostructure has been revealed and discussed. Additionally, we proposed a model of PL emission in Si/TiO<sub>2</sub> heterojunction. According to our research, two main competing recombination mechanisms occur during PL emission: radiative recombination through the surface states (surface recombination) and oxygen vacancies as well as recombination through the self-trapped excitons (volume recombination). Also, the volume and surface effects that influence the PL emission spectrum have been elucidated.

In this research, the Author experimentally found optimal conditions of MACE under variate concentrations of etchant (HF), oxidizing (H<sub>2</sub>O<sub>2</sub>) and catalytic (Ag nanoparticles) agents. He made the macro/mesoporous silicon samples using the MACE method. He assisted in developing and constructing a custom-made setup for PL spectra acquisition. He performed PL spectra measurements of porous silicon samples, as-prepared and annealed Si/TiO<sub>2</sub> with a variable number of ALD cycles. The Author has processed all the obtained PL data. Also, he contributed to developing the model of PL excitation mechanisms.

**Number of Ministerial points: 140**

**Impact factor: 3.7**

# Tailoring the Structural, Optical, and Photoluminescence Properties of Porous Silicon/TiO<sub>2</sub> Nanostructures

Igor Iatsunskiy,<sup>\*,†,‡</sup> Mykola Pavlenko,<sup>‡</sup> Roman Viter,<sup>‡,§</sup> Mariusz Jancelewicz,<sup>†</sup> Grzegorz Nowaczyk,<sup>†</sup> Ieva Baleviciute,<sup>||</sup> Karol Załęski,<sup>†</sup> Stefan Jurga,<sup>†</sup> Arunas Ramanavicius,<sup>||</sup> and Valentyn Smyntyna<sup>‡</sup>

<sup>†</sup>NanoBioMedical Centre, Adam Mickiewicz University, 85 Umultowska Str., 61-614 Poznan, Poland

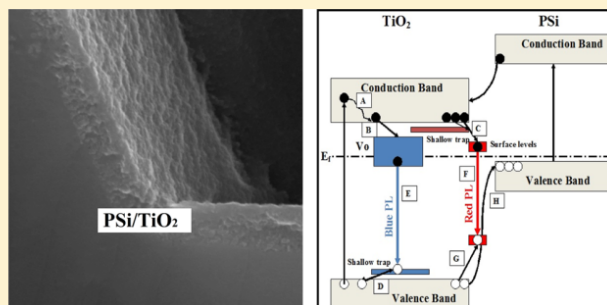
<sup>‡</sup>Department of Experimental Physics, Odessa National I.I. Mechnikov University, 42 Pastera Str., 65023 Odessa, Ukraine

<sup>§</sup>Institute of Atomic Physics and Spectroscopy, University of Latvia, 19 Raina Boulevard, LV 1586 Riga, Latvia

<sup>||</sup>Department of Chemistry Vilnius University, 24 Naugarduko Str., LT-03225 Vilnius, Lithuania

## Supporting Information

**ABSTRACT:** The structural, optical, and photoluminescence properties of porous silicon (PSi)/titanium dioxide (TiO<sub>2</sub>) nanostructures were investigated. PSi structures consisting of macro- and mesoporous layers were fabricated by metal-assisted chemical etching, and then TiO<sub>2</sub> was introduced inside the PSi matrix using the atomic layer deposition technique. We performed scanning electron microscopy, transmission electron microscopy (TEM), X-ray diffraction, energy dispersive X-ray spectroscopy, Raman spectroscopy, ellipsometry, and photoluminescence (PL) spectroscopy to characterize the prepared and annealed PSi/TiO<sub>2</sub> nanostructures. TEM and Raman analyses revealed that TiO<sub>2</sub> had a crystalline anatase structure. PL measurements of the PSi/TiO<sub>2</sub> composite system showed two broad peaks at approximately 2.4–3 eV (blue PL) and 1.7–1.9 eV (red PL). The mechanisms of the emissions were discussed, and it was found that two main competing recombination mechanisms take place, including radiative recombination through the surface states (surface recombination) and through oxygen vacancies and self-trapped excitons (volume recombination).



## 1. INTRODUCTION

Porous silicon (PSi) and PSi nanostructures based on PSi/TiO<sub>2</sub> have drawn increased attention for use in various applications, such as photovoltaics,<sup>1,2</sup> photoelectrochemical water splitting,<sup>3–5</sup> gas sensors,<sup>6</sup> Li-ion batteries,<sup>7–9</sup> and so forth. Nanostructures based on Si–TiO<sub>2</sub> show improved photocatalytic efficiency due to their enhanced separation of excited electrons and holes. PSi nanostructures also exhibit great potential in optical biosensor applications due to the possible tuning of a refractive index that can be used for the detection of biological substances or chemical vapors.<sup>10,11</sup> It is well-known that depending on the pore size PSi could be very efficiently detect molecules and other bio-agents comparable in size to the pore diameter. Therefore, the simultaneous use of two or more PSi layers (macro-, meso-, and/or micro-PSi) allows us to produce sensitive biosensors capable of detecting various types of molecules. Furthermore, PSi nanostructures are favorable because of the low cost of silicon and their compatibility with the modern integrated circuit (IC) industry. Undoubtedly, the improvement in electro-optical properties is dependent on the microstructure of the nanostructure. In this regard, studies on the morphology and physical properties of nanostructures has gained increasing attention in recent years.

In the present study, we report the structural and optical properties of the PSi/TiO<sub>2</sub> composite system. Metal-assisted chemical etching (MACE) is the most preferable method to fabricate PSi structures possessing different porosities and morphologies.<sup>12</sup> Here, PSi possesses two types of porosity, including a first level macroporous structure and second level mesoporous structure. TiO<sub>2</sub> was introduced inside the PSi matrix to fabricate the PSi/TiO<sub>2</sub> nanostructure. For this purpose, we used the atomic layer deposition (ALD) technique. ALD is a deposition process for highly uniform and conformal thin films. Because of the self-limiting reaction in the ALD process, films that are very conformal with thicknesses that are precisely controlled could be grown over large areas, even inside the PSi.<sup>13,14</sup> The morphology and phase structure were detected by scanning and transmission electron microscopy (SEM, TEM), X-ray diffraction (XRD), energy dispersive X-ray spectroscopy (EDX), and Raman spectroscopy. Optical properties have been analyzed by means of ellipsometry. In this paper, we also concentrated on the broad photoluminescence (PL) bands in the visible spectral region. Analysis of the PL spectra

Received: December 22, 2014

Revised: March 16, 2015

Published: March 16, 2015

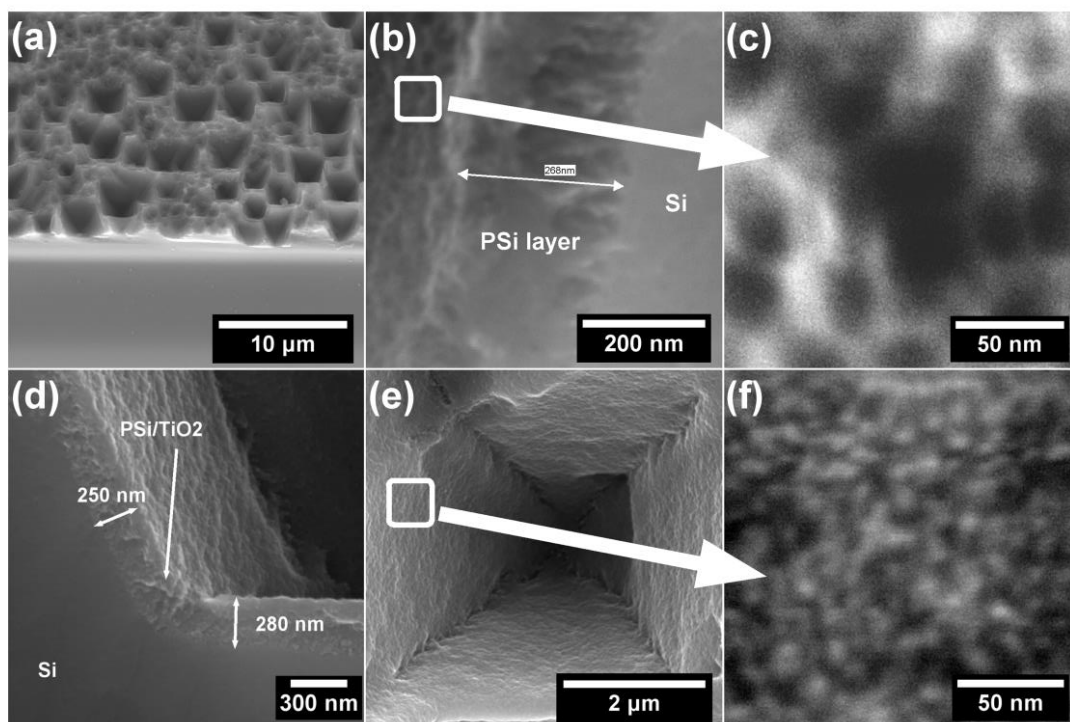


**Figure 1.** Cross-sectional view of SEM images of a (a) macroporous silicon surface fabricated by MACE, (b) mesoporous layer of PSi, and (c) mesoporous silicon surface (high magnification). (d) Cross-sectional view of prepared PSi/TiO<sub>2</sub> nanostructure after 150 ALD cycles. (e) Planar view SEM image of an individual macropore in the PSi/TiO<sub>2</sub> nanostructure after 150 ALD cycles. (f) Surface of the macropore in the PSi/TiO<sub>2</sub> nanostructure (high magnification).

indicates PL quenching due to electron–hole separation at the PSi/TiO<sub>2</sub> heterojunction. Mechanisms of the PL emissions, along with structural and optical changes induced by annealing, will be discussed.

## 2. EXPERIMENTAL SECTION

**Preparation of PSi.** The PSi samples were fabricated from (100) oriented and highly doped p-type Si (B-doped,  $q < 0.005 \Omega \text{ cm}$ ) utilizing MACE.<sup>12</sup> Silicon samples (1 × 1 cm), after standard RCA cleaning, were cleaned with acetone, isopropanol, and deionized water via ultrasonic cleaning. The silver particles, which act as catalysts to assist in the etching of silicon, were deposited on Si samples by immersion in 0.2 M HF and 10<sup>-3</sup> M AgNO<sub>3</sub> metallization aqueous solutions. The time of immersion was 60 s. Then, the samples were etched in aqueous solutions containing HF (40%), H<sub>2</sub>O<sub>2</sub> (30%), and ultrapure H<sub>2</sub>O at a ratio of 80:80:20 H<sub>2</sub>O<sub>2</sub>/H<sub>2</sub>O/HF for 60 min. After etching, the samples were dipped in HNO<sub>3</sub> solution to remove the silver particles for 30 min and were then dipped in HF (5%) solution to remove oxide. They were then cleaned with deionized water and blown dry with nitrogen. The etching and immersion procedures were performed at room temperature.

**ALD Coating.** The PSi samples were placed in an ALD reactor (Picosun). The TiO<sub>2</sub> thin films were deposited onto the PSi substrates using TiCl<sub>4</sub> and water as ALD precursors. Nitrogen (N<sub>2</sub>) flow was used as a carrier and purging gas. TiCl<sub>4</sub> precursor and water were evaporated at 20 °C. In this study, the standard cycle consisted of a 0.1 s TiCl<sub>4</sub> exposure, a 3 s N<sub>2</sub> purge, a 0.1 s exposure to water, and a 4 s N<sub>2</sub> purge. The total flow rate of N<sub>2</sub> was 150 standard cubic centimeters per minute (sccm). TiO<sub>2</sub> thin films were grown at 300 °C. The growth rate

was typically 0.5 Å per cycle for TiO<sub>2</sub> on the planar silicon surface. The growth per cycle was controlled by measuring the films thickness on Si-wafer reference substrates placed in the reactor. After TiO<sub>2</sub> deposition, some samples were annealed at 400 °C for an hour in an ambient atmosphere.

### Material Characterization and Optical Measurements.

Structural properties of PSi and ALD TiO<sub>2</sub> thin films were investigated by X-ray diffraction (XRD) (Empyrean diffractometer), scanning electron microscopy (SEM) (JEOL, JSM-7001F) with an energy dispersive X-ray (EDX) analyzer, transmission electron microscopy (TEM) (JEOL ARM 200F high-resolution transmission electron microscope (200 kV) with EDX analyzer), and Raman scattering (Renishaw micro-Raman spectrometer equipped with a confocal microscope (Leica) and laser ( $\lambda_{\text{excitation}} = 514 \text{ nm}$ )). The cross sections and lamellas for TEM investigations were prepared by Focused Ion Beam (JEOL, JIB-4000).

Optical properties of the samples have been studied by photoluminescence spectroscopy and ellipsometry measurements. Ellipsometry spectroscopy was used to obtain optical constants of PSi and TiO<sub>2</sub> thin films deposited on Si substrates. Semilab GESSE spectroscopic ellipsometer (extended visible: 1.23–5 eV). The ellipsometric measurements were carried out at a fixed incident angle of 75°, close to the Brewster's angle for a silicon substrate, and a variable wavelength between 300 nm and 1 μm. Then, the experimental  $\tan(\psi)$  and  $\cos(\delta)$  data were fitted using WinElli II software using a single layer TiO<sub>2</sub> adjusted model to obtain the film thicknesses with a goodness of fit over 0.999 in the full wavelength range. Photoluminescence (PL) of the samples was measured at room temperatures using a homemade setup. The excitation of PL

was performed with a nitrogen laser (337.7 nm), and the emission spectra were recorded in the range of 400–850 nm.

### 3. RESULTS AND DISCUSSION

**Structural Characterization.** Figure 1a shows the SEM image of macroporous silicon (macro-PSi) obtained by MACE. The cross-sectional SEM view of the PSi shows the presence of nearly pyramid-shaped pores (macropores) propagating into the bulk from the surface in a perpendicular manner. The average pore size (diagonal) is approximately 3–5  $\mu\text{m}$ , and the thickness of the macro-PSi layer is  $\sim 1.5 \mu\text{m}$ . The surface of an individual macropore consists of a mesoporous silicon (meso-PSi) layer with a thickness ranging from 200 to 300 nm (Figure 1b). The thickness of the bottom layer of the pore is bigger than the sidewall (Figure 1d). Formation of this complex porous structure can be explained by the model proposed by Chartier et al. where etching occurs at the pore walls (pore widening) and tips (pore deepening) due to injected holes, which may diffuse away from the pore tip along the pore walls.<sup>15</sup> Figure 1c shows that the layer of meso-PSi consists of a large number of small pores. The average pore size is approximately 15–30 nm (Figure 1c).

Cross-sectional SEM images indicate that  $\text{TiO}_2$  infiltrates and conformally coats the mesopores (Figure 1d). EDX measurements were carried out to evaluate the chemical composition of  $\text{PSi}/\text{TiO}_2$  and the distribution of titanium and oxygen atoms inside the porous structure. EDX confirms that PSi contains Ti, O, and Si not only on the top of the film but also within the porous matrix (not shown here). Figure 1e shows a planar SEM image of an individual macropore of  $\text{PSi}/\text{TiO}_2$  after 150 ALD cycles. The image shows that the inner surface of the macropore is quite rough. After the ALD process, the surface of the PSi layer consists of spherical grains uniformly distributed over the surface (Figure 1f). Depending on the number of ALD cycles, a typical grain ranged from 20 to 40 nm in size.

Figure 2a shows a TEM image of the PSi after 200 ALD cycles. The thickness of the layer is  $\sim 240 \text{ nm}$ . We noticed that the upper layer (40–60 nm from the top) of the meso-PSi has a higher density, probably due differences in the porosity. EDX analysis of this sample is shown in Figure 2b. The EDX profile image confirms that the Ti and O atoms quite uniformly penetrate into the meso-PSi matrix. Opposite to the deposition of films on flat surfaces, the precursor molecules have to diffuse into a porous structure. During the ALD process, molecules of precursors penetrate into the pore, forming the layer or other structures of  $\text{TiO}_2$  inside the PSi matrix.

High-resolution TEM (HRTEM) image of the  $\text{PSi}/\text{TiO}_2$  nanostructure is shown in Figure 2c. Using ImageJ software, the grain size and interplanar distances were calculated (Figure 2c, d). HRTEM image shows the formation of crystallites in the PSi matrix (Figure 2c). Lattice fringes are clearly visible, which prove crystallinity of the particles obtained. We determined the interplanar distances of 0.34 and 0.20 nm for anatase and 0.27, 0.16, and 0.13 nm for silicon, which correspond to lattice distances of (101) and (004) planes of anatase and (200), (311), and (200) planes of silicon, respectively. The interplanar distance for the (101) lattice plane was lower than that for anatase  $\text{TiO}_2$  as reported in the Joint Committee on Powder Diffraction Standards (JCPDS) database (0.352 nm). The decrease in the interplanar distance could be due to lattice strain effects. The average grain size of anatase varied from  $6 \pm 2 \text{ nm}$  to  $9 \pm 2 \text{ nm}$  for 150 and 200 ALD cycles, respectively. It

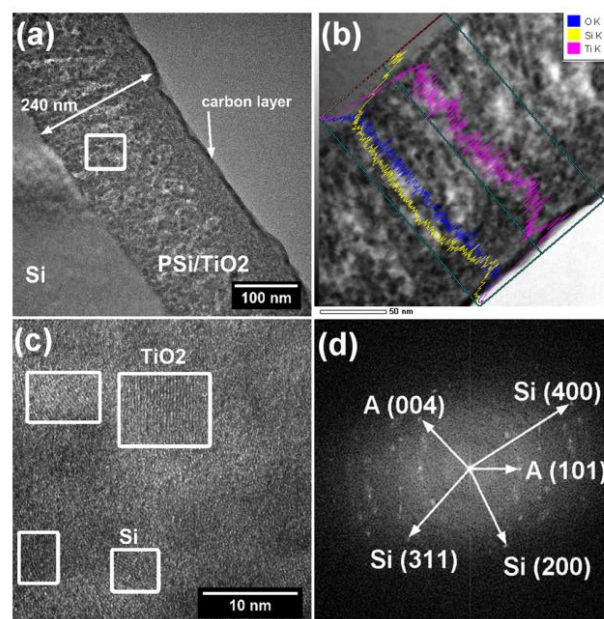


**Figure 2.** (a) Cross-sectional TEM image of  $\text{PSi}/\text{TiO}_2$  after 200 ALD cycles. (b) EDX profile analysis. (c) HRTEM image of the area highlighted with a white square in (a). (d) Inverse fast Fourier transform of the area highlighted with a white square in the HRTEM image (a). “A” can be identified as anatase.

was difficult to identify any individual grains corresponding to anatase for the samples prepared with 100 ALD cycles. Some heterojunctions of anatase  $\text{TiO}_2$  and Si were also observed by HRTEM.

To confirm the composition of  $\text{PSi}/\text{TiO}_2$ , Raman spectroscopy (Figure 3) and XRD (not reported here) have been used. Raman spectra of the prepared  $\text{PSi}/\text{TiO}_2$  showed no significant peaks of  $\text{TiO}_2$  in the background of the strong spectrum of PSi, indicating that the prepared  $\text{TiO}_2$  was amorphous (Figure 3a). Upon increasing the number of ALD cycles, the peaks corresponding to PSi become weaker due to high absorbance of the amorphous  $\text{TiO}_2$  layer covering the PSi. A Raman peak at  $146 \text{ cm}^{-1}$ , corresponding to the anatase phase of  $\text{TiO}_2$ , can clearly be observed after annealing at  $400 \text{ }^\circ\text{C}$  for 1 h in air, suggesting that the prepared amorphous phase crystallizes to anatase  $\text{TiO}_2$  (Figure 3b). This is typical of the anatase  $\text{TiO}_2$  phase, but the peak is broader and blue-shifted with respect to bulk anatase (peak position is  $144 \text{ cm}^{-1}$  and full width at half-maximum (fwhm) is  $7 \text{ cm}^{-1}$ ). The broadening and blue-shift of the Raman peaks are attributed to phonon confinement effects that usually exist in nanomaterials.<sup>16–19</sup> Upon increasing the number of ALD cycles, the intensity of the anatase Raman peak increases. A simple confinement model may be used to calculate the shape of the anatase mode at various nanocrystal sizes ( $L$ ).<sup>18,19</sup> In this model, the Raman spectrum is given by

$$I(\omega) \cong \int_{\text{BZ}} \frac{d^3q |C(0, q)|^2}{(\omega - \omega(q))^2 - \left(\frac{\Gamma_0}{2}\right)^2} \quad (1)$$

where  $|C(0, q)|^2 = \exp(-q^2 L^2 / (16\pi^2))$ ,  $\Gamma_0$  is the natural line width,  $\omega(q)$  is the dispersion relation for optical phonons, and  $\omega$  and  $q$  are the frequency and wavevector, respectively. The anatase Raman peaks are centered at  $147 \text{ cm}^{-1}$  (100 and 150 ALD cycles) and  $146 \text{ cm}^{-1}$  (200 cycles) with fwhm of 25, 24,

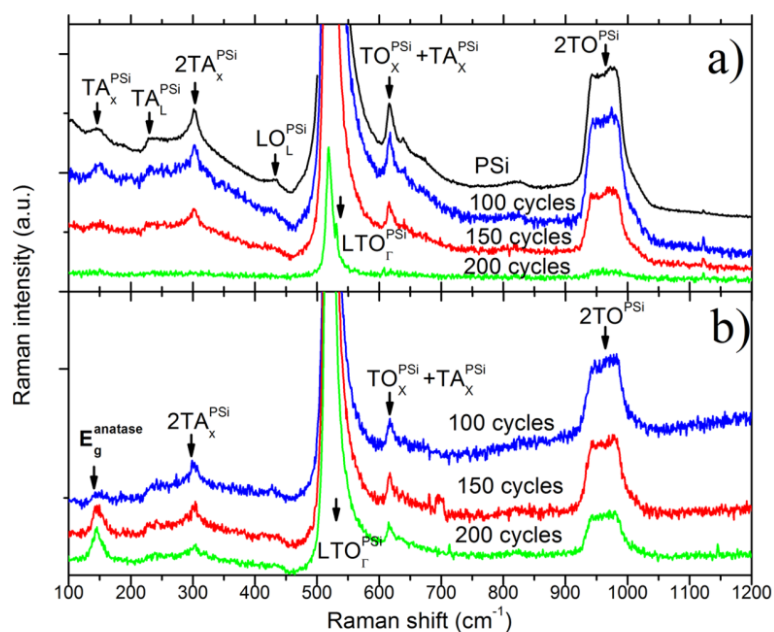


**Figure 3.** (a) Raman spectra of prepared PSi/TiO<sub>2</sub> nanostructures and PSi. The arrows indicate the Raman modes of the PSi. (b) Raman spectra of PSi/TiO<sub>2</sub> nanostructures annealed at 400 °C. The arrows indicate the Raman modes of PSi and anatase.

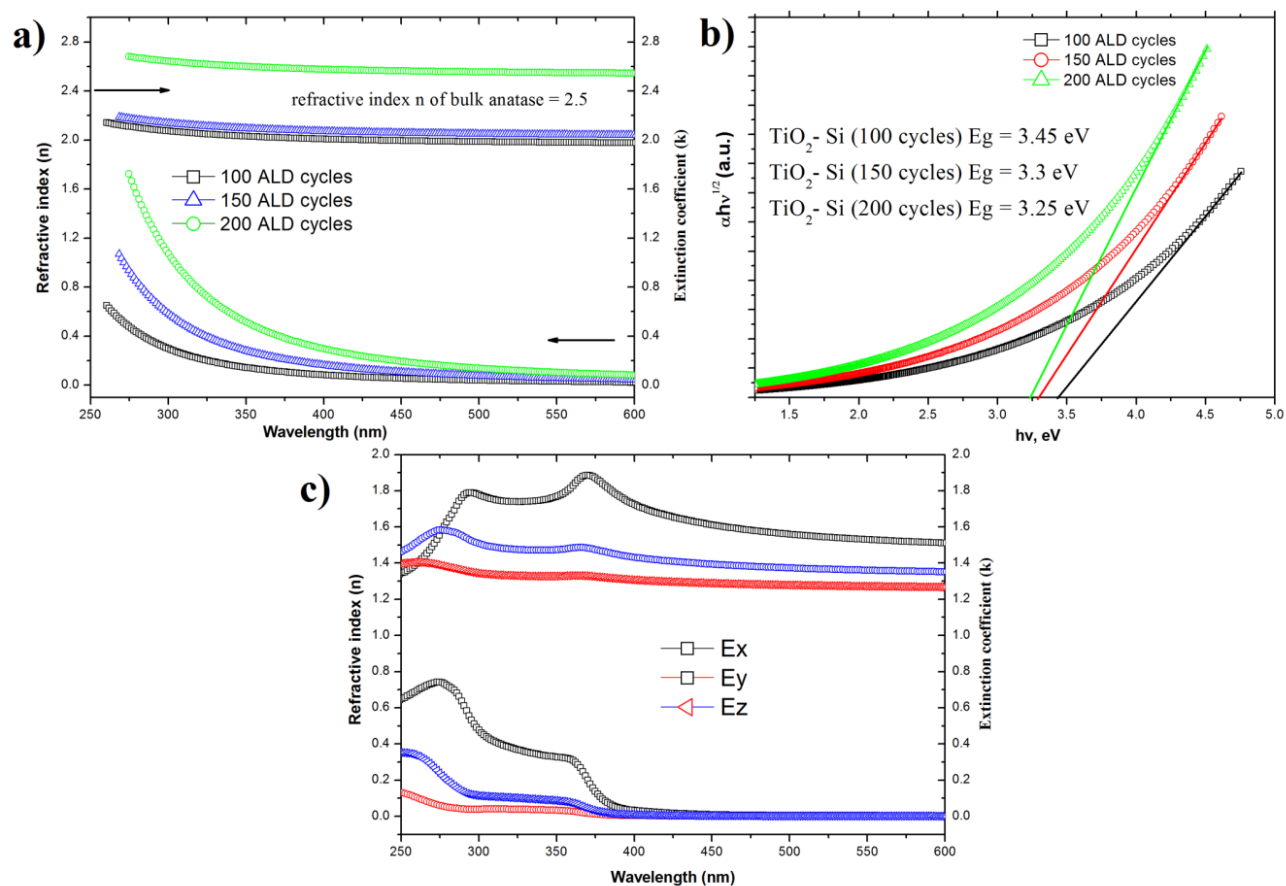


**Figure 4.** (a) Refractive index ( $n$ ) and extinction coefficient ( $k$ ) of TiO<sub>2</sub>-Si with differing numbers of ALD cycles. (b) Band gap estimation of TiO<sub>2</sub>-Si with differing numbers of ALD cycles. (c) Refractive index ( $n$ ) and extinction coefficient ( $k$ ) of PSi.  $E_x$ ,  $E_y$ , and  $E_z$  are components of the electric field vector.

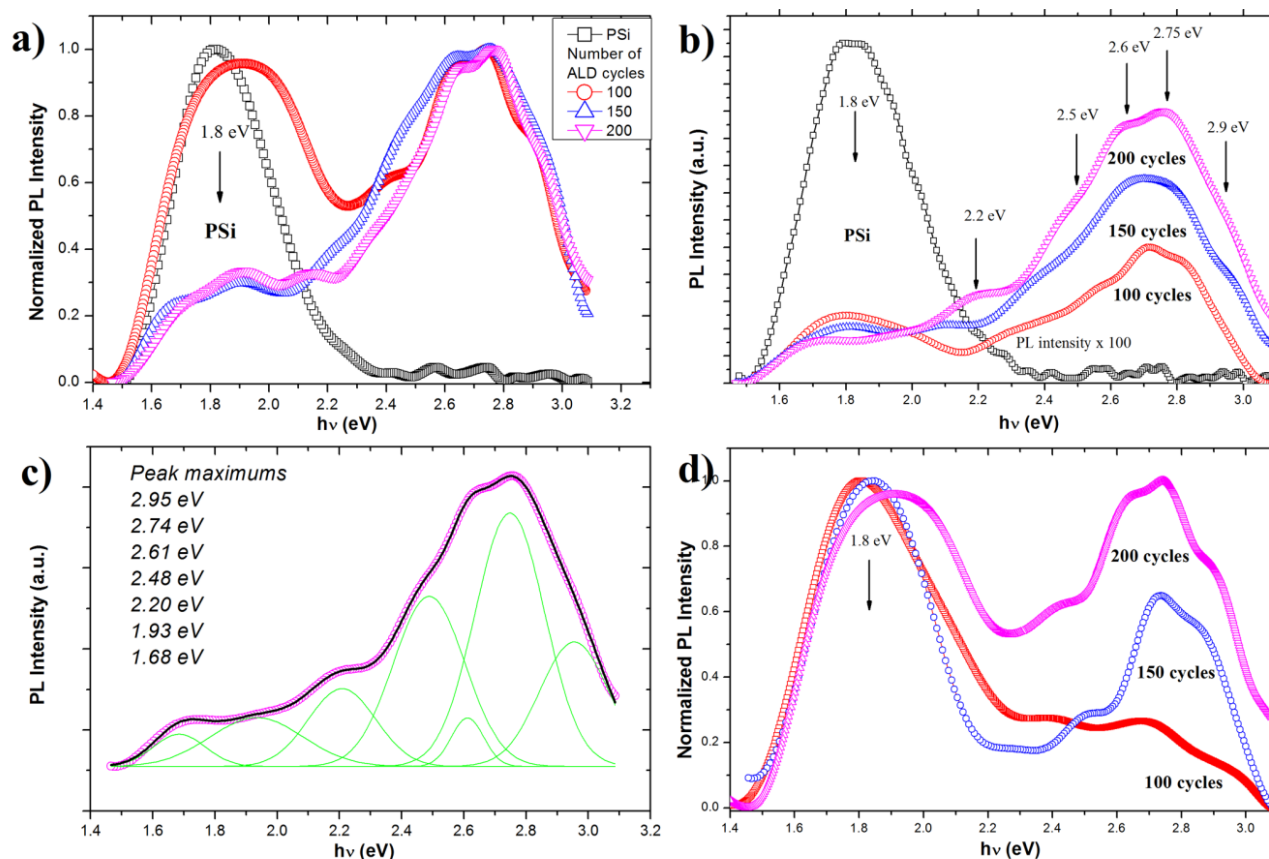


**Figure 5.** PL spectra of PSi and PSi/TiO<sub>2</sub> nanostructures with differing numbers of ALD cycles (a) as prepared, (b) as annealed, and (c) with curve fitting of the PL spectrum (PSi/TiO<sub>2</sub> nanostructure, 200 ALD cycles). (d) Normalized PL spectra of TiO<sub>2</sub>-Si with differing numbers of ALD cycles.

and 23 cm<sup>-1</sup> deposited by 100, 150, and 200 cycles, respectively. These correspond to crystal sizes of approximately 5, 6, and 7.8 nm, respectively. Comparing these results with TEM findings, we can conclude that a very small amount of anatase nanocrystals have formed in the prepared PSi/TiO<sub>2</sub> composites. Annealing of these samples leads to amorphous-to-crystalline phase transitions. However, we could observe the anatase peak at 146 cm<sup>-1</sup> for the prepared TiO<sub>2</sub> layer grown on the planar silicon surface (Figure S4, Supporting Information). This indicates that the mean crystallite size and the crystallinity of the ALD TiO<sub>2</sub> are influenced dramatically by the morphology of the substrate. In the case of the porous structure, additional thermal treatment is needed to form anatase crystals inside the PSi matrix.

**Optical and PL Properties.** TiO<sub>2</sub> layers were deposited on a silicon substrate in similar conditions in the same environment for optical measurements. The extinction coefficient (*k*) and refractive index (*n*) of ALD-deposited TiO<sub>2</sub> on the planar silicon surface and PSi nanolayers were calculated to be in the range of 260–1000 nm using the ellipsometry technique. It should be noted that it was impossible to calculate *n* and *k* for the PSi/TiO<sub>2</sub> nanostructures due to high light scattering. The spectral dependence of the extinction coefficient of the TiO<sub>2</sub> nanolayers is shown in Figure 4a. It can be seen that the extinction coefficient value increased with the number of ALD cycles. The absorption edge of the samples laid in the range of 260–400 nm, which is typical of TiO<sub>2</sub> nanostructures.

Band gap values of TiO<sub>2</sub> nanostructures from ellipsometry data were estimated.<sup>20–22</sup> Extinction coefficient *k* and absorption coefficient  $\alpha$  are related according to the following equation<sup>20</sup>

$$\alpha = \frac{4\pi k}{\lambda} \quad (2)$$

where  $\lambda$  is wavelength.

Because TiO<sub>2</sub> is an n-type semiconductor with indirect optical transitions, the relationship between band gap  $E_g$  and absorption coefficient  $\alpha$  can be described by the following equation<sup>23</sup>

$$(\alpha \times hv)^{1/2} \sim (hv - E_g) \quad (3)$$

where  $hv$  is photon energy.

The spectra dependence of the absorption data is plotted in specific coordinates in Figure 4b. It can be seen that the absorption edge demonstrated a blue-shift with a decreased number of ALD cycles. Using eq 3, the band gap values were determined graphically.<sup>21,22,24</sup> The obtained values were 3.45, 3.3, and 3.25 for TiO<sub>2</sub> nanolayers deposited by 100, 150, and 200 cycles, respectively. The band gap value of bulk TiO<sub>2</sub> (anatase) is  $\sim 3.2$  eV. The ALD-deposited TiO<sub>2</sub> nanolayers showed higher values of  $E_g$ , which could refer to the quantum confinement effect, that were affected by low grain size values.<sup>20–23</sup> These results have been confirmed by Raman spectroscopy (Figure S3, Supporting Information).

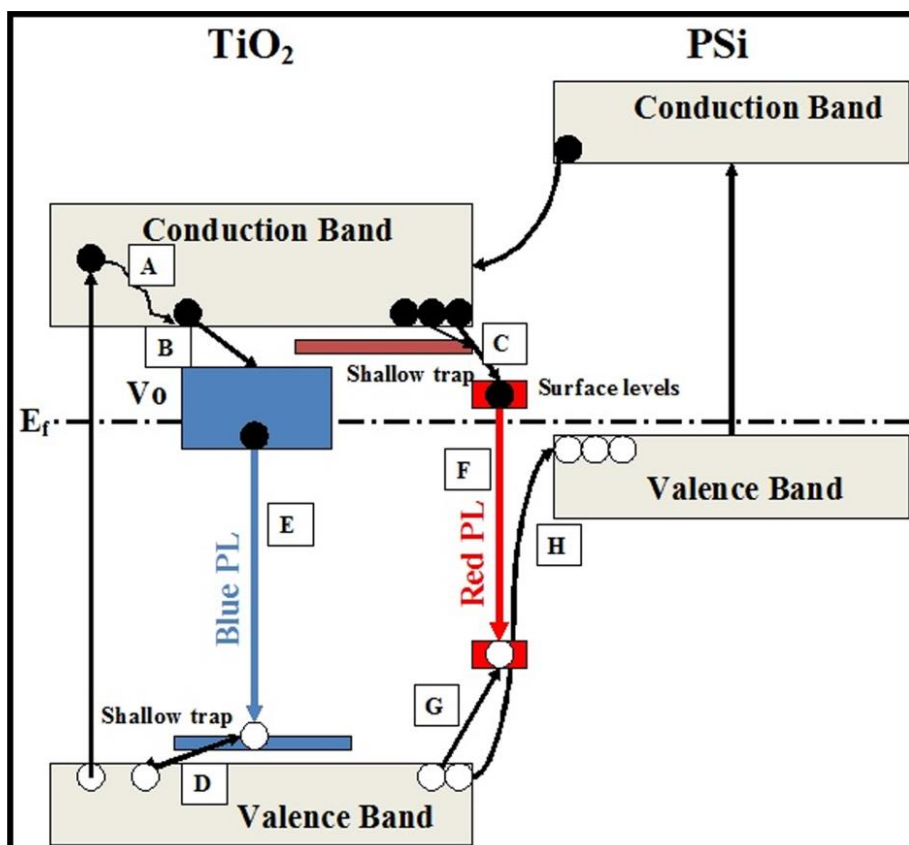


**Figure 6.** Schematic illustration of the relaxation processes of the photogenerated carriers in PSi/TiO<sub>2</sub>. Electrons (black circle), holes (white circle), and oxygen vacancies ( $V_O$ ) band. Processes: (A) electrons quenched to the bottom of the CB, (B) electrons captured by deep traps, (C) electrons captured by surface traps, (D) holes captured by shallow traps, (E) blue luminescence emission, (F) red luminescence emission, and (H) hole injection from TiO<sub>2</sub> to PSi.

The dependence of the refractive index on the wavelength is also shown in Figure 4a. The refractive index value is drastically increased for TiO<sub>2</sub> nanolayers deposited by 200 ALD cycles. The refractive index of the thin film could differ from their structural properties.<sup>20,24</sup> Previously, we had demonstrated a complex analysis of optical constants of ZnO/Al<sub>2</sub>O<sub>3</sub> nanolaminates with different thicknesses of a single layer.<sup>20</sup> It was shown that the refractive index of the ZnO layers increased with the thickness. The increase in the refractive index was explained by the increase in the packing density of thicker layers, which was confirmed by analysis of the structural properties.<sup>20,24</sup>

The investigated TiO<sub>2</sub> films showed a decreased band gap value with increased thickness, which means that the crystalline structure of the samples was transformed from nanostructured to bulk-like. Therefore, according to refs 20 and 24, the packing density of the films should increase, explaining the behavior of  $n(\lambda)$  dependence. Low values of the refractive index for thinner samples can be explained by the cluster-like structure or lower crystalline quality. However, as the films were deposited on the planar silicon surface at 300 °C, the operating temperature was enough for amorphous-to-crystalline phase transitions in the TiO<sub>2</sub> samples, which were confirmed by TEM and Raman spectroscopy (Figures S3 and S4, respectively, Supporting Information). Thus, the optical properties of the deposited TiO<sub>2</sub> samples are tailored by their structural parameters.

The spectral dependence of the extinction coefficient and the refractive index of the PSi are shown in Figure 4c, where the optical anisotropy of the PSi layer can be clearly seen. It is well-known that the PSi layer is composed of air and silicon. Therefore, its refractive index should range from 1.0 (refractive index of air) to 3.4 (refractive index of pure silicon) depending on its porosity.<sup>25</sup> Taking into account the values of the refractive index, we conclude that the porosity of the PSi layer has a range<sup>25,26</sup> of 75–85%.

As is well-known, the absorption spectrum of PSi is the sum of the different microscopic absorption processes. Absorption measurements are often complicated by difficulties in interpretation that arise from the inhomogeneity of PSi. However, what is clear from the absorption studies is that the spectra are shifted toward higher energy compared to that of bulk Si, which could refer to the quantum confinement effect. Using eq 2, the band gap of PSi was estimated, and the experimental  $E_g$  of the film is approximately 2.3–2.8 eV.

Photoluminescence measurements were performed to understand the presence of defects and recombination ability of charge carriers. TiO<sub>2</sub> introduced into the PSi matrix may change the surface structure and interface between TiO<sub>2</sub> and PSi. It is generally believed that visible emissions from TiO<sub>2</sub> films are mainly due to self-trapped excitons (STEs), oxygen vacancies ( $V_O$ ), and surface states.

The PL of PSi, TiO<sub>2</sub>-Si, and PSi/TiO<sub>2</sub> nanostructures were measured in the region of light wavelengths from 400 to 900

nm (Figure 5). The maximum of the PL peak for PSi was detected at 1.8 eV ( $690 \pm 5$  nm). After ALD deposition of TiO<sub>2</sub> on PSi, PL was investigated, and the PL spectra showed two broad peaks at approximately 2.4–3 eV (blue PL) and 1.7–1.9 eV (red PL) (Figure 5a, b). However, after the deposition of TiO<sub>2</sub>, the PL intensity is degraded dramatically. This might indicate that the PSi/TiO<sub>2</sub> nanostructure had a lower recombination rate. We suggest that the PSi/TiO<sub>2</sub> heterojunctions separate the photogenerated charge carriers due to a difference in the energy levels of their conduction bands (CB) and valence bands (VB) (shown later in Figure 6).

After multiplex Gaussian fitting of the annealed PSi–TiO<sub>2</sub> PL spectrum, we obtained seven PL bands (Figure 5c). The PL band at 2.95 eV corresponds to the STEs localized on the TiO<sub>6</sub> octahedral.<sup>27–31</sup> The bands at 2.74 and 2.48 eV are attributed to oxygen vacancies with two electrons<sup>27,32–34</sup> and one electron, respectively.<sup>27,32</sup> The PL band at 2.61 eV probably originates from surface Ti–OH bonds<sup>30,35</sup> or from neutral oxygen vacancy.<sup>32,36</sup> The band at 2.2 eV can be assigned to the trap level related to oxygen vacancies on the surface.<sup>30,37</sup> The peaks at 1.93 and 1.63 eV more likely originate from the surface states.<sup>38–40</sup> Zhang et al. have shown that the surface states responsible for the red PL are likely to be formed by some unsaturated surface atoms of TiO<sub>2</sub> nanocrystallites<sup>39</sup> related to Ti<sup>4+</sup>, Ti<sup>3+</sup>, and Ti<sup>2+</sup>.

Comparing prepared and annealed samples, we can conclude that two primary competing recombination mechanisms take place: radiative recombination through the surface states (surface recombination) corresponding to the red PL and radiative recombination through the oxygen vacancies (V<sub>O</sub>) and STE (volume recombination) corresponding to the blue PL. Thus, both the volume and surface area affect the intensity of the PL spectrum. However, when the amount of materials was decreased, the ratio of the surface area to volume was also increased, and the surface factor becomes a more important characteristic to the material's optical and PL properties (Figure 5d). Thus, the former mechanism should be crucial for TiO<sub>2</sub> with a high concentration of surface defects, which is typical for amorphous or low crystalline quality materials. After annealing, the crystallinity becomes very high, and the specific surface area decreases. Thus, when the number of defect states is decreased, the latter mechanism prevails over the former, and radiative recombination occurs through oxygen vacancies.

Figure 6 shows the simple scheme of possible relaxation processes in PSi/TiO<sub>2</sub>. Laser excitation at 337 nm excites the electrons to the upper CB and then excited electrons are quenched to the bottom CB (process A, Figure 6). Because of the presence of oxygen vacancies, the electrons do not directly recombine with holes in the VB. Instead, they are captured by the oxygen vacancies and then recombine with the holes in the VB (process B, Figure 6), accompanying radiative emission corresponding to the blue PL (process E, Figure 6). As was shown by Wang et al., some carriers (electrons and/or holes) are first captured by shallow defect states and then quenched to the luminescent sites through trap-to-trap hopping to finally produce visible luminescence.<sup>40</sup> On the other hand, photogenerated electrons and holes could be trapped by the surface states (processes C and G, Figure 6) and then recombine with emission corresponding to the red PL (process F, Figure 6).

It is well-known that reducing photogenerated charge carrier recombination in heterojunctions improves photocatalytic activity.<sup>1–5</sup> Because of the difference in the energy level of CB and VB at the PSi–TiO<sub>2</sub> interface, separation of the

photogenerated electrons and holes occurs very fast, reducing recombination of the photogenerated charge carriers. After irradiation, holes accumulated in the VB of TiO<sub>2</sub> migrate into the PSi VB (process H, Figure 6), thus decreasing radiative recombination and PL intensity. This process should be very intense in the depletion region of TiO<sub>2</sub> and should significantly decrease surface recombination.

## CONCLUSIONS

In summary, TiO<sub>2</sub>/PSi nanostructures were fabricated using metal-assisted chemical etching and atomic layer deposition. The crystalline structures, chemical compositions, and morphologies of the prepared and annealed TiO<sub>2</sub>/PSi nanostructures were established. The approximate size of TiO<sub>2</sub> nanocrystals inside the PSi matrix was estimated using TEM and Raman spectroscopy. By controlling the number of deposition cycles, the size of anatase nanocrystallites inside the PSi matrix could be controlled. Optical and photoluminescence properties of TiO<sub>2</sub>/PSi nanostructures are tailored by their structural parameters. The mechanisms of the PL emissions were discussed. Analysis of the PL spectra indicates PL quenching is due to electron–hole separation at the TiO<sub>2</sub>/PSi heterojunction. Combining the large effective surface area of TiO<sub>2</sub>/PSi nanostructures with fast charge carrier separation allows for improvement in the performance of photocatalysis, biosensors, and other optoelectronic devices.

## ASSOCIATED CONTENT

### Supporting Information

Plane-view SEM images and EDX analysis of the surface of prepared samples, cross-sectional SEM view of an individual pore, cross-sectional TEM images of the TiO<sub>2</sub> layer on the planar silicon surface, TEM images of PSi/TiO<sub>2</sub> nanostructures, Raman spectra of prepared ALD TiO<sub>2</sub> layers on the planar silicon surface, and high resolution XPS core level spectra of O 1s PSi/TiO<sub>2</sub> before and after annealing. This material is available free of charge via the Internet at <http://pubs.acs.org>.

## AUTHOR INFORMATION

### Corresponding Author

\*E-Mail: [yatsunskiy@gmail.com](mailto:yatsunskiy@gmail.com).

### Notes

The authors declare no competing financial interest.

## ACKNOWLEDGMENTS

Financial support from the National Centre for Research and Development under research grant “Nanomaterials and their Application to Biomedicine”, Contract No. PBS1/A9/13/2012, is gratefully acknowledged.

## REFERENCES

- (1) Avasthi, S.; McClain, W. E.; Man, G.; Kahn, A.; Schwartz, J.; Sturm, J. C. Hole-blocking Titanium-Oxide/Silicon Heterojunction and its Application to Photovoltaics. *Appl. Phys. Lett.* **2013**, *102*, 203901.
- (2) Hu, S.; Shaner, M. R.; Beardslee, J. A.; Lichterman, M.; Brunshwig, B.; Lewis, N. Amorphous TiO<sub>2</sub> Coatings Stabilize Si, GaAs, and GaP Photoanodes for Efficient Water Oxidation. *Science* **2014**, *6187*, 1005–1009.
- (3) Jian, S.; Xudong, W. Hierarchical TiO<sub>2</sub>–Si Nanowire Architecture with Photoelectrochemical Activity under Visible Light Illumination. *Energy Environ. Sci.* **2012**, *5*, 7918–7922.



- (4) Yun, J. H.; Boukai, A.; Yang, P. High Density n-Si/n-TiO<sub>2</sub> Core/Shell Nanowire Arrays with Enhanced Photoactivity. *Nano Lett.* **2009**, *9*, 410–415.
- (5) Takabayashi, S.; Nakamura, R.; Nakato, Y. A Nano-modified Si/TiO<sub>2</sub> Composite Electrode for Efficient Solar Water Splitting. *J. Photochem. Photobiol. A* **2004**, *166*, 107–113.
- (6) Arakelyan, V. M.; Martirosyan, Kh. S.; Galstyan, V. E.; Shahnazaryan, G. E.; Aroutiounian, V. M. Room Temperature Gas Sensor Based on Porous Silicon/Metal Oxide Structure. *Phys. Status Solidi C* **2007**, *4*, 2059–2062.
- (7) Lotfabad, E. M.; Kalisvaart, P.; Cui, K.; Kohandehghan, A.; Kupsta, M.; Olsena, B.; Mitlin, D. ALD TiO<sub>2</sub> Coated Silicon Nanowires for Lithium Ion Battery Anodes with Enhanced Cycling Stability and Coulombic Efficiency. *Phys. Chem. Chem. Phys.* **2013**, *15*, 13646.
- (8) Wei, Z.; Li, R.; Huang, T.; Yu, A. Fabrication and Electrochemical Properties of Si/TiO<sub>2</sub> Nanowire Array Composites as Lithium Ion Battery Anodes. *J. Power Sources* **2013**, *238*, 165–172.
- (9) Yan, D.; Bai, Y.; Yu, C.; Li, X.; Zhang, W. A Novel Pineapple-structured Si/TiO<sub>2</sub> Composite as Anode Material for Lithium Ion Batteries. *J. Alloys Compd.* **2014**, *609*, 86–92.
- (10) Li, J.; Sailor, M. J. Synthesis and Characterization of a Stable, Label-free Optical Biosensor from TiO<sub>2</sub>-coated Porous Silicon. *Biosens. Bioelectron.* **2014**, *55*, 372–378.
- (11) Karacali, T.; Hasar, U. C.; Ozbek, I. Y.; Oral, E. A.; Efeoglu, H. Novel Design of Porous Silicon Based Sensor for Reliable and Feasible Chemical Gas Vapor Detection. *J. Lightwave Technol.* **2013**, *31*, 295–305.
- (12) Huang, Z.; Geyer, N.; Werner, P.; de Boor, J.; Gösele, U. Metal-Assisted Chemical Etching of Silicon: A Review. *Adv. Mater.* **2011**, *23*, 285–308.
- (13) Nam, T.; Kim, J. M.; Kim, M. K.; Kim, H. Low-temperature Atomic Layer Deposition of TiO<sub>2</sub>, Al<sub>2</sub>O<sub>3</sub>, and ZnO Thin Films. *J. Korean Phys. Soc.* **2011**, *59*, 452–457.
- (14) Iatunskyi, I.; Kempinski, M.; Jancelewicz, M.; Zaleski, K.; Jurga, S.; Smyntyna, V. Structural and XPS Characterization of ALD Al<sub>2</sub>O<sub>3</sub> Coated Porous Silicon. *Vacuum* **2015**, *113*, 52–58.
- (15) Chartier, C.; Bastide, S.; Levy-Clément, C. Metal-Assisted Chemical Etching of Silicon in HF–H<sub>2</sub>O<sub>2</sub>. *Electrochim. Acta* **2008**, *53*, 5509–5516.
- (16) Šćepanović, M. J.; Grujić-Brojčin, M.; Dohčević-Mitrović, Z. D.; Popović, Z. V. Characterization of Anatase TiO<sub>2</sub> Nanopowder by Variable-Temperature Raman Spectroscopy. *Sci. Sintering* **2009**, *41*, 67–73.
- (17) Mazza, T.; Barborini, E.; Piseri, P.; Milani, P.; Cattaneo, D.; Bassi, A. Li.; Bottani, C. E. Raman Spectroscopy Characterization of TiO<sub>2</sub> Rutile Nanocrystals. *Phys. Rev. B* **2007**, *75*, 045416.
- (18) Choi, H. C.; Jung, Y. M.; Kim, S. B. Size Effects in the Raman Spectra of TiO<sub>2</sub> Nanoparticles. *Vib. Spectrosc.* **2005**, *37*, 33–38.
- (19) Zhu, K. R.; Zhang, M. S.; Chen, Q.; Yin, Z. Size and Phonon-Confinement Effects on Low-Frequency Raman Mode of Anatase TiO<sub>2</sub> Nanocrystal. *Phys. Lett. A* **2005**, *340*, 220–227.
- (20) Chaaya, A. A.; Viter, R.; Baleviciute, I.; Bechelany, M.; Ramanavicius, A.; Gertnere, Z.; Erts, D.; Smyntyna, V.; Miele, P. Tuning Optical Properties of Al<sub>2</sub>O<sub>3</sub>-ZnO Nanolaminates Synthesized by Atomic Layer Deposition. *J. Phys. Chem. C* **2014**, *118*, 3811–3819.
- (21) Chaaya, A. A.; Viter, R.; Bechelany, M.; Alute, Z.; Erts, D.; Zalesskaya, A.; Kovalevskis, K.; Rouessac, V.; Smyntyna, V.; Miele, P. Evolution of Microstructure and Related Optical Properties of ZnO Grown by Atomic Layer Deposition. *Beilstein J. Nanotechnol.* **2013**, *4*, 690–698.
- (22) Reddy, K. M.; Manorama, S. V.; Reddy, A. R. Bandgap Studies on Anatase Titanium Dioxide Nanoparticles. *Mater. Chem. Phys.* **2002**, *78*, 239–245.
- (23) Chaaya, A. A.; Viter, R.; Baleviciute, I.; Bechelany, M.; Ramanavicius, A.; Erts, D.; Smyntyna, V.; Miele, P. Optical and Structural Properties of Al<sub>2</sub>O<sub>3</sub>/ZnO Nanolaminates Deposited by ALD Method. *Phys. Status Solidi C* **2014**, *11*, 1505–1508.
- (24) Krishna, M. G.; Rao, K. N.; Mohan, S. Optical Properties of Ion Assisted Deposited Zirconia Thin Films. *J. Vac. Sci. Technol., A* **1992**, *10*, 3451–3455.
- (25) Arenas, M. C.; Hu, H.; Nava, R.; del Rio, J. A. Determination of the Complex Refractive Index of Porous Silicon Layers on Crystalline Silicon Substrates. *Int. J. Mod. Phys. B* **2010**, *24*, 4835.
- (26) Pap, A. E.; Kordas, K.; Vahakangas, J.; Uusimaki, A.; Leppavuori, S.; Pilon, L.; Szatmari, S. Optical Properties of Porous Silicon. Part III: Comparison of Experimental and Theoretical Results. *Opt. Mater.* **2006**, *28*, 506–513.
- (27) Yenchalwar, S. G.; Azhagan, V. K.; Shelke, M. V. Enhanced Photoluminescence and Photoactivity of Plasmon Sensitized nSiNWs/TiO<sub>2</sub> Heterostructures. *Phys. Chem. Chem. Phys.* **2014**, *16*, 17786.
- (28) Kernazhitsky, L.; Shymanovska, V.; Gavrilko, T.; Naumov, V.; Fedorenko, L.; Kshnyakin, V.; Baran, J. Room Temperature Photoluminescence of Anatase and Rutile TiO<sub>2</sub> Powders. *J. Lumin.* **2014**, *146*, 199–204.
- (29) Choudhury, B.; Choudhury, A. Tailoring Luminescence Properties of TiO<sub>2</sub> Nanoparticles by Mn Doping. *J. Lumin.* **2013**, *136*, 339–346.
- (30) Akhavan, O.; Ghaderi, E.; Rahimi, K. Adverse Effects of Graphene Incorporated in TiO<sub>2</sub> Photocatalyst on Minuscule Animals under Solar Light Irradiation. *J. Mater. Chem.* **2012**, *22*, 23260.
- (31) Nasr, M.; Chaaya, A. A.; Abboud, N.; Bechelany, M.; Viter, R.; Eid, C.; Khoury, A.; Miele, P. Photoluminescence: a Very Sensitive Tool to Detect the Presence of Anatase in Rutile Phase Electrospun TiO<sub>2</sub> Nanofibers. *Superlattices Microstruct.* **2014**, *77*, 18–24.
- (32) Chang, Y. H.; Liu, C. M.; Chen, C.; Cheng, H. E. The Effect of Geometric Structure on Photoluminescence Characteristics of 1-D TiO<sub>2</sub> Nanotubes and 2-D TiO<sub>2</sub> Films Fabricated by Atomic Layer Deposition. *J. Electrochem. Soc.* **2012**, *159*, 401–405.
- (33) Das, K.; Sharma, S. N.; Kumar, M.; De, S. K. Morphology Dependent Luminescence Properties of Co Doped TiO<sub>2</sub> Nanostructures. *J. Phys. Chem. C* **2009**, *113*, 14783–14792.
- (34) Abazovic, N. D.; Comor, M. I.; Dramicanin, M. D.; Jovanovic, D. I.; Ahrenkiel, S. P.; Nedeljkovic, J. M. Photoluminescence of Anatase and Rutile TiO<sub>2</sub> Particles. *J. Phys. Chem. B* **2006**, *110*, 25366–25370.
- (35) Zhang, J.; Chen, X.; Shen, Y.; Li, Y.; Hu, Z.; Chu, J. Synthesis, Surface Morphology, and Photoluminescence Properties Anatase Iron-Doped Titanium Dioxide Nano-crystalline Films. *Phys. Chem. Chem. Phys.* **2011**, *13*, 13096–13105.
- (36) Jun, J.; Jin, C.; Kim, H.; Kang, J.; Lee, C. The Structure and Photoluminescence Properties of TiO<sub>2</sub>-coated ZnS Nanowires. *Appl. Phys. A: Mater. Sci. Process.* **2009**, *96*, 813–818.
- (37) Knorr, F. J.; Zhang, D.; McHale, J. L. Influence of TiCl<sub>4</sub> Treatment on Surface Defect Photoluminescence in Pure and Mixed-Phase Nanocrystalline TiO<sub>2</sub>. *Langmuir* **2007**, *23*, 8686–8690.
- (38) Zhao, J.; Jia, C.; Duan, H.; Li, H.; Xie, E. Structural Properties and Photoluminescence of TiO<sub>2</sub> Nanofibers were Fabricated by Electrospinning. *J. Alloys Compd.* **2008**, *461*, 447–450.
- (39) Zhang, W. F.; Zhang, M. S.; Yin, Z.; Chen, Q. Photoluminescence in Anatase Titanium Dioxide Nanocrystals. *Appl. Phys. B: Lasers Opt.* **2000**, *70*, 261–265.
- (40) Wang, X.; Feng, Z.; Shi, J.; Jia, G.; Shen, S.; Zhouab, J.; Li, C. Trap States and Carrier Dynamics of TiO<sub>2</sub> Studied by Photoluminescence Spectroscopy under Weak Excitation Condition. *Phys. Chem. Chem. Phys.* **2010**, *12*, 7083–7090.

### 3.3. Enhancement of optical and mechanical properties of Si nanopillars by ALD TiO<sub>2</sub> coating

The employment of ordered nanopillar arrays opens up a lot of possibilities for efficiently utilizing complex composite nanostructures in diverse applications like biophotonics, photovoltaics, energy storage, etc. In this regard, it is necessary to estimate mechanical stability and the capability to tune the optical properties in such nanostructured arrays.

In this research, we have studied the mechanical and optical properties of pillar-like silicon nanostructures coated with the TiO<sub>2</sub> ALD layer. The silicon nanopillars were fabricated by combining NSL and MACE. Then, a typical ALD technique was applied to deposit the TiO<sub>2</sub> layer of defined thickness. A thorough analysis of the structural properties of the as-prepared and annealed 1D Si/TiO<sub>2</sub> nanocomposites was performed by methods of SEM, TEM, GIXRD and EDX. The acquisition of Raman, reflectance and PL spectra elucidated optical properties. The mechanical properties of 1D Si/TiO<sub>2</sub> nanocomposites were investigated by nanoindentation testing.

The acquired data clearly show that the optical and mechanical properties of the fabricated nanopillars are tailored by their morphology. Especially, inclusions of TiO<sub>2</sub> into mesoporous silicon matrix resulting in an enhancement of mechanical properties. Generally, it was found that the silicon matrix provides the structural stability of the obtained nanostructures, while inclusions of TiO<sub>2</sub> nanocrystallites provide fracture resistance and improve Young's modulus. As a result, Young's modulus of annealed Si/TiO<sub>2</sub> nanopillar arrays has a three-time higher value in comparison to pristine silicon nanopillar arrays.

In this research, the Author has performed NSL by a spin coating method and MACE on silicon substrates. He was involved in RIE processing of polystyrene nanospheres monolayer and ALD of TiO<sub>2</sub> thin films. He processed SEM/TEM and GIXRD data, prepared Figures 1 and 3, and calculated nanocrystallite sizes and strain values from GIXRD data. Also, the Author assisted in acquiring and processing the data obtained by PL, reflectance and Raman spectroscopies. He contributed to the manuscript by writing the introduction part, experimental part and description of structural properties in the “Results and discussion” part.

**Number of Ministerial points: 100**

**Impact factor: 3.9**



Cite this: *RSC Adv.*, 2016, 6, 97070

## Enhancement of optical and mechanical properties of Si nanopillars by ALD TiO<sub>2</sub> coating†

M. Pavlenko,<sup>ab</sup> E. L. Coy,<sup>a</sup> M. Jancelewicz,<sup>a</sup> K. Załęski,<sup>a</sup> V. Smyntyna,<sup>b</sup> S. Jurga<sup>a</sup> and I. Iatsunskiy<sup>\*a</sup>

The mechanical and optical properties of Si and TiO<sub>2</sub>-Si nanopillars (NPI) were investigated. Mesoporous silicon NPI arrays were fabricated by metal-assisted chemical etching and nanosphere lithography, and then pillars were covered by TiO<sub>2</sub> using the atomic layer deposition technique. We performed scanning electron microscopy (SEM), transmission electron microscopy (TEM), X-ray diffraction (XRD), energy dispersive X-ray spectroscopy (EDX), Raman spectroscopy, reflectance, photoluminescence (PL) spectroscopy and nanoindentation to characterize the as-prepared and annealed TiO<sub>2</sub>-Si NPI. The main structural and mechanical parameters of TiO<sub>2</sub>-Si NPI (grain size, strain, critical load, elastic recovery and Young's module) were calculated. Reflectance and PL spectroscopy were used to study the impact of morphology on optical properties of TiO<sub>2</sub>-Si NPI before and after annealing. It was established that the nanostructures of TiO<sub>2</sub> penetrated inside the porous matrix of Si pillar improve the mechanical properties of TiO<sub>2</sub>-Si NPI. The results of nanoindentation study have shown that Young's modulus of annealed TiO<sub>2</sub>-Si NPI is about three times higher than for the pure Si NPI.

Received 30th August 2016  
Accepted 5th October 2016

DOI: 10.1039/c6ra21742g

www.rsc.org/advances

### Introduction

Si nanopillars (NPI) are of great interest due to their potential applications in photovoltaics,<sup>1-3</sup> electronics,<sup>4,5</sup> sensors and biosensors,<sup>6-8</sup> and nanocapacitor arrays.<sup>9</sup> It has been demonstrated that Si NPI have several advantages over other silicon nanostructures such as enhanced light absorption,<sup>3,10</sup> efficient carrier transport,<sup>11</sup> superhydrophobicity,<sup>12</sup> strong carrier confinement,<sup>13</sup> and possibility to tune electronic and optical properties.<sup>14</sup> However, because of poor chemical stability and a high valence band maximum energy of Si comparing to hydrogen potential, it is difficult to simply use Si NPI in (photo) electrochemical applications. Therefore, nanocomposite structures based on Si NPI and metal oxides (*e.g.* Al<sub>2</sub>O<sub>3</sub>, TiO<sub>2</sub>, ZnO) have been proposed to eliminate these shortcomings.

It has been shown that nanocomposite materials based on porous Si (PSi), Si nanowires (SiNW) and Si NPI could demonstrate unique properties, not observed in other nanosilicon structures. Recent publications show that nanocomposites based on nanostructured Si and TiO<sub>2</sub> possess enhanced photocatalytic activity due to their fast photogenerated charge carrier separation, low reflectance and high surface area.<sup>15,16</sup> Another broad area of applications of such nanocomposites is

(bio)sensors.<sup>17,18</sup> Authors have shown that combination of metal oxide nanostructures and PSi matrix, with well-defined structural properties gives a good possibility to enhance the sensor signal and sensitivity of the sensor/biosensor through tailoring structural properties of nanocomposites which is one of the main and actual problems in the field of sensors and biosensors.

Thus, the fabrication of Si NPI nanocomposites, as well as the study of their physical/chemical and structural properties will explore a development of new functional materials with high surface area and advanced properties for applications in bio-photonics, nanoelectronics or (photo)catalysis. It is also worth to mention, the optical and mechanical properties of Si NPI nanocomposites are closely related to their morphology. Therefore, a thorough study on the effect of morphology on the optical and mechanical properties of TiO<sub>2</sub>-Si NPI is missing and further studies are still required.

A simple method to produce highly ordered Si NPI based on metal-assisted chemical etching (MACE) and nanosphere lithography, enabling control of the diameter, length and density of NPI arrays has been developed.<sup>19,20</sup> This approach allows controlling of the type, level, crystallographic orientation of dopant, and the orientation of Si NPI relative to the Si substrate. There is a number of methods to create nanocomposites of Si NPI. But as it was shown in recent researches, the most preferable method is Atomic Layer Deposition (ALD) technique.<sup>21,22</sup> It does not depend on substrate geometry and can be applied both for planar samples, 3D patterned substrates and porous media.<sup>23,24</sup> This method allows controlling the

<sup>a</sup>NanoBioMedical Centre, Adam Mickiewicz University in Poznan, Umultowska 85, 61-614, Poznan, Poland. E-mail: yatsunskiy@gmail.com; igoyat@amu.edu.pl

<sup>b</sup>Department of Experimental Physics, Odessa I.I. Mechnikov National University, Pasternak 42, 65026, Odessa, Ukraine

† Electronic supplementary information (ESI) available. See DOI: 10.1039/c6ra21742g

thickness of nanolayers or size of nanocrystallites inside the PSI and the chemical composition by controlling the ALD parameters.

In this work, we report the effect of morphology on the optical and mechanical properties of the TiO<sub>2</sub>-porous Si NPL composite system. To fabricate porous Si NPL, in this present study we used MACE and nanosphere lithography technique. Then Si NPL were covered by the TiO<sub>2</sub> using ALD. The morphology and phase composition of fabricated TiO<sub>2</sub>-porous Si NPL were studied by the scanning and transmission electron microscopy (SEM, TEM), XRD, energy dispersive X-ray spectroscopy (EDX) and Raman spectroscopy. Optical properties have been analysed by means of reflectance and photoluminescence (PL) spectroscopy. Structural, optical, and mechanical parameters of TiO<sub>2</sub>-porous Si NPL were estimated, and the correlation between them will be discussed. The mechanisms of the PL emissions will be proposed. The structural and optical changes induced by annealing will be discussed as well.

## Experimental

### Fabrication of Si nanopillars covered by ALD TiO<sub>2</sub>

Ordered arrays of Si ( $\rho < 0.005 \Omega \text{ cm}$  resistivity, polished on the (100) face, B-doped) NPL with hexagonal symmetry were fabricated by combination of nanosphere lithography technique and MACE. Silicon samples ( $1 \times 1 \text{ cm}^2$ ) were first cleaned by ethanol, acetone, and then by heating in a RCA solution (an aqueous mixture of 30% hydrogen peroxide (H<sub>2</sub>O<sub>2</sub>), 30% ammonium hydroxide (NH<sub>4</sub>OH), and DI water with the volume ratio of 1 : 1 : 5) at 80 °C for an hour, followed by a thorough rinse with DI water and drying in a stream of nitrogen (N<sub>2</sub>). Polystyrene nanosphere 10% solution (mean diameter 600 nm) was mixed with an equal amount of ethanol and then applied to the deposition of a monolayer mask on a clean silicon surface by floating technique.<sup>3</sup> After deposition the size of nanosphere was decreased to approximately 300 nm using reactive ion etching (RIE) (MicroSys 200) in oxygen plasma. Following parameters were used: RF power – 70 W, and pressure – 0.6 mbar. A 120 nm Au film was deposited, as a catalyst, by magnetron sputtering machine (Quorum Q160T) in Ar atmosphere (50 mA, pressure 10<sup>-2</sup> mbar). Then, the samples were etched in aqueous solution containing HF (40%), H<sub>2</sub>O<sub>2</sub> (30%), and ultrapure H<sub>2</sub>O at a ratio of 80 : 80 : 20 H<sub>2</sub>O<sub>2</sub>/H<sub>2</sub>O/HF for 15 min. The Au film was removed using a solution of Aqua Regia (HCl (35%) and HNO<sub>3</sub> (65%) at ratio 1 : 2) and then samples were dipped in HF (5%) solution for 3 min to remove native oxide. After all procedures samples of Si NPL were cleaned with deionized water and blown dry with N<sub>2</sub>.

The ALD TiO<sub>2</sub> was deposited onto the samples of Si NPL using TiCl<sub>4</sub> and water as ALD precursors. The ALD cycle consisted of 0.3 s exposure to TiCl<sub>4</sub>, 4 s N<sub>2</sub> purge, 0.3 s exposure to water and 4 s N<sub>2</sub> purge. The temperature of ALD was 200 °C. The number of deposition-purge cycles was 500 corresponding to approximately 20 nm of the TiO<sub>2</sub> film on the planar silicon surface. The growth rate was typically 0.4 Å per cycle for TiO<sub>2</sub> on the planar

silicon surface. After TiO<sub>2</sub> deposition some samples were annealed at 450 °C for an hour in an ambient atmosphere.

### Characterization

Structural and chemical compositions of NPL were analysed by transmission (JEOL ARM 200F) and scanning (JEOL, JSM-7001F) electron microscopy (TEM/SEM). The lamellas for TEM were prepared by focused ion beam (FIB-JEOL JIB-4000) by the method described in ref. 25. GIXRD measurements were performed on X'pert3 MRD (XL) from PANalytical, working with a Cu K $\alpha$  radiation source (wavelength of 1.54 Å) and operating at 45 kV and 40 mA. Raman scattering measurements were performed using a Renishaw micro-Raman spectrometer equipped with a confocal microscope (Leica). The Raman scattering spectra were excited by a 514 nm laser. The beam was focused on the samples with a 50 $\times$  microscope objective with a numerical aperture of 0.4. Optical properties of TiO<sub>2</sub>-Si NPL have been studied with reflectance (UV-vis spectrophotometer lambda 950 UV/vis/NIR range 300–1100 nm, 1 nm step) and photoluminescence spectroscopy (PL). PL of the samples was measured at room temperatures using a home-made setup. The excitation of PL was performed with a nitrogen laser (337.7 nm). Finally, mechanical properties of the samples were investigated by nanoindentation (Hysitron TI 950 TriboIndenter) using a Berkovich diamond indenter at maximum load of 40  $\mu\text{N}$ .

## Results and discussion

In order to examine the morphology of pristine Si NPL, and NPL after TiO<sub>2</sub> ALD, SEM and TEM characterizations were carried out. Fig. 1(a) shows the typical large-scale SEM image of the formed Si NPL. Non-uniform distribution of NPL arrays is a result of the way the polystyrene spheres are float-transferred onto the Si substrate. Nevertheless, relatively large areas, up to 10  $\mu\text{m}$ , are covered with the uniform hexagonal pillar arrays.

The cross-sectional TEM image of Si NPL is presented in the Fig. 1(b). The distance between two adjacent pillars is approximately 0.7  $\mu\text{m}$ , the diameter and the height are 0.4 and 1.5  $\mu\text{m}$ , respectively. Geometrical parameters of fabricated NPL could be controlled by varying the MACE and nanosphere lithography procedures. The outer surface of NPL is rough and porous. The roughness of the Si NPL is due to the roughness in the outer edge of polystyrene spheres (Fig. S1†). The porosity can be observed more clearly in the high-magnification SEM and TEM images of the NPL (Fig. 1(c–e)). Pillars have a mesoporous structure with an average pore size less than 10 nm. Below Si NPL a mesoporous layer of 1.5  $\mu\text{m}$  thick can be also observed. Bechelany *et al.* proposed one of the possible mechanism responsible for sidewall etching.<sup>26</sup> They have shown that gold assisted chemical etching (vertical etching) is in competition with chemical isotropic etching (sidewall etching) of the bulk Si enhanced by its high dopant concentration. After 500 cycles of ALD a conformal TiO<sub>2</sub> layer on the Si NPL was obtained (Fig. 1(f)). It is difficult to identify any individual grains of the TiO<sub>2</sub> (Fig. S2†). TEM results show that the porous inside the Si NPL are filled by TiO<sub>2</sub> (Fig. S3†).

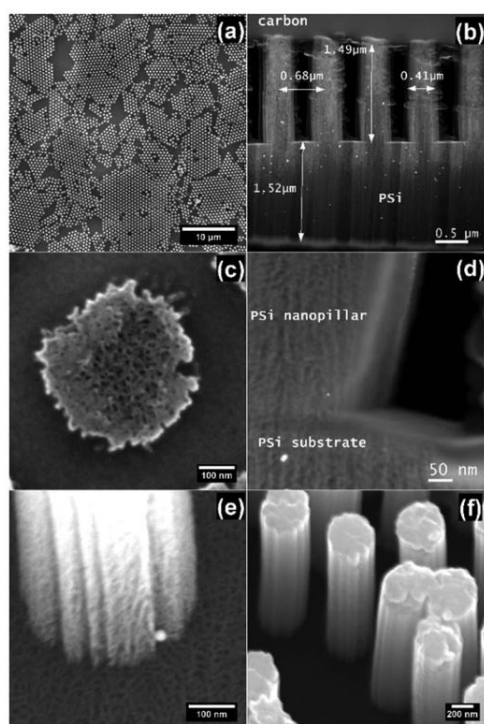


Fig. 1 Si and TiO<sub>2</sub>-Si NPL arrays, (a) plane view SEM image of pristine Si NPL, (b) cross-sectional TEM image of Si NPL, (c) the top surface of the pillar, (d) cross-sectional HRTEM image of Si NPL, (e) high resolution SEM image of the pillar, (f) SEM image of TiO<sub>2</sub>-Si NPL.

In addition, we have studied the elemental distribution over the NPL using EDX mapping. As can be seen in Fig. 2, both titanium (magenta) and oxygen (green) elements are distributed quite uniformly inside the Si NPL for as-deposited samples. One can also observe oxygen and titanium penetrating the PSi layer beneath the pillar. In the case of porous structures, during the

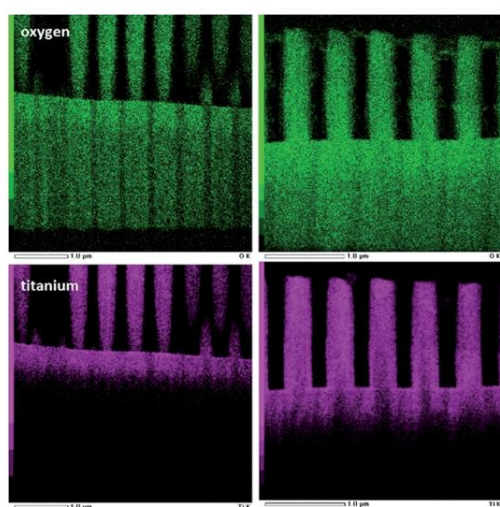


Fig. 2 EDX element mapping images of the TiO<sub>2</sub>-NPL before (left images) and after annealing (right images).

ALD process, molecules of precursors penetrate into the pore, and forming nanostructures of TiO<sub>2</sub> inside the porous matrix of Si NPL as well as the bottom PSi layer. The elemental distribution of titanium atoms remains almost the same after the annealing. However, we observed the increasing of oxygen concentration in the Si NPL and PSi layer indicating on enhanced oxidation of the Si during the annealing (Fig. S4†).

Fig. 3 shows the GIXRD of Si NPL covered with TiO<sub>2</sub> layer after 500 ALD cycles. For Si NPL we can see the most intensive Si peak located at 55.78° and corresponding to (311) orientation.<sup>27</sup> Titanium ALD deposition leads to the substantial X-ray scattering and considerable intensity decreasing. We do not observe XRD peaks corresponding to crystalline titanium phase. Thus, we can conclude that after ALD, titanium dioxide is mainly in an amorphous or highly polycrystalline phase what was also confirmed by TEM and Raman spectroscopy (shown later). After annealing, one can notice XRD peaks centred at 25.27°, 37.8°, 48.02° and 62.45° corresponding to (101), (004), (200) and (200) of TiO<sub>2</sub> anatase phase (JCPDS 21-1272), respectively. It might be explained by the amorphous-to-crystalline phase transition occurring in the TiO<sub>2</sub> during annealing.<sup>23</sup>

It is well known that XRD peak analysis is a powerful and simple method to estimate the nanocrystallites size and the lattice strain.<sup>28,29</sup> The average size of TiO<sub>2</sub> nanocrystallites can be determined using the Scherer equation:<sup>30</sup>

$$D = \frac{0.94\lambda}{\text{FWHM} \cos(\theta)}, \quad (1)$$

where  $D$  is the average size of nanocrystallites,  $\lambda$  – the X-ray wavelength, FWHM – full width at half maximum of the XRD peaks centered at  $\theta$  degree.

The strain-induced broadening in TiO<sub>2</sub> and Si nanocrystallites was calculated using the formula:<sup>31</sup>

$$\varepsilon = \frac{\text{FWHM}}{4tg(\theta)}. \quad (2)$$

Because of the total peak broadening is represented by the sum of the contributions of strain and crystallite size, the

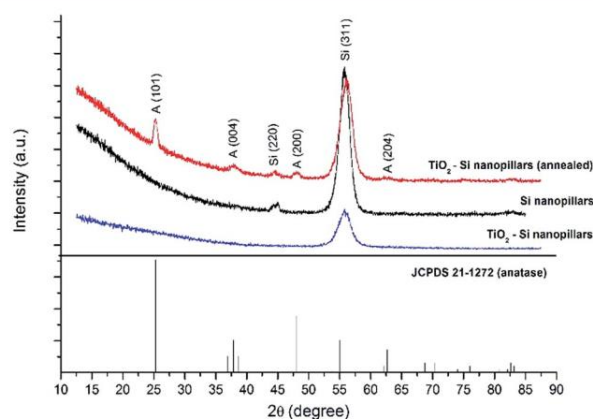


Fig. 3 GIXRD of Si NPL before and after ALD deposition with JCPDS (21-1272) data of anatase.

Williamson–Hall approach should be applied to determine the main broadening factor.<sup>32,33</sup> However, in order to apply the Williamson–Hall approach correctly, more XRD peaks should be considered in calculations.<sup>32,33</sup> In our case it was not applicable. Therefore, we have estimated the strain and crystallite size separately, using formula (1) and (2).

Calculated values of the average size of TiO<sub>2</sub> and Si nanocrystallites, and strains are presented in the Table 1. It is clearly seen, the average size of Si nanocrystallites remains almost the same after deposition and annealing. On the other hand, we can notice that the value of the strain in Si increases for as-deposited samples and takes the initial value ( $\varepsilon = 0.0149$ ) after annealing. This may be explained by considering that ALD TiO<sub>2</sub> penetrating inside the pores of Si NPI generates additional deformations, and thus increasing the strain value of silicon. With the annealing, the amorphous TiO<sub>2</sub> coalesces to form a continuous film of the anatase nanograins reducing the value of the strain. The increase in average crystallite size of anatase indicates an increase in the crystallinity of TiO<sub>2</sub>.

In order to determine the phase of obtained materials we also used  $\mu$ -Raman spectroscopy as very sensitive local method. Raman spectra for Si and TiO<sub>2</sub>-Si NPI are presented in Fig. 4. An intensive asymmetric, red-shifted peak at about 510 cm<sup>-1</sup> corresponds to phonon mode of nanosilicon.<sup>34</sup> The position and the shape of this peak indicate the presence of nanocrystalline and/or amorphous phase of the Si.<sup>35</sup> No peak from the c-Si substrate was seen in any of the Raman spectra. A broad peak between 900 and 1100 cm<sup>-1</sup> is related to few transverse optical phonons of PSi.<sup>36</sup>

In addition to nanostructured silicon studying, Raman spectroscopy was also used to detect and identify TiO<sub>2</sub>. The first intensive peak of TiO<sub>2</sub> is located at about 150 cm<sup>-1</sup> and attributed to E<sub>g</sub> mode. This is typical of the anatase TiO<sub>2</sub> phase, however the peak is broader and blue-shifted with respect to bulk anatase (peak position is 144 cm<sup>-1</sup> and FWHM is 7 cm<sup>-1</sup>).<sup>30</sup> Other Raman peaks at 200, 397 and 634 cm<sup>-1</sup> are also attributed to the anatase phase for E<sub>g</sub> and B<sub>1g</sub> modes, respectively.<sup>37,38</sup> After annealing the intensity of all anatase peaks increases, indicating increased crystallinity of TiO<sub>2</sub>. The broadening and blue-shift of the anatase Raman peak are attributed to phonon confinement effects that usually exist in nanomaterials.<sup>30</sup> In order to calculate the average size of anatase

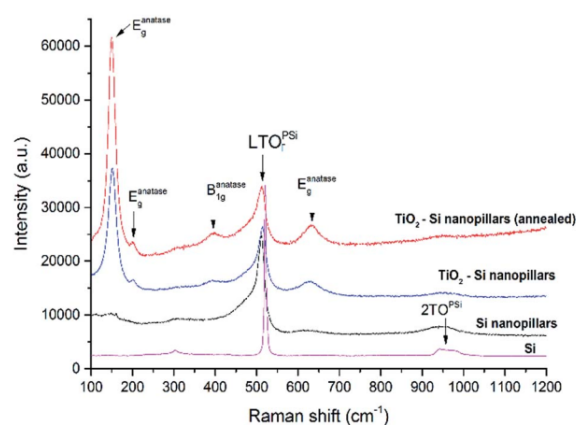


Fig. 4 Raman spectra of Si NPI before and after ALD deposition with the Raman spectrum of c-Si shown for comparison.

and silicon nanocrystallites we used a simple confinement model described in our previous publications.<sup>30,36</sup> In this model the first-order Raman spectrum  $I(\omega)$  for spherical nanocrystals is given by:

$$I(\omega) = \int_{\text{BZ}} \frac{4\pi q^2 \exp\left(-\frac{q^2 L^2}{16\pi^2}\right) d^3q}{(\omega - \omega(q))^2 - \left(\frac{\Gamma_0}{2}\right)^2}, \quad (3)$$

where  $\Gamma_0$  is the Raman linewidth at room temperature, and  $\omega(q)$  is the phonon dispersion curve (for anatase  $-\omega = \omega_0 + \Delta[1 - \cos(qa)]$ ,<sup>30</sup> and for silicon  $-\omega = A - Bq^2$ ,<sup>35</sup>  $\omega_0$  - maximum peak position,  $\Delta = 20$  cm<sup>-1</sup>,  $a = 0.3768$  nm,  $A$  and  $B$  - constants). The average size of anatase and silicon nanocrystallites was estimated and results are presented in the Table 1 (Fig. S5†). It is seen that the average crystallite size calculated from XRD and Raman spectroscopy differ by several nanometers. Taking into account that the penetration depth (PD) of the laser spot in the Raman spectroscopy differs from the X-ray beam PD, we can conclude that there is some distribution of the average crystallite size along the pillars and surface.

However, Khorasaninejad *et al.* showed that if confinement effects take place in nanosilicon, the red-shifting would be

Table 1 Structural and mechanical parameters of TiO<sub>2</sub>-Si NPI

Samples		Si NPI	TiO <sub>2</sub> -Si NPI	TiO <sub>2</sub> -Si NPI (annealed)		
Material		Si	Si	Anatase	Si	Anatase
XRD	Peak pos. [degree]	55.78	56.05	—	55.79	25.27
	FWHM [degree]	1.57	2.29	—	1.89	0.65
Raman	$D$ [nm]	5.89 ± 0.3	4.09 ± 0.6	—	4.95 ± 0.45	13.0 ± 0.4
	$\varepsilon$	0.0149	0.0189	—	0.0150	0.0127
	Peak pos. [cm <sup>-1</sup> ]	511.1	512.2	149.8	514	150.8
	FWHM [cm <sup>-1</sup> ]	16.48	19.77	21.7	18.2	18.8
	$D$ [nm]	8.1 ± 0.3	7.7 ± 0.3	7.3 ± 0.2	7.8 ± 0.3	11.6 ± 0.2
	$\varepsilon$	0.0107	0.0129	—	0.0118	—

approximately  $1\text{--}2\text{ cm}^{-1}$ .<sup>39</sup> In other cases, the compressive stress and defects affect mainly on the red-shifting. We calculated the value of the strain effect using following equation:<sup>40</sup>

$$\frac{\delta\omega}{\omega} = -3\gamma\epsilon, \quad (4)$$

where  $\delta\omega$  is the peak width, and  $\gamma = 1$  is the Gruneisen constant. Comparing strains calculated from XRD and Raman spectra, one can notice a slight difference in these values. However, the tendency, to increase the strain in nanosilicon after ALD and to reduce it after annealing, remains the same.

Fig. 5(a) shows the absolute reflectance of fabricated Si and TiO<sub>2</sub>-Si NPI at 8° incidence over the range of 200–1100 nm. The optical reflectivity for Si NPI decreases significantly comparing to polish Si surface, which is consistent with the results reported previously.<sup>41,42</sup> One can observe that the reflectivity of Si NPI decreases to approximately 2% throughout the entire range of wavelengths from 200 nm to 1100 nm, without any anti-reflection coatings. It might be explained by the existence of the porous structures of NPI, which induce the enhanced scattering and light absorption. The total reflectivity for the TiO<sub>2</sub>-Si NPI increases a few percent. While the reflectivity for annealed TiO<sub>2</sub>-Si NPI decreases and remains in the same order as the reflectivity of pristine Si NPI. This effect could be explained by

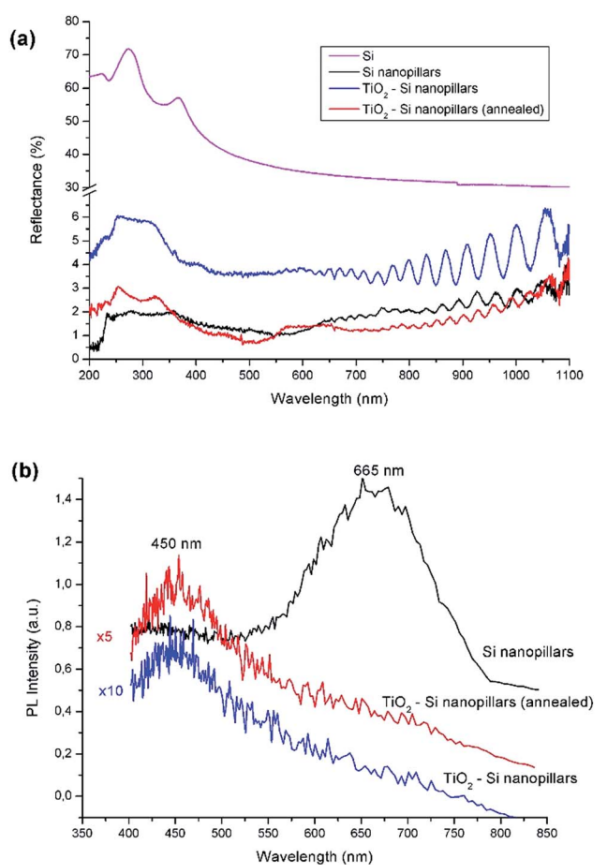


Fig. 5 (a) Absolute optical reflectance and (b) PL spectra from the Si and TiO<sub>2</sub>-Si NP arrays.

the change of refractive index due to pores filling and further crystallization of TiO<sub>2</sub>.<sup>30</sup>

The PL of Si and TiO<sub>2</sub>-Si NPI were measured in the region of light wavelengths from 400 to 850 nm (Fig. 5(b)). The maximum of the PL peak for pristine Si NPI was detected at  $665 \pm 5$  nm (1.87 eV), which revealed the good quality of the nanostructured Si. This red emission from PSi NPI is mainly due to the quantum confinement in Si nanocrystallites.<sup>43</sup> After ALD deposition of TiO<sub>2</sub>, the PL spectra showed one broad peak at approximately  $450 \pm 5$  nm (2.75 eV). The PL band at 2.75 eV is attributed to oxygen vacancies with two electrons in the anatase.<sup>44,45</sup> However, after the deposition of TiO<sub>2</sub>, the PL intensity is degraded because of a lower recombination rate. We can explain this by the enhanced separation of the photogenerated charge carriers due to a difference in the energy levels of their conduction and valence bands.<sup>36</sup> Previously, we have shown that two types of defects (volume and surface) affect on the PL of the TiO<sub>2</sub> inside the PSi.<sup>30</sup> PL relating to volume defects (oxygen vacancies) should be crucial for TiO<sub>2</sub> with a low concentration of surface defects, which is typical for high crystalline quality materials. Thus, after annealing, the crystallinity becomes very high, and we can observe the increasing of PL through oxygen vacancies in the TiO<sub>2</sub>.

At this point, it is clear that the porous nature of the NPI allows the inclusion of TiO<sub>2</sub> increasing the internal strain of the pillars and, perhaps, reinforcing its structural properties. The nanomechanical properties of the pillars are investigated using nanoindentation. Previous studies have shown that the porosity of Si has a direct correlation with its elastic constant,<sup>46</sup> thus by proving the elastic response of pure NPI, the Young's modulus can be extracted by the Oliver-Pharr method and the overall porosity of the pillars estimated.<sup>47</sup>

Pillars were tested by scanning a small region of the surface ( $4 \times 4\ \mu\text{m}$ ) and performing low compression tests on specific pillars. Load vs. displacement curves are presented in Fig. 6 and extracted data in the Table 2. Young's modulus of pure silicon pillars corresponds to relative density of 0.2%, or an overall porosity of 70–80%,<sup>48</sup> furthermore the general behavior of the NPI follows that of a super elastic material, with total recovery above 90%, extracted from the ratio between maximum load ( $H_{\text{max}}$ ) and contact depth ( $H_c$ ). Interestingly enough, Si-TiO<sub>2</sub> NPI show a clear plasto-elastic response, observed in the unload section of the curve, this response is compatible with both, the elastic response of the pillar and the highly plastic deformation of amorphous TiO<sub>2</sub> inside the NPI. The annealing of the structures shows the clear improvement on crystallinity of the anatase phase (Fig. 3), which, as shown in Fig. 6(a), dramatically increases the Young modulus of the pillars. This improvement is associated with the nanocrystalline particles confined in the porous after their crystallization, NPI would behave as nanocomposite like structure in which the Si confinement will bring the structural stability, while the nanocrystals provide the fracture resistance and improved Young's modulus observed,<sup>49</sup> behaviour previously observed in amorphous,<sup>50</sup> and amorphous-to-crystalline structured nanolaminates.<sup>51</sup>

Another important parameter evaluated by nanoindentation is the critical load ( $P_{\text{crit}}$ ), which can be understood as the

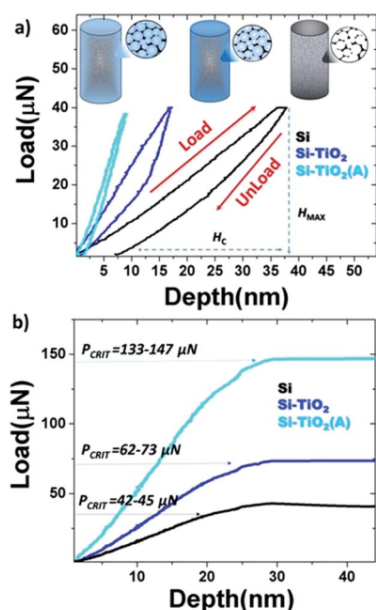


Fig. 6 Nanoindentation curves (load vs. displacement) for nanopillars of Si, Si-TiO<sub>2</sub> and Si-TiO<sub>2</sub> (A-annealed).

Table 2 Mechanical parameters of TiO<sub>2</sub>-Si NPL obtained from nanoindentation

Samples	Si NPL	TiO <sub>2</sub> -Si NPL	TiO <sub>2</sub> -Si NPL (annealed)
Young's modulus [GPa]	6.1 ± 0.5	8.7 ± 0.5	18.4 ± 1.5
Elastic recovery (%)	81	93	95
Critical load [μN]	42–45	62–73	133–147

fracture and collapse of the pillars under uniaxial pressure Fig. 6(b). The critical load values show the monotonic increment of the pillars resilience with the inclusion of TiO<sub>2</sub> inside the porous and its highest values after the annealing of the samples (Table 2). The critical loads found are compatible with those of monocrystalline nanowires of ZnO reported in the literature,<sup>52</sup> although the measured Young's modulus is much lower, the critical load is not. This shows the important enhancement of the mechanical properties of the Si NPL with the inclusion of TiO<sub>2</sub> and posterior annealing.

## Conclusions

In summary, TiO<sub>2</sub>-porous Si NPL were fabricated using MACE and ALD. The morphology, optical and mechanical properties of TiO<sub>2</sub>-porous Si nanopillars were studied, and the main structural and mechanical parameters were estimated. The average value of strains and the approximate size of Si and TiO<sub>2</sub> nanocrystals were estimated using XRD and Raman spectroscopy. It was established that optical and mechanical properties of TiO<sub>2</sub>-Si NPL are tailored by their morphology. The quenching

of the PL emission and optical reflectance decreasing were discussed relatively to morphology of TiO<sub>2</sub>-Si NPL. It was shown that the inclusion of TiO<sub>2</sub> in the porous matrix of Si improve the mechanical properties of TiO<sub>2</sub>-Si NPL. The results obtained in this research are very promising for the improved use of Si NPL covered by TiO<sub>2</sub> in photocatalysis and biosensors applications,<sup>7,8</sup> where it is important to have structures with a large effective surface area and fast charge carrier separation.

## Acknowledgements

This work was partially supported by the Erasmus Mundus "Eminence-2" project.

## References

- 1 E. Kim, Y. Cho, A. Sohn, H. Hwang, Y. U. Lee, K. Kim, H.-H. Park, J. Kim, J. W. Wu and D.-W. Kim, *Sci. Rep.*, 2016, **6**, 29472.
- 2 J. Shieh, Y. C. Li, C. Y. Ji, C. C. Chiu and H. Y. Lin, *J. Renewable Sustainable Energy*, 2015, **7**, 033102.
- 3 F. Teng, N. Li, L. Liu, D. Xu, D. Xiao and N. Lu, *RSC Adv.*, 2016, **6**, 15803–15807.
- 4 T. Kirkpatrick, C. B. Simmons, A. J. Akey, N. Tabet and T. Buonassisi, *J. Appl. Phys.*, 2016, **119**, 194501.
- 5 E. Mills, J. Cannarella, Q. Zhang, S. Bhadra, C. B. Arnold and S. Y. Chou, *J. Vac. Sci. Technol., B: Nanotechnol. Microelectron.: Mater., Process., Meas., Phenom.*, 2014, **32**, 06FG10.
- 6 H. S. Wasisto, S. Merzsch, A. Stranz, A. Waag, E. Uhde, T. Salthammer and E. Peiner, *Sens. Actuators, B*, 2013, **189**, 146–156.
- 7 B. D. Choudhury, R. Casquel, M. J. Bañuls, F. J. Sanza, M. F. Laguna, M. Holgado, R. Puchades, A. Maquieira, C. A. Barrios and S. Anand, *Opt. Mater. Express*, 2014, **4**, 1345–1354.
- 8 M. Kandziolka, J. J. Charlton, I. I. Kravchenko, J. a. Bradshaw, I. a. Merkulov, M. J. Sepaniak and N. V. Lavrik, *Anal. Chem.*, 2013, **85**, 9031–9038.
- 9 S. Chang, J. Oh, S. T. Boles and C. V Thompson, *Appl. Phys. Lett.*, 2010, **96**, 153108.
- 10 a. Smyrnakis, E. Almpanis, V. Constantoudis, N. Papanikolaou and E. Gogolides, *Nanotechnology*, 2015, **26**, 85301.
- 11 V. Gowrishankar, S. R. Scully, A. T. Chan, M. D. McGehee, Q. Wang and H. M. Branz, *J. Appl. Phys.*, 2008, **103**, 064511.
- 12 B. Kiraly, S. Yang and T. J. Huang, *Nanotechnology*, 2013, **24**, 245704.
- 13 X. Zhao, C. M. Wei, L. Yang and M. Y. Chou, *Phys. Rev. Lett.*, 2004, **92**, 236805.
- 14 R. Ghosh, P. K. Giri, K. Imakita and M. Fujii, *Nanotechnology*, 2014, **25**, 45703.
- 15 Y. J. Hwang, A. Boukai and P. Yang, *Nano Lett.*, 2009, **3**, 410–415.
- 16 S. Sampath, P. Maydannik, T. Ivanova, M. Shestakova, R. Nagumothu and V. Alagan, *Superlattices Microstruct.*, 2016, **97**, 155–166.



- 17 D. Yan, S. Li, S. Liu, M. Tan, D. Li and Y. Zhu, *J. Solid State Electrochem.*, 2016, **20**, 459–468.
- 18 J. Liao, Z. Li, G. Wang, C. Chen, S. Lv and M. Li, *Phys. Chem. Chem. Phys.*, 2016, **18**, 4835–4841.
- 19 S. Soleimani-Amiri, A. Gholizadeh, S. Rajabali, Z. Sanaee and S. Mohajerzadeh, *RSC Adv.*, 2014, **4**, 12701–12709.
- 20 H. Lin, M. Fang, H.-Y. Cheung, F. Xiu, S. Yip, C.-Y. Wong and J. C. Ho, *RSC Adv.*, 2014, **4**, 50081–50085.
- 21 Y. Yan, D. Wang and P. Schaaf, *Dalton Trans.*, 2014, **43**, 8480–8485.
- 22 B. Zhong, T. Zhang, X. X. Huang, G. W. Wen, J. W. Chen, C. J. Wang and Y. D. Huang, *Mater. Lett.*, 2015, **151**, 130–133.
- 23 I. Iatsunskiy, M. Jancelewicz, G. Nowaczyk, M. Kempinski, B. Peplińska, M. Jarek, K. Załęski, S. Jurga and V. Smyntyna, *Thin Solid Films*, 2015, **589**, 303–308.
- 24 R. Viter, I. Iatsunskiy, V. Fedorenko, S. Tumenas, Z. Balevicius, A. Ramanavicius, S. Balme, M. Kempin, G. Nowaczyk, S. Jurga and M. Bechelany, *J. Phys. Chem. C*, 2016, **120**, 5124–5132.
- 25 I. Iatsunskiy, E. Coy, R. Viter, G. Nowaczyk, M. Jancelewicz, I. Baleviciute, K. Załęski and S. Jurga, *J. Phys. Chem. C*, 2015, **119**, 20591–20599.
- 26 B. Mikhael, B. Elise, M. Xavier, S. Sebastian, M. Johann and P. Laetitia, *ACS Appl. Mater. Interfaces*, 2011, **3**, 3866–3873.
- 27 M. Kanayama, T. Oku, T. Akiyama, Y. Kanamori, S. Seo, J. Takami, Y. Ohnishi, Y. Ohtani and M. Murozono, *Energy Power Eng.*, 2013, **5**, 18–22.
- 28 K. Thamaphat, P. Limsuwan and B. Ngotawornchai, *Nat. Sci.*, 2008, **42**, 357–361.
- 29 A. Monshi, *World J. Nano Sci. Eng.*, 2012, **2**, 154–160.
- 30 I. Iatsunskiy, M. Pavlenko, R. Viter, M. Jancelewicz, G. Nowaczyk, I. Baleviciute, K. Załęski, S. Jurga, A. Ramanavicius and V. Smyntyna, *J. Phys. Chem. C*, 2015, **119**, 7164–7171.
- 31 C. Suryanarayana and M. G. Norton, *Microsc. Microanal.*, 1998, **4**, 513–515.
- 32 V. Mote, Y. Purushotham and B. Dole, *Journal of Theoretical and Applied Physics*, 2012, **6**, 6.
- 33 D. Arora, K. Asokan, A. Mahajan, H. Kaur and D. P. Singh, *RSC Adv.*, 2016, **6**, 78122–78131.
- 34 S. Piskanec, M. Cantoro, a. Ferrari, J. Zapfen, Y. Lifshitz, S. Lee, S. Hofmann and J. Robertson, *Phys. Rev. B: Condens. Matter Mater. Phys.*, 2003, **68**, 2–5.
- 35 Z. Sui, P. P. Leong, I. P. Herman, G. S. Higashi and H. Temkin, *Appl. Phys. Lett.*, 1992, **60**, 2086–2088.
- 36 I. Iatsunskiy, G. Nowaczyk, S. Jurga, V. Fedorenko, M. Pavlenko and V. Smyntyna, *Optik*, 2015, **126**, 1650–1655.
- 37 I. A. Alhomoudi and G. Newaz, *Thin Solid Films*, 2009, **517**, 4372–4378.
- 38 A. Gajovi, M. Stubičar, M. Ivanda and K. Furi, *J. Mol. Struct.*, 2001, **563–564**, 315–320.
- 39 M. Khorasaninejad, M. M. Adachi, J. Walia, K. S. Karim and S. S. Saini, *Phys. Status Solidi*, 2013, **5**, 373–377.
- 40 T. Kamiya, M. Kishi, a. Ushirokawa and T. Katoda, *Appl. Phys. Lett.*, 1981, **38**, 377–379.
- 41 J.-W. Kang, Y.-J. Kang, S. Jung, M. Song, D.-G. Kim, C. S. Kim and S. H. Kim, *Sol. Energy Mater. Sol. Cells*, 2012, **103**, 76–79.
- 42 P. R. Pudasaini and A. a. Ayon, *Microelectron. Eng.*, 2013, **110**, 126–131.
- 43 J. Zi, K. Zhang and X. Xie, *Phys. Rev. B: Condens. Matter Mater. Phys.*, 1997, **55**, 9263–9266.
- 44 S. G. Yenchalwar, V. K. Azhagan and M. V. Shelke, *Phys. Chem. Chem. Phys.*, 2014, **16**, 17786–17791.
- 45 Y.-H. Chang, C.-M. Liu, C. Chen and H.-E. Cheng, *J. Electrochem. Soc.*, 2012, **159**, D401–D405.
- 46 D. Bellet, P. Lamagnère, A. Vincent and Y. Bréchet, *J. Appl. Phys.*, 1996, **80**, 3772.
- 47 W. C. Oliver and G. M. Pharr, *J. Mater. Res.*, 1992, **7**, 1564–1583.
- 48 O. Dmitrieva, D. Raabe, S. Müller and P. W. Dondl, *Lecture Notes in Applied and Computational Mechanics*, 2015, **78**, 205–218.
- 49 D. Martínez-Martínez, in *Encyclopedia of Tribology*, ed. Q. J. Wang and Y.-W. Chung, Springer US, Boston, MA, 2013, pp. 2359–2364.
- 50 E. Coy, L. Yate, Z. Kabacińska, M. Jancelewicz, S. Jurga and I. Iatsunskiy, *Mater. Des.*, 2016, **111**, 584–591.
- 51 R. Raghavan, M. Bechelany, M. Parlinska, D. Frey, W. M. Mook, A. Beyer, J. Michler and I. Utke, *Appl. Phys. Lett.*, 2012, **100**, 191912.
- 52 E. Robak, E. Coy, M. Kotkowiak, S. Jurga, K. Załęski and H. Drozdowski, *Nanotechnology*, 2016, **27**, 175706.

### **3.4. Silicon/TiO<sub>2</sub> core-shell nanopillar photoanodes for enhanced photoelectrochemical water oxidation**

In order to protect a silicon electrode against photo-corrosion in an aqueous electrolyte solution, protective chemically stable layers are widely used. In this regard, transition metal oxides are extensively studied to yield optimal PEC performance in a wide range of incident solar light wavelengths. Understanding the dependence on the pH of the electrolyte solution, the influence of doping type and the optimization of surface geometry are essential in designing an efficient photoelectrode for water-splitting applications.

This research is focused on studies of the PEC performance of core-shell Si/TiO<sub>2</sub> photoanodes based on silicon nanopillar arrays. Samples of Si/TiO<sub>2</sub> photoanodes were prepared by a combination of NSL, MACE and ALD on p-type and n-type silicon substrates. Morphological and optical properties of fabricated nanostructures were investigated by SEM and TEM, as well as by reflectance and Raman spectroscopies. A linear voltammetry characterization has been used to demonstrate the PEC performance of Si/TiO<sub>2</sub> photoanodes depending on their morphology and the influence of the pH values in the electrolyte solution. It has been shown that the photoanode based on n-Si/n-TiO<sub>2</sub> core-shell nanopillar arrays demonstrates much better PEC performance than p-Si/n-TiO<sub>2</sub> owing to its favorable bands bending at the Si/TiO<sub>2</sub> heterojunction. Optimal morphological characteristics for the highest PEC performance were defined according to the analysis of linear voltammetry data. Furthermore, the influence of pH value on PEC performance has been discussed. The obtained results clearly demonstrate the advantages and perspectives of pillar-like Si/TiO<sub>2</sub> nanocomposite arrays for photocatalytic water-splitting applications.

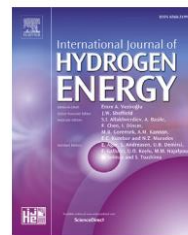
In this research, the Author has performed the synthesis of silicon nanopillar arrays by a combination of NSL and MACE as well as assisted in ALD of TiO<sub>2</sub> thin film. He contributed to SEM, Raman and reflectance data acquisition as well as performed its processing along with visualization in Figures 1 and 2. Also, the Author has drawn Figure 3 and significantly contributed to writing all parts of the article except the discussion of linear voltammetry results.

**Number of Ministerial points: 140**

**Impact factor: 7.2**

Available online at [www.sciencedirect.com](http://www.sciencedirect.com)

ScienceDirect

journal homepage: [www.elsevier.com/locate/he](http://www.elsevier.com/locate/he)

## Silicon/TiO<sub>2</sub> core-shell nanopillar photoanodes for enhanced photoelectrochemical water oxidation



Mykola Pavlenko<sup>a</sup>, Katarzyna Siuzdak<sup>b</sup>, Emerson Coy<sup>a</sup>,  
Mariusz Jancelewicz<sup>a</sup>, Stefan Jurga<sup>a</sup>, Igor Iatsunskiy<sup>a,\*</sup>

<sup>a</sup> NanoBioMedical Centre, Adam Mickiewicz University, 85 Umultowska Str., 61-614, Poznan, Poland

<sup>b</sup> Centre of Laser and Plasma Engineering, The Szwalski Institute of Fluid-Flow Machinery, Polish Academy of Science, Fiszera 14 Str., 80-231 Gdansk, Poland

### ARTICLE INFO

#### Article history:

Received 17 August 2017

Received in revised form

3 October 2017

Accepted 6 October 2017

Available online 27 October 2017

#### Keywords:

Silicon nanopillar

TiO<sub>2</sub>

Water splitting

Photoanode

Atomic layer deposition

### ABSTRACT

Nanostructured Si/TiO<sub>2</sub> core-shell nanopillar (NP) photoanodes were synthesized to overcome photodegradation stability of Si and to enhance the efficiency for photoelectrochemical water splitting. The core-shell structures were fabricated by atomic layer deposition of TiO<sub>2</sub> onto Si nanopillars synthesized by metal-assisted chemical etching and nanosphere lithography. Scanning electron microscopy, transmission electron microscopy, Raman and reflectance spectroscopies were utilized to characterize fabricated photoanodes. The obtained Si/TiO<sub>2</sub> core-shell NP arrays exhibit less than 6% of optical reflectance in UV and visible region, providing good optical absorption. Photoelectrochemical (PEC) water oxidation of fabricated photoanodes was studied. We showed that n-Si/n-TiO<sub>2</sub> NP exhibited a larger photocurrent than p-Si/n-TiO<sub>2</sub> due to a barrier at the heterojunction. Optimal morphological parameter of Si/TiO<sub>2</sub> NP for enhanced PEC water splitting were found. We demonstrated its enhanced PEC performance with a photocurrent density of 1.5 mA/cm<sup>2</sup> under simulated solar radiation with intensity of 100 mW/cm<sup>2</sup>. The relationship between the PEC performance and the electrolyte pH was also discussed. The design of the geometry of Si/TiO<sub>2</sub> core-shell NP arrays offers a new approach for preparing stable and highly efficient photoanodes for PEC water splitting.

© 2017 Hydrogen Energy Publications LLC. Published by Elsevier Ltd. All rights reserved.

### Introduction

One of the best approaches in development of renewable energy resources is a hydrogen production technology based on utilization of solar energy in photocatalytic process. Photoelectrochemical (PEC) water splitting is a direct route to capture solar irradiation and to produce hydrogen. A semiconductor immersed in an aqueous electrolyte absorbs photons and generates electron-hole pairs that are separated

by a built-in electric field and transported to the semiconductor-electrolyte interphase where they dissociate water molecules into hydrogen and oxygen. One of the main challenges in PEC water splitting is the development of photoanodes with high stability and efficiency [1].

In recent years many publications are focused on application of multidimensional nanostructures for PEC process. Among multidimensional nanostructures, 1D nanostructures (nanowires, nanopillars, nanotubes etc.) is considered to be

\* Corresponding author.

E-mail address: [yatsunskiy@gmail.com](mailto:yatsunskiy@gmail.com) (I. Iatsunskiy).

<https://doi.org/10.1016/j.ijhydene.2017.10.033>

0360-3199/© 2017 Hydrogen Energy Publications LLC. Published by Elsevier Ltd. All rights reserved.

more efficient among them [2–4]. Nanopillars (NP) provide a unique approach combining desirable characteristics of excellent photoelectrodes. It is well known that efficient photoelectrodes requires good light absorption, fast photo-generated charge separation and mass transport of reactants. The elongated geometry of NP enables sufficient light absorption. NP arrays poses highly developed surface area, efficient mass transfer, and rapid electron–hole separation along radial axis.

Development of efficient nanostructured photoanodes for water-splitting requires photocatalysts providing a high photocurrent density and good stability. Silicon (Si) is a feasible commercial PEC material, one of the dominant earth-abundant and enhanced solar light absorption semiconductor with a small band gap ( $E_g = 1.1$  eV). Nanostructured Si is commonly used for PEC water splitting due to its enhanced absorption properties and high surface area [5–7]. For example, porous silicon (PSi) [6] or silicon nanowires (Si-NW) [8] can trap the incident light owing to the surface peculiarities and effectively increase the interfacial area. Oh et al. have shown the photoanode built on the array of silicon nanowires which demonstrates excellent antireflectivity over a wide spectral range (300–1000 nm) and superior hydrogen production in comparison to flat-surface [8].

However, Si photoelectrodes undergoes irreversible changes induced by corrosion and surface passivation during the electrochemical reactions. Moreover, it is thermodynamically impossible to use Si photoelectrode for direct water oxidation because its valence band maximum energy is higher than oxidation potential. Therefore, a composite semiconductor electrode based on the heterojunction should be proposed to overcome these shortcomings. Encapsulation of the Si NP into the photocatalyst shell leads to formation of a complex nanocomposite structure, so-called core-shell, and sustains an effective light absorption and charge separation at the interface [3,9–12]. The use of  $\text{TiO}_2$  as a shell to protect Si from corrosion is straightforward because it is considered as one of the most stable photocatalytic materials [13–15]. Because of its high  $E_g$  (~3 eV),  $\text{TiO}_2$  shell transmits visible light which can be further absorbed by Si core. Thus,  $\text{TiO}_2$ -Si interfaces behave as dual absorber tandem photoelectrodes [16–19].

Among various deposition techniques, the atomic layer deposition (ALD) is a method that enables to conformally and uniformly deposit broad class of materials. ALD provides an occurrence of self-limited chemical reactions which lead to formation of ultrathin film even for complex porous [20], or 1D nanostructures [21,22]. Application of ultrathin  $\text{TiO}_2$  film about 1–2 nm as a protective layer for n-type plane Si surface was firstly introduced by Chen et al. [23]. The process of water oxidation during the research was sustained steadily under various pH conditions, including extreme factors, which led to quick degradation of pure  $\text{TiO}_2$  photoanode. An amorphous  $\text{TiO}_2$  ALD coverage up to 12 nm applied to  $\text{p}^+$ -type of silicon was also introduced by Scheuermann et al. [14] Yu et al. [24] fabricated an efficient photoanode onto black Si wafer using 8 nm  $\text{TiO}_2$  ALD layer. In combination with thin film of the oxygen evolution catalysts this heterostructured photoanode is accomplished the photocurrent density of  $32.3 \text{ mA} \times \text{cm}^2$  at an external potential of 1.48 V. These types of photoanodes

also demonstrate a good chemical stability in every pH electrolyte solutions. Another research groups [25,26], also made a successful attempts of application a  $\text{TiO}_2$  film as a protection layer for various nanocomposite photoanodes and showed that the application of  $\text{TiO}_2$  thin film effectively prevents passivation and subsequent degradation of Si in harsh electrolytes. Additionally, as it was shown in Ref. [27] the  $\text{TiO}_2/\text{Si}$  n/n heterojunction possess of a sufficient energy barrier which reflects minority holes back to the  $\text{TiO}_2$ .

In this article, we report a fabrication of Si/ $\text{TiO}_2$  core-shell NP photoanodes by a combination of nanosphere lithography, metal-assisted chemical etching (MACE), and ALD. To the best of our knowledge, the comprehensive analysis of Si NP arrays with ALD  $\text{TiO}_2$  coverage depending on pH conditions and morphological peculiarities of the nanocomposite structure is not represented in full extent in the literature. The PEC behavior of the pillar-based nanocomposite structure should be correlated with characteristics of  $\text{TiO}_2$  layer. Consequently, we performed a comprehensive investigation on the influence of pH conditions, pillar length and  $\text{TiO}_2$  thickness onto the PEC efficiency. In this study we prepared arrays of aligned p- and n-type silicon nanopillars covered by ALD  $\text{TiO}_2$  layer with various thicknesses and then studied their PEC efficiency depending on pH conditions and morphological peculiarities.

## Materials and methods

### Core-shell $\text{TiO}_2/\text{Si}$ nanopillars fabrication

Commercially available n-type (100) (phosphorus doped,  $4.5 \Omega \text{ cm}$ ) and p-type (100) (boron doped,  $4.5 \Omega \text{ cm}$ ) polished silicon wafers were used in this study. Core-shell  $\text{TiO}_2/\text{SiNP}$  arrays were prepared by a method similar to our previous paper [28]. First, vertical Si NP arrays were fabricated by combining nanosphere lithography (NSL), reactive ion etching (RIE) and MACE processes, and then the  $\text{TiO}_2$  layer with different thickness was deposited onto the samples of SiNP using  $\text{TiCl}_4$  and water as ALD precursors. The combination of these methods allowed us to control the geometrical parameters of SiNP (diameter, length) and to tune the thickness of  $\text{TiO}_2$  layer. The growth rate was typically  $0.4 \text{ \AA/cycle}$  for  $\text{TiO}_2$  on the planar silicon surface. After  $\text{TiO}_2$  deposition samples were annealed at  $450 \text{ }^\circ\text{C}$  for an hour in an ambient atmosphere. In order to study the influence of the pillars length and the thickness of  $\text{TiO}_2$  layer on PEC performance, samples with different geometrical parameters were produced. The length of pillars varied in the range of 1–15  $\mu\text{m}$  and the  $\text{TiO}_2$  layer thickness from 5 nm (125 ALD cycles) to 60 nm (1500 ALD cycles).

### Characterization

Structural and chemical compositions of  $\text{TiO}_2/\text{SiNP}$  were analyzed by scanning (JEOL, JSM-7001F) and transmission (JEOL ARM 200F) electron microscopy (TEM/SEM). The lamellas for TEM were prepared by focused ion beam (FIB-JEOL JIB-4000) by the method described in Ref. [29] Raman scattering measurements were performed using a Renishaw micro-Raman spectrometer equipped with a confocal microscope (Leica).

The Raman scattering spectra were excited by a 488 nm and 514 nm laser. The beam was focused on the samples with a 100 microscope objective with a numerical aperture of 0.4. GIXRD measurements were performed on X'pert3 MRD (XL) from PANalytical, working with a Cu K $\alpha$  radiation source (wavelength of 1.54 Å) and operating at 45 kV and 40 mA. Optical properties of TiO<sub>2</sub>/SiNP have been studied with reflectance spectroscopy (UV–vis spectrophotometer lambda 950 UV/vis/NIR range 300–1100 nm, 1 nm step).

#### Photoelectrochemical (PEC) measurements

Characterization of working electrode was performed using the potentiationstat-galvanostat system AutoLab PGStat 302N in a standard three-electrode assembly at 295 K. The flat Si or SiNP substrate with TiO<sub>2</sub> coverage stayed as a working electrode. For electrochemical studies, the specimen holder made from Polyether ether ketone material was fabricated. It enables contact between limited geometric electrode surface and the electrolyte. The diameter of round sample area wetted by electrolyte was 4 mm giving area of 0.1256 cm<sup>2</sup> used then for calculation of current density values. The counter electrode consisted of Pt gauze and Ag/AgCl/3 M KCl stayed as the reference electrode. As the electrolyte 0.5 M K<sub>2</sub>SO<sub>4</sub> (pH = 7), 0.5 M H<sub>2</sub>SO<sub>4</sub> (pH = 0), 1 M KOH (pH = 14) were used purged with argon for 50 min before the electrochemical test and during measurements an Ar-cushion above the electrolyte was kept. Electrode potentials were converted to the reversible hydrogen electrode (RHE) using equation:  $RHE = E_{ref} + E_{ref}^0 + 0.0591 \cdot pH$ .

The linear voltammetry (LV) curves in potential range of  $-1.0 \div +1.5$  V were registered with the scan rate of 10 mV/s

in dark and under UV–vis illumination. The chronoamperometry (CA) measurements were registered at fixed potential of +0.5, +1.0, and +1.5 V vs. Ag/AgCl/3 M KCl under chopped irradiation. Each dark and light period equals 20 s.

The samples were irradiated with a 150 W Xenon lamp (Osram XBO 150) equipped with an AM 1.5 filter allowing to obtain simulated solar light. The irradiance of incident light was calibrated to 100 mW/cm<sup>2</sup> using a reference cell (Si solar cell, Rera).

## Results and discussion

### Structural, chemical and optical characterization of TiO<sub>2</sub>/SiNP

In order to examine the morphology of pristine SiNP, and core-shell TiO<sub>2</sub>/SiNP, SEM and TEM characterizations were carried out. Fig. 1 shows the morphological differences between the SiNP arrays before and after TiO<sub>2</sub> ALD deposition. As shown in Fig. 1a, large areas, up to 10  $\mu$ m of ordered hexagonal SiNP arrays with an excellent vertical alignment were obtained. We could control the geometrical parameters of SiNP by varying the MACE and nanosphere lithography procedures. In this study, we only varied the etching time to effectively control the length of the SiNP (Fig. 1h), while their diameter was in the limited range of 300–400 nm. As shown in Fig. 1h, cylindrical SiNPs with lengths of approximately 1.4  $\mu$ m and 6  $\mu$ m were obtained by 15 min etching, for n- and p-type Si, respectively. On the other hand, SiNPs obtained by a longer etching time (>20 min for p-type, and >30 min for n-type) exhibited a pillars

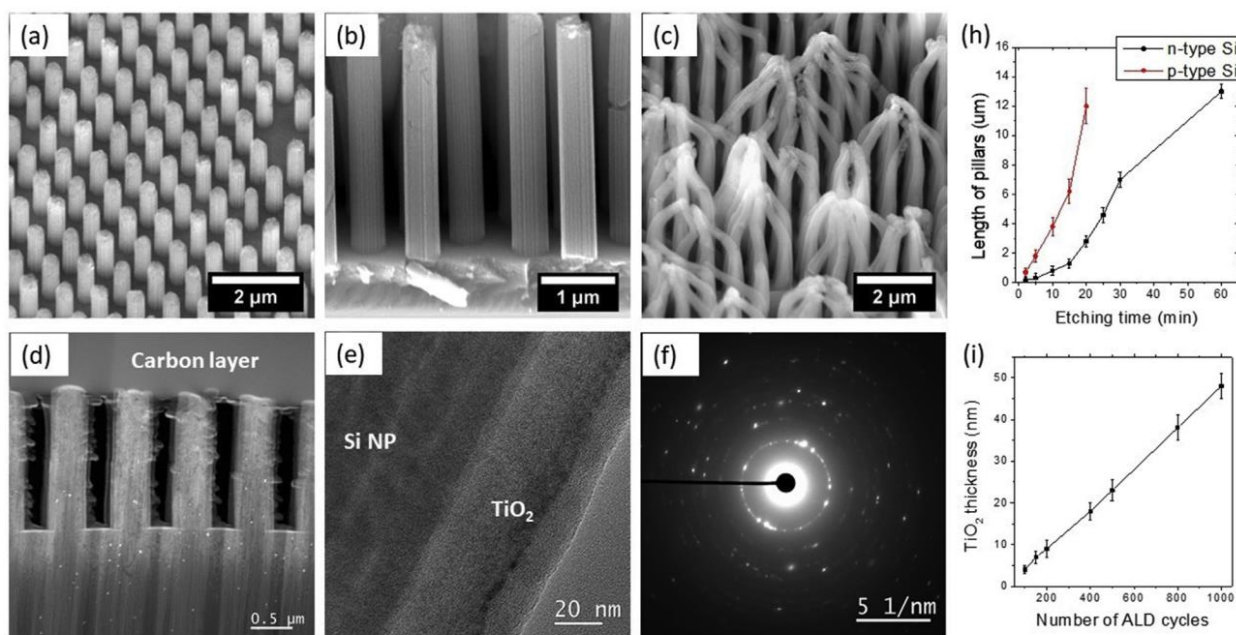


Fig. 1 – SEM images of (a) of p-type SiNP array in large scale; (b) n-type SiNP; (c) bounded SiNP; (d) cross-sectional TEM image and (e) HRTEM of TiO<sub>2</sub>/SiNP after 500 ALD cycles; (f) the electron diffraction pattern of a polycrystalline anatase phase after annealing; relationship between (h) the length of SiNP vs MACE etching time; (i) the TiO<sub>2</sub> layer thickness vs number of ALD cycles.

bounding what can reduce the active surface area and, as a consequence, to decrease the PEC efficiency (Fig. 1c, SI Fig. S1).

Formation of the uniform  $\text{TiO}_2$  coating was distinguished by ALD. The cross-sectional views of the  $\text{TiO}_2/\text{SiNP}$  sample (Fig. 1d and e) reveal that  $\text{TiO}_2$  layer uniformly deposited along the Si pillar and on the bottom surface of the flat Si substrate. The thickness of the  $\text{TiO}_2$  layer could be tuned by the number of ALD cycles (Fig. 1i). Fig. 1e shows the HRTEM image of as-deposited  $\text{TiO}_2$  layer (40 nm). It was hard to reveal any crystalline grains what indicates the amorphous or highly polycrystalline structure of as-prepared ALD layers. In order to increase the crystallinity, an additional thermal annealing should be performed. The electron diffraction analysis reveals the increasing of crystalline phase after calcination (Fig. 1f). The lattice spacing were measured to be 0.20 and 0.34 nm, corresponding to (004) and (101) planes of anatase, respectively [30]. In addition, we have studied the elemental distribution over the  $\text{TiO}_2/\text{SiNP}$  sample using EDX mapping. Both titanium and oxygen elements are distributed quite uniformly for as-deposited samples (SI, Fig. S1c).

The samples of the  $\text{TiO}_2/\text{SiNP}$  were further characterized by Raman spectroscopy, as a very sensitive method, in order to determine the phase of the  $\text{TiO}_2$  layer. Fig. 2a and b shows the Raman spectra of  $\text{TiO}_2/\text{SiNP}$  with different number of ALD

cycles, before and after annealing. Raman spectra of the as-deposited  $\text{TiO}_2/\text{SiNP}$  showed no significant peaks of anatase, indicating the amorphous or highly polycrystalline phase of  $\text{TiO}_2$ . However, upon increasing the number of ALD cycles a Raman peak at  $141\text{ cm}^{-1}$ , corresponding to the anatase phase of  $\text{TiO}_2$ , can clearly be observed [30]. However this peak is broader and shifted with respect to bulk anatase (peak position is  $144\text{ cm}^{-1}$ ) what could be attributed to phonon confinement effects in anatase nanoparticles with an average size less than 5–7 nm [30]. After annealing these signals become slightly higher. It is suggested here that a partial transformation of amorphous-to-crystalline phase might occur.

The absorption of the photoactive material plays an important role for any photo-driven process and its application in the utilization of light energy to water splitting. In order to obtain absorption characteristics of fabricated samples, reflectance measurements have been performed. Fig. 2c and d shows the absolute reflectance of fabricated SiNP with different length and  $\text{TiO}_2/\text{SiNP}$  at  $8^\circ$  incidence over the range of 300–1100 nm. The reflectance of polished silicon is also plotted for comparison. The average reflectivity, in the visible range, of the SiNP arrays with pillar heights of 0.7  $\mu\text{m}$ , 1.3  $\mu\text{m}$ , 4  $\mu\text{m}$  and 6  $\mu\text{m}$  were 16%, 9%, 5% and 4%, respectively. The

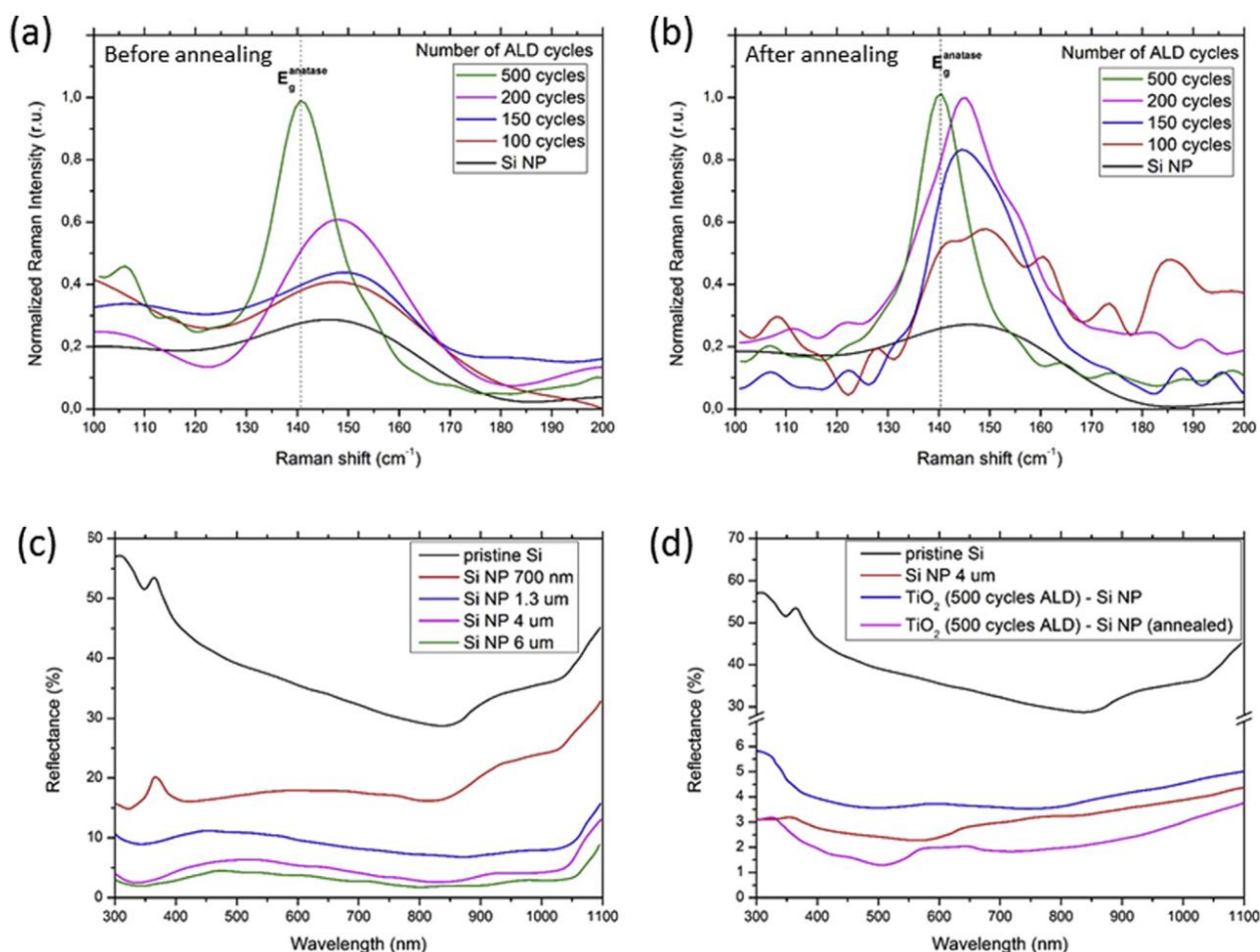


Fig. 2 – Raman spectra of anatase peak (a) before and (b) after annealing of samples; (c) Reflectance spectra of (c) pristine Si and SiNP with different height and (d) pristine Si, SiNP and  $\text{TiO}_2/\text{SiNP}$  before and after annealing.

results reveal that long SiNPs would effectively decrease the reflection and thus increase the absorption of UV and visible light. The total reflectivity for the 4  $\mu\text{m}$  SiNP after  $\text{TiO}_2$  ALD deposition (500 cycles) increases a few percent. While the reflectivity for annealed  $\text{TiO}_2/\text{SiNP}$  decreases down to 2%. We can explain this reflectance decreasing by the light trapping effect and by the changing of refractive index of  $\text{TiO}_2$  due to crystallization of anatase [28]. The enhanced light absorption promised the enhanced photoactivity of the  $\text{TiO}_2/\text{SiNP}$ .

#### Photoelectrochemical performance of $\text{TiO}_2/\text{SiNP}$

##### Effect of the Si type

PEC water splitting is one of the most promising areas for application of Si/ $\text{TiO}_2$  heterojunctions. In the first stage of our investigations we aimed to study the influence of Si type on the PEC performance of fabricated samples. In our study, we have used two types of SiNP (n- and p-type) with the same resistivity ( $4.5 \Omega \cdot \text{cm}$ ) and orientation (100). Fig. 3 shows the schematic representation of band energies and the charge transfer mechanisms during PEC water splitting processes. Semiconductor heterojunctions of n-Si/n- $\text{TiO}_2$  or p-Si/n- $\text{TiO}_2$  having different band bending properties are shown in Fig. 3 (top image). Despite of the fact that n/n heterojunction has a

potential energy barrier, Hwang et al. have shown that the n/n heterojunction is more promising for PEC application than p/n [16]. In this case, the photogenerated holes which will oxidize  $\text{OH}^-$  to oxygen, and thus increasing the photoanodic current, are reflected by the potential barrier at the n-Si/n- $\text{TiO}_2$  junction back into the  $\text{TiO}_2$  layer. Moreover, the n-Si/n- $\text{TiO}_2$  heterojunction reduces recombination and therefore it shows the highest value of photocurrent [16,18].

The PEC performance of n-Si/n- $\text{TiO}_2$  NP is shown in the Fig. 4. It is clearly seen the increasing of photocurrent density under light irradiation. The maximum value of photocurrent density was about  $1.5 \text{ mA/cm}^2$  what is sufficiently good for these structures comparing to other photoanodes [24,31]. These photoanodes have also shown excellent photostability under prolonged irradiation (see SI, Fig. S2). The p-Si/n- $\text{TiO}_2$  NP did not exhibit any photoactivity. Furthermore, when the samples were illuminated, the registered current decreases comparing to current registered in dark under the same polarization conditions that result from their instability towards electrode polarization in anodic regime (SI, Fig. S3).

In the Fig. 3 we have also presented the charge transfer mechanisms in n-Si/n- $\text{TiO}_2$  NP. Upon illumination, the electrons ( $e^-$ ) and holes ( $h^+$ ) are generated inside both the  $\text{TiO}_2$  shell and SiNP core because the  $\text{TiO}_2$  is transparent under

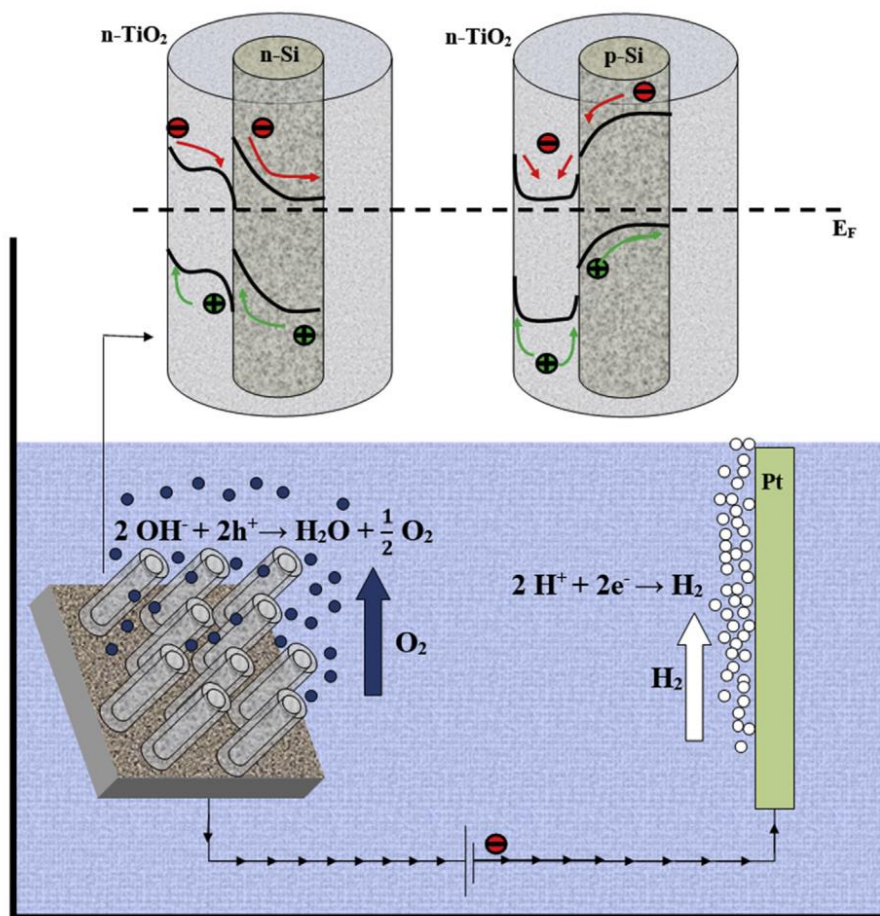


Fig. 3 – Schematic representation of band energies, charge transfer and water splitting processes in  $\text{TiO}_2/\text{SiNP}$  for n- and p-type Si ( $E_F$  – Fermi level).

visible light. The photogenerated electrons in the TiO<sub>2</sub> shell move toward Si core due to the Schottky barrier at the interface with the electrolyte, meanwhile holes move toward the TiO<sub>2</sub>/electrolyte interface. Then holes at the TiO<sub>2</sub>/electrolyte interface oxidize OH<sup>-</sup> to oxygen. The photogenerated and injected from TiO<sub>2</sub> electrons in the n-Si move via an external circuit to the Pt counter electrode and reduce protons to generate H<sub>2</sub>. The reaction of oxidation and reduction are shown in the Fig. 3. In the case of p-Si/n-TiO<sub>2</sub> heterojunction, the flow of electrons and holes at the junction of p-Si/n-TiO<sub>2</sub> is opposite to the desirable direction.

#### Effect of pillars height and TiO<sub>2</sub> thickness

Our next step was to investigate the influence of SiNP length on the photocurrent density in TiO<sub>2</sub>/SiNP. Fig. 5 shows linear voltammetry curves of photocurrent density versus potential depending on the length of SiNP. Here, 1, 3, 5 and 7 μm long SiNP were prepared followed by 500 ALD cycles of TiO<sub>2</sub> coating (~20 nm thickness). The pillars density distribution of SiNP was nearly identical. The maximum value of photocurrent density was obtained for samples with 5 μm height. The onset potentials of the photoactive samples were located at the same position (~1.16 V vs. RHE), one of the most negative values for Si photoanodes without a buried junction. It is logical to assume, longer SiNP provide higher photocurrent density because of the higher surface area. However, it should be noted that photocurrent density for 7 μm SiNP was lower than that of the 5 μm sample. This decreasing of photocurrent is possibly related to the difficulty of oxygen removing out of

the SiNP interior due to their bending and interconnections (see Fig. 1c).

In order to estimate the effect of TiO<sub>2</sub> layer on PEC performance we calculated the average value of photocurrent density (at the constant potential of 1.5 V vs. Ag/AgCl/3 M KCl) depending on the thickness of TiO<sub>2</sub>. As shown in Fig. 6 with the thickness increased from 5 to 60 nm, the photocurrent density increased up to 40 nm thickness and then dropped. The optimum TiO<sub>2</sub> thickness was about 40 nm. This value of the TiO<sub>2</sub> thickness was able to provide the highest photocurrent density and the smallest onset potential. The value of photocurrent grows with increasing TiO<sub>2</sub> layer thickness due to the enhanced absorption of light. It is well-known that in order to maximize the charge carrier generation and collection, the thickness of the TiO<sub>2</sub> layer must be equal to the reverse value of the absorption coefficient (the optical penetration depth). Indeed, in many works it has been shown that approximately 40 nm TiO<sub>2</sub> layer thickness is the optimum value [16,32]. Our results are in a good agreement with previously reported data by Hwang et al. [16], Shi et al. [33], and more recently by Shaner et al. [18].

#### Photocurrent by electrolyte pH

It is obvious, the pH of the electrolyte significantly affects the water splitting process [14,34,35]. Linear voltammetry curves of photocurrent density versus potential were measured at three different pH conditions using the identical sample, TiO<sub>2</sub>/SiNP with 40 nm ALD layer. As was mentioned in Experimental, the electrolytes 0.5 M K<sub>2</sub>SO<sub>4</sub> (pH = 7), 0.5 M H<sub>2</sub>SO<sub>4</sub>

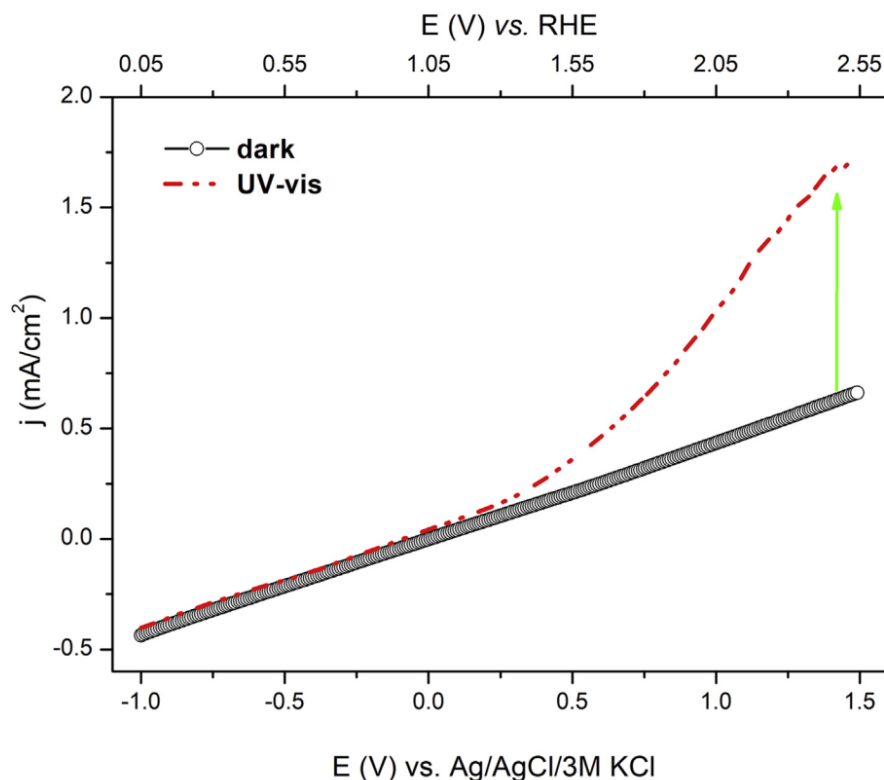
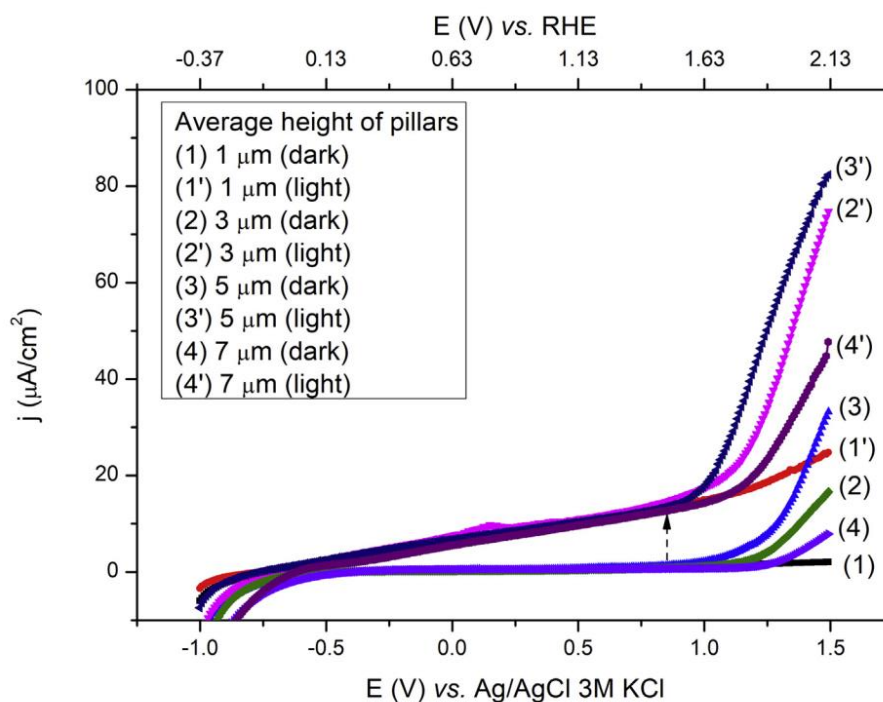


Fig. 4 – Linear voltammetry curves of photocurrent density versus potential in TiO<sub>2</sub>/SiNP for n-type Si. Length of SiNP – 5 μm; ALD TiO<sub>2</sub> thickness – 40 nm; electrolyte solution – 0.5 M K<sub>2</sub>SO<sub>4</sub> (pH = 7).





**Fig. 5** – Linear voltammetry curves of photocurrent density versus potential depending on the length of SiNP in TiO<sub>2</sub>/SiNP for n-type Si after annealing. ALD TiO<sub>2</sub> thickness – 10 nm; electrolyte solution – 0.5 M K<sub>2</sub>SO<sub>4</sub> (pH = 7).

(pH = 0), 1 M KOH (pH = 14) were used purged with argon for 50 min before the electrochemical test and during measurements the flow of argon above the solution was kept. Fig. 7 shows photoresponse at pH = 0, 7 and 14, respectively. In all the solutions, samples are characterized with some photoactivity and photostability. However, in neutral and acidic

solutions have shown more significant photoresponse than basic one.

It is known that increased concentration of OH<sup>-</sup> groups effectively traps holes from the TiO<sub>2</sub> surface and thus increasing the carrier-to-ion transfer rate. In this case the high pH is beneficial for the photoanode operation. However, it is

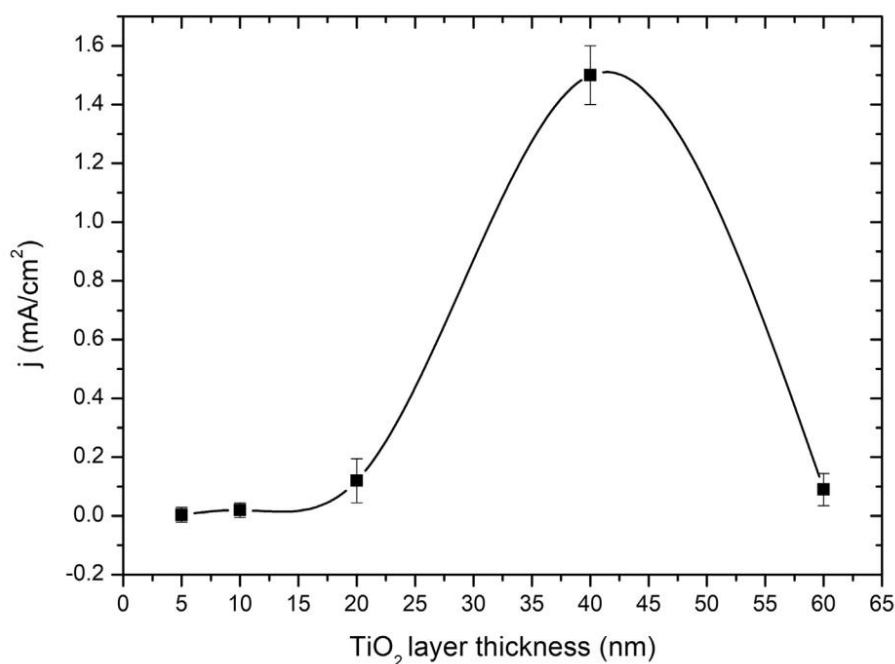


**Fig. 6** – Thickness dependence of photocurrent density of TiO<sub>2</sub>/SiNP. Constant potential (vs. Ag/AgCl 3 M KCl) – 1.5 V; electrolyte solution – 0.5 M K<sub>2</sub>SO<sub>4</sub> (pH = 7).

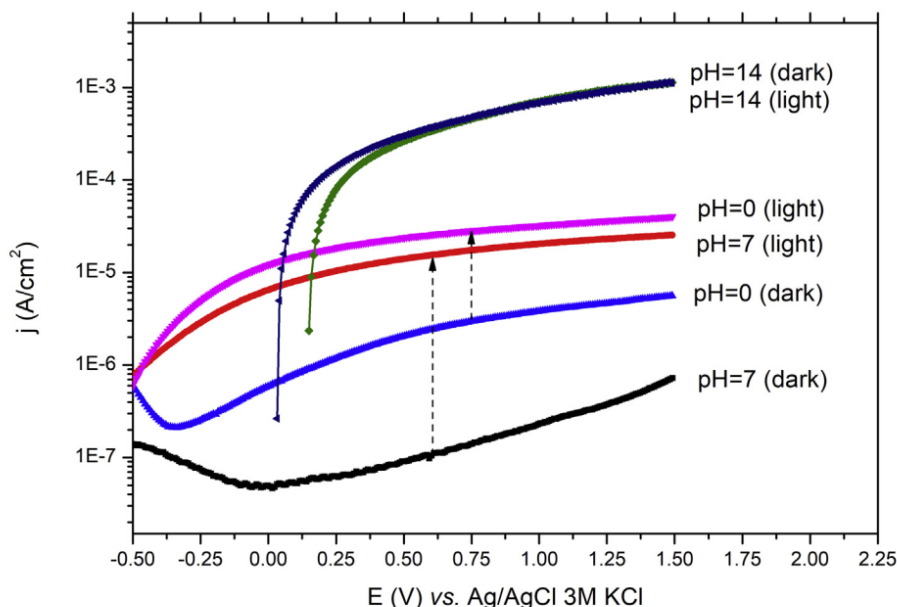
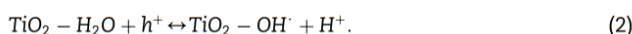
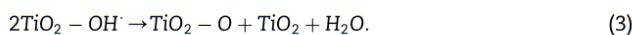


**Fig. 7** – Linear voltammetry curves of photocurrent density versus potential depending on the pH of electrolyte solution in  $\text{TiO}_2/\text{SiNP}$  for n-type Si. ALD  $\text{TiO}_2$  thickness – 40 nm.

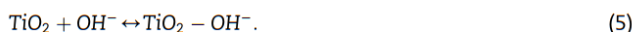
desirable to operate under acidic conditions, because high pH leads to the surface degradation, and as a consequence, to the electrode instability. Crawford et al. have shown that the effect of pH can be understood in terms of reactions occurring at the  $\text{TiO}_2$  surface [35]. There are two pathways during the oxidation of water molecules on the  $\text{TiO}_2$  surface. First, a water molecule adsorbs to the surface (reaction (1)), then trap the hole ( $h^+$ ) forming hydroxyl radical ( $\text{OH}^\bullet$ ) and releasing a proton ( $\text{H}^+$ ) (reaction (2)):



Then  $\text{OH}^\bullet$  radicals can react in two irreversible steps forming water (3) and oxygen (4):



Second pathway is the oxidation of hydroxyl radicals. In this case, a hydroxide ion adsorbs to the surface (5) and then trap the hole forming hydroxyl radical (6):



Then, reactions (3) and (4) occur. Analyzing these two mechanisms, Crawford et al. concluded that the water adsorption pathway dominates (1) under neutral and acidic conditions. As the solution becomes more basic, the hydroxide pathway, which evolves oxygen more rapidly, becomes prevalent (2). Therefore, the rate of photocatalytic oxidation, and as a consequence the oxygen concentration on the photoanode, increases with the increased hydroxide

concentration at higher pH. On the other hand,  $\text{O}_2$  can adsorb to the surface and trap electrons. By trapping electrons, absorbed  $\text{O}_2$  molecules may deactivate surface sites and inhibit the photocatalytic reaction.

## Conclusion

In conclusion, the  $\text{Si}/\text{TiO}_2$  core-shell NP photoanodes were fabricated via the effective and facile method based on a two-step route combining MACE and ALD. The morphology, optical and PEC properties of  $\text{Si}/\text{TiO}_2$  core-shell NP photoanodes were studied.  $\text{TiO}_2/\text{SiNP}$  photoanodes exhibit enhanced photoactivity for water splitting due to the more effective photo-generated carriers, the carrier separation at the  $\text{TiO}_2$ -Si interface and large specific surface area which increase the light capture. This work suggests that ALD  $\text{TiO}_2$  coating could bring significant performance gain to Si NP photoanodes in terms of both charge separation efficiency and catalyst stability. The results demonstrate the advantage of nanopillar core-shell heterostructures in photocatalytic water splitting processes.

## Acknowledgments

M.P. acknowledges the financial support from the National Science Centre (NCN) of Poland by the PRELUDIUM 12 project UMO-2016/23/N/ST3/01356. I.I. also acknowledges the financial support from the NCN of Poland by the SONATA 11 project UMO-2016/21/D/ST3/00962. K.S. acknowledge the financial support from the National Science Centre (NCN) of Poland by the SONATA project N 2012/07/D/ST5/02269 and K.S. is also supported by Foundation for Polish Science (FNP).

## Appendix A. Supplementary data

Supplementary data related to this article can be found at <https://doi.org/10.1016/j.ijhydene.2017.10.033>.

## REFERENCES

- Coridan RH, Nielander AC, Francis S a, McDowell MT, Dix V, Chatman SM, et al. Methods for comparing the performance of energy-conversion systems for use in solar fuels and solar electricity generation. *Energy Environ Sci* 2015;8:2886–901. <https://doi.org/10.1039/C5EE00777A>.
- Hoang S, Gao PX. Nanowire array structures for photocatalytic energy conversion and utilization: a review of design concepts, assembly and integration, and function enabling. *Adv Energy Mater* 2016;6. <https://doi.org/10.1002/aenm.201600683>.
- Kawasaki S, Takahashi R, Yamamoto T, Kobayashi M, Kumigashira H, Yoshinobu J, et al. Photoelectrochemical water splitting enhanced by self-assembled metal nanopillars embedded in an oxide semiconductor photoelectrode. *Nat Commun* 2016;7:11818. <https://doi.org/10.1038/ncomms11818>.
- Kim DR, Lee CH, Cho IS, Jang H, Jeon MS, Zheng X. Three-dimensional hetero-integration of faceted GaN on Si pillars for efficient light energy conversion devices. *ACS Nano* 2017. <https://doi.org/10.1021/acsnano.7b01967>.
- Liu D, Li L, Gao Y, Wang C, Jiang J, Xiong Y. The nature of photocatalytic “water splitting” on silicon nanowires. *Angew Chem Int Ed Engl* 2015;54:2980–5. <https://doi.org/10.1002/anie.201411200>.
- Chandrasekaran S, McInnes SJP, Macdonald TJ, Nann T, Voelcker NH. Porous silicon nanoparticles as a nanophotocathode for photoelectrochemical water splitting. *RSC Adv* 2015;5:85978–82. <https://doi.org/10.1039/C5RA12559F>.
- Chawla P, Tripathi M. Surface modification of semiconductor photoanode for photoelectrochemical water splitting. *Int J Hydrogen Energy* 2016;41:7987–92. <https://doi.org/10.1016/j.ijhydene.2015.11.118>.
- Oh I, Kye J, Hwang S. Enhanced photoelectrochemical hydrogen production from silicon nanowire array photocathode. *Nano Lett* 2012;12:298–302. <https://doi.org/10.1021/nl203564s>.
- Hwang YJ, Wu CH, Hahn C, Jeong HE, Yang P. Si/InGaN Core/shell hierarchical nanowire arrays and their photoelectrochemical properties. *Nano Lett* 2012;12:1678–82. <https://doi.org/10.1021/nl3001138>.
- Xiong Z, Zheng M, Liu S, Ma L, Shen W. Silicon nanowire array/Cu<sub>2</sub>O crystalline core–shell nanosystem for solar-driven photocatalytic water splitting. *Nanotechnology* 2013;24:265402. <https://doi.org/10.1088/0957-4484/24/26/265402>.
- Han C, Yan L, Zhao W, Liu Z. TiO<sub>2</sub>/CeO<sub>2</sub> core/shell heterojunction nanoarrays for highly efficient photoelectrochemical water splitting. *Int J Hydrogen Energy* 2017;42:12276–83. <https://doi.org/10.1016/j.ijhydene.2017.03.068>.
- Shi M, Pan X, Qiu W, Zheng D, Xu M, Chen H. Si/ZnO core-shell nanowire arrays for photoelectrochemical water splitting. *Int J Hydrogen Energy* 2011;36:15153–9. <https://doi.org/10.1016/j.ijhydene.2011.07.145>.
- Santinacci L, Diouf MW, Barr MKS, Fabre B, Joanny L, Gouttefangeas F, et al. Protected light-trapping silicon by a simple structuring process for sunlight-assisted water splitting. *ACS Appl Mater Interfaces* 2016;8:24810–8. <https://doi.org/10.1021/acsami.6b07350>.
- Scheuermann AG, Lawrence JP, Kemp KW, Ito T, Walsh A, Chidsey CED, et al. Design principles for maximizing photovoltage in metal-oxide-protected water-splitting photoanodes. *Nat Mater* 2015;15:1–8. <https://doi.org/10.1038/nmat4451>.
- Ge M, Cai J, Iocozzia J, Cao C, Huang J, Zhang X, et al. A review of TiO<sub>2</sub> nanostructured catalysts for sustainable H<sub>2</sub> generation. *Int J Hydrogen Energy* 2017;42:8418–49. <https://doi.org/10.1016/j.ijhydene.2016.12.052>.
- Hwang YJ, Boukai A, Yang P. High density n-Si/n-TiO<sub>2</sub> core/shell nanowire arrays with enhanced photoactivity 2009. *Nano Lett* 2009;3:410–5. <https://doi.org/10.1021/nl8032763>.
- Ao X, Tong X, Sik Kim D, Zhang L, Knez M, Müller F, et al. Black silicon with controllable macropore array for enhanced photoelectrochemical performance. *Appl Phys Lett* 2012;101:111901. <https://doi.org/10.1063/1.4752231>.
- Shaner MR, McDowell MT, Pien A, Atwater HA, Lewis NS. Si/TiO<sub>2</sub> tandem-junction microwire arrays for unassisted solar-driven water splitting. *J Electrochem Soc* 2016;163:H261–4. <https://doi.org/10.1149/2.0141605jes>.
- Ros C, Andreu T, Hernández-Alonso MD, Penelas-Pérez G, Arbiol J, Morante JR. Charge transfer characterization of ALD-grown TiO<sub>2</sub> protective layers in silicon photocathodes. *ACS Appl Mater Interfaces* 2017. <https://doi.org/10.1021/acsami.7b02996>.
- Iatsunskiy I, Jancelewicz M, Nowaczyk G, Kempinski M, Peplirńska B, Jarek M, et al. Atomic layer deposition TiO<sub>2</sub> coated porous silicon surface: structural characterization and morphological features. *Thin Solid Films* 2015;589:303–8. <https://doi.org/10.1016/j.tsf.2015.05.056>.
- Johnson RW, Hultqvist A, Bent SF. A brief review of atomic layer deposition: from fundamentals to applications. *Mater Today* 2014;17:236–46. <https://doi.org/10.1016/j.mattod.2014.04.026>.
- Iatsunskiy I, Vasylenko A, Viter R, Kempinski M, Nowaczyk G, Jurga S, et al. Tailoring of the electronic properties of ZnO-polyacrylonitrile nanofibers: experiment and theory. *Appl Surf Sci* 2017. <https://doi.org/10.1016/j.apsusc.2017.03.111>.
- Chen YW, Prange JD, Dühnen S, Park Y, Gunji M, Chidsey CED, et al. Atomic layer-deposited tunnel oxide stabilizes silicon photoanodes for water oxidation. *Nat Mater* 2011;10:539–44. <https://doi.org/10.1038/nmat3047>.
- Yu Y, Zhang Z, Yin X, Kvit A, Liao Q, Kang Z, et al. Enhanced photoelectrochemical efficiency and stability using a conformal TiO<sub>2</sub> film on a black silicon photoanode. *Nat Energy* 2017;2:17045. <https://doi.org/10.1038/nenergy.2017.45>.
- Seger B, Pedersen T, Laursen AB, Vesborg PCK, Hansen O, Chorkendorff I. Using TiO<sub>2</sub> as a conductive protective layer for photocathodic H<sub>2</sub> evolution. *J Am Chem Soc* 2013;135:1057–64. <https://doi.org/10.1021/ja309523t>.
- Wang P, Wen X, Amal R, Ng YH. Introducing a protective interlayer of TiO<sub>2</sub> in Cu<sub>2</sub>O–CuO heterojunction thin film as a highly stable visible light photocathode. *RSC Adv* 2015;5:5231–6. <https://doi.org/10.1039/C4RA13464H>.
- Avasthi S, McClain WE, Man G, Kahn A, Schwartz J, Sturm JC. Hole-blocking titanium-oxide/silicon heterojunction and its application to photovoltaics. *Appl Phys Lett* 2013, 203901. 1–4.
- Pavlenko M, Coy EL, Jancelewicz M, Zaleski K, Smyntyna V, Jurga S, et al. Enhancement of optical and mechanical properties of Si nanopillars by ALD TiO<sub>2</sub> coating. *RSC Adv* 2016;6:97070–6. <https://doi.org/10.1039/C6RA21742G>.
- Iatsunskiy I, Coy E, Viter R, Nowaczyk G, Jancelewicz M, Baleviciute I, et al. Study on structural, mechanical, and

- optical properties of  $\text{Al}_2\text{O}_3$ – $\text{TiO}_2$  nanolaminates prepared by atomic layer deposition. *J Phys Chem C* 2015;119:20591–9. <https://doi.org/10.1021/acs.jpcc.5b06745>.
- [30] Iatsunskyi I, Pavlenko M, Viter R, Jancelewicz M, Nowaczyk G, Baleviciute I, et al. Tailoring the structural, optical, and photoluminescence properties of porous silicon/ $\text{TiO}_2$  nanostructures. *J Phys Chem C* 2015;119:7164–71. <https://doi.org/10.1021/acs.jpcc.5b01670>.
- [31] Cho IS, Chen Z, Forman AJ, Kim DR, Rao PM, Jaramillo TF, et al. Branched  $\text{TiO}_2$  nanorods for photoelectrochemical hydrogen production. *Nano Lett* 2011;11:4978–84. <https://doi.org/10.1021/nl2029392>.
- [32] Matarrese R, Nova I, Li Bassi A, Casari CS, Russo V, Palmas S. Preparation and optimization of  $\text{TiO}_2$  photoanodes fabricated by pulsed laser deposition for photoelectrochemical water splitting. *J Solid State Electrochem* 2017. <https://doi.org/10.1007/s10008-017-3639-7>.
- [33] Shi J, Hara Y, Sun C, Anderson MA, Wang X. Three-dimensional high-density hierarchical nanowire architecture for high-performance photoelectrochemical electrodes. *Nano Lett* 2011;11:3413–9. <https://doi.org/10.1021/nl201823u>.
- [34] Pal M, Wu H, Jing Y, Li X, Zhu H, Wang C, et al. Core–shell Silicon@Mesoporous  $\text{TiO}_2$  heterostructure: towards solar-powered photoelectrochemical conversion. *ChemNanoMat* 2016;2:647–51. <https://doi.org/10.1002/cnma.201600085>.
- [35] Crawford S, Thimsen E, Biswas P. Impact of different electrolytes on photocatalytic water splitting. *J Electrochem Soc* 2009;156:H346–51. <https://doi.org/10.1149/1.3090177>.

### **3.5. Enhancing photocatalytic performance and solar absorption by Schottky nanodiodes heterojunctions in mechanically resilient palladium coated TiO<sub>2</sub>/Si nanopillars by atomic layer deposition**

An improvement in PEC efficiency is a significant issue in developing complex nanocomposite materials for photocatalytic applications. Palladium nanoparticles have been extensively investigated in the context of HER on diverse photocatalytic nanomaterials. Its application in Si/TiO<sub>2</sub> heterojunction is expected to facilitate charge separation and heat transfer efficiency owing to the formation of Schottky nanodiodes inward of the TiO<sub>2</sub> layer and the employment of SPR. In the case of silicon-based photoanodes, it is possible to extend the absorption range and enhance the efficiency of water-splitting reactions.

This research is addressed to investigate the synergistic effect caused by Si/TiO<sub>2</sub> heterojunction in combination with Pd nanoparticles. Structural properties of the fabricated Si/TiO<sub>2</sub> nanopillar arrays with ALD-deposited Pd nanoparticles were investigated by SEM, HRTEM, GIXRD and EDX. A set of low-load indentation experiments on single-stand nanopillars was conducted to confirm the advanced mechanical stability of obtained Pd/TiO<sub>2</sub>/Si nanocomposite. Diffuse reflectance and absorbance data were collected to prove the positive effect of Pd on the optical properties of Si/TiO<sub>2</sub>. Linear voltammetry, chronoamperometry and EIS data were used to estimate the PEC performance of the Pd/TiO<sub>2</sub>/Si photoanode. Also, complementary photodegradation tests in rhodamine B solution and water evaporation rate assessment were conducted to estimate the rates of charge carriers and heat transfer. It was shown the superior PEC performance of Pd/TiO<sub>2</sub>/Si photoanode compared to Si/TiO<sub>2</sub>, along with the occurrence of either OER or HER. This effect could be ascribed to superior absorbance in the UV and IR parts of spectra in the presence of Pd nanoparticles. The detailed mechanism of the enhancement was discussed in detail, and its model has been developed taking into account the acquired experimental results.

In this research, the Author performed the synthesis of silicon nanopillar arrays with relative procedures such as MACE, NSL and RIE as well as the ALD of TiO<sub>2</sub> for the fabrication of Si/TiO<sub>2</sub> nanocomposite. He assisted in acquiring and processing the optical spectroscopy data from Si/TiO<sub>2</sub> and Pd/TiO<sub>2</sub>/Si samples. He contributed to the discussion of the obtained results, draft reviewing and development of the charge transfer model in the Pd/TiO<sub>2</sub>/Si.

**Number of Ministerial points: 200**

**Impact factor: 15.1**



Contents lists available at ScienceDirect

Chemical Engineering Journal

journal homepage: [www.elsevier.com/locate/cej](http://www.elsevier.com/locate/cej)

## Enhancing photocatalytic performance and solar absorption by schottky nanodiodes heterojunctions in mechanically resilient palladium coated TiO<sub>2</sub>/Si nanopillars by atomic layer deposition



Emerson Coy<sup>a,\*</sup>, Katarzyna Siuzdak<sup>b</sup>, Mykola Pavlenko<sup>a</sup>, Karol Załęski<sup>a</sup>, Octavio Graniel<sup>c</sup>, Marcin Ziółek<sup>d</sup>, Sebastien Balme<sup>c</sup>, Philippe Miele<sup>c</sup>, Matthieu Weber<sup>c</sup>, Mikhael Bechelany<sup>c,\*</sup>, Igor Iatsunskyi<sup>a,\*</sup>

<sup>a</sup> NanoBioMedical Centre, Adam Mickiewicz University, Wszechnicy Piastowskiej 3, 61-614 Poznan, Poland

<sup>b</sup> Centre of Laser and Plasma Engineering, The Szewalski Institute of Fluid-Flow Machinery, Fiszerza 14 Str., 80-231 Gdansk, Poland

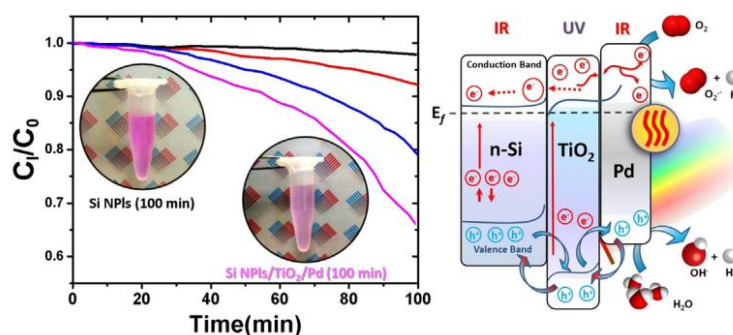
<sup>c</sup> Institut Européen des Membranes, IEM – UMR 5635, ENSCM, CNRS, Univ Montpellier, Montpellier, France

<sup>d</sup> Faculty of Physics, Adam Mickiewicz University in Poznań, Umultowska 85, 61-614 Poznań, Poland

### HIGHLIGHTS

- The synergistic effect of Pd decorated TiO<sub>2</sub>/Si nanopillars for photocatalytic applications was investigated.
- A comprehensive physico-chemical characterization of the pillars will be presented.
- The capability of this route to enable and enhance the catalytic activity to the as-prepared structures will be discussed.
- The ability of these pillars to boost water evaporation rates will be demonstrated.
- The general cooperative performance of nanostructures will be explained by a combined OER/HER mechanism.

### GRAPHICAL ABSTRACT



### ARTICLE INFO

#### Keywords:

Photocatalytic  
Solar heat conversion  
Atomic layer deposition  
Nanopillars  
Photodegradation

### ABSTRACT

The development of highly efficient photocatalytic materials and composites has been one of the main goals in the energy and environmental fields. To this date, however, the efficiency and stability of photocatalytic materials are still very low. This work shows a novel strategy of Pd coated TiO<sub>2</sub>/Si nanopillars produced by atomic layer deposition with a wide light absorption window. The structures show significantly improved performance due to the synergistic effect of Pd decorated TiO<sub>2</sub>/Si nanopillars, and the cooperative effect between Hot and Photoexcited electrons and Schottky nanojunctions. The performance of the composites is evaluated, the enhancement mechanism is explained and the advantages of the rational design of these materials are discussed.

\* Corresponding authors.

E-mail addresses: [coyeme@amu.edu.pl](mailto:coyeme@amu.edu.pl) (E. Coy), [mikhael.bechelany@umontpellier.fr](mailto:mikhael.bechelany@umontpellier.fr) (M. Bechelany), [igoyat@amu.edu.pl](mailto:igoyat@amu.edu.pl) (I. Iatsunskyi).

<https://doi.org/10.1016/j.cej.2019.123702>

Received 15 September 2019; Received in revised form 28 November 2019; Accepted 3 December 2019

Available online 05 December 2019

1385-8947/ © 2019 Elsevier B.V. All rights reserved.

## 1. Introduction

Solar water splitting mediated by photocatalytically active nanostructures is one of the most promising strategies toward the potential implementation of hydrogen energy in the future [1–3]. Electrolysis, the production of molecular hydrogen by electrical means from aqueous solutions, produces a high yield of usable hydrogen at a rather energetically expensive cost, making it an unpractical solution for a hydrogen-based economy [4]. On the other hand, photoactive materials could be used to harness our plentiful solar radiation to generate electron-rich centres for catalytic production of hydrogen or combined remediation strategies [5]. Nowadays, several architectures have been proposed to improve the absorption of sunlight in various materials to boost the efficiency of hydrogen producing devices. A common strategy found throughout the literature aims to broaden the absorption window of photoactive materials [5], which typically resides below the visible wavelength of light (UV) [6,7]. This broadening attempt is due to the rather large bandgap of common light-harvesting materials like Titanium oxide (TiO<sub>2</sub>) and Zinc oxide (ZnO) [8], that limits their conversion efficiency.

Another strategy to improve the photoactivity of these materials is to control their morphology and exploit confinement or nanometric effects [6,9,10]. During the last few years, several groups (including our own) have been actively working on silicon (Si) nanopillars (NPLs) [6,11] due to their well-established commercial and industrial applicability, availability, and the relatively small bandgap ( $E_g = 1.1$  eV) of silicon. Moreover, Si-NPLs are quite attractive structures that have shown wider absorption and enhanced performance due to the clear increment of their active surface [12,13]. However, as photoanode, bare Si suffers from fast degradation and corrosion in aqueous environments, which dramatically limits its operation time [14]. Several strategies based on the introduction of protective coatings to hinder surface passivation have been proposed to extend the lifetime of Si based photoanodes [15,16]. Additional studies have shown the advantages of TiO<sub>2</sub> or ZnO coatings on the performance of Si-NPLs [17–19], due to their optical tunability [6], mechanical reinforcement [11,20], and high photoactive performance [6,11].

Recently, photoactive junctions of precious metals and semiconducting materials have shown enhanced carrier transport capabilities of photogenerated electrons which could provide a more efficient catalytic performance for water splitting [21–28]. In principle, photoactive junctions between precious metals and semiconducting oxides are more efficient when contact areas are maximized. Thus, nanocomposite-like structures are preferred over heterostructures, although they have shown important results in photocatalysis [29]. Nevertheless, the maximal efficiency of photojunctions on nanostructured surfaces, such NPLs, is rather demanding since the anchoring of the particles is limited by physical techniques [30,31], or by the anchoring point of thermal decomposition methods [32]. Atomic Layer Deposition (ALD) is a well-established technique for the synthesis of thin films and nanoparticles, as these nanomaterials can be prepared with an extreme control over their dimensions [33], excellent uniformity over the substrate, and conformality on nanometer-sized [33–35]. Recently, we developed and tested an ALD route for the deposition of a highly conformal Pd layer, in which the nucleation and surface coverage can be maximized while retaining anchoring strength [36–38]. The efficiency of this method was further tested in Pd/TiO<sub>2</sub> nanotubes junction for environmental applications [39].

On the other hand, several groups have shown the importance of photothermal water vaporization as a strategy for remediation and photocatalysis [40,41]. One of the advantages of this methodology is the direct conversion of solar energy into chemical energy due to the efficient light-harvesting [40], heat confinement [42], and no need to transport or inject electrons into the system [40,41]. As expected, one of the main strategies to induce full solar spectrum absorption is nanostructuring and/or nanopatterning of surfaces to reduce their optical

reflection [43]. Additionally, metals have shown outstanding performance as solar absorbers, due to rather large excitation, plasmonic effects [44], and heat transport properties [45]. For instance, palladium (Pd) has been used as main collector of solar energy in steam generation applications with outstanding results [42]. Similarly, the cooperative nature of Au@TiO<sub>2</sub> junctions for photocatalysis and solar evaporation in remediation strategies has also been shown [46].

In the present work, we investigate the synergistic effect of Pd decorated TiO<sub>2</sub>/Si-NPLs for photocatalytic applications. The effective decoration of Pd by ALD will be demonstrated. Additionally the capability of this route to enable and enhance the catalytic activity to the as-prepared structures will be discussed. The improvement of catalytic performance of the nanostructures will be followed by an additional enhancement in heat absorption by the Pd layer. A comprehensive physico-chemical characterization of the pillars will be presented by means of X-ray diffraction (XRD), Scanning Electron Microscopy (SEM), Transmission Electron Microscopy (TEM), Energy Dispersive Spectroscopy (EDX), Nanoindentation, Ultraviolet Visible spectroscopy (UV-Vis). The synergistic effect originating from the noble metal and the ordered substrate will be revealed by Electro Impedance Spectroscopy (EIS), Chronoamperometry, and Cyclic Voltammetry (CV). Also, we will show that water evaporation rates are boosted, and that the general cooperative performance of nanostructures, although complex in nature, could be explained by a combined OER/HER mechanism. The general applicability of the photocatalytic properties of TiO<sub>2</sub>/Si and solar absorption of the Pd/TiO<sub>2</sub> junctions are evaluated and allow for a further strategy to enhance the performance of photoactive junctions exploiting a broader range of the light spectra.

## 2. Results and discussion

### 2.1. Structural and optical characterization

The structure and morphology of Si-NPLs were investigated primarily by SEM and XRD. Fig. 1. After the Metal-assisted chemical etching (MACE) procedure, pillars are predominantly placed in an hexagonal matrix (Fig. S1), with an average diameter of  $450 \pm 50$  nm, length of  $3.0 \pm 0.2$   $\mu$ m, and base separation of  $200 \pm 50$  nm (Fig. 1a,b). After the coating process of TiO<sub>2</sub> by ALD, a layer of  $25 \pm 3$  nm was observed, and the general morphology of the Si pillars was unaffected. The phase of the layers was investigated by GI-XRD (Fig. 1c). The patterns show two main peaks at around  $\sim 25^\circ$  and  $\sim 47^\circ$  2theta, corresponding to the (1 0 1) and (2 0 0) peaks respectively, which are distinctive of anatase phase. After Pd coating ( $50 \pm 4$  nm), a single small peak at around  $\sim 40^\circ$  2theta is observed, corresponding to the (1 1 1) and confirming the crystallinity of both TiO<sub>2</sub> and Pd coating processes. TEM and EDX mappings, Fig. 1d, shows the core shell structure of the Pd/TiO<sub>2</sub>/Si pillars with well-defined thickness and distribution, additionally, independent maps are shown in Fig. S2. Quantification obtained from the TEM-cross-section, focusing on the pillars region showed the following composition in Atom%: Pd = 25.0, Ti = 22.8, Si = 36.3, O = 12.8 and C = 3.1. The high resolution TEM images show the conformal structure of the coatings. Moreover, the FFT patterns shown in the inset confirm the GI-XRD results by showing TiO<sub>2</sub> anatase and Pd crystalline phases. It is important to notice the conformal growth of the Pd layer over the TiO<sub>2</sub> with a well-defined interface and rather short mixing.

Previously we investigated the mechanical enhancement of TiO<sub>2</sub> coated Si-NPLs [11]. Our results showed a considerable enhancement on mechanical resilience of the structures due to crystallization of TiO<sub>2</sub> nanocrystals on the superficial pores of the Si-NPLs and the chemical binding of TiO<sub>2</sub> on the silicon structure [47]. The effect of the Pd conformal coating on the TiO<sub>2</sub>/Si-NPLs is shown in Fig. 2a. The low load regime shows the presence of a big elastoplastic contribution after Pd coating. Although this behaviour is observed in metals and Pd is a relative soft metal (121 GPa), it remains harder than gold (78 GPa).

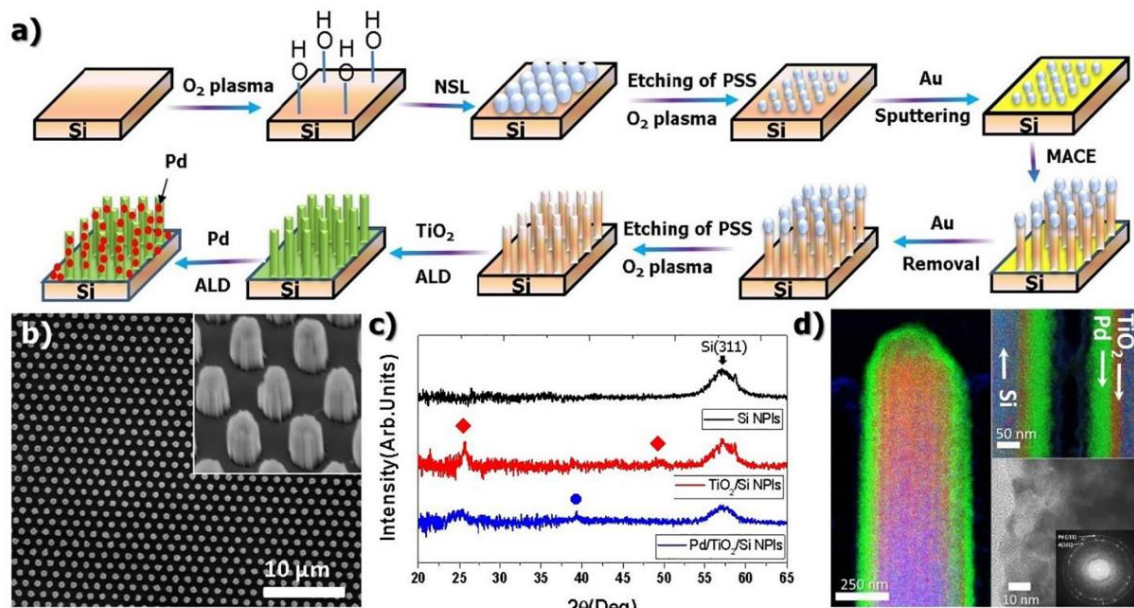


Fig. 1. a) Schematic representation of the procedure for sample preparation of Si-NPIs, the ALD coating by  $\text{TiO}_2$  and Pd. b) SEM micrographs of large area ordered pillars prepared by Metal-assisted chemical etching (MACE). Inset shows close view of the top of the pillars. c) GI-XRD images taken for bare pillars,  $\text{TiO}_2$  coated and Pd coated, showing the distinctive peaks for Anatase  $\text{TiO}_2$  (♦) and Pd (●). d) STEM-EDX images showing the elemental mapping of the core shell pillars. The sample is a FIB cross-section, green is Palladium, red shows Titanium and blue the silicon area. Inset shows the HR-TEM images with FFT indexed peaks of  $\text{TiO}_2$  and Pd. (For interpretation of the references to colour in this figure legend, the reader is referred to the web version of this article.)

Additionally, nanoindentation experiments have shown to have strong dependency on porosity [48], (especially for Si) allowing to calculate the average porosity of the Si-NPIs. The average porosity of the as-prepared samples was calculated to be in the range of 70–80%

according to the load vs displacement experiments. These results provided a Young's Modulus of ~3–5 GPa (Fig. S3). After  $\text{TiO}_2$  and further inclusion of Pd, mechanical properties are enhanced. As reported before, the inclusion of  $\text{TiO}_2$  by ALD fills the porous superficial layers of

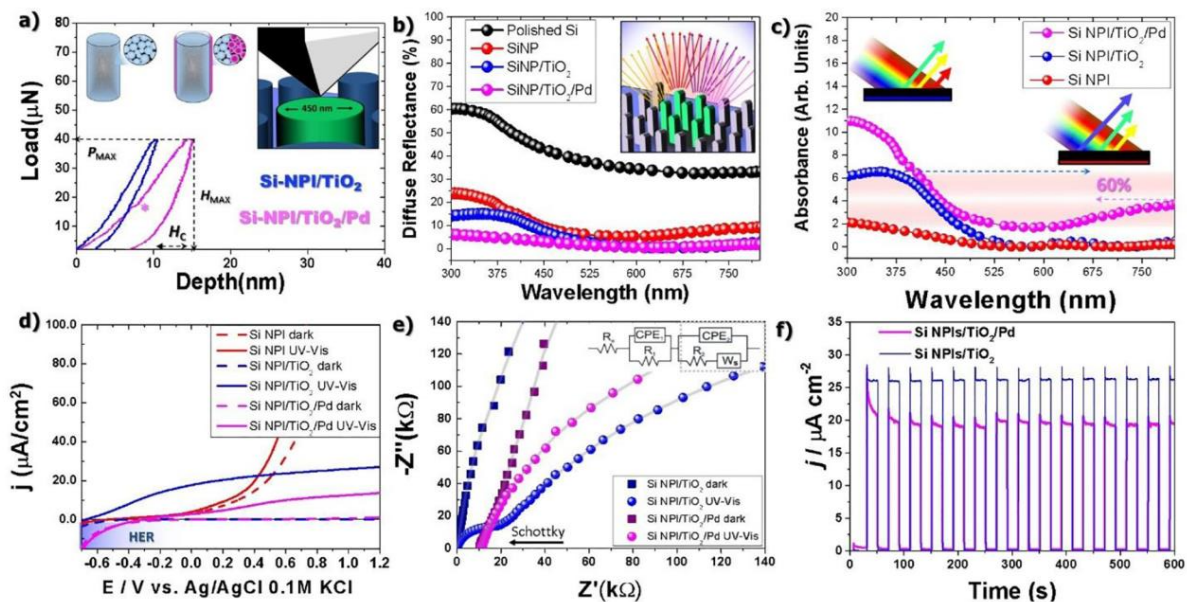
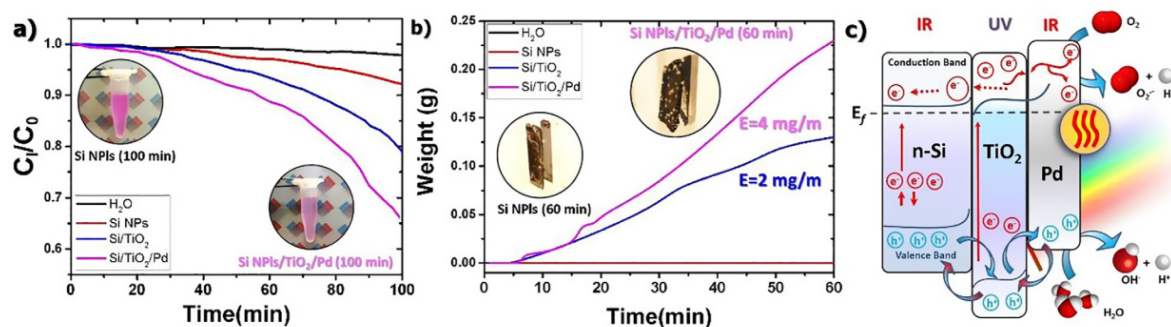


Fig. 2. a) low-load indentation experiments on single pillars,  $H_{\text{max}}$ ,  $P_{\text{max}}$  and  $H_c$  show the maximum penetration, maximum load and residual imprint respectively. Insets show diagrams of the structure and indentation experiments. b) Diffusive reflectance spectra of the samples. c) Absorbance spectra of the prepared samples, insets show schematics of the absorption. Dashed lines are a guide to eye pointing to the IR enhanced response that corresponds to ~60% of the UV absorption of bare  $\text{TiO}_2$  samples. d) Linear voltammetry curves recorded for all the samples, dashed lines correspond to dark conditions while full lines to illuminated conditions. Blue shaded region corresponds to the negative potentials where hydrogen evolution reaction takes place. e) Nyquist plots of the  $\text{TiO}_2$  and Pd/ $\text{TiO}_2$  coated samples. Lines show the response in illuminated conditions (●) and in dark conditions (■). Gray faded lines are the fitted curves. Inset shows the circuit model used for fitting the data. f) Chronoamperometric response of  $\text{TiO}_2$  and Pd/ $\text{TiO}_2$  samples during multiple light on/off cycles collected at + 1.0 V vs. Ag/AgCl/0.1 M KCl. (For interpretation of the references to colour in this figure legend, the reader is referred to the web version of this article.)





**Fig. 3.** a) Degradation studies of Rhodamine B under UV illumination. Inset shows the pre and post decolorized solution b) Water evaporation efficiency under solar simulator conditions, inset show the quick covering of bubbles of the Pd sample over the as prepared Si-NPLs. c) Shows the proposed mechanism in the cooperative degradation and photocatalysis of rhodamine b under sun-simulated conditions.

the pillars and crystallizes in the anatase phase (Fig. 1c) thus providing extra mechanical resilience towards deformation (Fig. 2a). Moreover, after Pd covering, the samples show a larger plastic deformation than the one observed in TiO<sub>2</sub>/Si and Pd coated samples. However, the increased plastic deformation provides resilience of the conformal Pd coating by allowing the atoms to move away from the indenting pressure point (in the so called pile-up effect) without breaking the nanocomposite. This effect contributes to the further sealing of the surface and prevents failure of the surface by cracking at low loads. Overall, the mechanical changes in the pillars point show enhancement over the as-prepared Si-NPLs.

Optical properties (absorbance and reflectance) play a crucial role for the photo-driven processes. They are reported in Fig. 2b and c. The diffuse reflectance measurements show the low dispersion of light of the Pd coated samples, which is attributed to the nanopillar and nanocomposite structure of the films. The absorption was calculated with the Kubelka-Munk model [49]. Absorption spectra for the samples are presented in Fig. 2c (Fig. S4 for polished Si). As expected, the TiO<sub>2</sub> coated samples show an improved absorption below 450 nm due to its known optical bandgap. Furthermore, the absorption of the samples coated with Pd shows not only a 2-fold increment in the UV region, when compared with TiO<sub>2</sub>, but also an important increment in the visible region. The boost is considerably, considering the no absorbance of Si and TiO<sub>2</sub>/Si samples, additionally, it is important to remark that the increment of the visible region of Pd, correspond to 60% of the UV region absorption of TiO<sub>2</sub> ( $A\text{-TiO}_2(< 450\text{nm}) = 7.1$  and  $A\text{-Pd/TiO}_2(> 650\text{nm}) = 4.3$ ). These changes show a clear enhancement in both UV and IR absorption induced by Pd coated samples. This enhancement promises the enhanced photoactivity of the produced nanocomposites.

## 2.2. Electrochemical and heat absorption performance

In order to assess the efficiency of the Pd/TiO<sub>2</sub>/Si structures, photoelectrochemical studies were performed. First, current density vs applied voltage were recorded and are shown in Fig. 2d. It is important to remark that TiO<sub>2</sub>/Si sample exhibits an important increment on photocurrent under the UV–vis light experimental conditions, while showing negligible response under dark conditions. Although the bare Si-NPLs already show certain efficiency under dark conditions, these results present the proper conformal covering of the TiO<sub>2</sub> layer on the Si-NPLs. Additionally, for the Pd coated sample, no response or any other feature in dark conditions was observed, which follows a similar behaviour as the one for bare Si-NPLs. It is worth to underline that the Pd inclusion, although providing a smaller photocurrent than TiO<sub>2</sub> coated samples (~80%), also activates the negative potential region of the plots, which correspond to the hydrogen evolution reaction (HER) section of the voltamperogram shown in Fig. 2d. The presence of HER is tied to the known efficiency of Pd towards hydrogen production as part of the Platinum like noble metals [50]. Fig. 2e shows the Nyquist plots

of both the TiO<sub>2</sub>/Si-NPLs coated samples and Pd/TiO<sub>2</sub>/Si-NPLs. The fitted model includes two contributions for the under illumination TiO<sub>2</sub>/Si-NPLs while a single contribution is modelled for the rest. In these plots, the high frequency regime (small semicircle near the Shottky) is visible for illuminated conditions, while these contributions are not observed for dark or Pd coated samples. This observation points to a rather small resistivity of TiO<sub>2</sub> toward the high mobility of carriers in TiO<sub>2</sub> under illumination, which is expected for such an interface like this. However, the large and single semicircle of the Pd coated samples, coupled with the Schottky contact, suggests a lower performance of the samples as well as shielding of the photo-active centres of the film. Nevertheless, the visible changes in the EIS under illumination coupled with the chronoamperometry results, shown in Fig. 2f, which unequivocally demonstrates a rather low shielding of the photoactive centres, a 20% decrement in efficiency by the Pd coating and a rather stable response (other samples in Fig. S5).

Although OER results, shown in Fig. 2, suggest a decrease in performance by the Pd coating (Fig. 2f), the complementary tests shown in Fig. 3a show an enhancement photodegradation. In the typical photodegradation tests, the samples are used for the photo decomposition of rhodamine B in aqueous solutions [51,52]. The samples covered with Pd show faster decolourisation than TiO<sub>2</sub>/Si-NPLs and bare Si-NPLs. Although the final decomposition of the Rhodamine B was not tested and the efficiency of our materials does not compete with powdered materials [51,52], the experiments show a clear indication of difference in initiation of the degradation process, which is definitely enhanced by the Pd coated samples over TiO<sub>2</sub>/Si-NPLs. Additionally, the results shown in Fig. 2c suggests that a higher absorption of UV light is occurring on Pd-coated samples, while also displaying absorption on the IR region. Therefore, water evaporation rate experiments were conducted as presented in Fig. 3b. We would like to highlight that these experiments were performed using full solar spectrum covering UV and visible range. The water evaporation results show the rapid generation of bubbles and weight loss due to heat transfer. The absorption of light, both in UV and IR clearly shows a boost of the structures towards evaporation, which opens several questions towards the applicability and mechanism of these effects.

## 2.3. Mechanism and origin of the enhancement

In order to understand the origin of the enhancement in photodegradation and heat absorption of the nanostructures, several aspects need to be addressed. It has been previously shown that heat can improve the photodegradation rate of rhodamine, especially for nanoparticle-based materials [53]. However, this enhancement effect has a limit since the high temperature tends to increase charge recombination and thus reducing efficiency [54]. Fig. S6 shows the temperature recorded during the water evaporation experiment and no considerable changes on water temperature were recorded. This shows that,

although heat transfer is expected, this is not the main factor responsible for the improvement. A plausible explanation is the synergistic effect between the hot-electron and carrier movements occurring at the semiconducting interfaces [55]. Simplifying the whole mechanism and ignoring the contribution of Pd, UV light should be absorbed by the TiO<sub>2</sub> layer, exciting the electrons from the valence to the conduction band and transferring them to the *n*-type Si nanopillars. Photogenerated holes are then gathered at the surface driving the OER. On the other hand, considering the case in which only Pd/TiO<sub>2</sub> heterojunctions are formed, the UV light would again generate electrons, which could be then transferred to the Pd surface and drive the HER [56] or take part in the degradation of pollutants [39]. However, it is safe to say that in our case, when the electron transfer is happening between Pd/TiO<sub>2</sub>/Si, the electron transfer seems contradictory.

Pd/TiO<sub>2</sub> junctions are commonly used as sensing platforms of hydrogen due to the Schottky barrier formed between Pd and TiO<sub>2</sub> [57]. Pd is often used due to its remarkable sensitivity towards hydrogen, which is related to changes in its work function and dielectric behaviour in the presence of small quantities of hydrogen [58]. This behaviour prompts the question: why is there a limited transfer of electrons within Pd/TiO<sub>2</sub>/Si junctions resulting from the Pd/TiO<sub>2</sub> interface? The general barrier of Pd/TiO<sub>2</sub> has an energy of 0.85 eV and the electron flow is established from TiO<sub>2</sub> towards Pd since electrons are confined to the metal nanoparticles in these nanodiodes [59]. However, the exposition to visible light and the presence of *n*-type Si makes the understanding of the electron flow difficult, which gets more complicated due to the surface Plasmon resonance, hot-electron transfer in Pd, and direct band-gap excitation by IR wavelength in Si [60]. Moreover, in photocatalysis, it has been shown that the enhancement effect can happen when small quantity of TiO<sub>2</sub> are added to Pd [61], or vice versa, when Pd is doping TiO<sub>2</sub> [62]. In our case, EDX shows large inclusions of Pd on the general structure of the nanopillar, which points to the first case.

One partial solution is the case in which both HER and OER can both potentially take place. Under UV irradiation, the light is absorbed by TiO<sub>2</sub>, generating an overpopulation of electron in the conduction band, these electrons are then quickly transferred to the *n*-type silicon pillars, leading the electron flow “inwards” between TiO<sub>2</sub> and *n*-type silicon. Additionally, the electron transfer generates a charge imbalance at the Pd/TiO<sub>2</sub> interface, which allows holes to be collected at the Pd surface (OER). This case provides the perfect environment for the production of super oxide anion radicals, such as O<sub>2</sub><sup>-</sup> and OH<sup>-</sup> as reported in several experimental studies, for Pd [23], TiO<sub>2</sub> [63], Metal/TiO<sub>2</sub> [22,24] and Pd/TiO<sub>2</sub> junctions [64]. Conversely, when IR light is considered, light is not absorbed by the TiO<sub>2</sub> layer and electrons are excited at the *n*-type Si-NPLs while generating a flow of electrons towards the surface and to the TiO<sub>2</sub> (HER). This synergistic effect was proposed by Tao Ji *et al.* [55] and takes into account the dual nature of light radiation absorption, IR and UV, on similar systems. For the case presented here, the addition of nanostructured Pd layer allows for the additional generation of hot carriers at the Pd surface [65]. Hot carriers are generated by SPR, and in the presence of a Schottky barrier, allow the faster separation of carriers and longer lifetime of catalytically active centers (HER). Therefore, the general mechanism can be illustrated as presented in Fig. 3c where the full electromagnetic spectrum of the sun is considered. The IR wavelengths activate electrons in *n*-type Si-NPLs (~1000 nm), medium wavelengths generate hot-carriers by surface plasmon resonance (SPR), (600–860 nm) (Fig. 2c) [58] and the UV part of the spectra generates electrons in the TiO<sub>2</sub> layer (< 500 nm). In zero bias conditions, like in a submerged sample, the flow of electrons is directed to the surface, where generated hot carriers promote HER on the Pd surface while changing its work function and pushing the electron flow further towards HER. Moreover, since oxygen is present in the solution, hydrogen should be released as water vapor, while oxygen deprived regions should generate H<sub>2</sub> gas. Nevertheless, in the case of degradation of contaminants, the continuous injection of electrons will

drive the degradation of rhodamine as shown in the literature [66]. Finally, the generation of gas bubbles increases the absorption of IR light and heat like in a small scale greenhouse effect, which overall increases the water evaporation efficiency of the system.

### 3. Conclusions

To conclude, in this study we have successfully prepared conformal Pd coating on TiO<sub>2</sub>/Si-NPLs by ALD. The resulting structures show superior mechanical resilience than those of pure Si-NPLs, which expands their applicability in mechanical demanding environments. The Pd coating slightly diminishes the photoactivity towards OER of the nanostructures due to the Schottky contacts generated by the Pd/TiO<sub>2</sub> nanodiodes. Nevertheless, in zero bias conditions, the absorption of selected parts of the solar spectrum by each element of heterojunction namely UV spectra by TiO<sub>2</sub>, near infrared by Pd particles in the shape of SPR generated excitons, and medium far infrared by *n*-type Si-NPLs, promotes an electron flux that drives the reaction towards HER on the nanostructures. The combination of these factors make these nanostructures highly applicable in solar driven water remediation and sun absorption boosted by HER, while remaining competitive in biased photocatalysis towards OER. Further studies are needed in order to determine the general limit of this synergistic architecture. Finally, further studies on thermal stability, Pd binding on TiO<sub>2</sub> surfaces and the influence of Pd thickness would definitely optimize the architecture here proposed, the presented methodology shows the clear applicability of Schottky nanodiodes and tunability of the OER/HER reaction on single structures for wide solar spectra water remediation.

### 4. Experimental

**Fabrication and Nanostructuring:** Commercially available *n*-type (1 0 0) (phosphorus doped, 0.01–0.02 Ω·cm) polished silicon wafers were used in this study. SiNPLs were prepared by a method similar to our previous papers [6,11]. Briefly, Si-NPLs were fabricated by combining nanosphere lithography (NSL), reactive ion etching (RIE) and metal-assisted chemical etching (MACE). Silicon samples were cleaned by ethanol, acetone, and dionized water (DI). Polystyrene nanosphere 10% solution (mean diameter 800 nm) was mixed with an equal amount of ethanol and then applied to the deposition of a monolayer mask on a silicon surface by spin-coating technique. Then, the size of nanosphere was decreased using (RIE) (MicroSys 200) in oxygen plasma (RF power – 70 W, pressure – 0.6 mbar). After the 50 nm layer gold deposition (magnetron sputtering machine Quorum Q160T), the samples were etched in aqueous solution containing HF (40%), H<sub>2</sub>O<sub>2</sub> (30%), and ultrapure H<sub>2</sub>O at a ratio of 80:80:20, respectively. The Au layer was removed using a solution of Aqua Regia (HCl (35%) and HNO<sub>3</sub> (65%) at ratio 1:2) and then samples were dipped in HF (5%) solution for 5 min to remove native oxide, cleaned by DI and blown dry with N<sub>2</sub>. After nanopillars fabrication, the ALD TiO<sub>2</sub> layer (400 ALD cycles) was deposited using TiCl<sub>4</sub> and water as ALD precursors at 200 °C. The growth rate was typically 0.45 Å/cycle on the planar Si surface. The ALD cycle consisted of 0.5 s exposure to TiCl<sub>4</sub>, 8 s N<sub>2</sub> purge, 0.5 s exposure to water and 8 s N<sub>2</sub> purge. ALD of Pd was based on Pd(hfac)<sub>2</sub> and formalin. The conformal Pd coating was achieved by applying 200 ALD at 220 °C. The typical ALD cycle consisted of 5 s pulse of Pd(hfac)<sub>2</sub>, 15 s exposure, and 10 s purge, followed by a 1 s pulse of formalin, 15 s exposure, and 60 s purge with Ar. The bubbler containing the Pd(hfac)<sub>2</sub> precursor was heated at 70 °C, and the formalin container was kept at room temperature.

**Physico-Chemical Characterization:** Samples were investigated by Grazing Incident X-ray spectrometry (GI-XRD) in a X'pert<sup>3</sup>(XL) MRD PANalytical, working in a 40kv 45 mA and Cu Kα (λ = 1.54 Å). Scanning Electron Microscopy (SEM) in a JEOL JSMM7001F microscope. High Resolution Electron Microscopy (HR-TEM), in a JEOL ARM 200F microscope working at 200 kV, equipped with an Energy

Dispersive X-ray Spectroscopy (EDX). Samples were cut for examination using a Focus Ion Beam (FIB) system by JEOL–JIB-4000. Nanoindentation experiments were performed in a Triboindenter TI-950 by Hysitron, methodology and other technical parameters were described in detail elsewhere [6,11,20,67]. Optical response was studied in UV–Vis spectrophotometer Lambda 950UV/VIS/NR with 1 nm step. Finally, the diffuse reflectance was measured in an Ocean Optics QE PRO spectrometer coupled with an integrating sphere.

**Electrochemical Characterization:** Characterization of working electrodes was performed using the potentiostat-galvanostat system AutoLab PGStat 302 N in a standard three-electrode assembly at room temperature. Counter electrode was Pt gauze and reference electrode was Ag/AgCl/0.1 M KCl. The electrolyte (180 mL) of 0.5 M K<sub>2</sub>SO<sub>4</sub> (pH = 7), was flushed with argon gas (99.999% purity), for 40 min before measurements. The samples were irradiated with a solar simulator (LOT Oriel) equipped with an AM 1.5G filter allowing to obtain full spectrum UV–vis light. The irradiance of incident light was calibrated to 100 mW/cm<sup>2</sup> using a reference cell (Si solar cell calibrated for air mass 1.5G 100 W/m<sup>2</sup> @ 25 °C, Rera). Electrochemical impedance spectroscopy (EIS), in dark and UV–vis conditions, were performed in the frequency range: 0.1 Hz – 20 kHz, at the amplitude of 10 mV and open circuit voltage as the potential of working electrode. EIS data was analyzed and fitted using the electrochemical equivalent circuit (EEQC) in Z-View software, using a Constant Phase Elements in parallel with a resistor (R-CPE) for TiO<sub>2</sub>/Pd and TiO<sub>2</sub> in dark, while two (2) R-CPE circuits in series were used for the TiO<sub>2</sub> under illumination [68,69]. The elements fitted showed a goodness-of-fit-value ( $\chi^2$ ) below  $\sim 10^{-4}$ . Cyclic voltammetry (dark conditions) covers potential range from –0.6 to + 0.6 V vs. Ag/AgCl/0.1 M KCl at a scanning speed of 50 mV/s. Linear voltamperometry (dark and UV–vis conditions) curves were recorded from –0.7 to + 1.2 V vs. Ag/AgCl/0.1 M KCl at the scanning speed of 10 mV/s. Finally, chronoamperometry (dark/UV–vis for a change) were measured in polarization conditions: +1.0 V vs. Ag/AgCl/0.1 M KCl with irradiation/dark periods of 20 s.

**Heat Absorption and Photodegradation:** Heat absorption experiments were performed by placing a 1 × 0.5 cm sample in an optically graded quartz cuvette and adding 10 ml of deionized water (Milli-Q water 18.2 MΩ cm). Samples were placed in a vertical position against the back window of the cuvette in order to collect the entire incident light at a 90° angle. Solar simulator (Photon Institute – Poland) was focused on the samples to reach 1 Sun illumination (100 mW/cm<sup>2</sup>) by using a calibrated silicon solar cell (15151, ABET). Cuvettes were rinsed with plenty of deionized water after experiment and fresh water was used for new experiments (room temperature  $\sim 23^\circ$ ). Water temperature was monitored by a thermocouple in contact with the water slightly above the incident light. Water evaporation was continuously measured by a microbalance in which the cuvette was suspended by a holder (see Fig. S7).

Photodegradation experiments were evaluated using rhodamine B as a model organic dye. The concentration of rhodamine B solution was  $5 \times 10^{-2}$  mg/mL. Before irradiation, the samples (1 × 0.5 cm<sup>2</sup>) were dipped in the solution and then stirred in the darkness for 30 min to reach adsorption–desorption equilibrium. The UV–vis light irradiation was carried out in a quartz cuvette using Xe lamp (Lambda LS model LB-LS/OF 30R, 4.5 Watts/300 W) at distant of 30 cm from the surface of solution in horizontal geometry. Then the absorption spectrum was constantly recorded by the Ocean Optics USB spectrometer (QE65-PRO). The remaining concentration of rhodamine B in the solution was estimated using absorbance spectrum at  $\lambda = 550$  nm. The calibration curve of absorbance was used to estimate the photocatalytic activity of the samples.

#### Declaration of Competing Interest

The authors declare that they have no known competing financial interests or personal relationships that could have appeared to

influence the work reported in this paper.

#### Acknowledgement

I.I. acknowledges the financial support from the National Science Centre of Poland by the SONATA 11 project UMO-2016/21/D/ST3/00962. M.P. acknowledges the financial support from the National Science Centre (NCN) of Poland by the PRELUDIUM 12 project UMO-2016/23/N/ST3/01356 and the National Centre for Research and Development (NCBR) by the project POWR.03.02.00-00-I032/16. K.S. acknowledges the financial support from the National Science Centre (NCN) of Poland by Sonata-BIS no 2017/26/E/ST5/00416. E.C., M.W., M.B. and I.I. acknowledge the support of RISE- H2020-EU.1.3.3. grant (ID:778157) CanBioSe. Finally, authors acknowledge the support from Prof. Stefan Jurga (CNBM-AMU).

#### Author Contributions

All authors have given approval to the final version of the manuscript.

#### Appendix A. Supplementary data

Supplementary data to this article can be found online at <https://doi.org/10.1016/j.cej.2019.123702>.

#### References

- [1] F. Haydous, M. Döbeli, W. Si, F. Waag, F. Li, E. Pomjakushina, A. Wokaun, B. Gökce, D. Pergolesi, T. Lippert, Oxynitride thin films versus particle-based photoanodes: a comparative study for photoelectrochemical solar water splitting, *ACS Appl. Energy Mater.* 2 (1) (2019) 754–763.
- [2] T. Hisatomi, K. Domen, Reaction systems for solar hydrogen production via water splitting with particulate semiconductor photocatalysts, *Nat. Catal.* 2 (5) (2019) 387–399.
- [3] Z. Wang, C. Li, K. Domen, Recent developments in heterogeneous photocatalysts for solar-driven overall water splitting, *Chem. Soc. Rev.* 48 (7) (2019) 2109–2125.
- [4] J.O. Abe, A.P.I. Popoola, E. Ajenifuja, O.M. Popoola, Hydrogen Energy, Economy and Storage: Review and Recommendation, *Int. J. Hydrogen Energy* 44 (29) (2019) 15072–15086.
- [5] A. Kertmen, E. Barbé, M. Szkoda, K. Siuzdak, V. Babić, P. Torruella, I. Iatsunskyi, M. Kotkowiak, K. Rytel, S. Estradé, F. Peiró, S. Jurga, Y. Li, E. Coy, Photoelectrochemically active N-adsorbing ultrathin TiO<sub>2</sub> Layers for water-splitting applications prepared by pyrolysis of oleic acid on iron oxide nanoparticle surfaces under nitrogen environment, *Adv. Mater. Interfaces* (2018) 1801286.
- [6] M. Pavlenko, K. Siuzdak, E. Coy, M. Jancelewicz, S. Jurga, I. Iatsunskyi, Silicon/TiO<sub>2</sub> core-shell nanopillar photoanodes for enhanced photoelectrochemical water oxidation, *Int. J. Hydrogen Energy* 42 (51) (2017) 30076–30085.
- [7] D. Flak, E. Coy, G. Nowaczyk, L. Yate, S. Jurga, Tuning the photodynamic efficiency of TiO<sub>2</sub> nanotubes against HeLa cancer cells by Fe-Doping, *RSC Adv.* 5 (103) (2015) 85139–85152.
- [8] Z. Kang, H. Si, S. Zhang, J. Wu, Y. Sun, Q. Liao, Z. Zhang, Y. Zhang, Interface engineering for modulation of charge carrier behavior in ZnO photoelectrochemical water splitting, *Adv. Funct. Mater.* 29 (15) (2019) 1808032.
- [9] X. Chai, H. Zhang, Q. Pan, J. Bian, Z. Chen, C. Cheng, 3D ordered urchin-like TiO<sub>2</sub>@Fe<sub>2</sub>O<sub>3</sub> arrays photoanode for efficient photoelectrochemical water splitting, *Appl. Surf. Sci.* 470 (2019) 668–676.
- [10] C.-L. Huang, X.-F. Chuah, C.-T. Hsieh, S.-Y. Lu, NiFe alloy nanotube arrays as highly efficient bifunctional electrocatalysts for overall water splitting at high current densities, *ACS Appl. Mater. Interfaces* 11 (27) (2019) 24096–24106.
- [11] M. Pavlenko, E.L. Coy, M. Jancelewicz, K. Załęski, V. Smyntyna, S. Jurga, I. Iatsunskyi, Enhancement of optical and mechanical properties of Si nanopillars by ALD TiO<sub>2</sub> coating, *RSC Adv.* 6 (99) (2016) 97070–97076.
- [12] C. Lv, Z. Chen, Z. Chen, B. Zhang, Y. Qin, Z. Huang, C. Zhang, Silicon nanowires loaded with iron phosphide for effective solar-driven hydrogen production, *J. Mater. Chem. A* 3 (34) (2015) 17669–17675.
- [13] P. Dytrych, V. Drinek, J. Bumba, F. Kastanek, O. Solcova, Silicon nanowires' based photoanode for hydrogen evolution, *Int. J. Hydrogen Energy* 43 (39) (2018) 18136–18141.
- [14] Q. Cai, W. Hong, C. Jian, J. Li, W. Liu, Insulator layer engineering toward stable Si photoanode for efficient water oxidation, *ACS Catal.* 8 (10) (2018) 9238–9244.
- [15] Y. Yu, Z. Zhang, X. Yin, A. Kvit, Q. Liao, Z. Kang, X. Yan, Y. Zhang, X. Wang, Enhanced photoelectrochemical efficiency and stability using a conformal TiO<sub>2</sub> film on a black silicon photoanode, *Nat. Energy* 2 (6) (2017) 17045.
- [16] A.G. Scheuermann, J.P. Lawrence, A.C. Meng, K. Tang, O.L. Hendricks, C.E.D. Chidsey, P.C. McIntyre, Titanium oxide crystallization and interface defect passivation for high performance insulator-protected schottky junction MIS

- photoanodes, ACS Appl. Mater. Interfaces 8 (23) (2016) 14596–14603.
- [17] Y.J. Hwang, A. Boukai, P. Yang, High density N-Si/n-TiO<sub>2</sub> core/shell nanowire arrays with enhanced photoactivity, Nano Lett. 9 (1) (2009) 410–415.
- [18] C. Ros, T. Andreu, M.D. Hernández-Alonso, G. Penelas-Pérez, J. Arbiol, J.R. Morante, Charge transfer characterization of ALD-grown TiO<sub>2</sub> protective layers in silicon photocathodes, ACS Appl. Mater. Interfaces 9 (21) (2017) 17932–17941.
- [19] F.-Q. Zhang, Y. Hu, R.-N. Sun, H. Fu, K.-Q. Peng, Gold-sensitized silicon/ZnO core/shell nanowire array for solar water splitting, Front. Chem. 7 (2019) 206.
- [20] E. Robak, E. Coy, M. Kotkowiak, S. Jurga, K. Załęski, H. Drozdowski, The effect of Cu doping on the mechanical and optical properties of zinc oxide nanowires synthesized by hydrothermal route, Nanotechnology 27 (17) (2016) 175706.
- [21] Z. Jia, M. Ben Amar, D. Yang, O. Brinza, A. Kanaev, X. Duten, A. Vega-González, Plasma catalysis application of gold nanoparticles for acetaldehyde decomposition, Chem. Eng. J. 347 (2018) 913–922.
- [22] L. Cheng, D. Zhang, Y. Liao, F. Li, H. Zhang, Q. Xiang, Constructing functionalized plasmonic gold/titanium dioxide nanosheets with small gold nanoparticles for efficient photocatalytic hydrogen evolution, J. Colloid Interface Sci. 555 (2019) 94–103.
- [23] D. Li, C. Wang, D.S. Strmcnik, D.V. Tripkovic, X. Sun, Y. Kang, M. Chi, J.D. Snyder, D. van der Vliet, Y. Tsai, V.R. Stamenkovic, S. Sun, N.M. Markovic, Functional links between Pt Single crystal morphology and nanoparticles with different size and shape: the oxygen reduction reaction case, Energy Environ. Sci. 7 (12) (2014) 4061–4069.
- [24] M. Luna, J.M. Gatica, H. Vidal, M.J. Mosquera, Au-TiO<sub>2</sub>/SiO<sub>2</sub> photocatalysts with NO<sub>x</sub> depolluting activity: influence of gold particle size and loading, Chem. Eng. J. 368 (2019) 417–427.
- [25] W. Yang, Y. Xiong, L. Zou, Z. Zou, D. Li, Q. Mi, Y. Wang, H. Yang, Plasmonic Pd nanoparticle- and plasmonic Pd nanorod-decorated bivo<sub>4</sub> electrodes with enhanced photoelectrochemical water splitting efficiency across visible-NIR region, Nanoscale Res. Lett. 11 (1) (2016) 283.
- [26] W. Hong, Q. Cai, R. Ban, X. He, C. Jian, J. Li, W. Liu, High-performance silicon photoanode enhanced by gold nanoparticles for efficient water oxidation, ACS Appl. Mater. Interfaces 10 (7) (2018) 6262–6268.
- [27] R. Tang-Kong, R. Winter, R. Brock, J. Tracy, M. Eizenberg, R.H. Dauskardt, P.C. McIntyre, The role of catalyst adhesion in ALD-TiO<sub>2</sub> protection of water splitting silicon anodes, ACS Appl. Mater. Interfaces 10 (43) (2018) 37103–37109.
- [28] A. Wang, L. Zhao, J. Yu, W. Zhou, B. Chu, H. Liu, Co Nanoparticles@N-Doped Carbon Coated on Carbon Nanotube@Defective Silica as Non-Noble Photocathode for Efficient Photoelectrochemical Hydrogen Generation, Int. J. Hydrogen Energy 43 (19) (2018) 9279–9286.
- [29] W. Zhou, Y. Guan, D. Wang, X. Zhang, D. Liu, H. Jiang, J. Wang, X. Liu, H. Liu, S. Chen, PdO/TiO<sub>2</sub> and Pd/TiO<sub>2</sub> heterostructured nanobelts with enhanced photocatalytic activity, Chem. - An Asian J. 9 (6) (2014) 1648–1654.
- [30] M.B. Zakaria, V. Malgras, T. Nagata, J. Kim, Y. Bando, A. Fatehmulla, A.M. Aldhafiri, W.A. Farooq, Y. Jikihara, T. Nakayama, Y. Yamauchi, J. Lin, Gold nanoparticles anchored on mesoporous zirconia thin films for efficient catalytic oxidation of carbon monoxide at low temperatures, Microporous Mesoporous Mater. 288 (2019) 109530.
- [31] Y.E. Silina, M. Koch, P. Herbeck-Engel, I. Iatsunskiy, Exploring the potential of high resolution inductively coupled plasma mass spectrometry towards non-destructive control and validation of electroless gold nanoparticles onto silicon nanowires hybrids, Anal. Methods (2019).
- [32] X. Rao, C. Guyon, S. Ognier, B. Da Silva, C. Chu, M. Tatoulian, A.A. Hassan, High density gold nanoparticles immobilized on surface via plasma deposited APTES film for decomposing organic compounds in microchannels, Appl. Surf. Sci. 439 (2018) 272–281.
- [33] M.J. Weber, M.A. Verheijen, A.A. Bol, W.M.M. Kessels, Sub-nanometer dimensions control of core/shell nanoparticles prepared by atomic layer deposition, Nanotechnology 26 (9) (2015) 094002.
- [34] M. Leskelä, M. Ritala, Atomic layer deposition chemistry: recent developments and future challenges, Angew. Chemie Int. Ed. 42 (45) (2003) 5548–5554.
- [35] M. Weber, A. Julbe, A. Ayral, P. Miele, M. Bechelany, Atomic layer deposition for membranes: basics, challenges, and opportunities, Chem. Mater. 30 (21) (2018) 7368–7390.
- [36] M. Weber, N. Tuleushova, J. Zgheib, C. Lamboux, I. Iatsunskiy, E. Coy, V. Flaud, S. Tingry, D. Comu, P. Miele, M. Bechelany, Y. Holade, Enhanced electrocatalytic performance triggered by atomically bridged boron nitride between palladium nanoparticles and carbon fibers in gas-diffusion electrodes, Appl. Catal. B Environ. 257 (2019) 117917.
- [37] M. Weber, J.-Y. Kim, J.-H. Lee, J.-H. Kim, I. Iatsunskiy, E. Coy, P. Miele, M. Bechelany, S.S. Kim, Highly efficient hydrogen sensors based on pd nanoparticles supported on boron nitride coated ZnO Nanowires, J. Mater. Chem. A 7 (14) (2019) 8107–8116.
- [38] M. Weber, J.-H. Kim, J.-H. Lee, J.-Y. Kim, I. Iatsunskiy, E. Coy, M. Drobek, A. Julbe, M. Bechelany, S.S. Kim, High-performance nanowire hydrogen sensors by exploiting the synergistic effect of Pd nanoparticles and metal-organic framework membr. ACS Appl. Mater. Interfaces 10 (40) (2018) 34765–34773.
- [39] A. Merenda, M. Weber, M. Bechelany, F.-M. Allioux, L. Hyde, L. Kong, L.F. Dumée, Fabrication of Pd-TiO<sub>2</sub> nanotube photoactive junctions via atomic layer deposition for persistent pesticide pollutants degradation, Appl. Surf. Sci. 483 (2019) 219–230.
- [40] M. Gao, L. Zhu, C.K. Peh, G.W. Ho, Solar absorber material and system designs for photothermal water vaporization towards clean water and energy production, Energy Environ. Sci. (2019).
- [41] L. Zhu, T. Ding, M. Gao, C.K.N. Peh, G.W. Ho, Shape conformal and thermal insulative organic solar absorber sponge for photothermal water evaporation and thermoelectric power generation, Adv. Energy Mater. 9 (22) (2019) 1900250.
- [42] L. Zhu, M. Gao, C.K.N. Peh, G.W. Ho, Solar-driven photothermal nanostructured materials designs and prerequisites for evaporation and catalysis applications, Mater. Horizons (2018).
- [43] J. Cai, L. Qi, Recent advances in antireflective surfaces based on nanostructure arrays, Mater. Horizons 2 (1) (2015) 37–53.
- [44] R. Asapu, N. Claes, R.-G. Ciocarlan, M. Minjauw, C. Detavernier, P. Cool, S. Bals, S.W. Verbruggen, Electron transfer and near-field mechanisms in plasmonic gold-nanoparticle-modified TiO<sub>2</sub> photocatalytic systems, ACS Appl. Nano Mater. 2 (7) (2019) 4067–4074.
- [45] P. Zolotavin, A. Alabastri, P. Nordlander, D. Natelson, Plasmonic heating in Au nanowires at low temperatures: the role of thermal boundary resistance, ACS Nano 10 (7) (2016) 6972–6979.
- [46] J. Huang, Y. He, L. Wang, Y. Huang, B. Jiang, Bifunctional Au@TiO<sub>2</sub> core-shell nanoparticle films for clean water generation by photocatalysis and solar evaporation, Energy Convers. Manag. 132 (2017) 452–459.
- [47] S.M. George, Atomic layer deposition: an overview, Chem. Rev. 110 (1) (2010) 111–131.
- [48] D. Bellet, P. Lamagnère, A. Vincent, Y. Bréchet, Nanoindentation investigation of the Young's modulus of porous silicon, J. Appl. Phys. 80 (7) (1996) 3772–3776.
- [49] I. Brytavskiy, K. Hušková, V. Myrdul, M. Pavlenko, E. Coy, K. Zaleski, D. Gregušová, L. Yate, V. Smyntyna, I. Iatsunskiy, Effect of porous silicon substrate on structural, mechanical and optical properties of MOCVD and ALD ruthenium oxide nanolayers, Appl. Surf. Sci. 471 (2019) 686–693.
- [50] S. Sarkar, S.C. Peter, An overview on Pd-based electrocatalysts for the hydrogen evolution reaction, Inorg. Chem. Front. 5 (9) (2018) 2060–2080.
- [51] A. Mehrdad, B. Massouji, R. Hashemzadeh, Kinetic study of degradation of rhodamine B in the presence of hydrogen peroxide and some metal oxide, Chem. Eng. J. 168 (3) (2011) 1073–1078.
- [52] P. Wilhelm, D. Stephan, Photodegradation of rhodamine B in aqueous solution via SiO<sub>2</sub>@TiO<sub>2</sub> nano-spheres, J. Photochem. Photobiol. A Chem. 185 (1) (2007) 19–25.
- [53] N.A.M. Barakat, M.A. Kanjwal, I.S. Chronakis, H.Y. Kim, Influence of temperature on the photodegradation process using Ag-Doped TiO<sub>2</sub> nanostructures: negative impact with the nanofibers, J. Mol. Catal. A Chem. 366 (2013) 333–340.
- [54] Y.-H. Chiu, T.-F.M. Chang, C.-Y. Chen, M. Sone, Y.-J. Hsu, Mechanistic insights into photodegradation of organic dyes using heterostructure photocatalysts, Catalysts 9 (5) (2019) 430.
- [55] T. Ji, Z. Cui, W. Zhang, Y. Cao, Y. Zhang, S. He, M. Xu, Y. Sun, R. Zou, J. Hu, UV and visible light synergetic photodegradation using rutile TiO<sub>2</sub> nanorod arrays based on a p-n junction, Dalt. Trans. 46 (13) (2017) 4296–4302.
- [56] J. Wu, S. Lu, D. Ge, L. Zhang, W. Chen, H. Gu, Photocatalytic properties of Pd/TiO<sub>2</sub> nanosheets for hydrogen evolution from water splitting, RSC Adv. 6 (72) (2016) 67502–67508.
- [57] N. Yamamoto, S. Tomomura, T. Matsuoka, H. Tsubomura, A study on a palladium-titanium oxide schottky diode as a detector for gaseous components, Surf. Sci. 92 (2–3) (1980) 400–406.
- [58] A. Tittel, P. Mai, R. Taubert, D. Dregely, N. Liu, H. Giessen, Palladium-based plasmonic perfect absorber in the visible wavelength range and its application to hydrogen sensing, Nano Lett. 11 (10) (2011) 4366–4369.
- [59] X.Z. Ji, G.A. Somorjai, Continuous hot electron generation in Pt/TiO<sub>2</sub>, Pd/TiO<sub>2</sub>, and Pt/GaN catalytic nanodiodes from oxidation of carbon monoxide, J. Phys. Chem. B 109 (47) (2005) 22530–22535.
- [60] M.R. Khan, T.W. Chuan, A. Yousuf, M.N.K. Chowdhury, C.K. Cheng, Schottky barrier and surface plasmonic resonance phenomena towards the photocatalytic reaction: study of their mechanisms to enhance photocatalytic activity, Catal. Sci. Technol. 5 (5) (2015) 2522–2531.
- [61] D.S. García-Zaleta, A.M. Torres-Huerta, M.A. Domínguez-Crespo, A. García-Murillo, R. Silva-Rodrigo, R.L. González, Influence of phases content on Pt/TiO<sub>2</sub>, Pd/TiO<sub>2</sub> catalysts for degradation of 4-chlorophenol at room temperature, J. Nanomater. 2016 (2016) 1–15.
- [62] M. Tsuji, D. Shimamoto, K. Uto, M. Hattori, H. Ago, Enhancement of catalytic activity of AgPd/Pd/TiO<sub>2</sub> nanoparticles under UV and visible photoirradiation, J. Mater. Chem. A 4 (38) (2016) 14649–14656.
- [63] Y. Nosaka, S. Komori, K. Yawata, T. Hirakawa, A.Y. Nosaka, Photocatalytic OH Radical Formation in TiO<sub>2</sub> Aqueous Suspension Studied by Several Detection Methods, Phys. Chem. Chem. Phys. 5 (20) (2003) 4731–4735.
- [64] H. Zhang, D. Meng, B. Fu, H. Fan, R. Cai, P.P. Fu, X. Wu, Separation of charge carriers and generation of reactive oxygen species by TiO<sub>2</sub> nanoparticles mixed with differently-coated gold nanorods under light irradiation, J. Environ. Sci. Heal. Part C 37 (2) (2019) 81–98.
- [65] H. Robatjazi, S.M. Bahaaddin, C. Doiron, I. Thomann, Direct plasmon-driven photoelectrocatalysis, Nano Lett. 15 (9) (2015) 6155–6161.
- [66] F.H. AlHamed, M.A. Rauf, S.S. Ashraf, Degradation Studies of rhodamine B in the presence of UV/H<sub>2</sub>O<sub>2</sub>, Desalination 239 (1–3) (2009) 159–166.
- [67] E. Coy, L. Yate, Z. Kabacińska, M. Jancelewicz, S. Jurga, I. Iatsunskiy, Topographic reconstruction and mechanical analysis of atomic layer deposited Al<sub>2</sub>O<sub>3</sub>/TiO<sub>2</sub> nanolaminates by nanoindentation, Mater. Des. 111 (2016) 584–591.
- [68] M.E. Orazem, B. Tribollet, Electrochemical Impedance Spectroscopy; John Wiley & Sons Inc: Hoboken, NJ, USA, 2008.
- [69] L. Liasa, A. Electrochemical Impedance Spectroscopy and Its Applications. In Modern Aspects of Electrochemistry; Kluwer Academic Publishers: Boston; pp 143–248.

### **3.6. Enhanced solar-driven water splitting of 1D core-shell Si/TiO<sub>2</sub>/ZnO nanopillars**

A further improvement of the PEC performance of silicon-based photoanode could be achieved by enhancement of the charge separation ability and optical properties of the metal oxide protective layer. Hence, a deposition of an additional metal oxide layer with a suitable band gap position like ZnO is an optimal solution.

This research is focused on investigating structural, optical and PEC properties of core-shell Si/TiO<sub>2</sub>/ZnO nanocomposites based on ordered silicon nanopillar arrays. A combination of NSL, MACE and successive ALD of TiO<sub>2</sub> and ZnO layers fabricated the Si/TiO<sub>2</sub>/ZnO nanocomposites. Structural properties of the obtained nanocomposite were investigated by means of SEM, TEM and GIXRD. The obtained data show high crystalline quality and conformity of the TiO<sub>2</sub>/ZnO shell. Optical properties were elucidated via diffuse reflectance and transmittance spectra acquisition. Electrochemical properties and stability of 1D Si/TiO<sub>2</sub>/ZnO nanocomposites were estimated through linear voltammetry, chronoamperometry and EIS. Performed studies have shown a superior PEC performance of 1D Si/TiO<sub>2</sub>/ZnO compared to 1D Si/TiO<sub>2</sub> and Si/ZnO core-shell nanocomposites owing to efficient separation of photoinduced charge carriers in TiO<sub>2</sub>/ZnO shell. Additionally, favorable energy bands bending facilitate holes transfer to the electrolyte interface and electrons injection into the silicon core. Also, the model of charge transfer through heterojunctions in Si/TiO<sub>2</sub>/ZnO is proposed and discussed according to collected EIS data. An effect of annealing on the 1D Si/TiO<sub>2</sub>/ZnO nanocomposite has been discussed. Despite the lower IPCE in comparison to its competitor materials, the 1D Si/TiO<sub>2</sub>/ZnO clearly shows an effect of protective shell engineering on the PEC performance of silicon photoanode.

In this research, the Author has performed the synthesis of silicon nanopillar arrays and assisted in ALD of TiO<sub>2</sub>/ZnO layers. He contributed to the acquisition and processing of data from SEM/TEM, GIXRD and optical spectroscopies as well as made calculations of nanocrystallite sizes, band gap values and photoconversion efficiency characteristics. He prepared all figures and significantly contributed to writing all parts of the paper. Also, he contributed to developing the model of charge carriers transport in 1D core-shell Si/TiO<sub>2</sub>/ZnO nanocomposites and performed simulations of EIS spectra to prove the proposed model.

**Number of Ministerial points: 140**

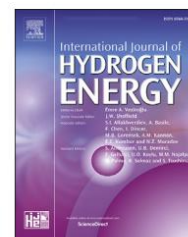
**Impact factor: 7.2**



ELSEVIER

Available online at [www.sciencedirect.com](http://www.sciencedirect.com)

ScienceDirect

journal homepage: [www.elsevier.com/locate/he](http://www.elsevier.com/locate/he)

## Enhanced solar-driven water splitting of 1D core-shell Si/TiO<sub>2</sub>/ZnO nanopillars

Mykola Pavlenko <sup>a</sup>, Katarzyna Siuzdak <sup>b</sup>, Emerson Coy <sup>a</sup>, Karol Załęski <sup>a</sup>,  
Mariusz Jancelewicz <sup>a</sup>, Igor Iatsunskiy <sup>a,\*</sup>

<sup>a</sup> NanoBioMedical Centre, Adam Mickiewicz University, 3 Wszechnicy Piastowskiej Str., 61-614, Poznan, Poland

<sup>b</sup> Centre of Laser and Plasma Engineering, The Szewalski Institute of Fluid-Flow Machinery, Fiszerza 14 Str., 80-231 Gdansk, Poland

### HIGHLIGHTS

- 1D core-shell Si/TiO<sub>2</sub>/ZnO nanopillars for PEC performance have been produced.
- Si/TiO<sub>2</sub>/ZnO photoanodes exhibit enhanced photoactivity for water splitting.
- The influence of Si–TiO<sub>2</sub>–ZnO interfaces onto the PEC efficiency was shown.
- The mechanisms of PEC water splitting processes in Si/TiO<sub>2</sub>/ZnO were proposed.

### ARTICLE INFO

#### Article history:

Received 12 June 2019

Received in revised form

13 November 2019

Accepted 25 November 2019

Available online 25 December 2019

#### Keywords:

Photocatalytic water-splitting

Silicon nanopillars

TiO<sub>2</sub>/ZnO nanocomposites

Atomic layer deposition

Core-shell nanostructures

One-dimensional nanostructures

### ABSTRACT

In this work, 1D core-shell Si/metal oxide nanopillar (NP) photoanodes were synthesized for enhanced solar-driven water splitting processes. The core-shell structures were fabricated by atomic layer deposition of different metal oxides (TiO<sub>2</sub> and ZnO) onto Si NP, which were synthesized by metal-assisted chemical etching and nanosphere lithography. In order to characterize produced photoanodes various experimental techniques (SEM/TEM, XRD, Transmittance, Reflectance, Raman spectroscopy) were applied. Photoelectrochemical (PEC) water oxidation of produced photoanodes was studied. It was shown that composition of n-Si/TiO<sub>2</sub>/ZnO NP exhibited enhanced photocurrents due to barrier effects. The enhanced PEC properties of core-shell Si/TiO<sub>2</sub>/ZnO NP are caused by efficient charge separation of photogenerated electron-hole pairs in the TiO<sub>2</sub>/ZnO shell and effective holes transfer to the shell-electrolyte interface. The superior photoelectrochemical performance of a photoanode based on core-shell Si/TiO<sub>2</sub>/ZnO NP has been confirmed through electrochemical impedance spectroscopy and voltamperometric measurements under electrode irradiation. 1D core-shell Si/TiO<sub>2</sub>/ZnO NP offer a new approach for preparing stable and highly efficient photoanodes for PEC water-splitting process.

© 2019 Hydrogen Energy Publications LLC. Published by Elsevier Ltd. All rights reserved.

\* Corresponding author.

E-mail addresses: [yatsunskiy@gmail.com](mailto:yatsunskiy@gmail.com), [igoyat@amu.edu.pl](mailto:igoyat@amu.edu.pl) (I. Iatsunskiy).

<https://doi.org/10.1016/j.ijhydene.2019.11.231>

0360-3199/© 2019 Hydrogen Energy Publications LLC. Published by Elsevier Ltd. All rights reserved.

## Introduction

Photocatalytic water-splitting process is a sustainable and efficient method for production of renewable energy sources such as hydrogen and oxygen with no reliance on usage of fossil fuels. A commercial application of photocatalytic water-splitting process is a way to solve the problem of carbon dioxide emission [1–3]. During the last decade significant efforts have been focused on investigation on solar water-splitting process [4–7] and development of cost-effective photoelectrodes for oxygen evolution reaction (OER) as well the hydrogen evolution reaction (HER). Among a large amount of different investigated materials and composites [8,9] suitable for efficient water-splitting process, the transition metal oxides represent a promising choice for development of efficient photoelectrodes which are sustainable against corrosion and photodegradation [10–13].

Among all transition metal oxides, ZnO and TiO<sub>2</sub> still attract much interest for water-splitting application because of facile synthesis, low cost, high abundance and non-toxicity for the environment [14,15]. The light absorbance of these materials has been successfully enhanced by means of significant increasing the specific surface area via synthesis of one-dimensional (1D) nanostructures such as nanorods and nanowires [16–20]. The resulted 1D nanostructures have shown promising results in the application of water-splitting process in UV range [16–18]. In addition, the photoelectrochemical (PEC) efficiency of ZnO and TiO<sub>2</sub> can be enhanced via the fabrication of TiO<sub>2</sub>/ZnO heterostructure [21] that effectively separates the photogenerated electron-hole pairs and overcomes the individual deficiencies of each material. Unfortunately, the aforementioned 1D nanostructures cannot achieve high PEC efficiency in visible range because of wide band gap about 3.2 eV. Thus, only 5% of solar spectrum (UV range) utilized effectively.

An effective utilization of the visible part of the solar spectrum can be achieved by the application of photoactive semiconductors with low band gap energy, such as silicon (Si), for example [22]. In our previous works we have successfully fabricated and showed the substantial photocatalytic activity as well as the stability of the Si/TiO<sub>2</sub> core-shell nanopillars (NP) under water-splitting conditions [23,24]. Kulmas et al. have demonstrated a novel Si/TiO<sub>2</sub>/ZnO photoanode based on porous silicon (PSi) substrate and showed its improved charge carriers separation during the OER [25]. However, nanocomposites based on PSi/TiO<sub>2</sub>/ZnO possess low specific surface area in comparison with 1D nanostructures. Besides, the vertically aligned crystalline-amorphous ZnO/TiO<sub>2</sub> core-shell nanowires have shown high photocurrent density due to the synergistic effect of the crystalline-amorphous core-shell heterostructures and the influence of 1D structuration [26]. We have assumed that combination of SiNP with a metal heterostructures based on TiO<sub>2</sub>/ZnO should facilitate the charge carrier separation of photogenerated electrons and holes because of barrier effects, and as a consequence increase the PEC efficiency.

Taking into account the latest studies of TiO<sub>2</sub>/ZnO heterostructures and the superior role of 1D nanoarchitecture in the development of photoanodes [27,28] we have fabricated

vertically aligned Si nanopillars (SiNP) with TiO<sub>2</sub>/ZnO shell. The metal-assisted chemical etching (MACE) has been used for the fabrication and the control of the morphology of vertically aligned and evenly distributed SiNP. In order to obtain a conformal layer of metal oxides, the atomic layer deposition technique (ALD) has been used.

In the present study we report on PEC properties of 1D core-shell SiNP/TiO<sub>2</sub>/ZnO nanostructures applied for OER. The integration of Si, TiO<sub>2</sub> and ZnO into 1D core-shell nanostructure enables the overcoming of individual shortcomings of each material such as high recombination rate and low stability in aqueous electrolytic solutions. In the proposed design of a photoanode the SiNP arrays effectively protected from photocorrosion by TiO<sub>2</sub>/ZnO shell. Besides, it sustains the separation of electron-hole pairs and the transfer of photogenerated holes to the electrolyte. Moreover, the coupling of high-band gap energy metal oxides with low-band gap energy Si enables an effective utilization of visible solar spectrum that increases the efficiency of proposed photoanodes.

## Materials and methods

### Core-shell SiNP/TiO<sub>2</sub>/ZnO fabrication

The SiNP arrays were fabricated by MACE [29,30] and polystyrene nanosphere lithography, as described in our previous research [23]. The deposition of TiO<sub>2</sub> and ZnO layers were realized in Picosun ALD reactor. Three sets of samples were produced: SiNP/TiO<sub>2</sub> (200 ALD cycles), SiNP/ZnO (50 ALD cycles), and SiNP/TiO<sub>2</sub> (100 ALD cycles)/ZnO (25 ALD cycles). The growth rates were typically 0.45 Å/cycle for TiO<sub>2</sub> and 2.1 Å/cycle for ZnO, respectively. These numbers of ALD cycles correspond to 5 nm layer for each metal oxide on planar surface for double-layered shell and 10 nm for single-layered shell. Such thin layers of metal oxides were chosen in order to implement the conformal coverage of SiNP as was described in Ref. [25]. The titanium tetrachloride (TiCl<sub>4</sub>) and water were used as precursors for ALD deposition of TiO<sub>2</sub> [12]. The diethylzinc ((C<sub>2</sub>H<sub>5</sub>)<sub>2</sub>Zn) and water were used as precursors for ALD deposition of ZnO [31]. After every cycle the ALD chamber was purged by intense flow of N<sub>2</sub> in order to remove the byproducts. After ALD deposition some samples were annealed at 450 °C for an hour in ambient atmosphere.

### Characterization

Structural properties of samples were analyzed by scanning electron microscope (SEM) JEOL JSM – 7001F and transmission electron microscope (TEM) JEOL ARM 200F. Lamellas for TEM analysis were prepared by focused ion beam (FIB) system JEOL JIB-4000 by the method described in our previous research [23,32]. The GIXRD measurements were performed by Xpert3 MRD (XL) from PANalytical, working with a Cu K $\alpha$  radiation source (wavelength of 1.54 Å) and operating at 45 kV and 40 mA.

Optical properties of TiO<sub>2</sub>, ZnO and TiO<sub>2</sub>/ZnO ALD layers deposited on FTO substrate have been studied with UV–vis spectrophotometer lambda 950 UV/VIS/NIR range

300–1100 nm, 1 nm step. The diffuse reflectance measurements of SiNP/TiO<sub>2</sub>, SiNP/ZnO and SiNP/TiO<sub>2</sub>/ZnO nanocomposites were performed by Ocean Optics QE PRO spectrometer combined with integrating sphere.

### Photoelectrochemical (PEC) measurements

A typical three-electrode cell was used for characterization of fabricated nanocomposites. Characterization of working electrode was performed using the potentostat-galvanostat system AutoLabPGStat 302 N in a standard three-electrode assembly at room temperature. The platinum gauze was used as counter electrode and the Ag/AgCl/0.1 M KCl as reference electrode.

The 0.5 M K<sub>2</sub>SO<sub>4</sub> electrolyte solution was preliminary deaerated with Ar for 40 min before measurements and the constant solution flow of Ar above the electrolyte was kept during all measurements. The electrochemical cell equipped with a quartz window.

The samples were irradiated with a 150 W Xenon lamp (Oriol LS0500) equipped with an AM 1.5 filter allowing to obtain simulated solar light. The irradiance of incident light was calibrated to 100 mW/cm<sup>2</sup> using reference cell (Si solar cell, Rera). The electrochemical impedance spectroscopy (EIS) was measured in the dark and under illumination conditions in frequency range of 0.1 Hz–20 kHz at amplitude of 10 mV. The chronoamperometry measurements were performed under chopped illumination with 20 s period under polarization conditions +0.5 and +1.0 V vs. Ag/AgCl/0.1 M KCl (results are shown in SI).

The photoconversion efficiency (applied bias photon-to-current conversion efficiency (ABPE)) of the fabricated nanocomposites is defined as:

$$\eta = \frac{j(E_{\text{H}_2\text{O}}^0 - E_{\text{RHE}})}{I_p} \times 100\%$$

where  $j$  is the measured photocurrent density,  $I_p$  - power of incident simulated solar light, which is equal to 100 mW/cm<sup>2</sup>,  $E_{\text{H}_2\text{O}}^0$  is a water-splitting potential of 1.23 V,  $E_{\text{RHE}}$  is the measured potential of PCE cell recalculated vs. reversible hydrogen electrode through the Nernst equation:

$$E_{\text{RHE}} = E_{\text{Ag/AgCl}} + E_{\text{Ag/AgCl}}^0 + 0.059 \text{ pH},$$

where  $E_{\text{Ag/AgCl}}$  is the external potential measured against the Ag/AgCl reference electrode,  $E_{\text{Ag/AgCl}}^0$  is the standard electrode potential of Ag/AgCl electrode, equals 0.1976 V.

## Results and discussion

### Structural, chemical and optical characterization of 1D SiNP/TiO<sub>2</sub>/ZnO core-shell nanostructure

In order to study the structure and morphology of SiNP/TiO<sub>2</sub>, SiNP/ZnO, and SiNP/TiO<sub>2</sub>/ZnO SEM and TEM characterization were performed. The SiNP array fabricated by MACE is depicted in Fig. 1a. The fabricated SiNP arrays demonstrate good alignments and distribution over the whole surface of the sample. The average length of SiNP is about 1.5 μm (Fig. S1)

and the lateral size (diameter) lies in the range of 400–450 nm. The conformal layers of TiO<sub>2</sub> and/or ZnO are formed after ALD process. The resulted core-shell SiNP/TiO<sub>2</sub>/ZnO nanostructure is shown in Fig. 1b.

In order to elucidate the chemical composition of prepared core-shell nanostructures the EDX analysis was performed. The EDX mapping (Fig. 1c) of the cross-section of single-stand SiNP covered with TiO<sub>2</sub> and ZnO layers shows a considerable difference in the distribution of chemical elements over the pillar. Fig. 1c demonstrates that ALD TiO<sub>2</sub> penetrates into the bulk of SiNP because of the porous morphology of the initial Si pillar (Fig. 2b). Thus, we may conclude that Si and TiO<sub>2</sub> form the core of this structure. On the other hand, ALD ZnO homogeneously covers the core, thus forming the core-shell structure of SiNP/TiO<sub>2</sub>/ZnO.

GIXRD spectra were acquired from the SiNP/TiO<sub>2</sub>, SiNP/ZnO and SiNP/TiO<sub>2</sub>/ZnO to investigate the crystalline phase before and after annealing (Fig. 1d). From the XRD pattern, it can be confirmed that ZnO is identified as wurzite phase according to the JCPDC #36–1451, for the diffraction peaks located at  $2\theta = 31.9^\circ$ ,  $34.1^\circ$ , and  $36.2^\circ$ , which are corresponding to the (100), (002), and (101) planes, respectively. The shape and intensity of these peaks remains almost the same after annealing. This result indicates the formation of polycrystalline phase of ZnO layer directly after ALD process. The as-prepared SiNP/TiO<sub>2</sub> and SiNP/TiO<sub>2</sub>/ZnO nanostructures show no peaks that might be ascribed to crystalline TiO<sub>2</sub>. It demonstrates that ALD TiO<sub>2</sub> is in amorphous or highly polycrystalline phase after the deposition and/or annealing. The anatase phase is detected only for annealed sample SiNP/TiO<sub>2</sub>(a) with an average thickness of titanium about 10 nm.

In order to elucidate the structural properties of produced samples, TEM and HRTEM studies have been performed. The mesoporous structure of SiNP was confirmed by TEM studies what is in a good agreement with our previous research [23,24]. Inclusions of TiO<sub>2</sub> phase in the mesopores are clearly seen in Fig. 2a. Fast Fourier Transform (FFT) analysis indicates the highly polycrystalline phase of (101) anatase. The HRTEM image of SiNP/ZnO nanostructure is shown in Fig. 2b. One may observe the polycrystalline ZnO structure that is consistent with the GIXRD measurements.

Since the optical properties of 1D core-shell nanostructures plays an important role in photocatalytic reactions we measured the diffuse reflectance and the optical transmittance for TiO<sub>2</sub>, ZnO, TiO<sub>2</sub>/ZnO layers on SiNP and FTO substrates, respectively. Fig. 3a shows the diffuse reflectance spectra acquired from SiNP, SiNP/TiO<sub>2</sub>, SiNP/ZnO and SiNP/TiO<sub>2</sub>/ZnO core-shell nanostructures. All samples show the same patterns of reflectance that are similar to SiNP and demonstrate low reflectance (less than 10%) in the visible range. The total reflectance for SiNP/TiO<sub>2</sub>, and SiNP/ZnO samples is slightly lower comparing to bare SiNP, which may indicate the increasing of absorbance and/or scattering. The lowest reflectance is observed for SiNP/TiO<sub>2</sub> core-shell nanostructures (less than 4% in the visible range). But it should be noted that the highest photocatalytic efficiency is not always ascribed to nanostructures with low reflectance (high absorbance) properties [33,34].



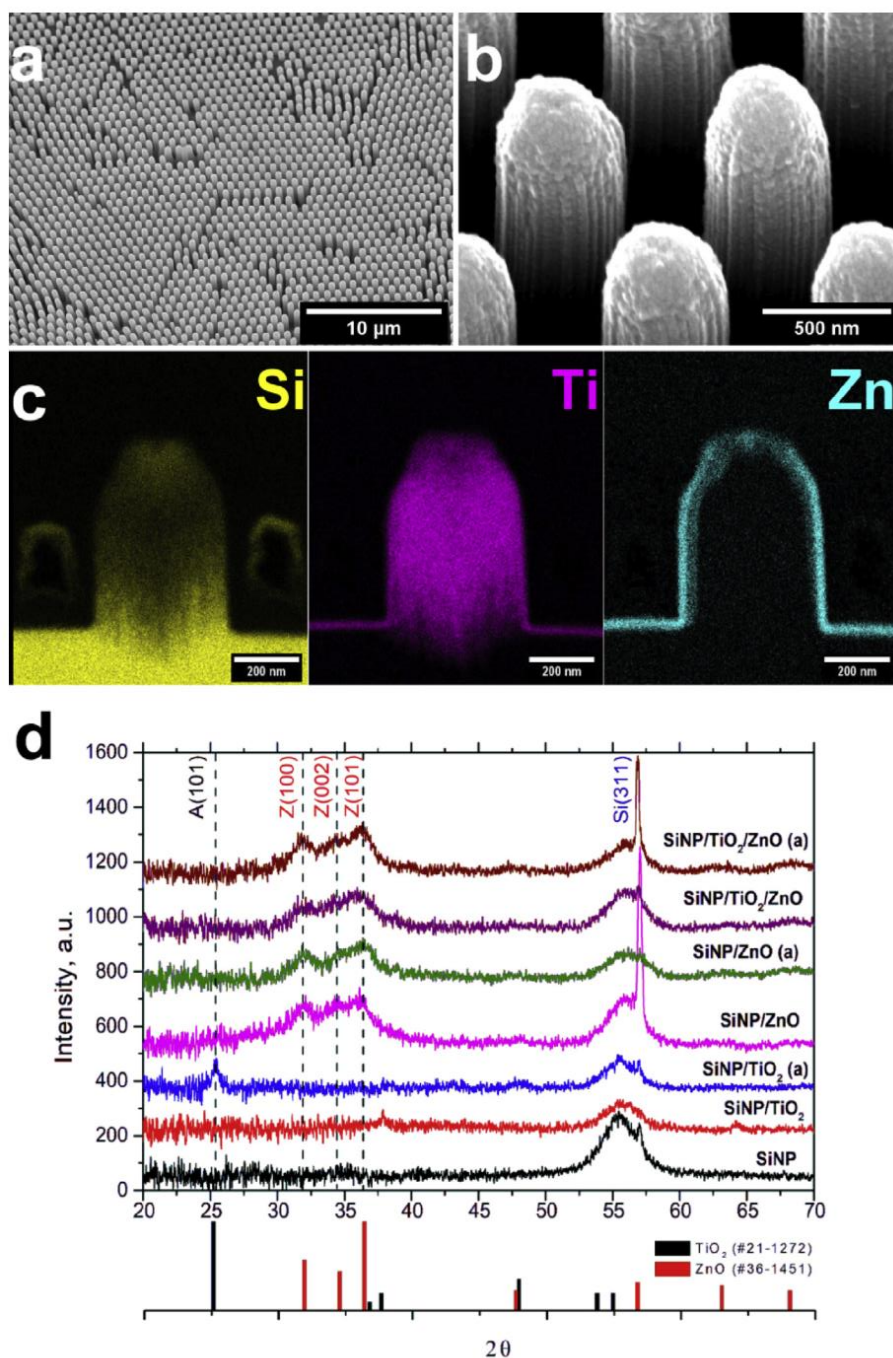


**Fig. 1** – (a) SEM image of SiNP array; (b) tilted SEM image of SiNP/TiO<sub>2</sub>/ZnO; (c) TEM EDX mapping of single-stand core-shell SiNP/TiO<sub>2</sub>/ZnO; (d) GIXRD spectra of as-prepared and annealed SiNP/TiO<sub>2</sub>, SiNP/ZnO and SiNP/TiO<sub>2</sub>/ZnO. The reference XRD spectra of TiO<sub>2</sub> anatase (JCPDS #21–1272) and ZnO wurtzite (JCPDC #36–1451) are represented below, the identified peaks marked as A (101) for anatase and Z (100), Z (002), Z (101) for wurtzite.

The TiO<sub>2</sub>, ZnO and TiO<sub>2</sub>/ZnO layers were also deposited on FTO substrates to investigate the optical properties of separate layers. Fig. 3b shows the transmittance spectra and Tauc plots for TiO<sub>2</sub> (10 nm), ZnO (10 nm) and TiO<sub>2</sub>/ZnO (5/5 nm). It is clearly seen that absorption edges of TiO<sub>2</sub>, ZnO and TiO<sub>2</sub>/ZnO are located in the UV range. Estimated values of band gap energies are about 3.76, 3.86 and 3.69 eV, respectively. High values of band gap energies might be explained by the

quantum confinement effect and mechanical strains accumulating at the interface of TiO<sub>2</sub>/ZnO. These results demonstrate that the coupling effect of TiO<sub>2</sub> and ZnO layers shifts the absorption edge, decreases the band gap energy and, as a consequence, enhances the optical absorption. Such effect improves the photocatalytic performance of TiO<sub>2</sub>/ZnO coupled layers and the OER efficiency of SiNP/TiO<sub>2</sub>/ZnO core-shell nanocomposites.

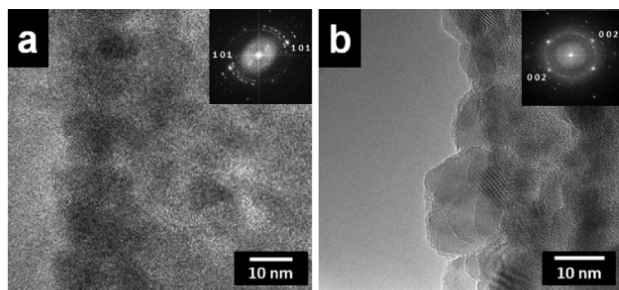


Fig. 2 – TEM images of: (a) HRTEM of SiNP/TiO<sub>2</sub>, (b) HRTEM of SiNP/ZnO. FFT patterns for SiNP/TiO<sub>2</sub> and SiNP/ZnO heterostructures are displayed in the insets.

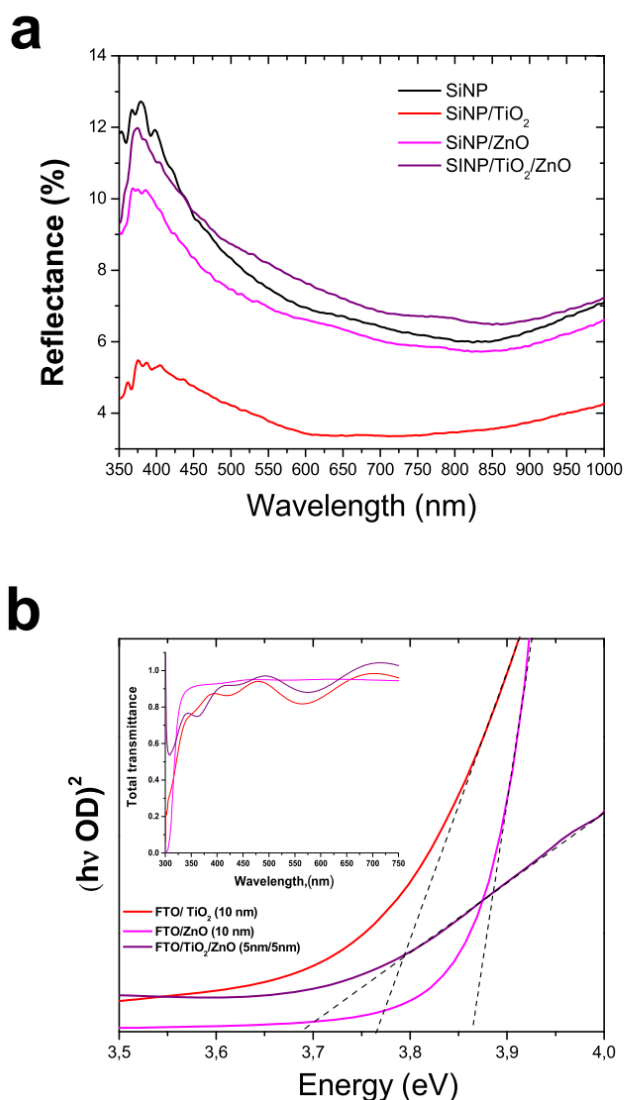
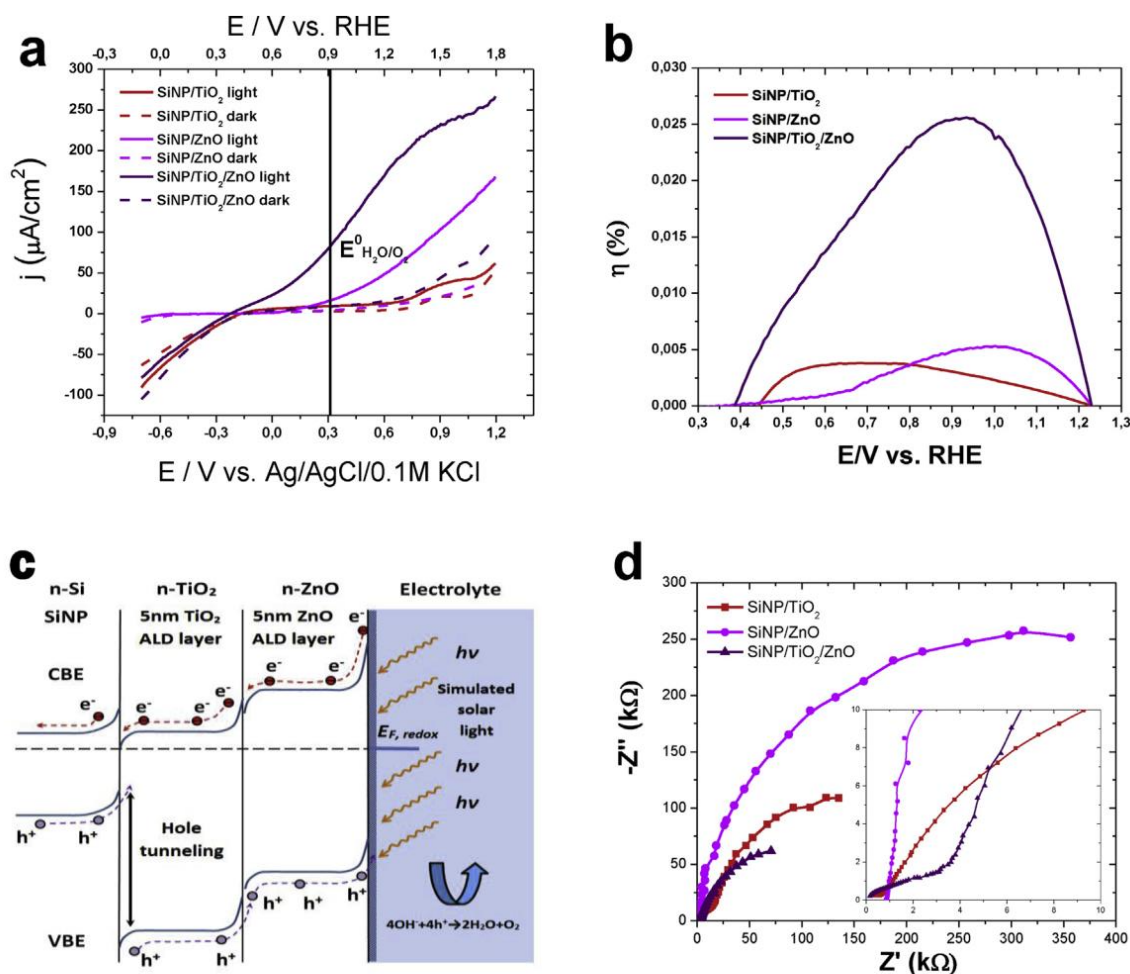


Fig. 3 – (a) Diffuse reflectance spectra of SiNP, SiNP/ZnO, SiNP/TiO<sub>2</sub> and SiNP/TiO<sub>2</sub>/ZnO heterostructures with 10 nm of TiO<sub>2</sub>, 10 nm of ZnO and 5 nm TiO<sub>2</sub>/5 nm ZnO ALD layers respectively. (b) Absorption edges of TiO<sub>2</sub>, ZnO and TiO<sub>2</sub>/ZnO ALD layers with different thickness of each layer. The resulted total transmittance is depicted in the inset.

### Photoelectrochemical performance of SiNP/TiO<sub>2</sub>/ZnO core-shell nanostructures

To investigate the PEC properties of SiNP/TiO<sub>2</sub>, SiNP/ZnO and SiNP/TiO<sub>2</sub>/ZnO core-shell nanostructures the linear voltamperometry (J-V) characteristics have been collected. The measured J-V curves of fabricated core-shell nanostructures are plotted in Fig. 4a. It is clearly seen the considerably higher photocurrent densities acquired from SiNP/TiO<sub>2</sub>/ZnO in the all range of applied potentials. It shows almost 60 times higher value of photocurrent density in comparison to SiNP/TiO<sub>2</sub> and 4 times higher than SiNP/ZnO at the water-splitting potential of 1.23 V vs. RHE (0.63 V vs. Ag/AgCl) marked as E<sup>0</sup>H<sub>2</sub>O. The calculated ABPE curves (Fig. 4b) indicate noticeable efficiency of as-prepared SiNP/TiO<sub>2</sub>/ZnO (max. 0.025%) in comparison to as-prepared SiNP/ZnO (max. 0.005%) and SiNP/TiO<sub>2</sub> (max. 0.0045%). The ABPE value for SiNP/TiO<sub>2</sub>/ZnO (0.025%) photoanode is definitely low comparing to high efficient PEC systems as Bi-NiFeO<sub>x</sub>/BiVO<sub>4</sub> (2.25%), NiOOH/FeOOH/BiVO<sub>4</sub> (1.75%), NiO/CoO<sub>x</sub>/BiVO<sub>4</sub> (1.5%), NiOOH/FeOOH/N-BiVO<sub>4</sub> (2.2%) [35]. However, it is compatible with other silicon photoanodes based on Co<sub>3</sub>O<sub>4</sub>/TiO<sub>2</sub>/Si nanorods (0.5%) [36], and Ni-Si (0.1%) [37]. It might be concluded that the charge separation and transfer in SiNP/TiO<sub>2</sub>/ZnO nanostructures occur much more efficiently than for SiNP/ZnO and SiNP/TiO<sub>2</sub>. The multi-interfaces between Si/TiO<sub>2</sub> and TiO<sub>2</sub>/ZnO reduce recombination significantly. This enhancement is attributed to the barrier effects in SiNP/TiO<sub>2</sub>/ZnO nanostructure and favorable band bending that facilitates the effective charge carrier separation, electrons towards the Si and holes to the ZnO-electrolyte interface. SiNP/TiO<sub>2</sub>/ZnO photoanodes have also demonstrated excellent photostability upon prolonged illumination (SI, Fig. S2).

The detailed charge transfer mechanism and the band diagram of electron-hole pairs transfer in SiNP/TiO<sub>2</sub>/ZnO core-shell nanostructure is depicted in Fig. 4c. Si/TiO<sub>2</sub>/ZnO nanostructures can be represented by heterostructures, which includes Si/TiO<sub>2</sub> and TiO<sub>2</sub>/ZnO interfaces. The absorbed light induces the formation of electron-hole pairs. The visible light passes through the transparent TiO<sub>2</sub>/ZnO shell and the electron-hole pairs are generating inside the near-surface of SiNP. Whereas, the UV light induces electron-hole generation in the TiO<sub>2</sub> and the ZnO shell. The photogenerated holes move toward the electrolyte and oxidize surface hydroxyl groups to O<sub>2</sub> follow the next half-reaction: 4OH<sup>-</sup> + 4 h<sup>+</sup> → 2H<sub>2</sub>O + O<sub>2</sub>↑. Due to presence of Schottky barrier between the photoanode and the electrolyte, photogenerated electrons (inside ZnO and TiO<sub>2</sub>) move to the Si. Despite the high energy barrier between Si and TiO<sub>2</sub>, holes can tunnel through the very thin TiO<sub>2</sub> layer and then move to the ZnO shell. In order to confirm our assumption about the tunnel mechanism of charge carrier transfer through TiO<sub>2</sub> we have measured EIS for Si/TiO<sub>2</sub>/ZnO samples with different thicknesses of TiO<sub>2</sub> 5, 10 and 15 nm, respectively (Table S1). EIS results indicate the gradual increasing of the interface resistivity with the TiO<sub>2</sub> thickness what prove the tunnel mechanism [38,39]. Besides, Gao et al. proposed an addition charge carrier (for holes) transfer mechanism based on the assumption that ALD TiO<sub>2</sub> nanolayer improve the quality of the heterogeneous interface and



**Fig. 4** – (a) The comparison of current densities versus applied potential of SiNP/TiO<sub>2</sub>, SiNP/ZnO and SiNP/TiO<sub>2</sub>/ZnO in the dark and under illumination. (b) Photoconversion efficiency (ABPE) vs. RHE. (c) Schematic band diagram of SiNP/TiO<sub>2</sub>/ZnO structure. (d) Nyquist plots of SiNP/TiO<sub>2</sub>, SiNP/ZnO and SiNP/TiO<sub>2</sub>/ZnO core-shell nanostructures. The inset figures show the enlarged high frequency region and an equivalent electrical circuit.

remove the SiO<sub>2</sub> [40]. As a consequence, holes transfer through the Si–TiO<sub>2</sub> interface resulting in the efficient injection and fast charge carrier separation. The potential barrier at the TiO<sub>2</sub>/ZnO heterojunction facilitates holes migration towards the ZnO/electrolyte interface that increasing the photoanodic current. Simultaneously, the photogenerated electrons overcome the potential barriers and move to the counter electrode (Pt mesh) where complete the circuit by taking part in the reduction reaction.

In order to characterize the charge carrier migration of photoanodes EIS were measured in 0.5 M K<sub>2</sub>SO<sub>4</sub> electrolyte solution under simulated solar light illumination. Fig. 4d shows Nyquist plots collected from SiNP/TiO<sub>2</sub>, SiNP/ZnO and SiNP/TiO<sub>2</sub>/ZnO core-shell nanostructures. It is well-known that diameters of EIS semicircles in high frequency region correspond to the charge transfer resistance at the photoanode interface. It is clearly seen that the SiNP/TiO<sub>2</sub>/ZnO photoanode exhibits depressed semicircles at high frequencies compared with the other photoanodes. This suggests a decrease in the SiNP/TiO<sub>2</sub>/ZnO heterojunction resistance and the charge transfer resistance across the ZnO/

electrolyte interface what confirms facilitate charge transfer to photoanode interface during the OER. The impedance value is relatively low in high frequencies range which indicates the high rate of holes transfer through the Si/TiO<sub>2</sub> interface. The obtained results show significant influence of TiO<sub>2</sub>/ZnO shell on PEC properties of SiNP arrays and its superior efficiency in comparison to single TiO<sub>2</sub> and ZnO layers.

## Conclusion

In summary, we have synthesized a photoanode based on 1D core-shell SiNP/TiO<sub>2</sub>/ZnO nanostructure by the combination of MACE and ALD techniques. The fabricated photoanode has been successfully applied for photocatalytic water-splitting process and shows superior performance in comparison to SiNP/TiO<sub>2</sub> and SiNP/ZnO heterostructures. GIXRD, EDX and HRTEM investigations have revealed penetration of TiO<sub>2</sub> in the mesoporous structure of SiNP during ALD process and formation of SiNP/TiO<sub>2</sub> nanocomposite. An additional deposition of ZnO layer leads to the formation of core-shell

nanostructure that enhances the PEC performance. We proposed a model that describes the charge carrier transport in 1D core-shell SiNP/TiO<sub>2</sub>/ZnO nanostructure and confirmed it through EIS. The ultrathin layers of TiO<sub>2</sub> and ZnO in the SiNP/TiO<sub>2</sub>/ZnO display the noticeable separation of photo induced charge carriers and stability. Obtained results demonstrate the superior performance of 1D core-shell SiNP/TiO<sub>2</sub>/ZnO nanostructures in photocatalytic water splitting processes.

### Author contributions

Synthesis of nanostructures, MACE and Lithography: M.P., I.I., HR-TEM and FIB experiments and Analysis: M.P., E.C., K.Z. I.I., ALD Experiments: M.P., M.J., I.I., Photoelectrochemical Experiments and Analysis: M.P., I.I., K. S., Original Idea: I.I., Project Supervision: I.I.

### Acknowledgments

M.P. acknowledges the financial support from the National Science Centre (NCN) of Poland by the PRELUDIUM 12 project UMO-2016/23/N/ST3/01356, the National Center for Research and Development (NCBR) by the project POWR.03.02.00–00–I032/16 and co-financial by the Governments of Czech Republic, Hungary, Poland and Slovakia through International Visegrad Fund Grant (application ID 51810284). I.I. also acknowledges the financial support from the NCN of Poland by the SONATA 11 project UMO-2016/21/D/ST3/00962. K.S. acknowledges the financial support from the National Science Centre (NCN) of Poland by the Sonata-BIS project 2017/26/E/ST5/0041.

### Appendix A. Supplementary data

Supplementary data to this article can be found online at <https://doi.org/10.1016/j.ijhydene.2019.11.231>.

### REFERENCES

- [1] Li R. Latest progress in hydrogen production from solar water splitting via photocatalysis, photoelectrochemical, and photovoltaic-photoelectrochemical solutions. *Chin J Catal* 2017;38:5–12.
- [2] Lin L, Yu Z, Wang X. Crystalline carbon nitride semiconductors for photocatalytic water splitting. *Angew Chem Int Ed* 2019;58:6164–75.
- [3] Joy J, Mathew J, George SC. Nanomaterials for photoelectrochemical water splitting – review. *Int J Hydrogen Energy* 2018;43:4804–17.
- [4] Alibabaei L, Sherman BD, Norris MR, Brennaman MK, Meyer TJ. Visible photoelectrochemical water splitting into H<sub>2</sub> and O<sub>2</sub> in a dye-sensitized photoelectrosynthesis cell. *Proc Natl Acad Sci USA* 2015;112:3–6.
- [5] Xin Li JX, Xin Li XC, Yu Jiaguo, Low Jingxiang, Fang Yueping. Engineering heterogeneous semiconductors for solar water splitting. *J Mater Chem A* 2015;3:2485–534.
- [6] Zhou H, Yu F, Sun J, He R, Chen S, Chu C-W, et al. Highly active catalyst derived from a 3D foam of Fe(PO<sub>3</sub>)<sub>2</sub>/Ni<sub>2</sub>P for extremely efficient water oxidation. *Proc Natl Acad Sci* 2017;114:5607–11.
- [7] Faraji M, Yousefi M, Yousefzadeh S, Zirak M, Naseri N, Jeon TH, et al. Two-dimensional materials in semiconductor photoelectrocatalytic systems for water splitting. *Energy Environ Sci* 2019;12:59–95.
- [8] Joy J, Mathew J, George SC. ScienceDirect Nanomaterials for photoelectrochemical water splitting e review. *Int J Hydrogen Energy* 2018;43:4804–17.
- [9] Guo L, Chen Y, Su J, Liu M, Liu Y. Obstacles of solar-powered photocatalytic water splitting for hydrogen production: a perspective from energy flow and mass flow. *Energy* 2019;172:1079–86.
- [10] Yang Y, Niu S, Han D, Liu T, Wang G, Li Y. Progress in developing metal oxide nanomaterials for photoelectrochemical water splitting. *Adv Energy Mater* 2017;7:1700555.
- [11] Song F, Bai L, Moysiadou A, Lee S, Hu C, Liardet L, et al. Transition metal oxides as electrocatalysts for the oxygen evolution reaction in alkaline Solutions: an application-inspired renaissance. *J Am Chem Soc* 2018;140:7748–59.
- [12] Kertmen A, Barbé E, Szkoda M, Siuzdak K, Babić V, Torruella P, et al. Photoelectrochemically active N-adsorbing ultrathin TiO<sub>2</sub> layers for water-splitting applications prepared by pyrolysis of oleic acid on iron oxide nanoparticle surfaces under nitrogen environment. *Adv Mater Interfaces* 2018:1801286.
- [13] Brytavskiy I, Hušeková K, Myndrul V, Pavlenko M, Coy E, Zaleski K, et al. Effect of porous silicon substrate on structural, mechanical and optical properties of MOCVD and ALD ruthenium oxide nanolayers. *Appl Surf Sci* 2019;471:686–93.
- [14] Zayed M, Ahmed AM, Shaban M. Synthesis and characterization of nanoporous ZnO and Pt/ZnO thin films for dye degradation and water splitting applications. *Int J Hydrogen Energy* 2019;44:17630–48.
- [15] Feng W, Lin L, Li H, Chi B, Pu J, Li J. Hydrogenated TiO<sub>2</sub>/ZnO heterojunction nanorod arrays with enhanced performance for photoelectrochemical water splitting. *Int J Hydrogen Energy* 2017;42:3938–46.
- [16] Wang M, Ren F, Zhou J, Cai G, Cai L, Hu Y, et al. N doping to ZnO nanorods for photoelectrochemical water splitting under visible light: engineered impurity distribution and terraced band structure. *Sci Rep* 2015;5:12925.
- [17] Yang X, Wolcott A, Wang G, Sobo A, Fitzmorris RC, Qian F, et al. Nitrogen-doped ZnO nanowire arrays for photoelectrochemical water splitting. *Nano Lett* 2009;9:2331–6.
- [18] Ansari SA, Khan MM, Ansari MO, Cho MH. Nitrogen-doped titanium dioxide (N-doped TiO<sub>2</sub>) for visible light photocatalysis. *New J Chem* 2016;40:3000–9.
- [19] Szkoda M, Trzcinski K, Nowak AP, Coy E, Wicikowski L, Łapiński M, et al. Titania nanotubes modified by a pyrolyzed metal-organic framework with zero valent iron centers as a photoanode with enhanced photoelectrochemical, photocatalytic activity and high capacitance. *Electrochim Acta* 2018;278:13–24.
- [20] Viter R, Savchuk M, Starodub N, Balevicius Z, Tumenas S, Ramanaviciene A, et al. Photoluminescence immunosensor based on bovine leukemia virus proteins immobilized on the ZnO nanorods. *Sens Actuators B Chem* 2019;285:601–6.
- [21] Ayan Sarkar KM, Singh Asutosh K, Khan Gobinda Gopal, Sarkar Debasish. TiO<sub>2</sub>/ZnO core/shell nano-heterostructure arrays as photo-electrodes with enhanced visible light photoelectrochemical performance. *RSC Adv* 2014;4:55629–34.

- [22] Dytrych P, Drinek V, Bumba J, Kastanek F, Solcova O. Silicon nanowires' based photoanode for hydrogen evolution. *Int J Hydrogen Energy* 2018;43:18136–41.
- [23] Pavlenko M, Coy EL, Jancelewicz M, Załęski K, Smytyna V, Jurga S, et al. Enhancement of optical and mechanical properties of Si nanopillars by ALD TiO<sub>2</sub> coating. *RSC Adv* 2016;6:97070–6.
- [24] Pavlenko M, Siuzdak K, Coy E, Jancelewicz M, Jurga S, Iatsunskiy I. ScienceDirect Silicon/TiO<sub>2</sub> core-shell nanopillar photoanodes for enhanced photoelectrochemical water oxidation. *Int J Hydrogen Energy* 2017;42:30076–85.
- [25] Kulmas M, Paterson L, Höflich K, Bashouti MY, Wu Y, Göbel M, et al. Composite nanostructures of TiO<sub>2</sub> and ZnO for water splitting application: atomic layer deposition growth and density Functional theory investigation. *Adv Funct Mater* 2016;26:4882–9.
- [26] Jeong K, Deshmukh PR, Park J, Sohn Y, Shin WG. ZnO-TiO<sub>2</sub> core-shell nanowires: a sustainable photoanode for enhanced photoelectrochemical water splitting. *ACS Sustain Chem Eng* 2018;6:6518–26.
- [27] Kment S, Riboni F, Pausova S, Wang L, Wang L, Han H, et al. Photoanodes based on TiO<sub>2</sub> and  $\alpha$ -Fe<sub>2</sub>O<sub>3</sub> for solar water splitting – superior role of 1D nanoarchitectures and of combined heterostructures. *Chem Soc Rev* 2017;46:3716–69.
- [28] Yan L, Zhao W, Liu Z. 1D ZnO/BiVO<sub>4</sub> heterojunction photoanodes for efficient photoelectrochemical water splitting. *Dalton Trans* 2016;45:11346–52.
- [29] Han H, Huang Z, Lee W. Metal-assisted chemical etching of silicon and nanotechnology applications. *Nano Today* 2014;9:271–304.
- [30] Huang Z, Geyer N, Werner P, De Boor J, Gösele U. Metal-assisted chemical etching of silicon: a review. *Adv Mater Deerp Beach Fla* 2011;23:285–308.
- [31] Graniel O, Fedorenko V, Viter R, Iatsunskiy I, Nowaczyk G, Weber M, et al. Optical properties of ZnO deposited by atomic layer deposition (ALD) on Si nanowires. *Mater Sci Eng B* 2018;236–237:139–46.
- [32] Iatsunskiy I, Baitimirova M, Coy E, Yate L, Viter R, Ramanavicius A, et al. Influence of ZnO/graphene nanolaminate periodicity on their structural and mechanical properties. *J Mater Sci Technol* 2018;34:1487–93.
- [33] Huang S, Yu Y, Yan Y, Yuan J, Yin S, Cao Y. Enhanced photocatalytic activity of TiO<sub>2</sub> activated by doping Zr and modifying Pd. *RSC Adv* 2016;6:29950–7.
- [34] Babu SG, Vinoth R, Praveen Kumar D, Shankar MV, Chou H-L, Vinodgopal K, et al. Influence of electron storing, transferring and shuttling assets of reduced graphene oxide at the interfacial copper doped TiO<sub>2</sub> p–n heterojunction for increased hydrogen production. *Nanoscale* 2015;7:7849–57.
- [35] Ye K-H, Li H, Huang D, Xiao S, Qiu W, Li M, et al. Enhancing photoelectrochemical water splitting by combining work function tuning and heterojunction engineering. *Nat Commun* 2019;10:3687.
- [36] Tang R, Zhou S, Yuan Z, Yin L. Metal-Organic framework derived Co<sub>3</sub>O<sub>4</sub>/TiO<sub>2</sub>/Si heterostructured nanorod array photoanodes for efficient photoelectrochemical water oxidation. *Adv Funct Mater* 2017;27:1701102.
- [37] Oh K, Mériadec C, Lassalle-Kaiser B, Dorcet V, Fabre B, Ababou-Girard S, et al. Elucidating the performance and unexpected stability of partially coated water-splitting silicon photoanodes. *Energy Environ Sci* 2018;11:2590–9.
- [38] Didden A, Hillebrand P, Dam B, van de Krol R. Photocorrosion mechanism of TiO<sub>2</sub>-coated photoanodes. *Int J Photoenergy* 2015;2015:1–8.
- [39] Ghobadi A, Ulusoy TG, Garifullin R, Guler MO, Okyay AK. A heterojunction design of single layer hole tunneling ZnO passivation wrapping around TiO<sub>2</sub> Nanowires for superior photocatalytic performance. *Sci Rep* 2016;6:30587.
- [40] Gao L, Li Q, Chen H, Hayase S, Ma T. In situ fabrication of nanoepitaxial TiO<sub>2</sub> protection layer on Si substrate: hole chemical conduction instead of tunneling effect. *Sol RRL* 2017;1:1700064.

## Chapter 4 Papers, not included in the main research

### 4.1. Porous silicon-zinc oxide nanocomposites prepared by atomic layer deposition for biophotonic applications

The capabilities of PSi can be extended to applications for biosensor development. In order to obtain a highly responsive optical biosensor, the PSi matrix can be used for the fabrication of a nanocomposite with the proper PL properties. Since the ZnO-derived nanostructures have shown excellent biocompatibility and a strong PL response, the PSi/ZnO nanocomposite is an obvious choice for optical biosensor testing.

This research shows studies of structural and optical properties of PSi/ZnO nanocomposites produced by a combination of MACE and ALD techniques. The structural properties were investigated using SEM, TEM, GIXRD, EDX and XPS, whereas data for estimation of the optical properties were collected by diffuse reflectance and PL spectroscopies. A thorough XPS analysis shows the structure of the ZnO layer and its binding with the mesoporous Si matrix. Key mechanisms of PL excitation in PSi/ZnO have been defined and discussed. Additionally, the fabricated PSi/ZnO nanocomposite has been tested for biophotonic application. Aflatoxin B1 was successfully applied as a target for biosensing at the surface of PSi/ZnO and detected even at a concentration of 1 ng/ml via changes in the visible part of the PL spectrum. Also, it was shown that PSi/ZnO nanocomposite produced from p-type Si substrate is more favorable for biophotonic application than n-type Si.

In this research, the Author performed MACE on p-type and n-type silicon substrates and assisted in ALD of the ZnO layer. He processed SEM, TEM, EDX and diffuse reflectance data. He made all necessary calculations related to estimating ZnO nanocrystallite sizes from TEM and GIXRD data. He also made calculations in the context of the Kubelka-Munk model for diffuse reflectance data. He has prepared all figures except Figure 5 and significantly contributed to writing all parts of the paper except the discussion of AFB1 toxin detection.

**Number of Ministerial points: 140**

**Impact factor: 3.4**



Article

# Porous Silicon-Zinc Oxide Nanocomposites Prepared by Atomic Layer Deposition for Biophotonic Applications

Mykola Pavlenko <sup>1</sup>, Valerii Myndrul <sup>1</sup>, Gloria Gottardi <sup>2</sup>, Emerson Coy <sup>1</sup>, Mariusz Jancelewicz <sup>1</sup> and Igor Iatsunskiy <sup>1,\*</sup>

<sup>1</sup> NanoBioMedical Centre, Adam Mickiewicz University, Wszechnicy Piastowskiej 3, 61-614 Poznan, Poland; mykpav@amu.edu.pl (M.P.); valmyn@amu.edu.pl (V.M.); coyeme@amu.edu.pl (E.C.); marjan7@amu.edu.pl (M.J.)

<sup>2</sup> Fondazione Bruno Kessler, Center for Materials and Microsystems IRST, Via Sommarive 18, 38123 Trento, Italy; ggottard@fbk.eu

\* Correspondence: yatsunskiy@gmail.com or igoyat@amu.edu.pl; Tel.: +48-731-308-173

Received: 27 March 2020; Accepted: 22 April 2020; Published: 24 April 2020

**Abstract:** In the current research, a porous silicon/zinc oxide (PSi/ZnO) nanocomposite produced by a combination of metal-assisted chemical etching (MACE) and atomic layer deposition (ALD) methods is presented. The applicability of the composite for biophotonics (optical biosensing) was investigated. To characterize the structural and optical properties of the produced PSi/ZnO nanocomposites, several studies were performed: scanning and transmission electron microscopy (SEM/TEM), X-ray diffraction (XRD), X-ray photoelectron spectroscopy (XPS), diffuse reflectance, and photoluminescence (PL). It was found that the ALD ZnO layer fully covers the PSi, and it possesses a polycrystalline wurtzite structure. The effect of the number of ALD cycles and the type of Si doping on the optical properties of nanocomposites was determined. PL measurements showed a “shoulder-shape” emission in the visible range. The mechanisms of the observed PL were discussed. It was demonstrated that the improved PL performance of the PSi/ZnO nanocomposites could be used for implementation in optical biosensor applications. Furthermore, the produced PSi/ZnO nanocomposite was tested for optical/PL biosensing towards mycotoxins (Aflatoxin B1) detection, confirming the applicability of the nanocomposites.

**Keywords:** porous silicon; zinc oxide; atomic layer deposition; biosensors; photoluminescence

## 1. Introduction

It is well known that porous silicon (PSi), due to its high surface-to-volume ratio and superior photoluminescence (PL) properties, is an attractive material for optical (bio)sensing applications [1,2]. However, the instability of PSi properties in solutions due to the degradation process needs to be solved in order to obtain a stable response and repeatable results [3]. There are numerous approaches able to reduce the degradation; among them, the deposition of metal oxide onto the PSi is considered to be the most promising one [4–8]. Zinc oxide (ZnO) is one of the possible candidates that could be combined with PSi because of its excellent optical properties (e.g., stable PL signal in the wide optical range), and which may be used in biophotonic applications, particularly biosensors [9–11].

Nanocomposites based on PSi/ZnO have attracted more and more attention over the years [12–16]. The underlying reasons behind their popularity are attributed to the synergistic effects on physical and, particularly, optical properties of the PSi/ZnO, which are derived from the combination of individual features of both semiconductors [17–22]. The improved catalytic activity, high charge carrier mobility and relatively high biocompatibility make the PSi/ZnO nanocomposite a perfect material for a reliable long-term multipurpose (bio)sensor [23–26]. Moreover, the outstanding

## **4.2. Effect of porous silicon substrate on structural, mechanical and optical properties of MOCVD and ALD ruthenium oxide nanolayers**

A lot of diverse methods and techniques are used for the fabrication of complex nanocomposites for a variety of applications. MOCVD and ALD are prominent contemporary methods, and the resulting nanocomposites' pros and cons are important to analyze. Owing to its structural properties, especially high specific area, the PSi is an appropriate material for studying the features of MOCVD and ALD for nanocomposite fabrication. Since metal oxides and their combinations with silicon are substantial in producing electronic and optoelectronic devices, the deposition method's influence on the deposited layer's quality is crucial. As one of the commonly used materials for deposition, RuO<sub>2</sub> was used in the current research to test its layer's behavior after deposition using both PSi substrate techniques.

This research focuses on elucidating the structural and optical properties of RuO<sub>2</sub> thin films deposited by MOCVD and ALD on n-type porous silicon substrates. Investigations by SEM, TEM, XRD, EDX and XPS were applied to define the morphology, crystalline structure and composition of the RuO<sub>2</sub> layer depending on the deposition method. Optical properties were determined by Raman spectroscopy, diffuse reflectance and PL evaluation. Its structural features tailor the mechanical and optical properties of the PSi/RuO<sub>2</sub> nanocomposite, so the influence of the mechanical stress induced by the deposition of the RuO<sub>2</sub> layer has been investigated and discussed. It was shown that MOCVD gives non-uniform distribution along the pores, while ALD allows the formation of a conformal RuO<sub>2</sub> layer. The changes in crystallite size and deformation values are correlated with differences in the optical properties of MOCVD and ALD-produced layers.

In this research, the Author has synthesized n-type PSi substrates by MACE. He has processed SEM, TEM and GIXRD data as well as prepared Figures 1, 2 and 3. He has assisted in the acquisition and processing of diffuse reflectance data. He performed calculations of nanocrystallite sizes and relative deformations in PSi/RuO<sub>2</sub> nanostructures by Debye – Scherrer and Williamson – Hall methods. Also, he contributed to the writing of the paper in the discussion of “Morphology and structural properties”.

**Number of Ministerial points: 140**

**Impact factor: 6.7**

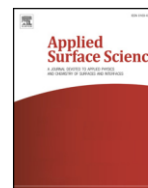




ELSEVIER

Contents lists available at ScienceDirect

Applied Surface Science

journal homepage: [www.elsevier.com/locate/apsusc](http://www.elsevier.com/locate/apsusc)

Full Length Article

## Effect of porous silicon substrate on structural, mechanical and optical properties of MOCVD and ALD ruthenium oxide nanolayers

Ievgen Brytavskiy<sup>a</sup>, Kristína Hušeková<sup>b</sup>, Valerii Myndrul<sup>c</sup>, Mykola Pavlenko<sup>c</sup>, Emerson Coy<sup>c</sup>, Karol Zaleski<sup>c</sup>, Dagmar Gregušová<sup>b</sup>, Luis Yate<sup>d</sup>, Valentyn Smyntyna<sup>a</sup>, Igor Iatsunskiy<sup>c,\*</sup>

<sup>a</sup> Odessa I.I. Mechnikov National University, 2, Dvoryanskaya Str., Odessa 65082, Ukraine

<sup>b</sup> Institute of Electrical Engineering Slovak Academy of Sciences, Dúbravská cesta 9, 841 04 Bratislava, Slovakia

<sup>c</sup> NanoBioMedical Centre, Adam Mickiewicz University, 85 Umultowska Str., 61-614 Poznań, Poland

<sup>d</sup> Surface Analysis and Fabrication Platform, CIC biomaGUNE, Paseo Miramón 182, 20009 Donostia-San Sebastián, Spain



## ARTICLE INFO

## Keywords:

Porous silicon  
Ruthenium oxide  
ALD  
MOCVD

## ABSTRACT

Ruthenium oxide (RuO<sub>2</sub>) has received significant attention in recent years for its photocatalytic properties and photoelectrochemical (PEC) performance. In the present research, RuO<sub>2</sub> nanolayers were grown on n-type porous silicon (PSi) by metal organic chemical vapor deposition (MOCVD) and atomic layer deposition (ALD). The morphology, mechanical and optical properties of produced nanostructures were studied by means of scanning electron microscopy (SEM), transmission electron microscopy (TEM), energy dispersive X-ray spectroscopy (EDX), X-ray diffraction (XRD), X-ray photoelectron spectroscopy (XPS), micro-Raman spectroscopy, diffuse reflectance and photoluminescence (PL) spectroscopy. It was shown that MOCVD gives non-uniform distribution of RuO<sub>2</sub> along the pore and it is deposited mainly in the near-surface of PSi, while distribution of ruthenium obtained by ALD looks conformal over the entire pore. The mean size of RuO<sub>2</sub> nanocrystallites and mechanical stresses were determined by TEM, XRD and Raman spectroscopy. It was demonstrated that samples obtained by ALD demonstrate a good crystallinity, while crystalline phase for samples produced by MOCVD improve with RuO<sub>2</sub> layer thickness increasing. It was established the formation of hydrated RuO<sub>2</sub> during ALD and MOCVD. It was shown that the samples produced by MOCVD have slightly higher electrical conductivity than ALD samples. The average value of energy gap ( $E_g$ ) for samples prepared by MOCVD depended on the number of injections. RuO<sub>2</sub> nanolayers quenched intrinsic PL from the PSi matrix. The correlation between structural, optical, and mechanical properties of samples produced by MOCVD and ALD was discussed.

## 1. Introduction

Porous silicon (PSi) – metal oxide (MOx) nanostructures and nanocomposites have a great potential in various applications, such as in photocatalysis [1,2], (bio)sensors [3,4], Li-ion batteries [5], etc. It is possible to tailor physical properties of nanocomposites by coupling PSi with different MOx (e.g. TiO<sub>2</sub>, ZnO, Al<sub>2</sub>O<sub>3</sub> etc.) [6]. In our previous works, we have shown that some optical parameters, as band gap energy ( $E_g$ ), refractive index ( $n$ ) and extinction coefficient ( $k$ ) could be tuned by varying the thickness of TiO<sub>2</sub> in nanocomposites based on TiO<sub>2</sub>/PSi [7], and TiO<sub>2</sub>/Si nanopillars [8,9]. This is critically important for development of novel nanocomposites which could be used as effective photoelectrodes in photoelectrochemical (PEC) water splitting or optical sensors [8–10]. Therefore, the improvement of PEC properties of PSi-MOx nanocomposites, which can be achieved by choosing

the appropriate MOx, is an important research topic.

Ruthenium oxide (RuO<sub>2</sub>) with a rutile phase has received significant attention in recent years for its photocatalytic properties and PEC performance [11–13]. It was shown that incorporation of RuO<sub>2</sub> on NaTaO<sub>3</sub> films allowed to achieve a maximum photoelectrochemical hydrogen production of 15.7 mmol h<sup>-1</sup> g<sup>-1</sup> with a solar-to-hydrogen (STH) conversion efficiency of 4.29% because of enhanced PEC activity of RuO<sub>2</sub> in the visible region [14]. Authors demonstrated the good photoconversion properties of RuO<sub>2</sub> and it seems that combination of RuO<sub>2</sub> with highly porous materials as PSi enables to develop high-quality material for solar water splitting. Thus, a nanocomposite based on the combination of PSi substrate with RuO<sub>2</sub> seems to be prospective photocatalytic material and requires a systematic investigation of its structural, optical and electrical properties.

Many deposition techniques have been used to fabricate RuO<sub>2</sub> films

\* Corresponding author.

E-mail address: [igoyat@amu.edu.pl](mailto:igoyat@amu.edu.pl) (I. Iatsunskiy).

<https://doi.org/10.1016/j.apsusc.2018.12.022>

Received 31 July 2018; Received in revised form 21 November 2018; Accepted 3 December 2018

Available online 04 December 2018

0169-4332/ © 2018 Elsevier B.V. All rights reserved.

### 4.3. One and two-phonon Raman scattering from nanostructured silicon

Nanosilicon or nanostructured silicon is a promising material with a wide range of applications, especially in optoelectronics and sensors. Therefore, it is important to investigate possible options for modifying its electronic and optical properties. The employment of phonon confinement effects in finite nanocrystallites opens up a lot of possibilities in this regard. One of the effective methods for the estimation of those effects is Raman-scattering. Thus, a comprehensive investigation of the first and second order of Raman-scattering provides valuable information on the vibrational modes in the nanosilicon.

This research is focused on thoroughly investigating Raman-scattering at nanostructured silicon with different morphology. The structural properties of MACE-produced nanosilicon samples were investigated by SEM and AFM methods. Obtained data show a substantial difference in the morphology of p-type nanosilicon depending on doping level and etchant concentration in the MACE process.

A typical Raman spectroscopy data acquisition technique was applied to the nanosilicon samples and showed noticeable differences depending on morphology and mechanical stress in the porous silicon matrix. Also, the influence of the heating effect induced by laser radiation on the Raman spectra has been discussed. The correspondence of the obtained results to the phonon confinement model has been analyzed and discussed. Additionally, the Raman spectrum was reconstructed, taking into account confinement effects and compressive stress and was compared to experimentally obtained data.

The second-order Raman scattering was also analyzed and discussed. It was found that the pattern of the Raman spectra of porous silicon is affected by the wavelength of excitation light. This effect was also thoroughly discussed, and a possible explanation was provided.

In this research, the Author contributed to the fabrication of porous silicon nanostructures with various morphology by the MACE method. He contributed to processing SEM/AFM data, discussing the obtained results and evaluating the final manuscript.

**Number of Ministerial points: 40**

**Impact factor: 3.1**



## One and two-phonon Raman scattering from nanostructured silicon



Igor Iatsunskiy<sup>a,b,\*</sup>, Grzegorz Nowaczyk<sup>b</sup>, Stefan Jurga<sup>b</sup>, Victoriia Fedorenko<sup>a</sup>, Mykola Pavlenko<sup>a</sup>, Valentyn Smytyna<sup>a</sup>

<sup>a</sup> Department of Experimental Physics, Odessa I.I. Mechnikov National University, Str. Pastera 42, 65023 Odessa, Ukraine

<sup>b</sup> NanoBioMedical Center, Adam Mickiewicz University in Poznan, Umultowska 85, PL 61614 Poznań, Poland

### ARTICLE INFO

#### Article history:

Received 9 April 2014

Accepted 21 May 2015

#### Keywords:

Nanostructured silicon

Raman scattering

Metal-assisted chemical etching

### ABSTRACT

Raman scattering from highly/low resistive nanostructured silicon films prepared by metal-assisted chemical etching was investigated. Raman spectrum of obtained silicon nanostructures was measured. Interpretation of observed one and two-phonon Raman peaks are presented. First-order Raman peak has a redshift and broadening. This phenomenon is analyzed in the framework of the phonon confinement model taking into account mechanical stress effects. Second-order Raman peaks were found to be shifted and broadened in comparison to those in the bulk silicon. The peak shift and broadening of two-phonon Raman scattering relates to phonon confinement and disorder. A broad Raman peak between 900 and 1100  $\text{cm}^{-1}$  corresponds to superposition of three transverse optical phonons  $\sim 2\text{TO}(X)$ ,  $2\text{TO}(W)$  and  $2\text{TO}(L)$ . Influence of excitation wavelength on intensity redistribution of two-phonon Raman scattering components ( $2\text{TO}$ ) is demonstrated and preliminary theoretical explanation of this observation is presented.

© 2015 Elsevier GmbH. All rights reserved.

### 1. Introduction

Nanostructured silicon is presently of widespread interest because Si is an extremely promising material not only for electronics but optoelectronics, solar cells, sensors etc. Raman scattering has become a standard tool to study the silicon and nanostructured silicon for many years [1–24]. Raman-scattering studies of nanomaterials give us information about energy dispersion, structure, bonding and disorder. The analysis of nanostructures is mainly based on the phonon confinement model in which the finite crystallite size is taken into account by weighting the phonon-scattering efficiency [4–24]. Confinement effects in nanostructures lead to modifications of the electronic, optical and vibrational properties. Unfortunately, if a first-order Raman spectrum of nanocrystalline silicon has been studied extensively, the second-order Raman scattering is investigated marginally [4,9,10].

In the second-order Raman scattering process, two phonons of equal and opposite momentum participate and produce either line or broad continuous spectrum. Zone edge phonons, which appear only in higher-order Raman scattering, correspond to large wave

vectors and are sensitive to short-range disorder. The nature of a material, such as crystalline or amorphous, can therefore be ascertained by analyzing the higher-order phonons as well. Study of second-order Raman scattering, in addition to first-order spectra, provides important information on the vibrational modes, energy structure, and morphology of nanostructured materials. Besides, second-order Raman scattering exhibits a higher sensitivity to nanoparticles size than first-order scattering [10].

In this paper we present the one- and two-phonon Raman spectra of nanostructured silicon fabricated by metal-assisted chemical etching. We have measured the Raman frequency shifts and line shapes at room temperature. We focused on the changes in the second-order Raman scattering. New effect dealing with second-order Raman scattering was found.

### 2. Experimental procedure

#### 2.1. Nanostructured silicon fabrication

The nanostructured silicon samples were fabricated using a metal-assisted chemical etching process (MACE) [25–27]. The MACE exhibits good process controllability to generate various nanostructured silicon surface morphologies. Similar to electrochemical etching to create porous silicon, MACE acts as a localized electrochemical etching process in which local electrodeless etching occurs at the metal/silicon interface, each nanometer-sized

\* Corresponding author at: NanoBioMedical Centre, Adam Mickiewicz University, 85 Umultowska str., 61-614, Poznan, Poland. Tel.: +48 73 13081 73.

E-mail addresses: [yatsunskiy@gmail.com](mailto:yatsunskiy@gmail.com) (I. Iatsunskiy), [cnbmadm@amu.edu.pl](mailto:cnbmadm@amu.edu.pl) (G. Nowaczyk).

#### **4.4. Structural and XPS studies of PSi/TiO<sub>2</sub> nanocomposites prepared by ALD and Ag-assisted chemical etching**

Introducing TiO<sub>2</sub> into the PSi matrix allows the nanocomposite formation with a wide range of possible applications. ALD technique is a promising technology for this purpose, enabling the growth of conformal TiO<sub>2</sub> coating of PSi. Since the interaction of Si and TiO<sub>2</sub> significantly influences the optical and chemical properties of the PSi/TiO<sub>2</sub> nanocomposite, it is essential to investigate the phase structure, morphology and other structural properties of the Si – TiO<sub>2</sub> interface.

This research focuses on studying the electronic and structural properties of PSi/TiO<sub>2</sub> nanocomposite fabricated by combining MACE and ALD techniques. Methods of SEM, TEM, EDX, Raman spectroscopy and XPS were implemented to elucidate the structural, optical and electronic properties of PSi/TiO<sub>2</sub>. The formation of the TiO<sub>2</sub> anatase phase in the PSi matrix after the application of ALD has been confirmed via Raman spectroscopy and discussed in the context of nanocomposite structure. The chemical composition has been analyzed via XPS spectra acquisition. The elemental ratio of chemical components has been estimated, and Auger parameters for PSi and PSi/TiO<sub>2</sub> have been obtained. Additionally, the analysis of the collected XPS core spectra enabled the determination of Si atom states in the nanocomposite and the behavior of Ti bonds depending on the number of ALD cycles. The chemical bonds of Ti and Si with O and H were also ascertained. Further analysis of collected valence band spectra showed the influence of defect states in PSi/TiO<sub>2</sub> nanocomposite, especially the influence of Ti<sup>3+</sup> surface states on the electronic properties of the nanocomposite had been discussed. The obtained results on modifying the electronic structure of PSi/TiO<sub>2</sub> nanocomposite are essential in developing related photocatalytic materials.

In this research, the Author contributed to the fabrication of porous silicon substrate by MACE, discussing the obtained results and manuscript evaluation.

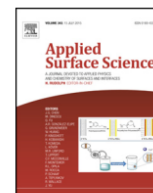
**Number of Ministerial points: 140**

**Impact factor: 6.7**



Contents lists available at ScienceDirect

Applied Surface Science

journal homepage: [www.elsevier.com/locate/apsusc](http://www.elsevier.com/locate/apsusc)

## Structural and XPS studies of PSi/TiO<sub>2</sub> nanocomposites prepared by ALD and Ag-assisted chemical etching



Igor Iatsunskiy<sup>a,\*</sup>, Mateusz Kempniński<sup>a,b</sup>, Grzegorz Nowaczyk<sup>a</sup>, Mariusz Jancelewicz<sup>a</sup>, Mykola Pavlenko<sup>c</sup>, Karol Załęski<sup>a</sup>, Stefan Jurga<sup>a,d</sup>

<sup>a</sup> NanoBioMedical Centre, Adam Mickiewicz University, 85 Umultowska Str., 61-614 Poznan, Poland

<sup>b</sup> Faculty of Physics, Adam Mickiewicz University, Umultowska 85, 61-614, Poland

<sup>c</sup> Department of Experimental Physics, Odessa National I.I. Mechnikov University, 42, Pastera Str., 65023 Odessa, Ukraine

<sup>d</sup> Department of Macromolecular Physics, Adam Mickiewicz University, Umultowska 85, 61-614 Poznan, Poland

### ARTICLE INFO

#### Article history:

Received 9 March 2015

Received in revised form 23 April 2015

Accepted 23 April 2015

Available online 2 May 2015

#### Keywords:

Atomic layer deposition

XPS

Porous silicon

Dioxide titanium

Nanocomposites

### ABSTRACT

PSi/TiO<sub>2</sub> nanocomposites fabricated by atomic layer deposition (ALD) and metal-assisted chemical etching (MACE) were investigated. The morphology and phase structure of PSi/TiO<sub>2</sub> nanocomposites were studied by means of scanning electron microscopy (SEM), transmission electron microscopy (TEM) with an energy dispersive X-ray spectroscopy (EDX) and Raman spectroscopy. The mean size of TiO<sub>2</sub> nanocrystals was determined by TEM and Raman spectroscopy. X-ray photoelectron spectroscopy (XPS) was used to analyze the chemical elemental composition by observing the behavior of the Ti 2p, O 1s and Si 2p lines. TEM, Raman spectroscopy and XPS binding energy analysis confirmed the formation of TiO<sub>2</sub> anatase phase inside the PSi matrix. The XPS valence band analysis was performed in order to investigate the modification of PSi/TiO<sub>2</sub> nanocomposites electronic structure. Surface defects states of Ti<sup>3+</sup> at PSi/TiO<sub>2</sub> nanocomposites were identified by analyzing of XPS valence band spectra.

© 2015 Elsevier B.V. All rights reserved.

### 1. Introduction

Nanocomposites based on silicon nanostructures and metal oxides (MOx) have drawn increased attention in different applications, such as in sensors and biosensors [1–5], catalysis [6–8], photovoltaics [9,10], electronics [11,12] and optics [13–15]. Among different metal oxides, TiO<sub>2</sub> is one of the most important materials. This material is used in many applications: photocatalysts [7,8], solar cell electrodes [16,17], and modern electronic optical devices [18]. Recent interest has been paid by researchers to the nano-scale TiO<sub>2</sub>, which has highly active surface area and demonstrates new properties, induced by quantum-size effects [19,20]. On the other hand, porous silicon (PSi) structures have unique physical properties such as the biocompatibility, the large surface area, flexibility in tuning the structural parameters and finally its compatibility with the modern IC (integrated circuit) industry. Nanocomposites based on PSi and TiO<sub>2</sub> benefit from the unique properties of both components for development and improvement of various optical and

electronic devices. PSi/TiO<sub>2</sub> nanocomposites also show improved photocatalytic efficiency due to the enhanced separation of excited electrons and holes. In this regard, the structure and electronic properties study of PSi/TiO<sub>2</sub> nanocomposites have gained increasing attention in the last years.

Here we report the first, to our knowledge, study of the structural and electronic properties of PSi/TiO<sub>2</sub> nanocomposites obtained by atomic layer deposition (ALD) and metal-assisted chemical etching (MACE). Titanium dioxide nanocrystals were introduced inside the PSi matrix to fabricate PSi/TiO<sub>2</sub> nanocomposites. For this purpose we used ALD. ALD is a deposition process for highly uniform and conformal thin films. Due to chemical reactions in the ALD process, very conformal and thickness controlled films can be grown over large areas even inside the PSi [12,21]. The surface morphology and phase structure of PSi/TiO<sub>2</sub> nanocomposites were detected by scanning electron microscopy (SEM), transmission electron microscopy (TEM) with an EDX analyzer, Raman spectroscopy and X-ray photoelectron spectroscopy (XPS). The results obtained are very promising for the improved use of PSi/TiO<sub>2</sub> nanocomposites in photocatalysts, photovoltaic and sensor application where it is important to tune their physical properties by the morphology of PSi/TiO<sub>2</sub>.

\* Corresponding author. Tel.: +48 731308173.  
E-mail address: [yatsunskiy@gmail.com](mailto:yatsunskiy@gmail.com) (I. Iatsunskiy).

## Chapter 5 Summary

### 5.1. Outline of research presented in this thesis

The photocatalytic water-splitting process has been a topic of intensive research in recent years. Many published studies on diverse single materials and complex nanocomposites exploit many contemporary techniques and methods, paving a pathway to developing an effective PEC cell. Since silicon is an abundant, widely used, and feasible processing material, the effective PEC cell on its base should significantly bolster hydrogen's economic development and make affordable commercially available devices for solar hydrogen generation. Considering the collected results and progress in the concept of PEC cell development, it is possible to realize the appealing idea of effectively utilizing a silicon-based photoelectrode for photocatalytic water-splitting. On the other hand, silicon material possesses some drawbacks, such as severe degradation in harsh aqueous solutions and recombination of charge carriers on defect sites. It also has many issues with proper operation parameters under solar light irradiation, such as an appropriate level and type of doping, electrolyte's pH value, effective specific area utility, the feasibility of heterojunction formation, etc. These drawbacks of silicon as a photocatalytic material open up several problems to be solved for its effective utilization for photocatalytic applications. Using a protective coating of a chemically stable material with proper conductive properties, such as transition metal oxide, substantially extends the usability of nanosilicon in PEC applications. In addition, studies on nanosilicon-based nanocomposites and investigation of silicon-derived heterojunctions boost the finding of solutions for concomitant problems in photonics, microelectronics, (bio)sensors design, etc.

Considering the aforementioned above, the main aim of this thesis was to investigate PSi-based nanocomposites with transition metal oxides as a nanostructured material for the photocatalytic application and to acquire knowledge regarding the employment of quantum confinement effects in such nanomaterial for applying in photocatalytic water-splitting at the visible part of solar light. In order to achieve this aim and find answers to the questions tackled in this thesis, the research results conducted in collaboration with other co-investigators are presented.

The articles presented in this thesis expound on structural, optical and PEC properties of PSi and PSi/MO<sub>x</sub> (TiO<sub>2</sub> and ZnO) nanocomposites. Although PSi is a widely studied

material, the investigation of quantum confinement effects in it and tuning the optical properties throughout the structural changes are still challenging. Additionally, the fabrication of multilayer nanocomposite structures based on PSi with preliminary defined features is not a trivial task. It requires a thorough study of the correlation of structural changes with optical features and the influence of the fabrication process on the resulting nanocomposite material. In this regard, implementing more effective methods, such as MACE and ALD, for nanocomposite fabrication requires thorough analysis and investigation.

The background of this thesis is presented in Chapters 1 and 2, where preceding theoretical and experimental results from literature sources are reviewed. Chapter 1 shows the primary approach and recent progress in designing and developing single materials and nanocomposite structures for photocatalytic water-splitting applications. Chapter 2 describes the fabrication methods and strategies of silicon application with various transition metal oxides in photocatalysis and water splitting. Chapter 3 presents the main research topics to answer the questions of this thesis.

Section 3.1. contains the statements of authorship and co-authorship. In section 3.2. a study on the structural and optical properties of PSi/TiO<sub>2</sub> nanocomposite is demonstrated. The changes in the structural properties of the ALD-grown TiO<sub>2</sub> layer on mesoporous MACE-derived Si substrate correlate with the changes in optical properties of the PSi/TiO<sub>2</sub> nanocomposite. Sheer changes in the Raman spectra as well as in refractive index and extinction coefficient, corroborate the influence of variation in TiO<sub>2</sub> anatase nanocrystallites size and the PSi pores size on tuning the PSi/TiO<sub>2</sub> properties through the quantum confinement effect. The influence of defect sites on charge carriers separation in PSi/TiO<sub>2</sub> is elucidated through PL mechanisms. The obtained results confirm the favorability of the chosen fabrication methods and the fabricated PSi/TiO<sub>2</sub> nanocomposite for photoanode engineering.

In section 3.3. is shown a study addressed further improving the optical properties of PSi/TiO<sub>2</sub> nanocomposite through 1D pillar-like patterning. The mechanical stability of the fabricated pillar-like structure was investigated as well. It was shown that TiO<sub>2</sub> anatase inclusions could improve the mechanical properties of 1D PSi/TiO<sub>2</sub> nanopillars and substantially depend on their crystallinity. An enhancement of crystallinity of the anatase phase in PSi material was acquired via annealing and corroborated by the results of  $\mu$ -Raman spectroscopy. The obtained results clearly demonstrate the influence of the quantum confinement effect on the optical properties of PSi/TiO<sub>2</sub> nanocomposite. Thus, these two studies answer to the first question tackled in this thesis.

In section 3.4. the 1D core-shell PSi/TiO<sub>2</sub> nanocomposite was investigated as a photoanode for the photocatalytic water-splitting process. Owing to the increased specific area due to the mesoporous nature of PSi and the fast separation of the photogenerated charge carriers at the Si-TiO<sub>2</sub> heterojunction, it displays an effective PEC response under photoanode operation. It was experimentally demonstrated that the charge carriers separation occurs more effectively at the n-PSi/n-TiO<sub>2</sub> heterojunction, while the p-PSi/n-TiO<sub>2</sub> heterojunction impedes the photo-induced charge transfer in the nanocomposite's bulk material. Due to an effective light trapping in 1D nanostructure and favorable positions of the energy bands, the PSi/TiO<sub>2</sub> nanocomposite gains sufficient photocurrent density (about 1.5 mA/cm<sup>2</sup>) along with relatively stable behavior under various pH in the electrolyte solution. Therefore, the obtained results allow the Author to answer the second question tackled in the thesis.

In section 3.5. is provided a study on the employment of SPR in the Pd-nanoparticles to enhance the properties of 1D PSi/TiO<sub>2</sub> nanocomposite. The ALD-synthesized Pd nanoparticles form Schottky nanojunctions within the 1D arrayed core-shell PSi/TiO<sub>2</sub> nanopillars, which leads to the enhancement of mechanical, optical and PEC properties. The conducted nanoindentation test shows that adding Pd nanoparticles into the PSi/TiO<sub>2</sub> structure results in superior mechanical properties. Crystallization of the TiO<sub>2</sub> anatase phase inside the PSi material provides enhanced mechanical resilience compared to bare PSi. After adding Pd nanoparticles, the stability to the plastic deformation increases further, owing to the pile-up effect. Acquired data of diffuse reflectance and absorbance indicate a significant influence of introduced Pd nanoparticles as absorption increment in UV and VIS regions as well as significantly decreased reflection in the visible region for PSi/TiO<sub>2</sub>/Pd nanocomposite. Linear voltammetry measurements demonstrate a noticeable negative photocurrent branch corresponding to HER induced by Pd nanoparticles as its photocatalytic activity toward H<sub>2</sub> production. Although the presence of Pd results in a lower photocurrent than for the PSi/TiO<sub>2</sub> and effects in shielding the photoactive centers, the chronoamperometry results show a stable behavior and good response of the PSi/TiO<sub>2</sub>/Pd photoanode. Additionally, PSi/TiO<sub>2</sub>/Pd nanocomposite shows a noticeable enhancement in photodegradation experiments owing to enhanced absorption in UV and IR regions. This enhancement can be explained by a synergistic effect between charge carriers and hot electrons transfer along the heterojunction interfaces in the PSi/TiO<sub>2</sub>/Pd nanocomposite. Considering all the obtained results, a model of charge carriers transport was developed and explained, considering enhanced light absorbance and the impact of SPR. These results provide an answer to the third question of the thesis.



In section 3.6. is demonstrated a study on the structural, optical and PEC properties of 1D arrayed core-shell P*Si*/TiO<sub>2</sub>/ZnO nanocomposite. This study was conducted to investigate the charge carriers separation in 1D core-shell P*Si*/TiO<sub>2</sub>/ZnO nanostructure and to estimate its performance in the photocatalytic water-splitting process. A conformal ALD-derived layer of ZnO represents the external “shell”, while the “core” is composed of P*Si*/TiO<sub>2</sub> nanocomposite due to TiO<sub>2</sub> diffusion inward the porous Si material. Analysis of structural and optical properties of the fabricated nanocomposites shows an advantage of TiO<sub>2</sub>/ZnO coupled layer compared to single TiO<sub>2</sub> and ZnO layers of the same thickness. Superior absorbance and band gap tuning capability in the TiO<sub>2</sub>/ZnO coupled layer depend on the mechanical strains at the TiO<sub>2</sub>-ZnO interface and quantum confinement effect, and could be tuned via the thickness and crystallinity of the comprised layers. The TiO<sub>2</sub>/ZnO shell has demonstrated noticeably higher PEC performance than the single TiO<sub>2</sub> anatase and ZnO wurtzite layers on silicon-based nanopillar arrays. A high crystallinity of the fabricated nanocomposite results in low recombination and effective separation of photoinduced charge carriers in the TiO<sub>2</sub>/ZnO shell. As a result, 1D core-shell P*Si*/TiO<sub>2</sub>/ZnO nanocomposite demonstrates a significantly higher photocurrent density, stability and ABPE characteristics. The separation and transfer of electron-hole pairs in the P*Si*/TiO<sub>2</sub>/ZnO nanocomposite were described in the context of the heterostructure model considering the obtained results of EIS, barrier and tunneling effects. Thus, this research provides an answer to the fourth question prompted in the thesis.

Chapter 4 contains four articles that are not related to the main topics of this thesis but include the Author’s contribution. In section 4.1. is provided a study on the employment of P*Si*/ZnO nanocomposite as a platform for biosensing applications. There was discussed the optical and structural properties of the nanocomposite and its impact on the optical biosensing response toward mycotoxins. In section 4.2. is demonstrated a study on the advantages of the ALD technique compared to the MOCVD technique for depositing a metal oxide layer on the P*Si* substrate. Structural, optical and mechanical properties of P*Si*/RuO<sub>2</sub> nanocomposite were investigated and discussed in the context of metal oxide proliferation along the micro/mesopores and nanocomposite formation. The study in section 4.3. is dedicated to Raman scattering in P*Si*. There is provided a comprehensive investigation on Raman spectroscopy data analysis for P*Si* substrate. And section 4.4. contains an investigation of P*Si*/TiO<sub>2</sub> nanocomposite. The results of XPS studies are shown and discussed structural properties of P*Si*/TiO<sub>2</sub> nanocomposite and the impact of MACE parameters.

In summary, the Author has demonstrated through a set of consistent research that the optical properties of P*Si*/TiO<sub>2</sub>, P*Si*/ZnO and P*Si*/TiO<sub>2</sub>/ZnO nanocomposites can be tuned by

their structural properties. Namely, it could be realized by 1D patterning, improving crystalline quality, pore size and the thickness of the metal oxide layer. The tuning of optical and structural features in the nanocomposites can be gained by changing the parameters of MACE (for PSi) and ALD (for TiO<sub>2</sub> and ZnO layers) technological processes. This thesis demonstrates that PSi with a protective coating of metal oxide can be used for photocatalytic applications, particularly water-splitting. The results of studies represented in Chapter 3 collectively show the positive impact of quantum confinement effect on the charge separation inward PSi/MO<sub>x</sub> nanocomposite and hindering the recombination rate. Although the PEC performance of the fabricated 1D core-shell PSi/TiO<sub>2</sub>/ZnO nanomaterial is significantly lower compared to competitive materials, it is possible to increase the efficiency further via the employment of the SPR effect and to enhance the charge separation in multilayer shell made of transition metal oxides. The results of this thesis enable the development of a strategy for employing silicon-based materials for photocatalytic applications and reveal the capability of noticeable enhancement of its PEC performance through nanostructuralization.

### 5.2. Future prospects

Using the nanosilicon-metal oxide nanocomposites for photocatalytic applications requires a thorough study of the behavior of electron-hole pairs depending on barrier, tunnel, SPR, and heat effects. Therefore, there are a lot of ways to implement further research.

The results of this thesis demonstrate a promising approach to plasmonic nanoparticles application in enhancing the core-shell PSi/TiO<sub>2</sub> photoanode efficiency. Incorporating Pd or Au nanoparticles into TiO<sub>2</sub>/ZnO or a more complex shell on 1D nanosilicon could further enhance the charge separation and synergistic effect. Additionally, the mechanical properties of such a complex nanocomposite structure and their dependence on morphological features are quite interesting to study.

The impact of doping concentration on charge carriers mobility in PSi-based core-shell nanocomposites is also an essential topic for investigation. A proper doping concentration in the Si core and in the external metal oxide shell could decrease the recombination on defect sites and increase the overall IPCE yield. Although the PSi/TiO<sub>2</sub>/ZnO nanocomposite presented in this thesis is not a competitive material for efficient use, it could gain a promising result in combination with another material in the Z-scheme PEC cell.

The mechanisms of heat transfer and detailed behavior of photoinduced electron-hole pairs in P*Si*/TiO<sub>2</sub>/Pd nanocomposite are still to be elucidated. The already acquired related data are incomplete, and a more detailed study and model development are needed.

Last but not least is the elucidation of ALD parameters for growing conformal low-defect metal oxide thin films on the P*Si* substrates with variable porosity. Although the ALD technique allows for gaining a highly conformal thin film coating, the influence of internal mechanical strains in the porous substrate and subsequent annealing could significantly interfere with the structure of the ALD-deposited layer. Therefore, an analysis of various adverse effects on the ALD-grown transition metal oxide thin film is required.

## Grants and scholarships

1. ERASMUS MUNDUS Eminence II scholarship for scientific project mobility to NanoBioMedical Centre at Adam Mickiewicz University from 16.07.2015 to 14.07.2016 and from 22.08.2016 to 10.06.2017.
2. PRELUDIUM 12 project (2016/23/N/ST3/01356) "Novel nanocomposites based on nanosilicon/metal oxide ( $\text{TiO}_2$ ,  $\text{ZnO}$ ) for efficient hydrogen production by photoelectrochemical water splitting"
3. Collaboration in Sonata 11 project (2016/21/D/ST3/00962) "Investigation of biophotonical and electrical properties for novel nanocomposites based on porous silicon - zinc oxide"
4. Visegrad Scholarship for the project "Novel heterostructures based on metal oxide and graphene materials for efficient water-splitting and hydrogen production" (scholarship individual number 51810284)
5. Collaboration in the project HORIZON 2020 (RISE-2017) "Novel 1D photonic metal oxide nanostructures for early stage cancer detection"
6. Polish National Center for Research and Development / European funds, Environmental interdisciplinary PhD studies program in nanotechnology POWR.03.02.00-00-I032/16 "Środowiskowe interdyscyplinarne studia doktoranckie w zakresie nanotechnologii"

## Author publication list

1. *Tailoring the Structural, Optical, and Photoluminescence Properties of Porous Silicon/TiO<sub>2</sub> Nanostructures*  
Igor Iatsunskyi, **Mykola Pavlenko**, Roman Viter, Mariusz Jancelewicz, Grzegorz Nowaczyk, Ieva Baleviciute, Karol Załęski, Stefan Jurga, Arunas Ramanavicius, Valentyn Smyntyna  
The Journal of Physical Chemistry C: 119, 13, 7164-7171, 2015  
[doi.org/10.1021/acs.jpcc.5b01670](https://doi.org/10.1021/acs.jpcc.5b01670)
2. *One and two-phonon Raman scattering from nanostructured silicon*  
Igor Iatsunskyi, Grzegorz Nowaczyk, Stefan Jurga , Victoriia Fedorenko, **Mykola Pavlenko**, Valentyn Smyntyna  
Optik: 126, 1650 – 1655, 2015  
[doi.org/10.1016/j.ijleo.2015.05.088](https://doi.org/10.1016/j.ijleo.2015.05.088)
3. *Structural and XPS studies of PSi/TiO<sub>2</sub> nanocomposites prepared by ALD and Ag-assisted chemical etching*  
Igor Iatsunskyi, Mateusz Kempinski, Grzegorz Nowaczyk, Mariusz Jancelewicz, **Mykola Pavlenko**, Karol Załęski, Stefan Jurga  
Applied Surface Science: 347 , 777–783, 2015  
[dx.doi.org/10.1016/j.apsusc.2015.04.172](https://dx.doi.org/10.1016/j.apsusc.2015.04.172)
4. *Enhancement of optical and mechanical properties of Si nanopillars by ALD TiO<sub>2</sub> coating*  
**Mykola Pavlenko**, Emerson L. Coy, Mariusz Jancelewicz, Karol Załęski, Valentyn Smyntyna, Stefan Jurga, Igor Iatsunskyi  
The Royal Society of Chemistry (RSC Advances): 6, 99, 97070-97076, 2016  
[doi.org/10.1039/c6ra21742g](https://doi.org/10.1039/c6ra21742g)
5. *Silicon/TiO<sub>2</sub> core-shell nanopillar photoanodes for enhanced photoelectrochemical water oxidation*  
**Mykola Pavlenko**, Katarzyna Siuzdak, Emerson Coy, Mariusz Jancelewicz, Stefan Jurga, Igor Iatsunskyi

International Journal of Hydrogen Energy: 42, 51, 30076-30085, 2017  
doi.org/10.1016/j.ijhydene.2017.10.033

6. *Effect of porous silicon substrate on structural, mechanical and optical properties of MOCVD and ALD ruthenium oxide nanolayers*  
Ievgen Brytavskiy, Kristína Hušeková, Valerii Myndrul, **Mykola Pavlenko**, Emerson Coy, Karol Zaleski, Dagmar Gregušová, Luis Yate, Valentyn Smyntyna, Igor Iatsunskiy  
Applied Surface Science: 471, 686–693, 2019  
doi.org/10.1016/j.apsusc.2018.12.022
  
7. *Enhancing Photocatalytic Performance and Solar Absorption by Schottky Nanodiodes Heterojunctions in Mechanically Resilient Palladium Coated TiO<sub>2</sub>/Si Nanopillars by Atomic Layer Deposition*  
Emerson Coy, Katarzyna Siuzdak, **Mykola Pavlenko**, Karol Załęski, Octavio Graniel, Marcin Ziółek, Sebastien Balme, Philippe Miele, Matthieu Weber, Mikhael Bechelany, Igor Iatsunskiy  
Chemical Engineering Journal: 392, 123702, 2020  
doi.org/10.1016/j.cej.2019.123702
  
8. *Enhanced solar-driven water splitting of 1D core-shell Si/TiO<sub>2</sub>/ZnO nanopillars*  
**Mykola Pavlenko**, Katarzyna Siuzdak, Emerson Coy, Karol Załęski, Mariusz Jancelewicz, Igor Iatsunskiy  
International Journal of Hydrogen Energy: 45, 50, 26426-26433, 2020  
doi.org/10.1016/j.ijhydene.2019.11.231
  
9. *Porous Silicon-Zinc Oxide Nanocomposites Prepared by Atomic Layer Deposition for Biophotonic Applications*  
**Mykola Pavlenko**, Valerii Myndrul, Gloria Gottardi, Emerson Coy, Mariusz Jancelewicz, Igor Iatsunskiy  
Materials: 1987, 13, 2020  
doi:10.3390/ma13081987

## Conference presentations and proceedings

1. *Ammonia detection using optical reflectance from porous silicon formed by metal-assisted chemical etching*

Igor Iatsunskyi, Valentyn Smyntyna, Mykolai Pavlenko, Olga Kanevska, Yuliia Kirik, Valeryi Myndrul

Proceedings of SPIE: 8901, 89010K-1, 2013

[doi.org/10.1117/12.2028497](https://doi.org/10.1117/12.2028497)

2. *Raman spectroscopy of nanostructured silicon fabricated by metal-assisted chemical etching*

Igor Iatsunskyi, Stefan Jurga, Valentyn Smyntyna, Mykolai Pavlenko, Valeriy Myndrul, Anastasia Zaleska

Proceedings of SPIE: 9132, 913217-1, 2014

[doi.org/10.1117/12.2051489](https://doi.org/10.1117/12.2051489)

3. *Structural and optical properties of  $TiO_2-Al_2O_3$  nanolaminates produced by atomic layer deposition*

Viktoriia Fedorenko, Igor Iatsunskyi, Mykolai Pavlenko, Mariusz Jancelewicz, Emerson Coy, Roman Viter

Proceedings of SPIE: 9649, 96490X-6, 2015

[doi.org/10.1117/12.2194295](https://doi.org/10.1117/12.2194295)

4. *Study on structural and optical properties of  $TiO_2$  ALD coated silicon nanopillars*

Mykola Pavlenko, Valerii Myndrul, Igor Iatsunskyi, Stefan Jurga, Valentyn Smyntyna

Proceedings of SPIE: 9884, 98842H-6, 2016

[doi.org/10.1117/12.2227122](https://doi.org/10.1117/12.2227122)

5. *Structural features of Au- $TiO_2$  bilayered laminates*

Mykola Pavlenko, Igor Iatsunskyi, Mariusz Jancelewicz, Grzegorz Nowaczyk , Stefan Jurga, Valentin Smyntyna

Poster presentation at NanoTech Poland International Conference & Exhibition, 22<sup>nd</sup>-25<sup>th</sup> June, Poznan, Poland, 2016

6. *Efficient core-shell silicon-TiO<sub>2</sub> photoanodes for water-splitting process*

Mykola Pavlenko, Katarzyna Siuzdak, Emerson Coy, Mariusz Jancelewicz, Stefan Jurga, Igor Iatsunskyi

Poster presentation at NanoTech Poland International Conference & Exhibition, 1<sup>st</sup>-3<sup>rd</sup> June, Poznan, Poland, 2017

7. *Metal oxide – silicon 1D nanocomposites as effective platform for optical applications*

Mykola Pavlenko, Katarzyna Siuzdak, Stefan Jurga, Mariusz Jancelewicz, Igor Iatsunskyi

Poster presentation at NanoTech Poland & 1<sup>st</sup> Symposium on Polydopamine, 6<sup>th</sup>-9<sup>th</sup> June, Poznan, Poland, 2018

8. *Synthesis and photoelectrochemical properties of 1D Si/TiO<sub>2</sub>/ZnO nanocomposites*

Mykola Pavlenko, Igor Iatsunskyi

Poster presentation at International Conference: Nanomaterials for biosensors and biomedical applications, 2<sup>st</sup>-4<sup>th</sup> July, Jurmala, Latvia, 2019

9. *Application of electrochemical impedance spectroscopy in development of effective silicon-metal oxide photoanodes for water-splitting*

Mykola Pavlenko, Katarzyna Siuzdak, Emerson Coy, Mariusz Jancelewicz, Igor Iatsunskyi, Stefan Jurga

Poster presentation at NanoTech Poland & Nanotechnology and Innovation in the Baltic Sea Region, 5<sup>th</sup>-8<sup>th</sup> June, Poznan, Poland, 2019



10. *One dimensional silicon-metal oxide nanostructures for water-splitting application*

Mykola Pavlenko, Katarzyna Siuzdak , Emerson Coy , Mariusz Jancelewicz , Stefan Jurga, Igor Iatsunskyi

Poster presentation at Ampere NMR School, 23<sup>rd</sup>-29<sup>th</sup> June, Zakopane, Poland, 2019

11. *Nanocomposites based on porous silicon/metal oxides for optical biosensors application*

Mykola Pavlenko, Igor Iatsunskyi

Poster presentation at NanoTech Poland, 9<sup>th</sup>-11<sup>th</sup> June, Poznan, Poland, 2021

12. *Fabrication of electrospun polymer nanofibers with introduced TiO<sub>2</sub> and WO<sub>3</sub> nanowires for photocatalytic and biosensing application*

Mykola Pavlenko, Valerii Myndrul, Markéta Klíčová, Pavel Holec, Kateřina Blatoňová, Igor Iatsunskyi

Poster presentation at NanoTech Poland 2022, 1<sup>st</sup>-3<sup>rd</sup> June, Poznan, Poland, 2022

## References

- [1] A. E. Gürel, Ü. Ağbulut, H. Bakır, A. Ergün, and G. Yıldız, 'A state of art review on estimation of solar radiation with various models', *Heliyon*, vol. 9, no. 2, p. e13167, Feb. 2023, doi: 10.1016/j.heliyon.2023.e13167.
- [2] J. Duan *et al.*, 'A multistep short-term solar radiation forecasting model using fully convolutional neural networks and chaotic aquila optimization combining WRF-Solar model results', *Energy*, vol. 271, p. 126980, May 2023, doi: 10.1016/j.energy.2023.126980.
- [3] A. Wallace. Copeland, O. D. Black, and A. B. Garrett, 'The Photovoltaic Effect.', *Chem. Rev.*, vol. 31, no. 1, pp. 177–226, Aug. 1942, doi: 10.1021/cr60098a004.
- [4] Y. Wang, C. Gao, X. Wang, H. Liu, and W. Shen, 'Controllable Electrochemical Deposition and Theoretical Understanding of Conformal Perovskite on Textured Silicon towards Efficient Perovskite/Silicon Tandem Solar Cells', *J. Phys. Chem. C*, vol. 125, no. 5, pp. 2875–2883, Feb. 2021, doi: 10.1021/acs.jpcc.0c11259.
- [5] H. Sun, J. Dai, W. Zhou, and Z. Shao, 'Emerging Strategies for Developing High-Performance Perovskite-Based Materials for Electrochemical Water Splitting', *Energy Fuels*, vol. 34, no. 9, pp. 10547–10567, Sep. 2020, doi: 10.1021/acs.energyfuels.0c02313.
- [6] H. O. Seo *et al.*, 'Ultrathin TiO<sub>2</sub> Films on ZnO Electron-Collecting Layers of Inverted Organic Solar Cell', *J. Phys. Chem. C*, vol. 115, no. 43, pp. 21517–21520, Nov. 2011, doi: 10.1021/jp2063589.
- [7] P.-F. Zhang, D. Wu, G.-P. Yang, and Y.-Y. Wang, 'Metal–Organic Frameworks as Heterogeneous Electrocatalysts for Water Splitting and CO<sub>2</sub> Fixation', *Crystal Growth & Design*, vol. 21, no. 6, pp. 3123–3142, Jun. 2021, doi: 10.1021/acs.cgd.0c01691.
- [8] P. Woods, H. Bustamante, and K.-F. Aguey-Zinsou, 'The hydrogen economy - Where is the water?', *Energy Nexus*, vol. 7, p. 100123, Sep. 2022, doi: 10.1016/j.nexus.2022.100123.
- [9] T. Amirthan and M. S. A. Perera, 'The role of storage systems in hydrogen economy: A review', *Journal of Natural Gas Science and Engineering*, vol. 108, p. 104843, Dec. 2022, doi: 10.1016/j.jngse.2022.104843.
- [10] K. J. Dillman and J. Heinonen, 'A “just” hydrogen economy: A normative energy justice assessment of the hydrogen economy', *Renewable and Sustainable Energy Reviews*, vol. 167, p. 112648, Oct. 2022, doi: 10.1016/j.rser.2022.112648.
- [11] S. K. Kar, S. Harichandan, and B. Roy, 'Bibliometric analysis of the research on hydrogen economy: An analysis of current findings and roadmap ahead', *International Journal of Hydrogen Energy*, vol. 47, no. 20, pp. 10803–10824, Mar. 2022, doi: 10.1016/j.ijhydene.2022.01.137.
- [12] P. M. Falcone, M. Hiete, and A. Sapio, 'Hydrogen economy and sustainable development goals: Review and policy insights', *Current Opinion in Green and Sustainable Chemistry*, vol. 31, p. 100506, Oct. 2021, doi: 10.1016/j.cogsc.2021.100506.
- [13] Q. Wang and K. Domen, 'Particulate Photocatalysts for Light-Driven Water Splitting: Mechanisms, Challenges, and Design Strategies', *Chem. Rev.*, vol. 120, no. 2, pp. 919–985, Jan. 2020, doi: 10.1021/acs.chemrev.9b00201.
- [14] M. G. Walter *et al.*, 'Solar Water Splitting Cells', *Chem. Rev.*, vol. 110, no. 11, pp. 6446–6473, Nov. 2010, doi: 10.1021/cr1002326.
- [15] W. Jin *et al.*, 'Natural leaf-inspired solar water splitting system', *Applied Catalysis B: Environmental*, vol. 322, p. 122086, Mar. 2023, doi: 10.1016/j.apcatb.2022.122086.
- [16] W. Chen *et al.*, 'Origins of high onset overpotential of oxygen reduction reaction at Pt-based electrocatalysts: A mini review', *Electrochemistry Communications*, vol. 96, pp. 71–76, Nov. 2018, doi: 10.1016/j.elecom.2018.09.011.
- [17] R. de Miguel, 'On the Nonequilibrium Thermodynamics of Large Departures from Butler–Volmer Behavior', *J. Phys. Chem. B*, vol. 110, no. 16, pp. 8176–8178, Apr. 2006, doi: 10.1021/jp060506p.

- [18] A. Govind Rajan and E. A. Carter, ‘Discovering Competing Electrocatalytic Mechanisms and Their Overpotentials: Automated Enumeration of Oxygen Evolution Pathways’, *J. Phys. Chem. C*, vol. 124, no. 45, pp. 24883–24898, Nov. 2020, doi: 10.1021/acs.jpcc.0c08120.
- [19] S. Divanis, T. Kutlusoy, I. M. Ingmer Boye, I. C. Man, and J. Rossmeisl, ‘Oxygen evolution reaction: a perspective on a decade of atomic scale simulations’, *Chem. Sci.*, vol. 11, no. 11, pp. 2943–2950, 2020, doi: 10.1039/C9SC05897D.
- [20] C. F. Dickens, C. Kirk, and J. K. Nørskov, ‘Insights into the Electrochemical Oxygen Evolution Reaction with ab Initio Calculations and Microkinetic Modeling: Beyond the Limiting Potential Volcano’, *J. Phys. Chem. C*, vol. 123, no. 31, pp. 18960–18977, Aug. 2019, doi: 10.1021/acs.jpcc.9b03830.
- [21] H. N. Nong *et al.*, ‘Key role of chemistry versus bias in electrocatalytic oxygen evolution’, *Nature*, vol. 587, no. 7834, pp. 408–413, Nov. 2020, doi: 10.1038/s41586-020-2908-2.
- [22] I. Roger, M. A. Shipman, and M. D. Symes, ‘Earth-abundant catalysts for electrochemical and photoelectrochemical water splitting’, *Nat Rev Chem*, vol. 1, no. 1, p. 0003, Jan. 2017, doi: 10.1038/s41570-016-0003.
- [23] F. A. L. Laskowski, M. R. Nellist, J. Qiu, and S. W. Boettcher, ‘Metal Oxide/(oxy)hydroxide Overlayers as Hole Collectors and Oxygen-Evolution Catalysts on Water-Splitting Photoanodes’, *J. Am. Chem. Soc.*, vol. 141, no. 4, pp. 1394–1405, Jan. 2019, doi: 10.1021/jacs.8b09449.
- [24] K. George, X. Zhang, and A. Bieberle-Hütter, ‘Why does NiOOH cocatalyst increase the oxygen evolution activity of  $\alpha$ -Fe<sub>2</sub>O<sub>3</sub>?’, *J. Chem. Phys.*, vol. 150, no. 4, p. 041729, Jan. 2019, doi: 10.1063/1.5063771.
- [25] A. Iqbal and K. H. Bevan, ‘Simultaneously Solving the Photovoltage and Photocurrent at Semiconductor–Liquid Interfaces’, *J. Phys. Chem. C*, vol. 122, no. 1, pp. 30–43, Jan. 2018, doi: 10.1021/acs.jpcc.7b08517.
- [26] N. Snir, N. Yatom, and M. Caspary Toroker, ‘Progress in understanding hematite electrochemistry through computational modeling’, *Computational Materials Science*, vol. 160, pp. 411–419, Apr. 2019, doi: 10.1016/j.commatsci.2019.01.001.
- [27] O. Zandi and T. W. Hamann, ‘Determination of photoelectrochemical water oxidation intermediates on hematite electrode surfaces using operando infrared spectroscopy’, *Nature Chem*, vol. 8, no. 8, pp. 778–783, Aug. 2016, doi: 10.1038/nchem.2557.
- [28] C. Y. Cummings, F. Marken, L. M. Peter, K. G. Uplu Wijayantha, and A. A. Tahir, ‘New Insights into Water Splitting at Mesoporous  $\alpha$ -Fe<sub>2</sub>O<sub>3</sub> Films: A Study by Modulated Transmittance and Impedance Spectroscopies’, *J. Am. Chem. Soc.*, vol. 134, no. 2, pp. 1228–1234, Jan. 2012, doi: 10.1021/ja209530s.
- [29] M. Bhati, Y. Chen, and T. P. Senftle, ‘Density Functional Theory Modeling of Photoelectrochemical Reactions on Semiconductors: H<sub>2</sub> Evolution on 3C-SiC’, *J. Phys. Chem. C*, vol. 124, no. 49, pp. 26625–26639, Dec. 2020, doi: 10.1021/acs.jpcc.0c07583.
- [30] B. H. Erné, F. Ozanam, and J.-N. Chazalviel, ‘The Mechanism of Hydrogen Gas Evolution on GaAs Cathodes Elucidated by In Situ Infrared Spectroscopy’, *J. Phys. Chem. B*, vol. 103, no. 15, pp. 2948–2962, Apr. 1999, doi: 10.1021/jp984765t.
- [31] L. Peter, ‘Photoelectrochemical Kinetics: Hydrogen Evolution on p-Type Semiconductors’, *J. Electrochem. Soc.*, vol. 166, no. 5, pp. H3125–H3132, 2019, doi: 10.1149/2.0231905jes.
- [32] H. Gerischer, ‘Electron-transfer kinetics of redox reactions at the semiconductor/electrolyte contact. A new approach’, *J. Phys. Chem.*, vol. 95, no. 3, pp. 1356–1359, Feb. 1991, doi: 10.1021/j100156a060.
- [33] S. Zhang and W. Leng, ‘Questioning the rate law in the analysis of water oxidation catalysis on hematite photoanodes’, *Nat. Chem.*, vol. 12, no. 12, pp. 1097–1098, Dec. 2020, doi: 10.1038/s41557-020-00569-y.
- [34] L. M. Peter, A. B. Walker, T. Bein, A. G. Hufnagel, and I. Kondofersky, ‘Interpretation of photocurrent transients at semiconductor electrodes: Effects of band-edge unpinning’, *Journal of Electroanalytical Chemistry*, vol. 872, p. 114234, Sep. 2020, doi: 10.1016/j.jelechem.2020.114234.
- [35] F. Le Formal *et al.*, ‘Rate Law Analysis of Water Oxidation on a Hematite Surface’, *J. Am. Chem. Soc.*, vol. 137, no. 20, pp. 6629–6637, May 2015, doi: 10.1021/jacs.5b02576.

- [36] B. M. Hunter, H. B. Gray, and A. M. Müller, 'Earth-Abundant Heterogeneous Water Oxidation Catalysts', *Chem. Rev.*, vol. 116, no. 22, pp. 14120–14136, Nov. 2016, doi: 10.1021/acs.chemrev.6b00398.
- [37] R. Abe, 'Recent progress on photocatalytic and photoelectrochemical water splitting under visible light irradiation', *Journal of Photochemistry and Photobiology C: Photochemistry Reviews*, vol. 11, no. 4, pp. 179–209, Dec. 2010, doi: 10.1016/j.jphotochemrev.2011.02.003.
- [38] R. M. Navarro, M. C. Alvarez-Galván, J. A. Villoria de la Mano, S. M. Al-Zahrani, and J. L. G. Fierro, 'A framework for visible-light water splitting', *Energy Environ. Sci.*, vol. 3, no. 12, p. 1865, 2010, doi: 10.1039/c001123a.
- [39] Q. Wang *et al.*, 'Molecularly engineered photocatalyst sheet for scalable solar formate production from carbon dioxide and water', *Nat Energy*, vol. 5, no. 9, pp. 703–710, Aug. 2020, doi: 10.1038/s41560-020-0678-6.
- [40] A. Fujishima and K. Honda, 'Electrochemical Photolysis of Water at a Semiconductor Electrode', *Nature*, vol. 238, no. 5358, pp. 37–38, Jul. 1972, doi: 10.1038/238037a0.
- [41] J. Brilliet *et al.*, 'Highly efficient water splitting by a dual-absorber tandem cell', *Nature Photon*, vol. 6, no. 12, pp. 824–828, Dec. 2012, doi: 10.1038/nphoton.2012.265.
- [42] G. K. Mor *et al.*, 'p-Type Cu–Ti–O Nanotube Arrays and Their Use in Self-Biased Heterojunction Photoelectrochemical Diodes for Hydrogen Generation', *Nano Lett.*, vol. 8, no. 7, pp. 1906–1911, Jul. 2008, doi: 10.1021/nl080572y.
- [43] S. Haussener, S. Hu, C. Xiang, A. Z. Weber, and N. S. Lewis, 'Simulations of the irradiation and temperature dependence of the efficiency of tandem photoelectrochemical water-splitting systems', *Energy Environ. Sci.*, vol. 6, no. 12, p. 3605, 2013, doi: 10.1039/c3ee41302k.
- [44] O. Khaselev and J. A. Turner, 'A Monolithic Photovoltaic-Photoelectrochemical Device for Hydrogen Production via Water Splitting', *Science*, vol. 280, no. 5362, pp. 425–427, Apr. 1998, doi: 10.1126/science.280.5362.425.
- [45] J. Jia *et al.*, 'Solar water splitting by photovoltaic-electrolysis with a solar-to-hydrogen efficiency over 30%', *Nat Commun*, vol. 7, no. 1, p. 13237, Oct. 2016, doi: 10.1038/ncomms13237.
- [46] L. Zhang, W. Wang, S. Sun, D. Jiang, and E. Gao, 'Selective transport of electron and hole among {0 0 1} and {1 1 0} facets of BiOCl for pure water splitting', *Applied Catalysis B: Environmental*, vol. 162, pp. 470–474, Jan. 2015, doi: 10.1016/j.apcatb.2014.07.024.
- [47] A. J. Bard, 'Photoelectrochemistry and heterogeneous photo-catalysis at semiconductors', *Journal of Photochemistry*, vol. 10, no. 1, pp. 59–75, Jan. 1979, doi: 10.1016/0047-2670(79)80037-4.
- [48] H. Li, W. Tu, Y. Zhou, and Z. Zou, 'Z-Scheme Photocatalytic Systems for Promoting Photocatalytic Performance: Recent Progress and Future Challenges', *Adv. Sci.*, vol. 3, no. 11, p. 1500389, Nov. 2016, doi: 10.1002/advs.201500389.
- [49] B. Ng, L. K. Putri, X. Y. Kong, Y. W. Teh, P. Pasbakhsh, and S. Chai, 'Z-Scheme Photocatalytic Systems for Solar Water Splitting', *Adv. Sci.*, vol. 7, no. 7, p. 1903171, Apr. 2020, doi: 10.1002/advs.201903171.
- [50] Y. Wen Teh, Y. Wei Goh, X. Ying Kong, B. Ng, S. Yong, and S. Chai, 'Fabrication of Bi<sub>2</sub>WO<sub>6</sub>/Cu/WO<sub>3</sub> All-Solid-State Z-Scheme Composite Photocatalyst to Improve CO<sub>2</sub> Photoreduction under Visible Light Irradiation', *ChemCatChem*, vol. 11, no. 24, pp. 6431–6438, Dec. 2019, doi: 10.1002/cctc.201901653.
- [51] B.-J. Ng, L. K. Putri, L.-L. Tan, P. Pasbakhsh, and S.-P. Chai, 'All-solid-state Z-scheme photocatalyst with carbon nanotubes as an electron mediator for hydrogen evolution under simulated solar light', *Chemical Engineering Journal*, vol. 316, pp. 41–49, May 2017, doi: 10.1016/j.cej.2017.01.054.
- [52] K. Maeda and K. Domen, 'Photocatalytic Water Splitting: Recent Progress and Future Challenges', *J. Phys. Chem. Lett.*, vol. 1, no. 18, pp. 2655–2661, Sep. 2010, doi: 10.1021/jz1007966.
- [53] R. Abe, K. Sayama, K. Domen, and H. Arakawa, 'A new type of water splitting system composed of two different TiO<sub>2</sub> photocatalysts (anatase, rutile) and a IO<sub>3</sub><sup>-</sup>/I<sup>-</sup> shuttle redox mediator', *Chemical Physics Letters*, vol. 344, no. 3–4, pp. 339–344, Aug. 2001, doi: 10.1016/S0009-2614(01)00790-4.

- [54] H. Tada, T. Mitsui, T. Kiyonaga, T. Akita, and K. Tanaka, 'All-solid-state Z-scheme in CdS–Au–TiO<sub>2</sub> three-component nanojunction system', *Nature Mater.*, vol. 5, no. 10, pp. 782–786, Oct. 2006, doi: 10.1038/nmat1734.
- [55] P. Zhou, J. Yu, and M. Jaroniec, 'All-Solid-State Z-Scheme Photocatalytic Systems', *Adv. Mater.*, vol. 26, no. 29, pp. 4920–4935, Aug. 2014, doi: 10.1002/adma.201400288.
- [56] V. Dutta *et al.*, 'Constructing carbon nanotubes@CuBi<sub>2</sub>O<sub>4</sub>/AgBiO<sub>3</sub> all solid-state mediated Z-scheme photocatalyst with enhanced photocatalytic activity', *Materials Letters*, vol. 320, p. 132374, Aug. 2022, doi: 10.1016/j.matlet.2022.132374.
- [57] N. Shezad *et al.*, 'Carbon Nanotubes Incorporated Z-Scheme Assembly of AgBr/TiO<sub>2</sub> for Photocatalytic Hydrogen Production under Visible Light Irradiations', *Nanomaterials*, vol. 9, no. 12, p. 1767, Dec. 2019, doi: 10.3390/nano9121767.
- [58] H. Zhang *et al.*, 'Carbon nitride-based Z-scheme photocatalysts for non-sacrificial overall water splitting', *Materials Today Energy*, vol. 23, p. 100915, Jan. 2022, doi: 10.1016/j.mtener.2021.100915.
- [59] X. Wang *et al.*, 'Enhanced photocatalytic hydrogen evolution by prolonging the lifetime of carriers in ZnO/CdS heterostructures', *Chem. Commun.*, no. 23, p. 3452, 2009, doi: 10.1039/b904668b.
- [60] G. Liu, L. Wang, H. G. Yang, H.-M. Cheng, and G. Q. (Max) Lu, 'Titania-based photocatalysts—crystal growth, doping and heterostructuring', *J. Mater. Chem.*, vol. 20, no. 5, pp. 831–843, 2010, doi: 10.1039/B909930A.
- [61] Y. Sasaki, H. Nemoto, K. Saito, and A. Kudo, 'Solar Water Splitting Using Powdered Photocatalysts Driven by Z-Schematic Interparticle Electron Transfer without an Electron Mediator', *J. Phys. Chem. C*, vol. 113, no. 40, pp. 17536–17542, Oct. 2009, doi: 10.1021/jp907128k.
- [62] Z. Li *et al.*, 'Electron-extracting system with enhanced photocatalytic hydrogen production performance: Synergistic utilization of Z-scheme and Ohmic heterojunctions', *Chemical Engineering Journal*, vol. 429, p. 132476, Feb. 2022, doi: 10.1016/j.cej.2021.132476.
- [63] S. Chen, S. S. Thind, and A. Chen, 'Nanostructured materials for water splitting - state of the art and future needs: A mini-review', *Electrochemistry Communications*, vol. 63, pp. 10–17, Feb. 2016, doi: 10.1016/j.elecom.2015.12.003.
- [64] J. Y. Soo, A. Saryati Ameruddin, and M. Khairul Ahmad, 'Co-sensitising cadmium selenide and cadmium telluride quantum dots on titanium dioxide nanorods via the SILAR method', *Chemical Physics Letters*, vol. 809, p. 140170, Dec. 2022, doi: 10.1016/j.cplett.2022.140170.
- [65] Q. Sun *et al.*, 'Design and synthesis of black phosphorus quantum dot sensitized inverse opal TiO<sub>2</sub> photonic crystal with outstanding photocatalytic activities', *Applied Surface Science*, vol. 609, p. 155442, Jan. 2023, doi: 10.1016/j.apsusc.2022.155442.
- [66] S. Monika, M. Mahalakshmi, and M. S. Pandian, 'TiO<sub>2</sub>/CdS/CdSe quantum dots co-sensitized solar cell with the staggered-gap (type-II) heterojunctions for the enhanced photovoltaic performance', *Ceramics International*, vol. 49, no. 6, pp. 8820–8826, Mar. 2023, doi: 10.1016/j.ceramint.2022.11.034.
- [67] R. Memming and G. Schwandt, 'Electrochemical properties of gallium phosphide in aqueous solutions', *Electrochimica Acta*, vol. 13, no. 6, pp. 1299–1310, Jun. 1968, doi: 10.1016/0013-4686(68)80058-1.
- [68] D. E. Aspnes and A. A. Studna, 'Dielectric functions and optical parameters of Si, Ge, GaP, GaAs, GaSb, InP, InAs, and InSb from 1.5 to 6.0 eV', *Phys. Rev. B*, vol. 27, no. 2, pp. 985–1009, Jan. 1983, doi: 10.1103/PhysRevB.27.985.
- [69] J. Ziegler *et al.*, 'Preparation and Characterization of GaP Semiconductor Electrodes for Photoelectrochemical Water Splitting', *Energy Procedia*, vol. 22, pp. 108–113, 2012, doi: 10.1016/j.egypro.2012.05.220.
- [70] M. Hettick, M. Zheng, Y. Lin, C. M. Sutter-Fella, J. W. Ager, and A. Javey, 'Nonepitaxial Thin-Film InP for Scalable and Efficient Photocathodes', *J. Phys. Chem. Lett.*, vol. 6, no. 12, pp. 2177–2182, Jun. 2015, doi: 10.1021/acs.jpcclett.5b00744.
- [71] M. H. Lee *et al.*, 'p-Type InP Nanopillar Photocathodes for Efficient Solar-Driven Hydrogen Production', *Angew. Chem. Int. Ed.*, vol. 51, no. 43, pp. 10760–10764, Oct. 2012, doi: 10.1002/anie.201203174.

- [72] Y. Lin *et al.*, ‘Role of TiO<sub>2</sub> Surface Passivation on Improving the Performance of p-InP Photocathodes’, *J. Phys. Chem. C*, vol. 119, no. 5, pp. 2308–2313, Feb. 2015, doi: 10.1021/jp5107313.
- [73] B. Seger, T. Pedersen, A. B. Laursen, P. C. K. Vesborg, O. Hansen, and I. Chorkendorff, ‘Using TiO<sub>2</sub> as a Conductive Protective Layer for Photocathodic H<sub>2</sub> Evolution’, *J. Am. Chem. Soc.*, vol. 135, no. 3, pp. 1057–1064, Jan. 2013, doi: 10.1021/ja309523t.
- [74] B. Seger *et al.*, ‘Silicon protected with atomic layer deposited TiO<sub>2</sub>: durability studies of photocathodic H<sub>2</sub> evolution’, *RSC Adv.*, vol. 3, no. 48, p. 25902, 2013, doi: 10.1039/c3ra45966g.
- [75] M. Ni, M. K. H. Leung, D. Y. C. Leung, and K. Sumathy, ‘A review and recent developments in photocatalytic water-splitting using TiO<sub>2</sub> for hydrogen production’, *Renewable and Sustainable Energy Reviews*, vol. 11, no. 3, pp. 401–425, Apr. 2007, doi: 10.1016/j.rser.2005.01.009.
- [76] P. Roy, S. Berger, and P. Schmuki, ‘TiO<sub>2</sub> Nanotubes: Synthesis and Applications’, *Angew. Chem. Int. Ed.*, vol. 50, no. 13, pp. 2904–2939, Mar. 2011, doi: 10.1002/anie.201001374.
- [77] J. Tian, Z. Zhao, A. Kumar, R. I. Boughton, and H. Liu, ‘Recent progress in design, synthesis, and applications of one-dimensional TiO<sub>2</sub> nanostructured surface heterostructures: a review’, *Chem. Soc. Rev.*, vol. 43, no. 20, pp. 6920–6937, 2014, doi: 10.1039/C4CS00180J.
- [78] K. Lee, A. Mazare, and P. Schmuki, ‘One-Dimensional Titanium Dioxide Nanomaterials: Nanotubes’, *Chem. Rev.*, vol. 114, no. 19, pp. 9385–9454, Oct. 2014, doi: 10.1021/cr500061m.
- [79] S. Hoang, S. Guo, N. T. Hahn, A. J. Bard, and C. B. Mullins, ‘Visible Light Driven Photoelectrochemical Water Oxidation on Nitrogen-Modified TiO<sub>2</sub> Nanowires’, *Nano Lett.*, vol. 12, no. 1, pp. 26–32, Jan. 2012, doi: 10.1021/nl2028188.
- [80] I. S. Cho *et al.*, ‘Highly Efficient Solar Water Splitting from Transferred TiO<sub>2</sub> Nanotube Arrays’, *Nano Lett.*, vol. 15, no. 9, pp. 5709–5715, Sep. 2015, doi: 10.1021/acs.nanolett.5b01406.
- [81] X. Liu, F. Wang, and Q. Wang, ‘Nanostructure-based WO<sub>3</sub> photoanodes for photoelectrochemical water splitting’, *Phys. Chem. Chem. Phys.*, vol. 14, no. 22, p. 7894, 2012, doi: 10.1039/c2cp40976c.
- [82] S. S. Thind, M. Tian, and A. Chen, ‘Direct growth and photo-electrochemical study of WO<sub>3</sub> nanostructured materials’, *Electrochemistry Communications*, vol. 43, pp. 13–17, Jun. 2014, doi: 10.1016/j.elecom.2014.03.002.
- [83] F. Amano, M. Tian, G. Wu, B. Ohtani, and A. Chen, ‘Facile Preparation of Platelike Tungsten Oxide Thin Film Electrodes with High Photoelectrode Activity’, *ACS Appl. Mater. Interfaces*, vol. 3, no. 10, pp. 4047–4052, Oct. 2011, doi: 10.1021/am200897n.
- [84] A. Kołodziejczak-Radzimska and T. Jesionowski, ‘Zinc Oxide—From Synthesis to Application: A Review’, *Materials*, vol. 7, no. 4, pp. 2833–2881, Apr. 2014, doi: 10.3390/ma7042833.
- [85] M. S. Islam, M. F. Hossain, and S. M. A. Razzak, ‘Enhanced photoelectrochemical performance of nanoparticle ZnO photoanodes for water-splitting application’, *Journal of Photochemistry and Photobiology A: Chemistry*, vol. 326, pp. 100–106, Jul. 2016, doi: 10.1016/j.jphotochem.2016.04.002.
- [86] S. B. A. Hamid, S. J. Teh, and C. W. Lai, ‘Photocatalytic Water Oxidation on ZnO: A Review’, *Catalysts*, vol. 7, no. 12, p. 93, Mar. 2017, doi: 10.3390/catal7030093.
- [87] A. K. Chandiran, M. Abdi-Jalebi, M. K. Nazeeruddin, and M. Grätzel, ‘Analysis of Electron Transfer Properties of ZnO and TiO<sub>2</sub> Photoanodes for Dye-Sensitized Solar Cells’, *ACS Nano*, vol. 8, no. 3, pp. 2261–2268, Mar. 2014, doi: 10.1021/nn405535j.
- [88] R. K. Gupta, K. Ghosh, and P. K. Kahol, ‘Fabrication and characterization of NiO/ZnO p–n junctions by pulsed laser deposition’, *Physica E: Low-dimensional Systems and Nanostructures*, vol. 41, no. 4, pp. 617–620, Feb. 2009, doi: 10.1016/j.physe.2008.10.013.
- [89] C. Hu, K. Chu, Y. Zhao, and W. Y. Teoh, ‘Efficient Photoelectrochemical Water Splitting over Anodized p-Type NiO Porous Films’, *ACS Appl. Mater. Interfaces*, vol. 6, no. 21, pp. 18558–18568, Nov. 2014, doi: 10.1021/am507138b.
- [90] Z. Zhang, C. Shao, X. Li, C. Wang, M. Zhang, and Y. Liu, ‘Electrospun Nanofibers of p-Type NiO/ n-Type ZnO Heterojunctions with Enhanced Photocatalytic Activity’, *ACS Appl. Mater. Interfaces*, vol. 2, no. 10, pp. 2915–2923, Oct. 2010, doi: 10.1021/am100618h.
- [91] K. Zheng *et al.*, ‘Ultrafast Charge Transfer from CdSe Quantum Dots to p-Type NiO: Hole Injection vs Hole Trapping’, *J. Phys. Chem. C*, vol. 118, no. 32, pp. 18462–18471, Aug. 2014, doi: 10.1021/jp506963q.

- [92] J. Li and N. Wu, ‘Semiconductor-based photocatalysts and photoelectrochemical cells for solar fuel generation: a review’, *Catal. Sci. Technol.*, vol. 5, no. 3, pp. 1360–1384, 2015, doi: 10.1039/C4CY00974F.
- [93] K. Sivula, F. Le Formal, and M. Grätzel, ‘Solar Water Splitting: Progress Using Hematite ( $\alpha$ -Fe<sub>2</sub>O<sub>3</sub>) Photoelectrodes’, *ChemSusChem*, vol. 4, no. 4, pp. 432–449, Apr. 2011, doi: 10.1002/cssc.201000416.
- [94] M. J. Katz, S. C. Riha, N. C. Jeong, A. B. F. Martinson, O. K. Farha, and J. T. Hupp, ‘Toward solar fuels: Water splitting with sunlight and “rust”’, *Coordination Chemistry Reviews*, vol. 256, no. 21–22, pp. 2521–2529, Nov. 2012, doi: 10.1016/j.ccr.2012.06.017.
- [95] H. Dotan, K. Sivula, M. Grätzel, A. Rothschild, and S. C. Warren, ‘Probing the photoelectrochemical properties of hematite ( $\alpha$ -Fe<sub>2</sub>O<sub>3</sub>) electrodes using hydrogen peroxide as a hole scavenger’, *Energy Environ. Sci.*, vol. 4, no. 3, pp. 958–964, 2011, doi: 10.1039/C0EE00570C.
- [96] X. Yang *et al.*, ‘Synthesis and characterization of an IrO<sub>2</sub>-Fe<sub>2</sub>O<sub>3</sub> electrocatalyst for the hydrogen evolution reaction in acidic water electrolysis’, *RSC Adv.*, vol. 7, no. 33, pp. 20252–20258, 2017, doi: 10.1039/C7RA01533J.
- [97] A. Paracchino, V. Laporte, K. Sivula, M. Grätzel, and E. Thimsen, ‘Highly active oxide photocathode for photoelectrochemical water reduction’, *Nature Mater.*, vol. 10, no. 6, pp. 456–461, Jun. 2011, doi: 10.1038/nmat3017.
- [98] D. Barreca *et al.*, ‘The Potential of Supported Cu<sub>2</sub>O and CuO Nanosystems in Photocatalytic H<sub>2</sub> Production’, *ChemSusChem*, vol. 2, no. 3, pp. 230–233, Mar. 2009, doi: 10.1002/cssc.200900032.
- [99] S. Xu, A. J. Du, J. Liu, J. Ng, and D. D. Sun, ‘Highly efficient CuO incorporated TiO<sub>2</sub> nanotube photocatalyst for hydrogen production from water’, *International Journal of Hydrogen Energy*, vol. 36, no. 11, pp. 6560–6568, Jun. 2011, doi: 10.1016/j.ijhydene.2011.02.103.
- [100] L. Zhang, Y.-N. Liu, M. Zhou, and J. Yan, ‘Improving photocatalytic hydrogen evolution over CuO/Al<sub>2</sub>O<sub>3</sub> by platinum-depositing and CuS-loading’, *Applied Surface Science*, vol. 282, pp. 531–537, Oct. 2013, doi: 10.1016/j.apsusc.2013.06.006.
- [101] J. Zhang, M. Deng, F. Ren, Y. Wu, and Y. Wang, ‘Effects of Mo/W codoping on the visible-light photocatalytic activity of monoclinic BiVO<sub>4</sub> within the GGA + U framework’, *RSC Adv.*, vol. 6, no. 15, pp. 12290–12297, 2016, doi: 10.1039/C5RA22659G.
- [102] A. Walsh, Y. Yan, M. N. Huda, M. M. Al-Jassim, and S.-H. Wei, ‘Band Edge Electronic Structure of BiVO<sub>4</sub>: Elucidating the Role of the Bi s and V d Orbitals’, *Chem. Mater.*, vol. 21, no. 3, pp. 547–551, Feb. 2009, doi: 10.1021/cm802894z.
- [103] J. K. Cooper *et al.*, ‘Electronic Structure of Monoclinic BiVO<sub>4</sub>’, *Chem. Mater.*, vol. 26, no. 18, pp. 5365–5373, Sep. 2014, doi: 10.1021/cm5025074.
- [104] K. Ding, B. Chen, Z. Fang, Y. Zhang, and Z. Chen, ‘Why the photocatalytic activity of Mo-doped BiVO<sub>4</sub> is enhanced: a comprehensive density functional study’, *Phys. Chem. Chem. Phys.*, vol. 16, no. 26, p. 13465, 2014, doi: 10.1039/c4cp01350f.
- [105] M. I. Díez-García and R. Gómez, ‘Progress in Ternary Metal Oxides as Photocathodes for Water Splitting Cells: Optimization Strategies’, *Solar RRL*, vol. 6, no. 4, p. 2100871, Apr. 2022, doi: 10.1002/solr.202100871.
- [106] S. Hussain *et al.*, ‘Fabrication of CuFe<sub>2</sub>O<sub>4</sub>/ $\alpha$ -Fe<sub>2</sub>O<sub>3</sub> Composite Thin Films on FTO Coated Glass and 3-D Nanospine Structures for Efficient Photoelectrochemical Water Splitting’, *ACS Appl. Mater. Interfaces*, vol. 8, no. 51, pp. 35315–35322, Dec. 2016, doi: 10.1021/acsami.6b12460.
- [107] I. N. Reddy, V. R. Lebaka, S. V. Chinni, R. Gobinath, J. Shim, and C. Bai, ‘Applied Potential Effect on ZnFe<sub>2</sub>O<sub>4</sub>-Fe<sub>2</sub>O<sub>3</sub> Heterostructure for Generation of Photocurrents under Irradiation’, *Crystals*, vol. 12, no. 12, p. 1726, Nov. 2022, doi: 10.3390/cryst12121726.
- [108] I. Sullivan, B. Zoellner, and P. A. Maggard, ‘Copper(I)-Based *p*-Type Oxides for Photoelectrochemical and Photovoltaic Solar Energy Conversion’, *Chem. Mater.*, vol. 28, no. 17, pp. 5999–6016, Sep. 2016, doi: 10.1021/acs.chemmater.6b00926.
- [109] D. Hu *et al.*, ‘Copper(II) tungstate nanoflake array films: sacrificial template synthesis, hydrogen treatment, and their application as photoanodes in solar water splitting’, *Nanoscale*, vol. 8, no. 11, pp. 5892–5901, 2016, doi: 10.1039/C5NR09210H.

- [110] C. R. Lhermitte and B. M. Bartlett, 'Advancing the Chemistry of  $\text{CuWO}_4$  for Photoelectrochemical Water Oxidation', *Acc. Chem. Res.*, vol. 49, no. 6, pp. 1121–1129, Jun. 2016, doi: 10.1021/acs.accounts.6b00045.
- [111] W. Ye, F. Chen, F. Zhao, N. Han, and Y. Li, 'CuWO<sub>4</sub> Nanoflake Array-Based Single-Junction and Heterojunction Photoanodes for Photoelectrochemical Water Oxidation', *ACS Appl. Mater. Interfaces*, vol. 8, no. 14, pp. 9211–9217, Apr. 2016, doi: 10.1021/acsami.6b03176.
- [112] Y. Gao, O. Zandi, and T. W. Hamann, 'Atomic layer stack deposition-annealing synthesis of  $\text{CuWO}_4$ ', *J. Mater. Chem. A*, vol. 4, no. 8, pp. 2826–2830, 2016, doi: 10.1039/C5TA06899A.
- [113] J. E. Yourey, K. J. Pyper, J. B. Kurtz, and B. M. Bartlett, 'Chemical Stability of  $\text{CuWO}_4$  for Photoelectrochemical Water Oxidation', *J. Phys. Chem. C*, vol. 117, no. 17, pp. 8708–8718, May 2013, doi: 10.1021/jp402048b.
- [114] H. Zhang *et al.*, 'Incorporation of Ag nanowires in  $\text{CuWO}_4$  for improved visible light-induced photoanode performance', *J. Mater. Chem. A*, vol. 3, no. 18, pp. 9638–9644, 2015, doi: 10.1039/C4TA07213H.
- [115] D. Kang, J. C. Hill, Y. Park, and K.-S. Choi, 'Photoelectrochemical Properties and Photostabilities of High Surface Area  $\text{CuBi}_2\text{O}_4$  and Ag-Doped  $\text{CuBi}_2\text{O}_4$  Photocathodes', *Chem. Mater.*, vol. 28, no. 12, pp. 4331–4340, Jun. 2016, doi: 10.1021/acs.chemmater.6b01294.
- [116] S. P. Berglund, F. F. Abdi, P. Bogdanoff, A. Chemseddine, D. Friedrich, and R. van de Krol, 'Comprehensive Evaluation of  $\text{CuBi}_2\text{O}_4$  as a Photocathode Material for Photoelectrochemical Water Splitting', *Chem. Mater.*, vol. 28, no. 12, pp. 4231–4242, Jun. 2016, doi: 10.1021/acs.chemmater.6b00830.
- [117] Y. Nakabayashi, M. Nishikawa, and Y. Nosaka, 'Fabrication of  $\text{CuBi}_2\text{O}_4$  photocathode through novel anodic electrodeposition for solar hydrogen production', *Electrochimica Acta*, vol. 125, pp. 191–198, Apr. 2014, doi: 10.1016/j.electacta.2014.01.088.
- [118] R. Patil, S. Kelkar, R. Naphade, and S. Ogale, 'Low temperature grown  $\text{CuBi}_2\text{O}_4$  with flower morphology and its composite with CuO nanosheets for photoelectrochemical water splitting', *J. Mater. Chem. A*, vol. 2, no. 10, pp. 3661–3668, 2014, doi: 10.1039/C3TA14906D.
- [119] A. Renaud *et al.*, 'CuGaO<sub>2</sub>: a promising alternative for NiO in p-type dye solar cells', *J. Mater. Chem.*, vol. 22, no. 29, p. 14353, 2012, doi: 10.1039/c2jm31908j.
- [120] J. Ahmed *et al.*, 'Scalable synthesis of delafossite  $\text{CuAlO}_2$  nanoparticles for p-type dye-sensitized solar cells applications', *Journal of Alloys and Compounds*, vol. 591, pp. 275–279, Apr. 2014, doi: 10.1016/j.jallcom.2013.12.199.
- [121] U. Kang *et al.*, 'Photosynthesis of formate from  $\text{CO}_2$  and water at 1% energy efficiency via copper iron oxide catalysis', *Energy Environ. Sci.*, vol. 8, no. 9, pp. 2638–2643, 2015, doi: 10.1039/C5EE01410G.
- [122] M. S. Prévot, N. Guijarro, and K. Sivula, 'Enhancing the Performance of a Robust Sol-Gel-Processed p-Type Delafossite  $\text{CuFeO}_2$  Photocathode for Solar Water Reduction', *ChemSusChem*, vol. 8, no. 8, pp. 1359–1367, Apr. 2015, doi: 10.1002/cssc.201403146.
- [123] C. G. Read, Y. Park, and K.-S. Choi, 'Electrochemical Synthesis of p-Type  $\text{CuFeO}_2$  Electrodes for Use in a Photoelectrochemical Cell', *J. Phys. Chem. Lett.*, vol. 3, no. 14, pp. 1872–1876, Jul. 2012, doi: 10.1021/jz300709t.
- [124] Y. Oh, W. Yang, J. Kim, S. Jeong, and J. Moon, 'Enhanced Photocurrent of Transparent  $\text{CuFeO}_2$  Photocathodes by Self-Light-Harvesting Architecture', *ACS Appl. Mater. Interfaces*, vol. 9, no. 16, pp. 14078–14087, Apr. 2017, doi: 10.1021/acsami.7b01208.
- [125] Y. J. Jang, Y. B. Park, H. E. Kim, Y. H. Choi, S. H. Choi, and J. S. Lee, 'Oxygen-Intercalated  $\text{CuFeO}_2$  Photocathode Fabricated by Hybrid Microwave Annealing for Efficient Solar Hydrogen Production', *Chem. Mater.*, vol. 28, no. 17, pp. 6054–6061, Sep. 2016, doi: 10.1021/acs.chemmater.6b00460.
- [126] Q. Yu *et al.*, 'A highly durable p-LaFeO<sub>3</sub>/n-Fe<sub>2</sub>O<sub>3</sub> photocell for effective water splitting under visible light', *Chem. Commun.*, vol. 51, no. 17, pp. 3630–3633, 2015, doi: 10.1039/C4CC09240F.
- [127] P. Tang, Y. Tong, H. Chen, F. Cao, and G. Pan, 'Microwave-assisted synthesis of nanoparticulate perovskite LaFeO<sub>3</sub> as a high active visible-light photocatalyst', *Current Applied Physics*, vol. 13, no. 2, pp. 340–343, Mar. 2013, doi: 10.1016/j.cap.2012.08.006.



- [128] M. I. Díez-García and R. Gómez, ‘Metal Doping to Enhance the Photoelectrochemical Behavior of LaFeO<sub>3</sub> Photocathodes’, *ChemSusChem*, vol. 10, no. 11, pp. 2457–2463, Jun. 2017, doi: 10.1002/cssc.201700166.
- [129] I. E. Castelli, J. M. García-Lastra, K. S. Thygesen, and K. W. Jacobsen, ‘Bandgap calculations and trends of organometal halide perovskites’, *APL Materials*, vol. 2, no. 8, p. 081514, Aug. 2014, doi: 10.1063/1.4893495.
- [130] M. Saliba *et al.*, ‘Cesium-containing triple cation perovskite solar cells: improved stability, reproducibility and high efficiency’, *Energy Environ. Sci.*, vol. 9, no. 6, pp. 1989–1997, 2016, doi: 10.1039/C5EE03874J.
- [131] J. Luo *et al.*, ‘Water photolysis at 12.3% efficiency via perovskite photovoltaics and Earth-abundant catalysts’, *Science*, vol. 345, no. 6204, pp. 1593–1596, Sep. 2014, doi: 10.1126/science.1258307.
- [132] Y. Liu, Y. Guo, Y. Liu, Z. Wei, K. Wang, and Z. Shi, ‘A Mini Review on Transition Metal Chalcogenides for Electrocatalytic Water Splitting: Bridging Material Design and Practical Application’, *Energy Fuels*, vol. 37, no. 4, pp. 2608–2630, Feb. 2023, doi: 10.1021/acs.energyfuels.2c03833.
- [133] B. Luo, G. Liu, and L. Wang, ‘Recent advances in 2D materials for photocatalysis’, *Nanoscale*, vol. 8, no. 13, pp. 6904–6920, 2016, doi: 10.1039/C6NR00546B.
- [134] R. Li *et al.*, ‘Flexible and high-performance electrochromic devices enabled by self-assembled 2D TiO<sub>2</sub>/MXene heterostructures’, *Nat Commun*, vol. 12, no. 1, p. 1587, Mar. 2021, doi: 10.1038/s41467-021-21852-7.
- [135] K. F. Mak, C. Lee, J. Hone, J. Shan, and T. F. Heinz, ‘Atomically Thin MoS<sub>2</sub>: A New Direct-Gap Semiconductor’, *Phys. Rev. Lett.*, vol. 105, no. 13, p. 136805, Sep. 2010, doi: 10.1103/PhysRevLett.105.136805.
- [136] T. L. Tan, M.-F. Ng, and G. Eda, ‘Stable Monolayer Transition Metal Dichalcogenide Ordered Alloys with Tunable Electronic Properties’, *J. Phys. Chem. C*, vol. 120, no. 5, pp. 2501–2508, Feb. 2016, doi: 10.1021/acs.jpcc.5b10739.
- [137] A. K. Singh, K. Mathew, H. L. Zhuang, and R. G. Hennig, ‘Computational Screening of 2D Materials for Photocatalysis’, *J. Phys. Chem. Lett.*, vol. 6, no. 6, pp. 1087–1098, Mar. 2015, doi: 10.1021/jz502646d.
- [138] D. Deng, K. S. Novoselov, Q. Fu, N. Zheng, Z. Tian, and X. Bao, ‘Catalysis with two-dimensional materials and their heterostructures’, *Nature Nanotech*, vol. 11, no. 3, pp. 218–230, Mar. 2016, doi: 10.1038/nnano.2015.340.
- [139] X. Yu, M. S. Prévot, N. Guijarro, and K. Sivula, ‘Self-assembled 2D WSe<sub>2</sub> thin films for photoelectrochemical hydrogen production’, *Nat Commun*, vol. 6, no. 1, p. 7596, Jul. 2015, doi: 10.1038/ncomms8596.
- [140] Y. Sun *et al.*, ‘Freestanding Tin Disulfide Single-Layers Realizing Efficient Visible-Light Water Splitting’, *Angew. Chem. Int. Ed.*, vol. 51, no. 35, pp. 8727–8731, Aug. 2012, doi: 10.1002/anie.201204675.
- [141] L. Yu *et al.*, ‘Iron Chalcogenide Photovoltaic Absorbers’, *Adv. Energy Mater.*, vol. 1, no. 5, pp. 748–753, Oct. 2011, doi: 10.1002/aenm.201100351.
- [142] M.-L. Tsai *et al.*, ‘Monolayer MoS<sub>2</sub> Heterojunction Solar Cells’, *ACS Nano*, vol. 8, no. 8, pp. 8317–8322, Aug. 2014, doi: 10.1021/nn502776h.
- [143] *Solid State Physics*. Elsevier, 2000. doi: 10.1016/B978-0-12-304460-0.X5000-2.
- [144] S. Latini, T. Olsen, and K. S. Thygesen, ‘Excitons in van der Waals heterostructures: The important role of dielectric screening’, *Phys. Rev. B*, vol. 92, no. 24, p. 245123, Dec. 2015, doi: 10.1103/PhysRevB.92.245123.
- [145] Y. Xu, W. Zhao, R. Xu, Y. Shi, and B. Zhang, ‘Synthesis of ultrathin CdS nanosheets as efficient visible-light-driven water splitting photocatalysts for hydrogen evolution’, *Chem. Commun.*, vol. 49, no. 84, p. 9803, 2013, doi: 10.1039/c3cc46342g.
- [146] A. Pareek, A. Gopalakrishnan, and P. H. Borse, ‘Efficiency and stability aspects of CdS photoanode for solar hydrogen generation technology’, *J. Phys.: Conf. Ser.*, vol. 755, p. 012006, Oct. 2016, doi: 10.1088/1742-6596/755/1/012006.
- [147] A. Pareek, R. Purbia, P. Paik, N. Y. Hebalkar, H. G. Kim, and P. H. Borse, ‘Stabilizing effect in nano-titania functionalized CdS photoanode for sustained hydrogen generation’, *International*

- Journal of Hydrogen Energy*, vol. 39, no. 9, pp. 4170–4180, Mar. 2014, doi: 10.1016/j.ijhydene.2013.12.185.
- [148] A. Pareek, P. Paik, and P. H. Borse, ‘Nanoniobia Modification of CdS Photoanode for an Efficient and Stable Photoelectrochemical Cell’, *Langmuir*, vol. 30, no. 51, pp. 15540–15549, Dec. 2014, doi: 10.1021/la503713t.
- [149] Y. Kageshima, H. Kumagai, T. Hisatomi, T. Minegishi, J. Kubota, and K. Domen, ‘Photoelectrochemical Solar Cells Consisting of a Pt-Modified CdS Photoanode and an  $\text{Fe}(\text{ClO}_4)_2/\text{Fe}(\text{ClO}_4)_3$  Redox Shuttle in a Nonaqueous Electrolyte’, *J. Phys. Chem. C*, vol. 120, no. 20, pp. 10781–10790, May 2016, doi: 10.1021/acs.jpcc.6b02406.
- [150] X. Chen and W. Shangguan, ‘Hydrogen production from water splitting on CdS-based photocatalysts using solar light’, *Front. Energy*, vol. 7, no. 1, pp. 111–118, Mar. 2013, doi: 10.1007/s11708-012-0228-4.
- [151] M. D. Bhatt and J. S. Lee, ‘Recent theoretical progress in the development of photoanode materials for solar water splitting photoelectrochemical cells’, *J. Mater. Chem. A*, vol. 3, no. 20, pp. 10632–10659, 2015, doi: 10.1039/C5TA00257E.
- [152] Z.-G. Chen *et al.*, ‘ZnS Branched Architectures as Optoelectronic Devices and Field Emitters’, *Adv. Mater.*, vol. 22, no. 21, pp. 2376–2380, Jun. 2010, doi: 10.1002/adma.200903643.
- [153] C.-M. Huang, L.-C. Chen, G.-T. Pan, T. C. K. Yang, W.-S. Chang, and K.-W. Cheng, ‘Effect of Ni on the growth and photoelectrochemical properties of ZnS thin films’, *Materials Chemistry and Physics*, vol. 117, no. 1, pp. 156–162, Sep. 2009, doi: 10.1016/j.matchemphys.2009.05.026.
- [154] M. Öztaş, M. Bedir, A. Necmeddin Yazici, E. Vural Kafadar, and H. Toktamış, ‘Characterization of copper-doped sprayed ZnS thin films’, *Physica B: Condensed Matter*, vol. 381, no. 1–2, pp. 40–46, May 2006, doi: 10.1016/j.physb.2005.12.248.
- [155] F. Kurnia, Y. H. Ng, R. Amal, N. Valanoor, and J. N. Hart, ‘Defect engineering of ZnS thin films for photoelectrochemical water-splitting under visible light’, *Solar Energy Materials and Solar Cells*, vol. 153, pp. 179–185, Aug. 2016, doi: 10.1016/j.solmat.2016.04.021.
- [156] J. Yuan *et al.*, ‘Fabrication of CuInS<sub>2</sub> thin film by electrodeposition of Cu–In alloy’, *Vacuum*, vol. 99, pp. 196–203, Jan. 2014, doi: 10.1016/j.vacuum.2013.06.005.
- [157] M. Krunks, O. Bijakina, T. Varema, V. Mikli, and E. Mellikov, ‘Structural and optical properties of sprayed CuInS<sub>2</sub> films’, *Thin Solid Films*, vol. 338, no. 1–2, pp. 125–130, Jan. 1999, doi: 10.1016/S0040-6090(98)01069-4.
- [158] J. Klaer *et al.*, ‘Efficient thin-film solar cells prepared by a sequential process’, *Semicond. Sci. Technol.*, vol. 13, no. 12, pp. 1456–1458, Dec. 1998, doi: 10.1088/0268-1242/13/12/022.
- [159] A. Iwase, Y. H. Ng, R. Amal, and A. Kudo, ‘Solar hydrogen evolution using a CuGaS<sub>2</sub> photocathode improved by incorporating reduced graphene oxide’, *J. Mater. Chem. A*, vol. 3, no. 16, pp. 8566–8570, 2015, doi: 10.1039/C5TA01237F.
- [160] Q. Li *et al.*, ‘The effect of Zn incorporation on the optical band gap of CuGaS<sub>2</sub>: Ti thin films’, *Materials Letters*, vol. 210, pp. 70–72, Jan. 2018, doi: 10.1016/j.matlet.2017.08.128.
- [161] R. Marchand, Y. Laurent, J. Guyader, P. L’Haridon, and P. Verdier, ‘Nitrides and oxynitrides: Preparation, crystal chemistry and properties’, *Journal of the European Ceramic Society*, vol. 8, no. 4, pp. 197–213, Jan. 1991, doi: 10.1016/0955-2219(91)90096-I.
- [162] D. Yamasita, ‘Recent progress of visible-light-driven heterogeneous photocatalysts for overall water splitting’, *Solid State Ionics*, vol. 172, no. 1–4, pp. 591–595, Aug. 2004, doi: 10.1016/j.ssi.2004.04.033.
- [163] K. Maeda *et al.*, ‘GaN:ZnO Solid Solution as a Photocatalyst for Visible-Light-Driven Overall Water Splitting’, *J. Am. Chem. Soc.*, vol. 127, no. 23, pp. 8286–8287, Jun. 2005, doi: 10.1021/ja0518777.
- [164] K. Maeda *et al.*, ‘Overall Water Splitting on  $(\text{Ga}_{1-x}\text{Zn}_x)(\text{N}_{1-x}\text{O}_x)$  Solid Solution Photocatalyst: Relationship between Physical Properties and Photocatalytic Activity’, *J. Phys. Chem. B*, vol. 109, no. 43, pp. 20504–20510, Nov. 2005, doi: 10.1021/jp053499y.
- [165] M. Higashi, K. Domen, and R. Abe, ‘Highly Stable Water Splitting on Oxynitride TaON Photoanode System under Visible Light Irradiation’, *J. Am. Chem. Soc.*, vol. 134, no. 16, pp. 6968–6971, Apr. 2012, doi: 10.1021/ja302059g.

- [166] G. Hitoki, T. Takata, J. N. Kondo, M. Hara, H. Kobayashi, and K. Domen, 'An oxynitride, TaON, as an efficient water oxidation photocatalyst under visible light irradiation ( $\lambda \leq 500$  nm)', *Chem. Commun.*, no. 16, pp. 1698–1699, 2002, doi: 10.1039/B202393H.
- [167] K. Maeda and K. Domen, 'New Non-Oxide Photocatalysts Designed for Overall Water Splitting under Visible Light', *J. Phys. Chem. C*, vol. 111, no. 22, pp. 7851–7861, Jun. 2007, doi: 10.1021/jp070911w.
- [168] M. Hara, J. Nunoshige, T. Takata, J. N. Kondo, and K. Domen, 'Unusual enhancement of H<sub>2</sub> evolution by Ru on TaON photocatalyst under visible light irradiation', *Chem. Commun.*, no. 24, p. 3000, 2003, doi: 10.1039/b309935k.
- [169] R. Abe, T. Takata, H. Sugihara, and K. Domen, 'The Use of TiCl<sub>4</sub> Treatment to Enhance the Photocurrent in a TaON Photoelectrode under Visible Light Irradiation', *Chem. Lett.*, vol. 34, no. 8, pp. 1162–1163, Aug. 2005, doi: 10.1246/cl.2005.1162.
- [170] H. S. Gujral *et al.*, 'Metal nitride-based nanostructures for electrochemical and photocatalytic hydrogen production', *Science and Technology of Advanced Materials*, vol. 23, no. 1, pp. 76–119, Dec. 2022, doi: 10.1080/14686996.2022.2029686.
- [171] M. Hara, E. Chiba, A. Ishikawa, T. Takata, J. N. Kondo, and K. Domen, 'Ta<sub>3</sub>N<sub>5</sub> and TaON Thin Films on Ta Foil: Surface Composition and Stability', *J. Phys. Chem. B*, vol. 107, no. 48, pp. 13441–13445, Dec. 2003, doi: 10.1021/jp036189t.
- [172] D. Yokoyama *et al.*, 'Ta<sub>3</sub>N<sub>5</sub> photoanodes for water splitting prepared by sputtering', *Thin Solid Films*, vol. 519, no. 7, pp. 2087–2092, Jan. 2011, doi: 10.1016/j.tsf.2010.10.055.
- [173] W.-J. Chun *et al.*, 'Conduction and Valence Band Positions of Ta<sub>2</sub>O<sub>5</sub>, TaON, and Ta<sub>3</sub>N<sub>5</sub> by UPS and Electrochemical Methods', *J. Phys. Chem. B*, vol. 107, no. 8, pp. 1798–1803, Feb. 2003, doi: 10.1021/jp027593f.
- [174] A. Ziani *et al.*, 'Carrier dynamics of a visible-light-responsive Ta<sub>3</sub>N<sub>5</sub> photoanode for water oxidation', *Phys. Chem. Chem. Phys.*, vol. 17, no. 4, pp. 2670–2677, 2015, doi: 10.1039/C4CP05616G.
- [175] A. Dabirian and R. van de Krol, 'High-Temperature Ammonolysis of Thin Film Ta<sub>2</sub>O<sub>5</sub> Photoanodes: Evolution of Structural, Optical, and Photoelectrochemical Properties', *Chem. Mater.*, vol. 27, no. 3, pp. 708–715, Feb. 2015, doi: 10.1021/cm503215p.
- [176] B. A. Pinaud, P. C. K. Vesborg, and T. F. Jaramillo, 'Effect of Film Morphology and Thickness on Charge Transport in Ta<sub>3</sub>N<sub>5</sub>/Ta Photoanodes for Solar Water Splitting', *J. Phys. Chem. C*, vol. 116, no. 30, pp. 15918–15924, Aug. 2012, doi: 10.1021/jp3041742.
- [177] P. Zhang, T. Wang, J. Zhang, X. Chang, and J. Gong, 'Bridging the transport pathway of charge carriers in a Ta<sub>3</sub>N<sub>5</sub> nanotube array photoanode for solar water splitting', *Nanoscale*, vol. 7, no. 31, pp. 13153–13158, 2015, doi: 10.1039/C5NR03013G.
- [178] L. Zhang *et al.*, 'TiO<sub>2</sub>/Au Nanoring/p-Si Nanohole Photocathode for Hydrogen Generation', *ACS Appl. Nano Mater.*, vol. 2, no. 6, pp. 3654–3661, Jun. 2019, doi: 10.1021/acsanm.9b00590.
- [179] S. Kasani, K. Curtin, and N. Wu, 'A review of 2D and 3D plasmonic nanostructure array patterns: fabrication, light management and sensing applications', *Nanophotonics*, vol. 8, no. 12, pp. 2065–2089, Oct. 2019, doi: 10.1515/nanoph-2019-0158.
- [180] D. B. Ingram and S. Linic, 'Water Splitting on Composite Plasmonic-Metal/Semiconductor Photoelectrodes: Evidence for Selective Plasmon-Induced Formation of Charge Carriers near the Semiconductor Surface', *J. Am. Chem. Soc.*, vol. 133, no. 14, pp. 5202–5205, Apr. 2011, doi: 10.1021/ja200086g.
- [181] F. Han, X. Mao, and Q.-H. Xu, 'Flower-like Au/Ag/TiO<sub>2</sub> nanocomposites with enhanced photocatalytic efficiency under visible light irradiation', *Sci. China Chem.*, vol. 60, no. 4, pp. 521–527, Apr. 2017, doi: 10.1007/s11426-016-9027-6.
- [182] S. W. Kang, P. R. Deshmukh, Y. Sohn, and W. G. Shin, 'Plasmonic gold sensitization of ZnO nanowires for solar water splitting', *Materials Today Communications*, vol. 21, p. 100675, Dec. 2019, doi: 10.1016/j.mtcomm.2019.100675.
- [183] D. Hu, P. Diao, D. Xu, and Q. Wu, 'Gold/WO<sub>3</sub> nanocomposite photoanodes for plasmonic solar water splitting', *Nano Res.*, vol. 9, no. 6, pp. 1735–1751, Jun. 2016, doi: 10.1007/s12274-016-1067-0.

- [184] W.-H. Hung, T.-M. Chien, and C.-M. Tseng, 'Enhanced Photocatalytic Water Splitting by Plasmonic  $\text{TiO}_2$ - $\text{Fe}_2\text{O}_3$  Cocatalyst under Visible Light Irradiation', *J. Phys. Chem. C*, vol. 118, no. 24, pp. 12676–12681, Jun. 2014, doi: 10.1021/jp5033965.
- [185] P. Subramanyam, B. Meena, G. N. Sinha, M. Deepa, and C. Subrahmanyam, 'Decoration of plasmonic Cu nanoparticles on  $\text{WO}_3/\text{Bi}_2\text{S}_3$  QDs heterojunction for enhanced photoelectrochemical water splitting', *International Journal of Hydrogen Energy*, vol. 45, no. 13, pp. 7706–7715, Mar. 2020, doi: 10.1016/j.ijhydene.2019.05.168.
- [186] S. Kim *et al.*, 'Plasmonic gold nanoparticle-decorated  $\text{BiVO}_4/\text{ZnO}$  nanowire heterostructure photoanodes for efficient water oxidation', *Catal. Sci. Technol.*, vol. 8, no. 15, pp. 3759–3766, 2018, doi: 10.1039/C8CY00685G.
- [187] C. Hu *et al.*, 'Plasmonic Au functionalized 3D  $\text{SrTiO}_3/\text{TiO}_2$  hollow nanosphere enables efficient solar water splitting', *Journal of Alloys and Compounds*, vol. 930, p. 167449, Jan. 2023, doi: 10.1016/j.jallcom.2022.167449.
- [188] A. Otto, 'Excitation of nonradiative surface plasma waves in silver by the method of frustrated total reflection', *Z. Physik*, vol. 216, no. 4, pp. 398–410, Aug. 1968, doi: 10.1007/BF01391532.
- [189] E. Kretschmann and H. Raether, 'Notizen: Radiative Decay of Non Radiative Surface Plasmons Excited by Light', *Zeitschrift für Naturforschung A*, vol. 23, no. 12, pp. 2135–2136, Dec. 1968, doi: 10.1515/zna-1968-1247.
- [190] J. R. Lakowicz, 'Plasmonics in Biology and Plasmon-Controlled Fluorescence', *Plasmonics*, vol. 1, no. 1, pp. 5–33, Mar. 2006, doi: 10.1007/s11468-005-9002-3.
- [191] J. Dostálek and W. Knoll, 'Biosensors based on surface plasmon-enhanced fluorescence spectroscopy (Review)', *Biointerphases*, vol. 3, no. 3, pp. FD12–FD22, Sep. 2008, doi: 10.1116/1.2994688.
- [192] W. Ahn, D. C. Ratchford, P. E. Pehrsson, and B. S. Simpkins, 'Surface plasmon polariton-induced hot carrier generation for photocatalysis', *Nanoscale*, vol. 9, no. 9, pp. 3010–3022, 2017, doi: 10.1039/C6NR09280B.
- [193] J. Li, S. K. Cushing, P. Zheng, F. Meng, D. Chu, and N. Wu, 'Plasmon-induced photonic and energy-transfer enhancement of solar water splitting by a hematite nanorod array', *Nat Commun*, vol. 4, no. 1, p. 2651, Oct. 2013, doi: 10.1038/ncomms3651.
- [194] R. G. Stephen and F. L. Riley, 'Oxidation of silicon by water', *Journal of the European Ceramic Society*, vol. 5, no. 4, pp. 219–222, Jan. 1989, doi: 10.1016/S0955-2219(89)80003-2.
- [195] R. M. Candea, M. Kastner, R. Goodman, and N. Hickok, 'Photoelectrolysis of water: Si in salt water', *Journal of Applied Physics*, vol. 47, no. 6, pp. 2724–2726, Jun. 1976, doi: 10.1063/1.322995.
- [196] L. Shen *et al.*, 'Nanostructured Silicon Photocathodes for Solar Water Splitting Patterned by the Self-Assembly of Lamellar Block Copolymers', *ACS Appl. Mater. Interfaces*, vol. 7, no. 47, pp. 26043–26049, Dec. 2015, doi: 10.1021/acsami.5b08661.
- [197] K. Sun, S. Shen, Y. Liang, P. E. Burrows, S. S. Mao, and D. Wang, 'Enabling Silicon for Solar-Fuel Production', *Chem. Rev.*, vol. 114, no. 17, pp. 8662–8719, Sep. 2014, doi: 10.1021/cr300459q.
- [198] H. Gerischer, 'On the stability of semiconductor electrodes against photodecomposition', *Journal of Electroanalytical Chemistry and Interfacial Electrochemistry*, vol. 82, no. 1–2, pp. 133–143, Sep. 1977, doi: 10.1016/S0022-0728(77)80253-2.
- [199] S. Hu, N. S. Lewis, J. W. Ager, J. Yang, J. R. McKone, and N. C. Strandwitz, 'Thin-Film Materials for the Protection of Semiconducting Photoelectrodes in Solar-Fuel Generators', *J. Phys. Chem. C*, vol. 119, no. 43, pp. 24201–24228, Oct. 2015, doi: 10.1021/acs.jpcc.5b05976.
- [200] S. W. Boettcher *et al.*, 'Photoelectrochemical Hydrogen Evolution Using Si Microwire Arrays', *J. Am. Chem. Soc.*, vol. 133, no. 5, pp. 1216–1219, Feb. 2011, doi: 10.1021/ja108801m.
- [201] B. Seger *et al.*, 'Hydrogen Production Using a Molybdenum Sulfide Catalyst on a Titanium-Protected n+p-Silicon Photocathode', *Angew. Chem. Int. Ed.*, vol. 51, no. 36, pp. 9128–9131, Sep. 2012, doi: 10.1002/anie.201203585.
- [202] D. Bae *et al.*, 'Protection of Si photocathode using  $\text{TiO}_2$  deposited by high power impulse magnetron sputtering for  $\text{H}_2$  evolution in alkaline media', *Solar Energy Materials and Solar Cells*, vol. 144, pp. 758–765, Jan. 2016, doi: 10.1016/j.solmat.2015.10.020.

- [203] B. Mei *et al.*, ‘Crystalline TiO<sub>2</sub>: A Generic and Effective Electron-Conducting Protection Layer for Photoanodes and -cathodes’, *J. Phys. Chem. C*, vol. 119, no. 27, pp. 15019–15027, Jul. 2015, doi: 10.1021/acs.jpcc.5b04407.
- [204] S. Y. Reece *et al.*, ‘Wireless Solar Water Splitting Using Silicon-Based Semiconductors and Earth-Abundant Catalysts’, *Science*, vol. 334, no. 6056, pp. 645–648, Nov. 2011, doi: 10.1126/science.1209816.
- [205] X.-Q. Bao and L. Liu, ‘Improved photo-stability of silicon nanobelt arrays by atomic layer deposition for efficient photocatalytic hydrogen evolution’, *Journal of Power Sources*, vol. 268, pp. 677–682, Dec. 2014, doi: 10.1016/j.jpowsour.2014.06.098.
- [206] L. Ji *et al.*, ‘A silicon-based photocathode for water reduction with an epitaxial SrTiO<sub>3</sub> protection layer and a nanostructured catalyst’, *Nature Nanotech*, vol. 10, no. 1, pp. 84–90, Jan. 2015, doi: 10.1038/nnano.2014.277.
- [207] D. Bae *et al.*, ‘Back-illuminated Si photocathode: a combined experimental and theoretical study for photocatalytic hydrogen evolution’, *Energy Environ. Sci.*, vol. 8, no. 2, pp. 650–660, 2015, doi: 10.1039/C4EE03723E.
- [208] J. Oh, T. G. Deutsch, H.-C. Yuan, and H. M. Branz, ‘Nanoporous black silicon photocathode for H<sub>2</sub> production by photoelectrochemical water splitting’, *Energy Environ. Sci.*, vol. 4, no. 5, p. 1690, 2011, doi: 10.1039/c1ee01124c.
- [209] I. Oh, J. Kye, and S. Hwang, ‘Enhanced Photoelectrochemical Hydrogen Production from Silicon Nanowire Array Photocathode’, *Nano Lett.*, vol. 12, no. 1, pp. 298–302, Jan. 2012, doi: 10.1021/nl203564s.
- [210] Y. Wang, W. Tian, F. Cao, D. Fang, S. Chen, and L. Li, ‘Boosting PEC performance of Si photoelectrodes by coupling bifunctional CuCo hybrid oxide cocatalysts’, *Nanotechnology*, vol. 29, no. 42, p. 425703, Oct. 2018, doi: 10.1088/1361-6528/aad7a0.
- [211] C.-J. Chen *et al.*, ‘Wide Range pH-Tolerable Silicon@Pyrite Cobalt Dichalcogenide Microwire Array Photoelectrodes for Solar Hydrogen Evolution’, *ACS Appl. Mater. Interfaces*, vol. 8, no. 8, pp. 5400–5407, Mar. 2016, doi: 10.1021/acsami.6b00027.
- [212] X. Ao *et al.*, ‘Black silicon with controllable macropore array for enhanced photoelectrochemical performance’, *Appl. Phys. Lett.*, vol. 101, no. 11, p. 111901, Sep. 2012, doi: 10.1063/1.4752231.
- [213] R. Fan *et al.*, ‘Stable and efficient multi-crystalline n<sup>+</sup>p silicon photocathode for H<sub>2</sub> production with pyramid-like surface nanostructure and thin Al<sub>2</sub>O<sub>3</sub> protective layer’, *Appl. Phys. Lett.*, vol. 106, no. 1, p. 013902, Jan. 2015, doi: 10.1063/1.4905511.
- [214] R. Fan *et al.*, ‘n-type silicon photocathodes with Al-doped rear p<sup>+</sup> emitter and Al<sub>2</sub>O<sub>3</sub>-coated front surface for efficient and stable H<sub>2</sub> production’, *Appl. Phys. Lett.*, vol. 106, no. 21, p. 213901, May 2015, doi: 10.1063/1.4921845.
- [215] J.-Y. Jung *et al.*, ‘Photoelectrochemical water splitting employing a tapered silicon nanohole array’, *J. Mater. Chem. A*, vol. 2, no. 3, pp. 833–842, 2014, doi: 10.1039/C3TA14439A.
- [216] H. K. Raut, V. A. Ganesh, A. S. Nair, and S. Ramakrishna, ‘Anti-reflective coatings: A critical, in-depth review’, *Energy Environ. Sci.*, vol. 4, no. 10, p. 3779, 2011, doi: 10.1039/c1ee01297e.
- [217] S. W. Boettcher *et al.*, ‘Energy-Conversion Properties of Vapor-Liquid-Solid-Grown Silicon Wire-Array Photocathodes’, *Science*, vol. 327, no. 5962, pp. 185–187, Jan. 2010, doi: 10.1126/science.1180783.
- [218] J. R. McKone *et al.*, ‘Evaluation of Pt, Ni, and Ni–Mo electrocatalysts for hydrogen evolution on crystalline Si electrodes’, *Energy Environ. Sci.*, vol. 4, no. 9, p. 3573, 2011, doi: 10.1039/c1ee01488a.
- [219] G. Yuan, K. Aruda, S. Zhou, A. Levine, J. Xie, and D. Wang, ‘Understanding the Origin of the Low Performance of Chemically Grown Silicon Nanowires for Solar Energy Conversion’, *Angew. Chem. Int. Ed.*, vol. 50, no. 10, pp. 2334–2338, Mar. 2011, doi: 10.1002/anie.201006617.
- [220] M. F. Lichterman *et al.*, ‘Protection of inorganic semiconductors for sustained, efficient photoelectrochemical water oxidation’, *Catalysis Today*, vol. 262, pp. 11–23, Mar. 2016, doi: 10.1016/j.cattod.2015.08.017.
- [221] D. Bae, B. Seger, P. C. K. Vesborg, O. Hansen, and I. Chorkendorff, ‘Strategies for stable water splitting via protected photoelectrodes’, *Chem. Soc. Rev.*, vol. 46, no. 7, pp. 1933–1954, 2017, doi: 10.1039/C6CS00918B.

- [222] M. J. Choi, J.-Y. Jung, M.-J. Park, J.-W. Song, J.-H. Lee, and J. H. Bang, 'Long-term durable silicon photocathode protected by a thin Al<sub>2</sub>O<sub>3</sub>/SiO<sub>x</sub> layer for photoelectrochemical hydrogen evolution', *J. Mater. Chem. A*, vol. 2, no. 9, p. 2928, 2014, doi: 10.1039/c3ta14443g.
- [223] B. Hoex, S. B. S. Heil, E. Langereis, M. C. M. Van De Sanden, and W. M. M. Kessels, 'Ultralow surface recombination of c-Si substrates passivated by plasma-assisted atomic layer deposited Al<sub>2</sub>O<sub>3</sub>', *Applied Physics Letters*, vol. 89, no. 4, p. 042112, Jul. 2006, doi: 10.1063/1.2240736.
- [224] J. Liang *et al.*, 'A thin-film silicon based photocathode with a hydrogen doped TiO<sub>2</sub> protection layer for solar hydrogen evolution', *J. Mater. Chem. A*, vol. 4, no. 43, pp. 16841–16848, 2016, doi: 10.1039/C6TA07701C.
- [225] Y. W. Chen *et al.*, 'Atomic layer-deposited tunnel oxide stabilizes silicon photoanodes for water oxidation', *Nature Mater*, vol. 10, no. 7, pp. 539–544, Jul. 2011, doi: 10.1038/nmat3047.
- [226] H. Gerischer, 'Charge transfer processes at semiconductor-electrolyte interfaces in connection with problems of catalysis', *Surface Science*, vol. 18, no. 1, pp. 97–122, Nov. 1969, doi: 10.1016/0039-6028(69)90269-6.
- [227] G. A. Shreve and N. S. Lewis, 'An Analytical Description of the Consequences of Abandoning the Principles of Detailed Balance and Microscopic Reversibility in Semiconductor Photoelectrochemistry', *J. Electrochem. Soc.*, vol. 142, no. 1, pp. 112–119, Jan. 1995, doi: 10.1149/1.2043848.
- [228] M. S. Wrighton, 'Thermodynamics and kinetics associated with semiconductor-based photoelectrochemical cells for the conversion of light to chemical energy', *Pure and Applied Chemistry*, vol. 57, no. 1, pp. 57–68, Jan. 1985, doi: 10.1351/pac198557010057.
- [229] T. Reier, M. Oezaslan, and P. Strasser, 'Electrocatalytic Oxygen Evolution Reaction (OER) on Ru, Ir, and Pt Catalysts: A Comparative Study of Nanoparticles and Bulk Materials', *ACS Catal.*, vol. 2, no. 8, pp. 1765–1772, Aug. 2012, doi: 10.1021/cs3003098.
- [230] V. Pfeifer *et al.*, 'In situ observation of reactive oxygen species forming on oxygen-evolving iridium surfaces', *Chem. Sci.*, vol. 8, no. 3, pp. 2143–2149, 2017, doi: 10.1039/C6SC04622C.
- [231] X. Li, J. Yu, J. Low, Y. Fang, J. Xiao, and X. Chen, 'Engineering heterogeneous semiconductors for solar water splitting', *J. Mater. Chem. A*, vol. 3, no. 6, pp. 2485–2534, 2015, doi: 10.1039/C4TA04461D.
- [232] H. She, P. Yue, J. Huang, L. Wang, and Q. Wang, 'One-step hydrothermal deposition of F:FeOOH onto BiVO<sub>4</sub> photoanode for enhanced water oxidation', *Chemical Engineering Journal*, vol. 392, p. 123703, Jul. 2020, doi: 10.1016/j.cej.2019.123703.
- [233] J. R. McKone, B. F. Sadtler, C. A. Werlang, N. S. Lewis, and H. B. Gray, 'Ni–Mo Nanopowders for Efficient Electrochemical Hydrogen Evolution', *ACS Catal.*, vol. 3, no. 2, pp. 166–169, Feb. 2013, doi: 10.1021/cs300691m.
- [234] M. Zeng and Y. Li, 'Recent advances in heterogeneous electrocatalysts for the hydrogen evolution reaction', *J. Mater. Chem. A*, vol. 3, no. 29, pp. 14942–14962, 2015, doi: 10.1039/C5TA02974K.
- [235] Y. Hou, X. Zhuang, and X. Feng, 'Recent Advances in Earth-Abundant Heterogeneous Electrocatalysts for Photoelectrochemical Water Splitting', *Small Methods*, vol. 1, no. 6, p. 1700090, Jun. 2017, doi: 10.1002/smt.201700090.
- [236] J. Kibsgaard, Z. Chen, B. N. Reinecke, and T. F. Jaramillo, 'Engineering the surface structure of MoS<sub>2</sub> to preferentially expose active edge sites for electrocatalysis', *Nature Mater*, vol. 11, no. 11, pp. 963–969, Nov. 2012, doi: 10.1038/nmat3439.
- [237] F. Wang *et al.*, 'Interface Engineered W<sub>x</sub>C@WS<sub>2</sub> Nanostructure for Enhanced Hydrogen Evolution Catalysis', *Adv. Funct. Mater.*, vol. 27, no. 7, p. 1605802, Feb. 2017, doi: 10.1002/adfm.201605802.
- [238] Y. Wan *et al.*, 'Tantalum Oxide Electron-Selective Heterocontacts for Silicon Photovoltaics and Photoelectrochemical Water Reduction', *ACS Energy Lett.*, vol. 3, no. 1, pp. 125–131, Jan. 2018, doi: 10.1021/acsenergylett.7b01153.
- [239] M. R. Shaner, J. R. McKone, H. B. Gray, and N. S. Lewis, 'Functional integration of Ni–Mo electrocatalysts with Si microwire array photocathodes to simultaneously achieve high fill factors and light-limited photocurrent densities for solar-driven hydrogen evolution', *Energy Environ. Sci.*, vol. 8, no. 10, pp. 2977–2984, 2015, doi: 10.1039/C5EE01076D.

- [240] J. D. Benck, S. C. Lee, K. D. Fong, J. Kibsgaard, R. Sinclair, and T. F. Jaramillo, 'Designing Active and Stable Silicon Photocathodes for Solar Hydrogen Production Using Molybdenum Sulfide Nanomaterials', *Adv. Energy Mater.*, vol. 4, no. 18, p. 1400739, Dec. 2014, doi: 10.1002/aenm.201400739.
- [241] Q. Ding *et al.*, 'Efficient Photoelectrochemical Hydrogen Generation Using Heterostructures of Si and Chemically Exfoliated Metallic MoS<sub>2</sub>', *J. Am. Chem. Soc.*, vol. 136, no. 24, pp. 8504–8507, Jun. 2014, doi: 10.1021/ja5025673.
- [242] Y. Nakato and H. Tsubomura, 'Silicon photoelectrodes modified with ultrafine metal islands', *Electrochimica Acta*, vol. 37, no. 5, pp. 897–907, Apr. 1992, doi: 10.1016/0013-4686(92)85041-I.
- [243] R. P. Srivastava and D. Khang, 'Structuring of Si into Multiple Scales by Metal-Assisted Chemical Etching', *Adv. Mater.*, vol. 33, no. 47, p. 2005932, Nov. 2021, doi: 10.1002/adma.202005932.
- [244] A. Zeniou, K. Ellinas, A. Olziersky, and E. Gogolides, 'Ultra-high aspect ratio Si nanowires fabricated with plasma etching: plasma processing, mechanical stability analysis against adhesion and capillary forces and oleophobicity', *Nanotechnology*, vol. 25, no. 3, p. 035302, Jan. 2014, doi: 10.1088/0957-4484/25/3/035302.
- [245] B. X. E. Desbiolles, A. Bertsch, and P. Renaud, 'Ion beam etching redeposition for 3D multimaterial nanostructure manufacturing', *Microsyst Nanoeng*, vol. 5, no. 1, p. 11, Apr. 2019, doi: 10.1038/s41378-019-0052-7.
- [246] E. Baquedano, R. Martinez, J. Llorens, and P. Postigo, 'Fabrication of Silicon Nanobelts and Nanopillars by Soft Lithography for Hydrophobic and Hydrophilic Photonic Surfaces', *Nanomaterials*, vol. 7, no. 5, p. 109, May 2017, doi: 10.3390/nano7050109.
- [247] R. Elbersen, W. Vrijseelaar, R. M. Tiggelaar, H. Gardeniers, and J. Huskens, 'Fabrication and Doping Methods for Silicon Nano- and Micropillar Arrays for Solar-Cell Applications: A Review', *Adv. Mater.*, vol. 27, no. 43, pp. 6781–6796, Nov. 2015, doi: 10.1002/adma.201502632.
- [248] P. Allongue, V. Costa-Kieling, and H. Gerischer, 'Etching of Silicon in NaOH Solutions: I. In Situ Scanning Tunneling Microscopic Investigation of n-Si(111)', *J. Electrochem. Soc.*, vol. 140, no. 4, pp. 1009–1018, Apr. 1993, doi: 10.1149/1.2056189.
- [249] M. A. Gosalvez, R. M. Nieminen, P. Kilpinen, E. Haimi, and V. Lindroos, 'Anisotropic wet chemical etching of crystalline silicon: atomistic Monte-Carlo simulations and experiments', *Applied Surface Science*, vol. 178, no. 1–4, pp. 7–26, Jul. 2001, doi: 10.1016/S0169-4332(01)00233-1.
- [250] R. Schuster, V. Kirchner, P. Allongue, and G. Ertl, 'Electrochemical Micromachining', *Science*, vol. 289, no. 5476, pp. 98–101, Jul. 2000, doi: 10.1126/science.289.5476.98.
- [251] G. Barillaro, A. Nannini, and F. Pieri, 'Dimensional Constraints on High Aspect Ratio Silicon Microstructures Fabricated by HF Photoelectrochemical Etching', *J. Electrochem. Soc.*, vol. 149, no. 3, p. C180, 2002, doi: 10.1149/1.1449953.
- [252] S. Matthias, F. Müller, and U. Gösele, 'Controlled nonuniformity in macroporous silicon pore growth', *Appl. Phys. Lett.*, vol. 87, no. 22, p. 224106, Nov. 2005, doi: 10.1063/1.2137688.
- [253] R. S. Wagner and W. C. Ellis, 'VAPOR-LIQUID-SOLID MECHANISM OF SINGLE CRYSTAL GROWTH', *Appl. Phys. Lett.*, vol. 4, no. 5, pp. 89–90, Mar. 1964, doi: 10.1063/1.1753975.
- [254] S. Barth, F. Hernandez-Ramirez, J. D. Holmes, and A. Romano-Rodriguez, 'Synthesis and applications of one-dimensional semiconductors', *Progress in Materials Science*, vol. 55, no. 6, pp. 563–627, Aug. 2010, doi: 10.1016/j.pmatsci.2010.02.001.
- [255] T. Mårtensson, M. Borgström, W. Seifert, B. J. Ohlsson, and L. Samuelson, 'Fabrication of individually seeded nanowire arrays by vapour–liquid–solid growth', *Nanotechnology*, vol. 14, no. 12, pp. 1255–1258, Dec. 2003, doi: 10.1088/0957-4484/14/12/004.
- [256] J. B. Hannon, S. Kodambaka, F. M. Ross, and R. M. Tromp, 'The influence of the surface migration of gold on the growth of silicon nanowires', *Nature*, vol. 440, no. 7080, pp. 69–71, Mar. 2006, doi: 10.1038/nature04574.
- [257] T. Shimizu, T. Xie, J. Nishikawa, S. Shingubara, S. Senz, and U. Gösele, 'Synthesis of Vertical High-Density Epitaxial Si(100) Nanowire Arrays on a Si(100) Substrate Using an Anodic

- Aluminum Oxide Template', *Adv. Mater.*, vol. 19, no. 7, pp. 917–920, Apr. 2007, doi: 10.1002/adma.200700153.
- [258] B. M. Kayes, M. A. Filler, M. C. Putnam, M. D. Kelzenberg, N. S. Lewis, and H. A. Atwater, 'Growth of vertically aligned Si wire arrays over large areas (>1cm<sup>2</sup>) with Au and Cu catalysts', *Appl. Phys. Lett.*, vol. 91, no. 10, p. 103110, Sep. 2007, doi: 10.1063/1.2779236.
- [259] K. E. Plass *et al.*, 'Flexible Polymer-Embedded Si Wire Arrays', *Adv. Mater.*, vol. 21, no. 3, pp. 325–328, Jan. 2009, doi: 10.1002/adma.200802006.
- [260] X. Li, 'Metal assisted chemical etching for high aspect ratio nanostructures: A review of characteristics and applications in photovoltaics', *Current Opinion in Solid State and Materials Science*, vol. 16, no. 2, pp. 71–81, Apr. 2012, doi: 10.1016/j.cossms.2011.11.002.
- [261] H. Han, Z. Huang, and W. Lee, 'Metal-assisted chemical etching of silicon and nanotechnology applications', *Nano Today*, vol. 9, no. 3, pp. 271–304, Jun. 2014, doi: 10.1016/j.nantod.2014.04.013.
- [262] Z. Huang, N. Geyer, P. Werner, J. de Boor, and U. Gösele, 'Metal-Assisted Chemical Etching of Silicon: A Review: In memory of Prof. Ulrich Gösele', *Adv. Mater.*, vol. 23, no. 2, pp. 285–308, Jan. 2011, doi: 10.1002/adma.201001784.
- [263] C. Q. Lai, H. Cheng, W. K. Choi, and C. V. Thompson, 'Mechanics of Catalyst Motion during Metal Assisted Chemical Etching of Silicon', *J. Phys. Chem. C*, vol. 117, no. 40, pp. 20802–20809, Oct. 2013, doi: 10.1021/jp407561k.
- [264] J. Yan, S. Wu, X. Zhai, X. Gao, and X. Li, 'Facile fabrication of wafer-scale, micro-spacing and high-aspect-ratio silicon microwire arrays', *RSC Adv.*, vol. 6, no. 90, pp. 87486–87492, 2016, doi: 10.1039/C6RA19104E.
- [265] R. A. Lai, T. M. Hymel, V. K. Narasimhan, and Y. Cui, 'Schottky Barrier Catalysis Mechanism in Metal-Assisted Chemical Etching of Silicon', *ACS Appl. Mater. Interfaces*, vol. 8, no. 14, pp. 8875–8879, Apr. 2016, doi: 10.1021/acsami.6b01020.
- [266] T. K. Adhila, R. D. Hemam, K. K. Nanda, and H. C. Barshilia, 'Effect of inhomogeneous mesoporosity and defects on the luminescent properties of slanted silicon nanowires prepared by facile metal-assisted chemical etching', *Journal of Applied Physics*, vol. 124, no. 10, p. 104303, Sep. 2018, doi: 10.1063/1.5044584.
- [267] Y. Jeong, C. Hong, Y. H. Jung, R. Akter, H. Yoon, and I. Yoon, 'Enhanced Surface Properties of Light-Trapping Si Nanowires Using Synergetic Effects of Metal-Assisted and Anisotropic Chemical Etchings', *Sci Rep*, vol. 9, no. 1, p. 15914, Nov. 2019, doi: 10.1038/s41598-019-52382-4.
- [268] R. Ghosh, K. Imakita, M. Fujii, and P. K. Giri, 'Effect of Ag/Au bilayer assisted etching on the strongly enhanced photoluminescence and visible light photocatalysis by Si nanowire arrays', *Phys. Chem. Chem. Phys.*, vol. 18, no. 11, pp. 7715–7727, 2016, doi: 10.1039/C5CP07161E.
- [269] K. Oda, Y. Nanai, T. Sato, S. Kimura, and T. Okuno, 'Correlation between photoluminescence and structure in silicon nanowires fabricated by metal-assisted etching: Correlation between photoluminescence and structure in silicon nanowires', *Phys. Status Solidi A*, vol. 211, no. 4, pp. 848–855, Apr. 2014, doi: 10.1002/pssa.201330163.
- [270] C. Chartier, S. Bastide, and C. Lévy-Clément, 'Metal-assisted chemical etching of silicon in HF–H<sub>2</sub>O<sub>2</sub>', *Electrochimica Acta*, vol. 53, no. 17, pp. 5509–5516, Jul. 2008, doi: 10.1016/j.electacta.2008.03.009.
- [271] Y. Song and J. Oh, 'Thermally driven metal-assisted chemical etching of GaAs with in-position and out-of-position catalyst', *J. Mater. Chem. A*, vol. 2, no. 48, pp. 20481–20485, Oct. 2014, doi: 10.1039/C4TA05095A.
- [272] M. DeJarld *et al.*, 'Formation of High Aspect Ratio GaAs Nanostructures with Metal-Assisted Chemical Etching', *Nano Lett.*, vol. 11, no. 12, pp. 5259–5263, Dec. 2011, doi: 10.1021/nl202708d.
- [273] H. Chen, H. Wang, X.-H. Zhang, C.-S. Lee, and S.-T. Lee, 'Wafer-Scale Synthesis of Single-Crystal Zigzag Silicon Nanowire Arrays with Controlled Turning Angles', *Nano Lett.*, vol. 10, no. 3, pp. 864–868, Mar. 2010, doi: 10.1021/nl903391x.
- [274] Z. Huang, T. Shimizu, S. Senz, Z. Zhang, N. Geyer, and U. Gösele, 'Oxidation Rate Effect on the Direction of Metal-Assisted Chemical and Electrochemical Etching of Silicon', *J. Phys. Chem. C*, vol. 114, no. 24, pp. 10683–10690, Jun. 2010, doi: 10.1021/jp911121q.



- [275] C. Chiappini, X. Liu, J. R. Fakhoury, and M. Ferrari, 'Biodegradable Porous Silicon Barcode Nanowires with Defined Geometry', *Adv. Funct. Mater.*, vol. 20, no. 14, pp. 2231–2239, Jun. 2010, doi: 10.1002/adfm.201000360.
- [276] X. Zhong, Y. Qu, Y.-C. Lin, L. Liao, and X. Duan, 'Unveiling the Formation Pathway of Single Crystalline Porous Silicon Nanowires', *ACS Appl. Mater. Interfaces*, vol. 3, no. 2, pp. 261–270, Feb. 2011, doi: 10.1021/am1009056.
- [277] Y. Qu, H. Zhou, and X. Duan, 'Porous silicon nanowires', *Nanoscale*, vol. 3, no. 10, p. 4060, 2011, doi: 10.1039/c1nr10668f.
- [278] P. Pieranski, 'Two-Dimensional Interfacial Colloidal Crystals', *Phys. Rev. Lett.*, vol. 45, no. 7, pp. 569–572, Aug. 1980, doi: 10.1103/PhysRevLett.45.569.
- [279] P. Patoka and M. Giersig, 'Self-assembly of latex particles for the creation of nanostructures with tunable plasmonic properties', *J. Mater. Chem.*, vol. 21, no. 42, p. 16783, 2011, doi: 10.1039/c1jm11936b.
- [280] J. R. Oh *et al.*, 'Wafer-scale colloidal lithography based on self-assembly of polystyrene nanospheres and atomic layer deposition', *J. Mater. Chem.*, vol. 20, no. 24, p. 5025, 2010, doi: 10.1039/b927532k.
- [281] T. Qiu *et al.*, 'Nanosphere Lithography: A Versatile Approach to Develop Transparent Conductive Films for Optoelectronic Applications', *Advanced Materials*, vol. 34, no. 19, p. 2103842, May 2022, doi: 10.1002/adma.202103842.
- [282] C. Stelling, C. R. Singh, M. Karg, T. A. F. König, M. Thelakkat, and M. Retsch, 'Plasmonic nanomeshes: their ambivalent role as transparent electrodes in organic solar cells', *Sci Rep*, vol. 7, no. 1, p. 42530, Feb. 2017, doi: 10.1038/srep42530.
- [283] J. Rybczynski, U. Ebels, and M. Giersig, 'Large-scale, 2D arrays of magnetic nanoparticles', *Colloids and Surfaces A: Physicochemical and Engineering Aspects*, vol. 219, no. 1–3, pp. 1–6, Jun. 2003, doi: 10.1016/S0927-7757(03)00011-6.
- [284] A. Kosiorek, W. Kandulski, H. Glaczynska, and M. Giersig, 'Fabrication of Nanoscale Rings, Dots, and Rods by Combining Shadow Nanosphere Lithography and Annealed Polystyrene Nanosphere Masks', *Small*, vol. 1, no. 4, pp. 439–444, Apr. 2005, doi: 10.1002/sml.200400099.
- [285] R. C. Rossi, M. X. Tan, and N. S. Lewis, 'Size-dependent electrical behavior of spatially inhomogeneous barrier height regions on silicon', *Appl. Phys. Lett.*, vol. 77, no. 17, pp. 2698–2700, Oct. 2000, doi: 10.1063/1.1319534.
- [286] J. C. Hulthen and R. P. Van Duyne, 'Nanosphere lithography: A materials general fabrication process for periodic particle array surfaces', *Journal of Vacuum Science & Technology A: Vacuum, Surfaces, and Films*, vol. 13, no. 3, pp. 1553–1558, May 1995, doi: 10.1116/1.579726.
- [287] W. Ruan, Z. Lu, N. Ji, C. Wang, B. Zhao, and J. Zhang, 'Facile Fabrication of Large Area Polystyrene Colloidal Crystal Monolayer via Surfactant-free Langmuir-Blodgett Technique', *Chemical Research in Chinese Universities*, vol. 23, no. 6, pp. 712–714, Nov. 2007, doi: 10.1016/S1005-9040(07)60155-X.
- [288] C. Haginoya, M. Ishibashi, and K. Koike, 'Nanostructure array fabrication with a size-controllable natural lithography', *Appl. Phys. Lett.*, vol. 71, no. 20, pp. 2934–2936, Nov. 1997, doi: 10.1063/1.120220.
- [289] P. Jiang and M. J. McFarland, 'Wafer-Scale Periodic Nanohole Arrays Templated from Two-Dimensional Nonclose-Packed Colloidal Crystals', *J. Am. Chem. Soc.*, vol. 127, no. 11, pp. 3710–3711, Mar. 2005, doi: 10.1021/ja042789+.
- [290] H. Van Bui, F. Grillo, and J. R. van Ommen, 'Atomic and molecular layer deposition: off the beaten track', *Chem. Commun.*, vol. 53, no. 1, pp. 45–71, 2017, doi: 10.1039/C6CC05568K.
- [291] D. Kim, H. Kang, J.-M. Kim, and H. Kim, 'The properties of plasma-enhanced atomic layer deposition (ALD) ZnO thin films and comparison with thermal ALD', *Applied Surface Science*, vol. 257, no. 8, pp. 3776–3779, Feb. 2011, doi: 10.1016/j.apsusc.2010.11.138.
- [292] G. Ali, S. S. Shinde, A. Sami, S. Kim, N. K. Wagh, and J.-H. Lee, 'Effect of interfacial passivation on inverted pyramid silicon/poly(3,4-ethylenedioxythiophene):Poly(styrenesulfonate) heterojunction solar cells', *Thin Solid Films*, vol. 709, p. 138139, Sep. 2020, doi: 10.1016/j.tsf.2020.138139.

- [293] P. Sinsersuksakul, J. Heo, W. Noh, A. S. Hock, and R. G. Gordon, 'Atomic Layer Deposition of Tin Monosulfide Thin Films', *Adv. Energy Mater.*, vol. 1, no. 6, pp. 1116–1125, Nov. 2011, doi: 10.1002/aenm.201100330.
- [294] C. H. Ahn, S. G. Cho, H. J. Lee, K. H. Park, and S. H. Jeong, 'Characteristics of TiN thin films grown by ALD using TiCl<sub>4</sub> and NH<sub>3</sub>', *Met. Mater. Int.*, vol. 7, no. 6, pp. 621–625, Nov. 2001, doi: 10.1007/BF03179261.
- [295] A. K. Singh, K. Adstedt, B. Brown, P. M. Singh, and S. Graham, 'Development of ALD Coatings for Harsh Environment Applications', *ACS Appl. Mater. Interfaces*, vol. 11, no. 7, pp. 7498–7509, Feb. 2019, doi: 10.1021/acsami.8b11557.
- [296] S. J. A. Zaidi, M. A. Basit, and T. J. Park, 'Advances in Atomic Layer Deposition of Metal Sulfides: From a Precursors Perspective', *Chem. Mater.*, vol. 34, no. 16, pp. 7106–7138, Aug. 2022, doi: 10.1021/acs.chemmater.2c00954.
- [297] R. G. Gordon, D. Hausmann, E. Kim, and J. Shepard, 'A Kinetic Model for Step Coverage by Atomic Layer Deposition in Narrow Holes or Trenches', *Chem. Vap. Deposition*, vol. 9, no. 2, pp. 73–78, Mar. 2003, doi: 10.1002/cvde.200390005.
- [298] J.-Y. Kim, J.-H. Ahn, S.-W. Kang, and J.-H. Kim, 'Step coverage modeling of thin films in atomic layer deposition', *Journal of Applied Physics*, vol. 101, no. 7, p. 073502, Apr. 2007, doi: 10.1063/1.2714685.
- [299] S. Cho, H. Kim, and M. M. Sung, 'Rapid growth of NiS<sub>x</sub> by atomic layer infiltration and its application as an efficient counter electrode for dye-sensitized solar cells', *Journal of Industrial and Engineering Chemistry*, vol. 77, pp. 470–476, Sep. 2019, doi: 10.1016/j.jiec.2019.05.013.
- [300] T. A. Ho *et al.*, 'Edge-On MoS<sub>2</sub> Thin Films by Atomic Layer Deposition for Understanding the Interplay between the Active Area and Hydrogen Evolution Reaction', *Chem. Mater.*, vol. 29, no. 17, pp. 7604–7614, Sep. 2017, doi: 10.1021/acs.chemmater.7b03212.
- [301] J. Yang and L. Liu, 'Trickle Flow Aided Atomic Layer Deposition (ALD) Strategy for Ultrathin Molybdenum Disulfide (MoS<sub>2</sub>) Synthesis', *ACS Appl. Mater. Interfaces*, vol. 11, no. 39, pp. 36270–36277, Oct. 2019, doi: 10.1021/acsami.9b12023.
- [302] T.-T. Lee *et al.*, 'Nucleation and growth mechanism for atomic layer deposition of Al<sub>2</sub>O<sub>3</sub> on two-dimensional WS<sub>2</sub> monolayer', *Journal of Vacuum Science & Technology A*, vol. 41, no. 1, p. 013201, Jan. 2023, doi: 10.1116/6.0001913.
- [303] A. W. Weimer, 'Particle atomic layer deposition', *J Nanopart Res*, vol. 21, no. 1, p. 9, Jan. 2019, doi: 10.1007/s11051-018-4442-9.
- [304] C. A. Wilson, J. A. McCormick, A. S. Cavanagh, D. N. Goldstein, A. W. Weimer, and S. M. George, 'Tungsten atomic layer deposition on polymers', *Thin Solid Films*, vol. 516, no. 18, pp. 6175–6185, Jul. 2008, doi: 10.1016/j.tsf.2007.11.086.
- [305] K. Sridharan, E. Jang, Y. M. Park, and T. J. Park, 'Superior Photostability and Photocatalytic Activity of ZnO Nanoparticles Coated with Ultrathin TiO<sub>2</sub> Layers through Atomic-Layer Deposition', *Chem. Eur. J.*, vol. 21, no. 52, pp. 19136–19141, Dec. 2015, doi: 10.1002/chem.201502876.
- [306] X. Liang *et al.*, 'Novel Processing to Produce Polymer/Ceramic Nanocomposites by Atomic Layer Deposition', *J American Ceramic Society*, vol. 90, no. 1, pp. 57–63, Jan. 2007, doi: 10.1111/j.1551-2916.2006.01359.x.
- [307] J. A. McCormick, B. L. Cloutier, A. W. Weimer, and S. M. George, 'Rotary reactor for atomic layer deposition on large quantities of nanoparticles', *Journal of Vacuum Science & Technology A: Vacuum, Surfaces, and Films*, vol. 25, no. 1, pp. 67–74, Jan. 2007, doi: 10.1116/1.2393299.
- [308] D. M. King, J. A. Spencer, X. Liang, L. F. Hakim, and A. W. Weimer, 'Atomic layer deposition on particles using a fluidized bed reactor with in situ mass spectrometry', *Surface and Coatings Technology*, vol. 201, no. 22–23, pp. 9163–9171, Sep. 2007, doi: 10.1016/j.surfcoat.2007.05.002.
- [309] L. F. Hakim, J. L. Portman, M. D. Casper, and A. W. Weimer, 'Aggregation behavior of nanoparticles in fluidized beds', *Powder Technology*, vol. 160, no. 3, pp. 149–160, Dec. 2005, doi: 10.1016/j.powtec.2005.08.019.
- [310] A. Y. Kovalgin *et al.*, 'Hot-Wire Assisted ALD: A Study Powered by In Situ Spectroscopic Ellipsometry', *Adv. Mater. Interfaces*, vol. 4, no. 18, p. 1700058, Sep. 2017, doi: 10.1002/admi.201700058.

- [311] M. Yang, A. A. I. Aarnink, A. Y. Kovalgin, Dirk. J. Gravesteijn, R. A. M. Wolters, and J. Schmitz, 'Comparison of tungsten films grown by CVD and hot-wire assisted atomic layer deposition in a cold-wall reactor', *Journal of Vacuum Science & Technology A: Vacuum, Surfaces, and Films*, vol. 34, no. 1, p. 01A129, Jan. 2016, doi: 10.1116/1.4936387.
- [312] V. Miikkulainen *et al.*, '(Invited) Photo-Assisted ALD: Process Development and Application Perspectives', *ECS Trans.*, vol. 80, no. 3, pp. 49–60, Aug. 2017, doi: 10.1149/08003.0049ecst.

## Copyrights and permissions



### Tailoring the Structural, Optical, and Photoluminescence Properties of Porous Silicon/TiO<sub>2</sub> Nanostructures

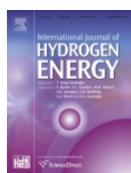
Author: Igor Iatsunskiy, Mykola Pavlenko, Roman Viter, et al

Publication: The Journal of Physical Chemistry C

Publisher: American Chemical Society

Date: Apr 1, 2015

Copyright © 2015, American Chemical Society



### Silicon/TiO<sub>2</sub> core-shell nanopillar photoanodes for enhanced photoelectrochemical water oxidation

Author: Mykola Pavlenko, Katarzyna Siuzdak, Emerson Coy, Mariusz Jancelewicz, Stefan Jurga, Igor Iatsunskiy

Publication: International Journal of Hydrogen Energy

Publisher: Elsevier

Date: 21 December 2017

© 2017 Hydrogen Energy Publications LLC. Published by Elsevier Ltd. All rights reserved.



### Enhancing photocatalytic performance and solar absorption by Schottky nanodiodes heterojunctions in mechanically resilient palladium coated TiO<sub>2</sub>/Si nanopillars by atomic layer deposition

Author:

Emerson Coy, Katarzyna Siuzdak, Mykola Pavlenko, Karol Załęski, Octavio Graniel, Marcin Ziótek, Sebastien Balme, Philippe Miele, Matthieu Weber, Mikhael Bechelany, Igor Iatsunskiy

Publication: Chemical Engineering Journal

Publisher: Elsevier

Date: 15 July 2020

© 2019 Elsevier B.V. All rights reserved.



### Effect of porous silicon substrate on structural, mechanical and optical properties of MOCVD and ALD ruthenium oxide nanolayers

Author:

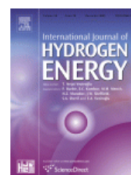
Ievgen Brytavskiy, Kristína Hušková, Valerii Myndrul, Mykola Pavlenko, Emerson Coy, Karol Zaleski, Dagmar Gregušová, Luis Yate, Valentyn Smyntyna, Igor Iatsunskiy

Publication: Applied Surface Science

Publisher: Elsevier

Date: 31 March 2019

© 2018 Elsevier B.V. All rights reserved.



### Enhanced solar-driven water splitting of 1D core-shell Si/TiO<sub>2</sub>/ZnO nanopillars

Author: Mykola Pavlenko, Katarzyna Siuzdak, Emerson Coy, Karol Załęski, Mariusz Jancelewicz, Igor Iatsunskiy

Publication: International Journal of Hydrogen Energy

Publisher: Elsevier

Date: 9 October 2020

© 2019 Hydrogen Energy Publications LLC. Published by Elsevier Ltd. All rights reserved.



### One and two-phonon Raman scattering from nanostructured silicon

Author: Igor Iatsunskiy, Grzegorz Nowaczyk, Stefan Jurga, Victoriia Fedorenko, Mykola Pavlenko, Valentyn Smyntyna

Publication: Optik - International Journal for Light and Electron Optics

Publisher: Elsevier

Date: September 2015

Copyright © 2015 Elsevier GmbH. All rights reserved.



### Structural and XPS studies of PSi/TiO<sub>2</sub> nanocomposites prepared by ALD and Ag-assisted chemical etching

Author: Igor Iatsunskiy, Mateusz Kempirski, Grzegorz Nowaczyk, Mariusz Jancelewicz, Mykola Pavlenko, Karol Załęski, Stefan Jurga

Publication: Applied Surface Science

Publisher: Elsevier

Date: 30 August 2015

Copyright © 2015 Elsevier B.V. All rights reserved.

## List of figures

**Figure 1.** Graphic representation of photo-driven water-splitting process occurring on TiO<sub>2</sub> nanoparticle as an example of main stages of water-splitting process occurring.

**Figure 2.** Schematic illustration of charge carriers photoexcitation on n-type and p-type semiconductors, and transfer to OER and HER sites, respectively

**Figure 3.** Various approaches in designing cells configuration for solar water splitting.

**Figure 4.** Configurations of photoanode, photocathode and combined PEC cells considering the energy diagrams of the employed semiconductor material.

**Figure 5.** Graphical representation of the photoinduced water-splitting on (a) single-component photocatalysts, (b) type-II heterojunction photocatalysts and (c) Z-scheme with electron mediator involved.

**Figure 6.** Band gaps values comparison of some materials widely used for photocatalytic water-splitting applications.

**Figure 7 .** Graphical representation of LSPR influence on the optical properties of the material [179]. (a) Plasmon oscillations in phase with the incident light induce field perturbation resulting in absorption and scattering changes. Effect for nanoparticles: (b) smaller than 15 nm and (c) larger than 15 nm.

**Figure 8.** Schematic representation of PEC operation of 1D ZnO heterostructures enhanced by Au plasmonic nanoparticles [182].

**Figure 9.** Graphical representation of SPP [179]: (a) propagation of SPP along the metal-dielectric interface boundary and decaying of its amplitude out of the interface, (b) representation of SPP existence and extreme values in  $\omega(k)$  space, (c) an illustration of SPP wave at the interface metal-dielectric, (d) representation of SPP existence under certain incident angles.

**Figure 10 .** Some examples of 1D Si nanostructures applications [243].

**Figure 11 .** (a) Graphical representation of main stages in a typical MACE process. (b) A representation of redox levels of commonly used metal catalysts in MACE along with the H<sub>2</sub>O<sub>2</sub> oxidant in relation to Si energy levels [243].

**Figure 12.** Schematic representation of main steps of a typical ALD process: (a) the introduction and chemisorption of the first precursor; (b) the first purging of the operational chamber with chemically inert gas, like argon or nitrogen; (c) the introduction of the second

precursor to react with the first one chemisorbed on the substrate; (d) the second purging the inert gas to remove the byproducts.

**Figure 13.** A representation of the ALD window related to the substrate temperature and the growth per cycle value.

### **List of tables**

**Table 1.** Schematic representation of OER occurrence involving active surface sites (M - notation of active surface site)